ESD-TR-67-453
ESTI FILE COPY

ESD RECORD COPY
RETURN TO
SCIENTIFIC & TECHNICAL INFORMATION DIVISION

ESD-TR-67-453

(Final Report)

LARGE APERTURE SEISMIC ARRAYS

June 1967

ESD ACCESSION LIST
ESTI Call No. AL 37644
Copy No. 1 of 1 cys.

DIRECTORATE OF PLANNING AND TECHNOLOGY
ELECTRONIC SYSTEMS DIVISION
AIR FORCE SYSTEMS COMMAND
UNITED STATES AIR FORCE
L. G. Hanscom Field, Bedford, Massachusetts

Sponsored by:

Advanced Research Projects Agency, Washington, D. C.
ARPA Order No. 800

This document has been approved for public release and sale; its distribution is unlimited.

(Prepared under Contract No. AF 19(628)-5981 by General Atronics Corp., 1200 East Mermaid Lane, Philadelphia, Pennsylvania 19118.)

AD657349

LEGAL NOTICE

When U. S. Government drawings, specifications or other data are used for any purpose other than a definitely related government procurement operation, the government thereby incurs no responsibility nor any obligation whatsoever; and the fact that the government may have formulated, furnished, or in any way supplied the said drawings, specifications, or other data is not to be regarded by implication or otherwise as in any manner licensing the holder or any other person or conveying any rights or permission to manufacture, use, or sell any patented invention that may in any way be related thereto.

OTHER NOTICES

Do not return this copy. Retain or destroy.

ESD-TR-67-453

(Final Report)

LARGE APERTURE SEISMIC ARRAYS

June 1967

DIRECTORATE OF PLANNING AND TECHNOLOGY
ELECTRONIC SYSTEMS DIVISION
AIR FORCE SYSTEMS COMMAND
UNITED STATES AIR FORCE
L. G. Hanscom Field, Bedford, Massachusetts

Sponsored by:

Advanced Research Projects Agency, Washington, D. C.
ARPA Order No. 800

This document has been approved for public release and sale; its distribution is unlimited.

(Prepared under Contract No. AF 19(628)-5981 by General Atronics Corp., 1200 East Mermaid Lane, Philadelphia, Pennsylvania 19118.)

FOREWORD

This research was supported by the Advanced Research Projects Agency. The Electronic Systems Division technical project officer for Contract AF 19(628)-5981 is Major Cleve P. Malone (ESL-2).

We wish to acknowledge the very considerable support and assistance that have been provided during the course of this program by the Advanced Research Projects Agency, the Earth Sciences Division of Teledyne, Inc., the Electronics Systems Division LASA Office, the Institute for Defense Analyses, the Lincoln Laboratory, and the Vela Seismological Center.

This technical report has been reviewed and is approved.

PAUL W. RIDENOUR, Lt. Col., USAF
Chief, LASA Office
Directorate of Planning and Technology
Electronic Systems Division

ABSTRACT

The topics presented in this report fall into three general categories. The first set of topics is concerned with the directional properties of large aperture seismic arrays. Theoretical derivations and calculated array patterns are presented for the following seismic arrays: the existing LASA-Montana, a random array with an aperture comparable to LASA-Montana (200 km), and a continental-size array with an aperture of several thousand kilometers. Finally, the use of LASA-Montana for determining epicenter of seismic events is discussed and results are presented that indicate errors on the order of 60 kilometers.

The second set of topics deals with array processing for enhancement of signal-to-noise ratio or discrimination between surface-focus events and earthquakes. Data on the correlation across LASA of various portions of seismograms are presented, and the implications for array processing gains are briefly discussed. Two tests for identifying earthquakes with depths between 10 and 40 km are introduced, and experiments on approximately 40 seismic events, on which both tests performed quite well, are summarized. Finally, the possibility of using DIMUS processing on a seismic array is discussed. Calculations are presented based on the conventional DIMUS processing as well as on a modified DIMUS scheme that appears to be significantly better.

The last set of topics involve spectral analyses. Calculations based on several seismic events show a significant amount of "signal" energy in the spectral region of 4 Hz in most of the records resulting from surface-focus events. Calculations based on records from deep Fiji Island earthquakes suggest an upper mantle Q of less than 500 for that region.

TABLE OF CONTENTS

SECTION	TITLE	PAGE
I	INTRODUCTION	1
	1.1 Directional Properties of Large Aperture Seismic Arrays	2
	1.2 Array Processing for S/N Enhancement or Discrimination	3
	1.3 Spectral Analyses	5
	1.4 Organization of Report	5
II	DERIVATION OF THE DIMENSIONS OF THE TELESEISMIC BEAM OF A LARGE APERTURE SEISMIC ARRAY	6
	2.1 Problem Definition	6
	2.2 Dependence of Array Contour Dimensions upon Array Dimensions	8
	2.3 Definition of Beamwidth	9
	2.4 Transverse Extent of the Array Contour	11
	2.5 Radial Extent of the Array Contour	12
	2.6 Application of Beam Theory to LASA	14
	2.7 Summary and Conclusions	15
III	ARRAY PATTERN COMPUTATIONS	17
	3.1 Radial and Transverse Beam Patterns	17
	3.2 Range Loss Corrections	20
	3.3 Summary of LASA Beam Pattern Results	21
IV	RANDOM ARRAY THEORY AND SIMULATION	26
	4.1 Radial Beam of an Array with Random Elements	26
	4.2 Random Array Simulation	28
	4.3 Summary and Conclusions	30
V	DETECTION OF NUCLEAR EXPLOSIONS IN THE PRESENCE OF LARGE NATURAL EVENTS	37
	5.1 Seismic Dipoles	38
	5.2 Calculated Patterns for Continental-Size Arrays	45
	5.3 Summary and Conclusions	48
VI	LOCATION OF EVENTS USING A SINGLE LASA	50
	6.1 Conventional and Array Location Techniques	50
	6.2 Limitation of Angular Accuracy by Additive Noise	52
	6.3 Effect of Timing Errors on Angular Accuracy	54
	6.4 Relationship Between Timing Errors, Array Gain, and Array Pointing Error	57
	6.5 Computational Procedures	58
	6.6 Experimental Results	60

TABLE OF CONTENTS - Continued

SECTION	TITLE	PAGE
VII	ARRAY PROCESSING FOR SIGNAL-TO-NOISE ENHANCEMENT	70
	7.1 DS Processing Gain as a Function of Signal and Noise Coherence	71
	7.2 DS Processing Gain -- Contributions of Local and Teleseismic Noise	73
	7.3 The Seismic Array as a Diversity System	74
	7.4 Summary and Conclusions	76
VIII	SPATIAL CORRELATION ACROSS AN ARRAY	78
	8.1 Spatial Correlations Observed Across LASA from LONGSHOT	78
	8.2 Spatial Correlation Observed Across Continental-Size Arrays	85
	8.3 Summary and Conclusions	86
IX	CODA CORRELATION AS A DISCRIMINANT	87
	9.1 Methods	87
	9.2 Results	88
	9.3 Discussion	91
	9.4 Dependence on Array Characteristics	92
	9.5 Summary and Conclusions	93
X	AUTOMATIC pP TEST FOR SHALLOW EARTHQUAKES	95
	10.1 Description of Automatic pP Test	96
	10.2 Parameter Choices	100
	10.3 Experimental Results	103
	10.4 Summary and Conclusions	118
XI	DIMUS ARRAY PROCESSING	124
	11.1 DIMUS Application to Seismic Arrays	125
	11.2 Detection Aspects of DIMUS Beamforming for LASA	126
	11.3 Identification with a DIMUS Array Processor	132
	11.4 Summary and Conclusions	137
XII	SPECTRAL ESTIMATES OF SEISMIC EVENTS	139
	12.1 Theoretical Analysis	140
	12.2 Computer Implementation of Spectral Calculations	148
	12.3 Sample Calculations on One Event	151
	12.4 Summary of Calculations on Five Seismic Events	158
	12.5 Summary of Assumptions and Potential Sources of Error	165
	12.6 Conclusions	166

TABLE OF CONTENTS - Continued

SECTION	TITLE	PAGE
XIII	ATTENUATION OF SEISMIC WAVES IN THE EARTH'S UPPER MANTLE	167
	13.1 Description of the Experiment	167
	13.2 Experimental Results	170
	13.3 Extension of the Method to Analyze Aseismic Regions	179
	13.4 Summary and Conclusions	179
APPENDIX A - TABLES		181
APPENDIX B - ANGULAR ACCURACY OF A PHASED SEISMIC ARRAY		191
REFERENCES		195

LIST OF FIGURES

2.1	Geometry of Teleseismic Array and Beam	7
2.2	Equivalent Linear Array	10
2.3	Geometry for the Computation of θ_t	10
2.4	Geometry for the Computation of θ_r	13
2.5	Smoothed Derivatives of the P Phase Travel Time Relevant to the Teleseismic Beam Dimensions	16
3.1	Geometry for Array Pattern Computations	18
3.2	Radial Pattern for LASA Focused at Amchitka	22
3.3	Transverse Pattern for LASA Focused at Amchitka	22
3.4	Radial Pattern for LASA Focused at Kuriles	23
3.5	Transverse Pattern for LASA Focused at Kuriles	23
3.6	Radial Pattern for LASA Focused at Kazakh	24
3.7	Transverse Pattern for LASA Focused at Kazakh	24
4.1	Geometry for Random Array Simulation	27
4.2	Random Array	29
4.3	Radial Pattern for Random Array Focused at Amchitka	32
4.4	Transverse Pattern for Random Array Focused at Amchitka	32
4.5	Radial Pattern for Random Array Focused at Kuriles	33
4.6	Transverse Pattern for Random Array Focused at Kuriles	33
4.7	Radial Pattern for Random Array Focused at Kazakh	34
4.8	Transverse Pattern for Random Array Focused at Kazakh	34
4.9	Effect of the Number of Elements on the Radial Pattern of a Random Array	35
4.10	Effect of the Number of Elements on the Transverse Pattern of a Random Array	36
5.1	Seismic Dipole	39
5.2	Seismic Dipole Output	39
5.3	Seismic Dipole Location for Pattern Computation	41
5.4	Expected Pattern for Seismic Dipole	41
5.5	Dipole Pattern	43
5.6	Region of the Total Pattern of the Dipole Illustrated in Figure 5.5	44
5.7	Pattern of an Array of Two Dipoles	44
5.8	Continental-Size Array Patterns (27 Elements)	46
5.9	Continental-Size Array Patterns (17 Elements)	47
6.1	RMS Pointing and Time Errors vs. Peak Array Output	59
6.2	Unsquinted Azimuth Beam	61
6.3	Azimuth Difference Pattern	62
6.4	Unsquinted Radial Beam	63
6.5	Radial Difference Beam	64
6.6	Maps of Computed Epicenters	69

LIST OF FIGURES - Continued

7.1	DS Gain of LASA vs. Average Local Noise Correlation	75
8.1	LONGSHOT Coda Correlation Across LASA	80
8.2	LONGSHOT P-Wave Correlation Across LASA	82
8.3	LONGSHOT Noise Correlation Across LASA	84
9.1	Coda Correlation Cumulative Distribution Functions	90
10.1	Geometry of Surface Reflection	97
10.2	Automatic pP Test (ε_j) - Earthquakes	105
10.3	Automatic pP Test Comparison of ε_j and η_j	108
10.4	Automatic pP Test (η_j) - Earthquakes	110
10.5	Automatic pP Test (η_j) - Surface-Focus Events	115
10.6	Automatic pP Test (η_j) - Dependence on Number of Stations	121
11.1	Algerian Event - Single Seismometer WMO	127
11.2	Analog and DIMUS Beams	128
11.3	Probability Density for Signal Plus Noise	130
11.4	Representative DIMUS Detection Capability	131
11.5	Statistical Equivalent of DIMUS for Gaussian Noise with rms Value σ_n	133
11.6	Comparison of Analog and DIMUS Processing	135
11.7	Comparison of Beam Processing Techniques	136
12.1	Examples of Two Time Windows and Their Transforms	142
12.2	Seismogram for Sample Spectral Calculation	152
12.3	Autocorrelation Function for Sample Spectral Calculation	152
12.4	Sample Spectral Calculations - Unfiltered	154
12.5	Sample Spectral Calculations - Filtered	155
12.6	Spectral Calculations Magnitude 6.3 Event	161
12.7	Spectral Calculations A0 Center Element - Four Events	162
12.8	Spectral Calculations B1 Center Element - Four Events	163
12.9	Spectral Calculations F4 Center Element - Four Events	164
13.1	Ray Paths for pP and P	168
13.2	Epicenter Locations	171
13.3	Least Squares Fits to the Experimental Ratios of Energy Spectra	173
13.4	Least Squares Fits to the Experimental Ratios of Energy Spectra	174
13.5	Least Squares Fits to the Experimental Ratios of Energy Spectra	175
13.6	Spectra for 7 October 1963 Event	176
13.7	Spectra for 7 December 1963 Event	177
13.8	Spectra for 26 April 1964 Event	178
B-1	Linear Phased Array Geometry	192

LIST OF TABLES

I	Standard Deviation of Local Anomaly Estimates for LASA Clusters for Three Regions	55
II	Comparison of C&GS and Computed Epicenters for LASA	66
III	Comparison of C&GS and Computed Bearings and Ranges for LASA	66
IV	Comparison of C&GS and Computed Epicenters for LASA Without the F-Ring	67
V	Comparison of C&GS and Computed Bearings and Ranges for LASA Without the F-Ring	67
VI	Amplitude-Inferred and Measured Pointing Errors for LASA	68
VII	Amplitude-Inferred and Measured Pointing Errors for LASA Without the F-Ring	68
VIII	Coda Correlation Across LASA	81
IX	Summary Table for Spectral Estimates	160
X	List of Events	182
XI	Summary of Depth Estimates and Correlations - 11 Earthquakes	183
XII	Summary of Estimates and Correlations - 20 Earthquakes	184-5
XIII	Summary of Depth Estimates and Correlations - 12 Surface-Focus Events	186
XIV	Station List for Calculations Summarized in Tables XI-XIII	187-8
XV	Station List for Array Pattern Presented in Figure 5.8	189
XVI	Station List for Array Pattern Presented in Figure 5.9	190

SECTION I

INTRODUCTION

This is the final report on Contract AF19(628)-5981. This report summarizes the work performed under this contract. The various topics studied under the contract fall into three general categories. Sections II through VI are primarily concerned with directional properties of large aperture seismic arrays. The arrays considered in these sections vary from LASA-Montana dimensions (200 km) to continental-size (3000-7000 km) arrays. Sections VII through XI also consider arrays with apertures varying from 200 km to 7000 km, but in these sections the emphasis is on signal-to-noise enhancement or discrimination rather than directional properties. Of course, these topics are not unrelated: an antenna's gain usually increases when its beamwidth decreases. Finally, Sections XII and XIII discuss spectral analyses of seismic records.

Brief summaries of the contents of the several sections follow. For the convenience of the reader, we shall first cite what we regard as "highlights" of this report. Several array pattern computations are presented. In order of increasing quality (in terms of beamwidth and sidelobe level), these include calculations based on: the existing LASA-Montana (Section III); "random" arrays with apertures comparable to LASA-Montana (Section IV); and "continental-size" arrays with apertures measured in thousands of kilometers (Section V).

Two calculations that appear to have considerable value for classifying earthquakes with depths between 10 and 40 km are discussed in Sections IX and X. Calculations based on approximately 40 seismic events are presented. These calculations indicate that these tests will function very well, at least for continental-size arrays. An ability to identify earthquakes in the 10-40 km depth region is considered to be of considerable value since deeper earthquakes are already relatively easy to identify as such.

Finally, the question of high-frequency content of seismograms resulting from surface-focus events has been studied. Results indicate a statistically significant amount of signal energy in the region of 4 Hz for most of the surface-focus event data processed to date. Whether or not this region of the spectrum will be useful in discriminating between earthquakes and nuclear tests remains to be determined, but the existence of significant amounts of high-frequency energy indicates that this possibility merits further study.

1.1 DIRECTIONAL PROPERTIES OF LARGE APERTURE SEISMIC ARRAYS

Section II presents a derivation of the dimensions of a teleseismic beam. These calculations are based on some simple spherical geometry, the J-B travel-time tables, and the assumption that the seismic signals of interest may be treated as continuous sine waves. The results of this derivation provide a relatively simple description of the width of a teleseismic beam (in geographical coordinates) in terms of the aperture of the seismic array and the range to the focus point. These results are compared with calculated array patterns for LASA and for a random array of LASA dimensions and reasonable agreement is observed. This derivation was originally intended to provide a rough estimate of the extent of the array pattern that would correspond to a given range and aperture. As it is now relatively easy (by means of the appropriate computer program) to calculate patterns for specific arrays, we do not anticipate any further use of the results of this derivation. Several of these computer-aided pattern calculations, which employ a more realistic signal than the continuous sine wave, are presented in Section III.

Section III presents calculated array patterns for LASA-Montana focused at each of three regions. The signal waveform used in these calculations was the LONGSHOT transient as observed at the center element of the LASA A0 cluster. For each of three regions, the transverse pattern and two radial patterns are given. One of the radial patterns includes the effect of attenuation and geometric spreading; the other does not.

As discussed in Section III, the clustering of seismometers in LASA is thought to lead to a pattern that differs little from the pattern that would be obtained by using only the 21 center elements. (In fact, the calculations of Section III are actually only based on the 21 center elements.) One consequence of this observation is that the LASA-Montana is essentially a very "thin" array, and therefore the sidelobes of its pattern are relatively large. This fact is illustrated by the calculations presented in Section III.

If there were no economic or other practical constraints that favored the clustering of seismometers, it would be very advantageous not to cluster seismometers. This observation is illustrated in Section IV, where one kind of unclustered array - the "random" array - is considered. Section IV briefly describes a simple theory of random arrays. These theoretical comments are illustrated by the calculated patterns for random arrays of the dimensions of LASA-Montana. These calculations indicate that an array comparable to LASA-Montana, but having a random distribution of elements across the aperture rather than a clustered distribution, would have an array pattern that is significantly superior to that of the existing clustered LASA.

Section V considers the problem of detecting a covert underground nuclear test in the presence of large natural earthquake. Two approaches to this problem are considered: the first consists of inserting a null in the array pattern in the direction of the earthquake; the second approach consists simply of steering the main beam of the array at the suspected test site. This method requires a much narrower main-beam and lower sidelobes than could be obtained from LASA. This suggests that continental-size arrays would be necessary. Calculated array patterns for such arrays are presented, and these show a beamwidth that is an order of magnitude less than that of LASA.

Section VI discusses various approaches to the problem of estimating epicenters from seismic records available from LASA-Montana. It has been found that the limiting factors for such measurements are the errors in estimating local travel-time anomalies and the travel-time tables used in the calculations. Errors in the measurements ranged from some 50 to 350 kilometers, with the larger errors attributed to use of the J-B travel-time tables. It is hypothesized that with the new Herrin tables, location errors can be held to less than the 50-kilometer figure cited above.

1.2 ARRAY PROCESSING FOR S/N ENHANCEMENT OR DISCRIMINATION

Section VII considers seismic array processing for the purpose of enhancing signal-to-noise ratio. For the simplest of processing schemes, delayed sum, simple formulas are derived which express the processing gain in terms of spatial correlations of signal and noise, and also in terms of the relative contributions of local and teleseismic noise. Finally, the similarities and differences between array processing in this context and diversity combining in the context of communications are discussed.

Section VIII presents data on spatial correlation that relate to the formulas of Section VII. Most of the calculations are based on LONGSHOT data as recorded at LASA. These data indicate good signal correlation and noise decorrelation between LASA clusters. Also discussed in this section are similar data for a continental-size array. These data also indicate good signal correlation and noise decorrelation across elements.

Section IX describes and illustrates a coda correlation discriminant which appears to be very effective at separating surface-focus events from earthquakes with depths between 10 and 40 km. (One surface-focus event out of the 12 studied was ambiguous, and all of the 24 moderate depth earthquakes were easily classified.) This test represents a strengthening of the complexity test used by several investigators. Here the presence of aftershocks following rapidly after the P-phase of the earthquakes is sought in the coherence of these signals as received at a number of seismometers, rather than by observation of the presence of pulses

of energy in the thirty second interval following the arrival of the P-phase. Basically the test consists of calculating the average paired correlation coefficient (zero lag) for the coda portions of the seismic records. For moderate depth earthquakes, values near 0.2 or 0.3 are expected. For other events, values near zero are expected. As is the case for the depth determinations discussed in the next paragraph, there exists the possibility that by increasing the coda interval used, or by the use of several coda windows, the correlation test could be extended to depths of several hundreds of kilometers. This extension has not, however, been attempted.

Section X presents an automatic test for estimating depth by means of coherent addition of the pP phase across a seismic array. This test is quite successful at choosing the correct depth for earthquakes in the 10-40 km depth region. For events outside that region (including surface-focus events) the test usually indicates that the depth is out of the 10-40 km region. The 40 km lower limit on depth estimates results from the limitation of the depths searched for pP to the region above the moho. This limitation was imposed as a convenience, so that an average propagation velocity could be employed in the calculations. Extension of this lower limit could be made by a larger search window which takes proper account of the velocity gradient below the moho. (If this could be adequately approximated for the region of interest.) Finally, it should be noted that there is considerable correlation between this estimate of depth and the coda correlation test previously described. In part, the coda correlation test is effective because of the presence of the pP-phase in the coda interval tested. The two tests are quite different,however, in the following sense. To be effective, the depth test requires that the ranges from the epicenter to the stations vary sufficiently to insure an appreciable moveout of the pP phase across the array. In the coda correlation test, this large extent in range is not necessary. Here the stations need only be separated from each other by an amount large enough so that the crustal reverberations below the receiving sites be decorrelated (approximately 100 km. See Section VIII). This suggests that it may be possible to use the coda correlation test in cases where no depth determination can be made.

Section XI discusses the properties of DIMUS (digital, multiple steered) processing for seismic arrays. Basically, this processing involves hard-limiting of each element output so that each sample of each seismogram is a single binary number. The advantages for data transmission and handling are clear. For large signal-to-noise ratios the DIMUS output can be considerably distorted. To correct for this problem, a modified DIMUS processing scheme, which uses analog (unclipped) information from one channel is presented. Calculations based on both the conventional and the modified DIMUS schemes are presented. These calculations suggest that the fidelity of the DIMUS output may be sufficient to allow application of various diagnostic tests for classifying seismic events.

1.3 SPECTRAL ANALYSES

Section XII summarizes work directed at exploring the existence and potential value for discrimination of high-frequency energy in seismograms. This section begins with a theoretical discussion of the statistical properties of spectral estimates of transients. Calculations have been performed on several seismic events, and these indicate that a statistically significant amount of signal energy is present in the neighborhood of 4 Hz in all but one of the seismic records from the surface-focus events that have been studied.

Section XIII employs the same spectral calculations for a somewhat different objective. The purpose of this study was to aid in the selection of future array sites with good high-frequency characteristics. This would be especially important if the high-frequency content of seismic signals, which is discussed in Section XII, should prove to have real significance. By comparing the spectra of the P and pP phases for very deep earthquakes, it is possible to infer the absorption characteristics of the upper mantle at the epicenter region. Three deep Fiji Island earthquakes have been studied. All of them lead to estimated Q's for the upper mantle in the Fiji region that are less than 500, indicating that the attenuation is one order of magnitude larger than expected from previous measurement. Section XIII also includes a proposed method for extending the study to treat the upper mantle of aseismic regions to aid in the site selection problem.

1.4 ORGANIZATION OF REPORT

The contents of the various sections, and the grouping of sections according to general categories, are discussed above. Since the calculations presented in many of the sections are based on the same collection of events, several summary tables apply to more than one section. All of the tables which apply to more than one section appear in Appendix A. Tables which apply to a single section appear in the appropriate section, except in a few cases where the table contains details that are not important for an understanding of the material presented in that section. In these cases, the tables appear in Appendix A.

The tables that a reader of this report is most likely to consult are the master list of events and the three tables summarizing the coda correlation and pP test calculations. Tables that appear for the sake of completeness, but are probably not of interest to the average reader, include those listing the stations used in the calculations employing continental-size arrays.

Finally, Appendix B presents a brief discussion of the effects of noise on the location precision available from an array. The results of this appendix are cited in Section VI.

SECTION II

DERIVATION OF THE DIMENSIONS OF THE TELESEISMIC BEAM OF A LARGE APERTURE SEISMIC ARRAY

2.1 PROBLEM DEFINITION

The purpose of this section is to derive certain geometrical characteristics associated with teleseismic arrays. These results have been presented without derivation in earlier reports (1,2).

Let us consider a collection of spatially separated seismometers whose outputs are combined to form a receiving array. The resulting array will tend to enhance signals emanating from certain directions and attenuate signals emanating from other directions.

These directional characteristics of the array are summarized in terms of the array pattern. The array pattern itself is characterized by a main beam whose center is in the direction of maximum array response and a number of minor beams, or sidelobes. The array pattern varies as a function of the frequency of the received signal. We shall consider the array pattern corresponding to the dominant period τ of the received seismic signal.

In the following, we shall limit our discussion to consideration of the main beam. Also, it will be assumed that far field conditions apply. The array pattern will be three-dimensional and hence it will be convenient to consider two-dimensional array patterns obtained from certain two-dimensional cuts taken from the three-dimensional array pattern. The extent of the main beam of the two-dimensional array pattern is specified in terms of the beamwidth of the array pattern. A number of definitions are available for beamwidth. An example is the 3 dB beamwidth which is defined as the angular distance between points on the two-dimensional array pattern at which the response is down 3 dB from the maximum response. We shall adopt a different definition of array beamwidth which offers certain mathematical simplifications. The chosen definition for array beamwidth will be explained below.

Consider the geometry of Figure 2.1, which shows a seismic array located at the pole of a spherical earth. Due to the nature of seismic propagation,it is necessary to define directions to the array in terms of curved ray paths such as $\overline{QS}$. Let the array be focused at a point S on the surface of the earth. That is, the array elements are adjusted by means of time delays to compensate for the differential travel times for seismic energy arriving from the point S to the various elements

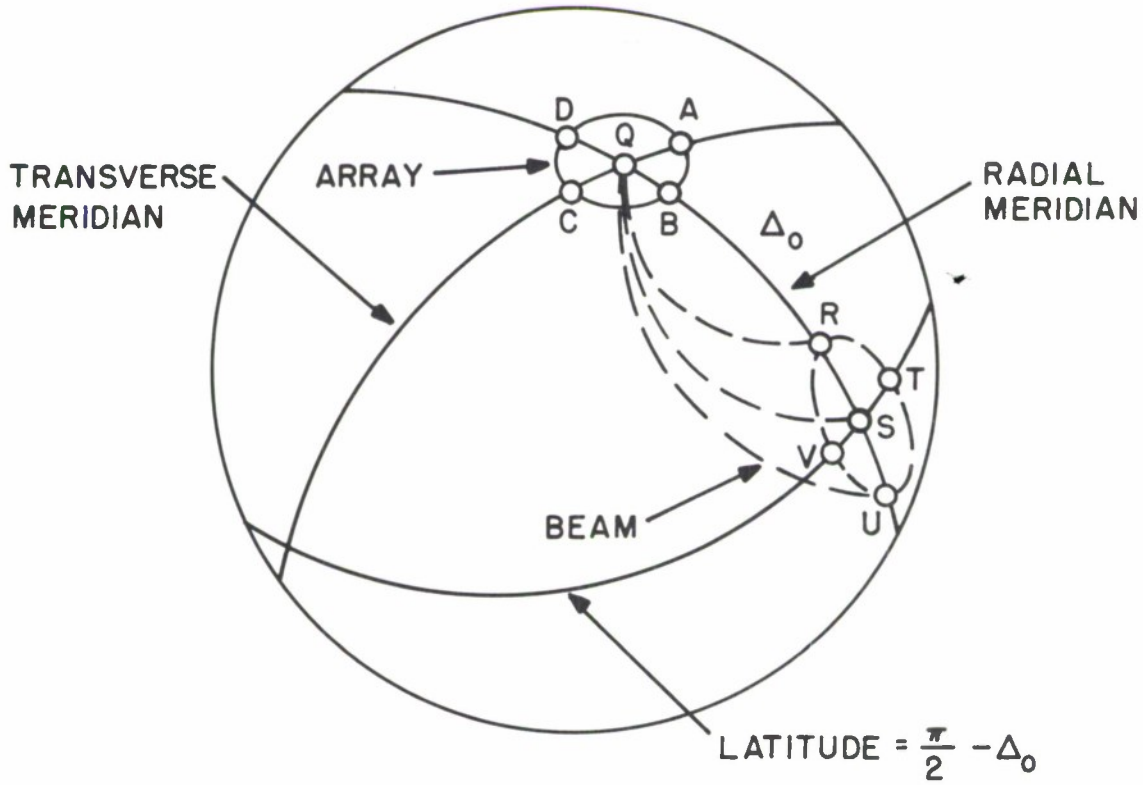


FIGURE 2.1
GEOMETRY OF TELESEISMIC ARRAY AND BEAM

of the array. The travel time compensation is based on alignment of the P-phase of the seismic signal at the array.

The extent of the resulting main beam is defined in terms of a "cone." Two bounding elements of this cone are shown as rays $\overline{QR}$ and $\overline{QU}$ in Figure 2.1. The bounding rays are selected to conform with the chosen definition of array beamwidth. The intersection of the cone of the main beam with the earth will result in the distorted ellipse RTUV with center at S. This ellipse can be considered as a gain contour. It is the dimensions of this ellipse that we desire to determine. These dimensions are a function of the array beamwidth and the spherical geometry relating points Q and S.

The relative geometry is defined in terms of the meridians $\overline{QS}$ and $\overline{QA}$, and the parallel of latitude $\overline{ST}$. The meridian $\overline{QS}$ connecting the array center to the focus point is called the radial meridian. The distance $\overline{QS}$ is specified in terms of the great circle distance Δ_o measured in radians. Thus the parallel of latitude $\overline{ST}$, which passes through the focus is at a latitude $\pi/2 - \Delta_o$. The meridian $\overline{QA}$ is taken to be that meridian through the point Q which is perpendicular to the radial meridian, and hence is called the transverse meridian.

We shall define the size of the elliptical gain contour in terms of its radial extent and its transverse extent. These dimensions are $\overline{VT}$ and $\overline{RU}$, respectively. The radial arc $\overline{RU}$ measured in radians will be called θ_r, and the transverse arc $\overline{VT}$ measured in radians will be called θ_t.

2.2 DEPENDENCE OF ARRAY CONTOUR DIMENSIONS UPON ARRAY DIMENSIONS

The radial extent θ_r of the gain contour is proportional to the array beamwidth obtained by considering the two-dimensional array pattern that results from passing a plane containing the arc QRS through the three-dimensional pattern. Let us call this resulting beamwidth the radial beamwidth. The array beamwidth in the plane producing the cut is directly proportional to the length of the projection of the array onto this plane. In the case of the radial beamwidth the projected array length in the radial plane is $\overline{BD}$.

Similarly, the transverse extent θ_t of the gain contour is proportional to the transverse beamwidth of the array. In defining the transverse beamwidth we must extend our concept of a cut plane slightly to accommodate the fact that the seismic energy travels along curved lines. Picture a curved sheet which contains the arcs $\overline{AC}$ and $\overline{VT}$, and which is curved so as to contain the ray paths connecting V and Q, and T and Q. The intersection of this curved sheet with the three-dimensional array pattern provides the desired transverse cut of the array pattern and

hence defines the transverse beamwidth. For this case the effective array length can be considered to be $\overline{CA}$.

Let us consider the projections discussed above a little further. Referring to Figure 2.1, the circular area ABCD represents the two-dimensional extent of the seismic array. Now when we consider, for example, the transverse pattern we imagine that the array elements are projected onto the curved line $\overline{CA}$. This results in a linear array extending from C to A. The projection will, in general, produce a linear array that has both space tapering and amplitude weighting of the array elements. Analysis of the resulting linear array will yield the two-dimensional array pattern produced by the cut.

2.3 DEFINITION OF BEAMWIDTH

From the previous paragraph we have seen that we can obtain the properties of the two-dimensional array pattern produced by a cut by studying an equivalent linear array. Figure 2.2 illustrates an arbitrary linear array of N elements. The main beam is shown steered away from the broadside direction by an angle ϕ_o. To accomplish steering of the beam it is necessary to provide a progressive delay across the array. Let the differential delay between end elements in the array due to the steering be called $\Delta\tau_S$. Note that for an array steered broadside no delays are required in the array elements and hence for this case $\Delta\tau_S=0$.

Now consider a seismic source in the far field at an angle ϕ from broadside. The arrival times of energy from this source to the various array elements will be different. These travel-time differences will be a function of the angle ϕ, element spacing, etc. Let us call the resulting travel-time difference between end elements of the array $\Delta\tau_A(\phi)$. Finally, we define a time difference, $\Delta\tau(\phi)$, between end elements which includes both the effect of built-in time delays and differential travel times.

$$\Delta\tau(\phi) = \Delta\tau_A(\phi) - \Delta\tau_S \qquad (2.1)$$

When $\phi = \phi_o$, the built-in time delays exactly compensate for the differential travel times and hence $\Delta\tau(\phi_o) = 0$. As we deviate the source away from the angle ϕ_o, $\Delta\tau(\phi)$ will either increase or decrease away from zero, depending upon the direction in which we leave ϕ_o. Hence the value of $\Delta\tau(\phi_o+\Delta\phi)$ locates our position on the main beam.

Now we are in position to be able to define array beamwidth. The array beamwidth, $\Delta\phi$, is defined by the following condition.

$$|\Delta\tau(\phi_o \pm \frac{\Delta\phi}{2})| = \tau/4 \qquad (2.2)$$

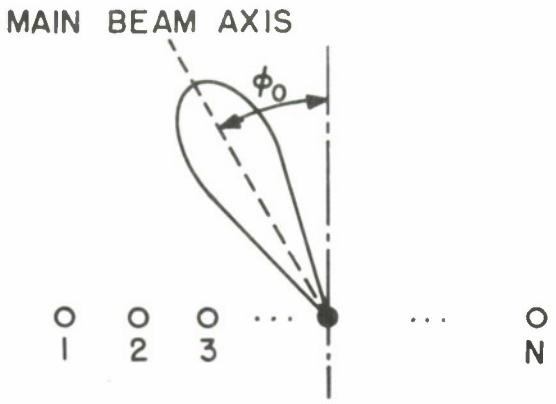


FIGURE 2.2
EQUIVALENT LINEAR ARRAY

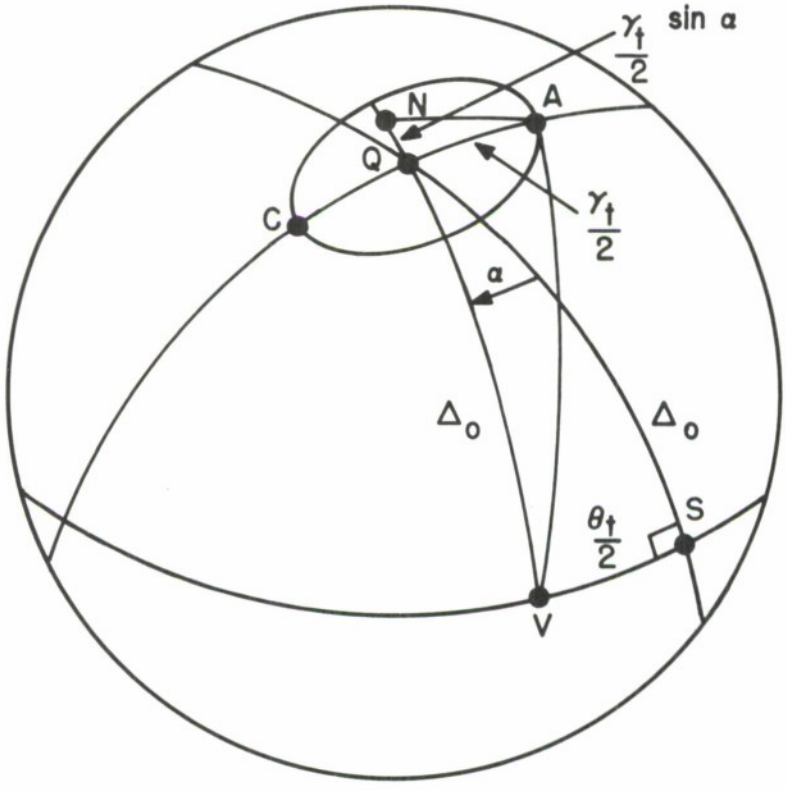


FIGURE 2.3
GEOMETRY FOR THE COMPUTATION OF θ_t

where τ is the dominant period of the seismic energy. That is, if we deviate the source $\pm\Delta\phi/2$ either side of the center of the main beam, the magnitude of the differential delay between end elements of the array will be a quarter of the period of the seismic energy.

Let us relate the above definition of array beamwidth to more common measures of beamwidth. For a linear array with uniformly spaced and uniformly weighted array elements the beamwidth $\Delta\phi$, defined above, corresponds for large N to half the distance between the zeroes of the main beam. Furthermore, for this case, $\Delta\phi$ closely approximates the 3 dB beamwidth of the array. The beamwidth $\Delta\phi$ will also correspond to half the distance between zeroes of the main beam for arrays whose amplitude weighting distributions are obtainable by successive convolutions starting with a uniform amplitude weighting. One example of this class would be a triangular weighting of array element amplitudes. However, the beamwidth $\Delta\phi$ will deviate from the 3 dB beamwidth for these arrays. The amount of deviation will increase as the amount of amplitude weighting becomes more severe.

2.4 TRANSVERSE EXTENT OF THE ARRAY CONTOUR

Shown in Figure 2.3 is the geometry pertinent to the calculation of the transverse extent of the gain contour, θ_t. As before, the array is focused at the point S, and hence $\overline{QS}$ is the axis of the main beam. The arc $\overline{CA}$ represents our equivalent linear array. Note for this case that the main beam of the transverse pattern is steered broadside to the equivalent linear array and hence $\Delta\tau_s = 0$.

Point V lies along the parallel of latitude through S. Further, it is one of the points of intersection of the cone of the main beam with the earth's surface. Hence, the transverse extent θ_t is just twice the distance $\overline{VS}$ measured in radians.

Based on our definition of beamwidth and the fact that $\Delta\tau_s = 0$, the differential travel time from V to the array element located at points A and C will be just $\tau/4$. Let us relate this travel time difference to the geometry of Figure 2.3. Let $d\Delta$ represent the differential distance between $\overline{VQ}$ and $\overline{VA}$ in radians. Let α be the difference in longitude in radians between the meridians $\overline{QS}$ and $\overline{QV}$. Using far field approximations, $d\Delta$ can be approximated by the arc $\overline{NQ}$ and hence

$$d\Delta \approx \frac{\gamma_t}{2} \sin\alpha \approx \frac{\gamma_t \alpha}{2} \qquad (2.3)$$

where γ_t is the transverse extent $\overline{CA}$ of the array measured in radians. The corresponding differential travel time dT is then given by

$$dT = \left.\frac{\partial T}{\partial \Delta}\right|_{\substack{h=\text{const.} \\ \Delta=\Delta_o}} d\Delta = T_\Delta(\Delta_o, h_o)\,d\Delta \tag{2.4}$$

where h_o is the depth of the seismic source (taken as zero for the example chosen), and the symbol T_Δ is used to represent the partial derivative of the travel time with respect to distance with source depth held constant. The differential travel time between the end array elements at points C and A will be 2dT and hence

$$2dT = \tau/4 \tag{2.5}$$

Combining Equations 2.3, 2.4 and 2.5, we obtain

$$\alpha = \frac{\tau}{4\gamma_t T_\Delta(\Delta_o, h_o)} \tag{2.6}$$

Now we relate the transverse extent θ_t of the array contour to the differential longitude, α, as follows:

$$\theta_t/2 = \alpha \sin\Delta_o \tag{2.7}$$

Thus

$$\theta_t = \frac{\tau}{2\gamma_t T_\Delta(\Delta_o, h_o)} \sin\Delta_o \tag{2.8}$$

We can relate the transverse extent of gain contour given by Equation 2.8 to the corresponding extent $\hat{\theta}_t$ of the 3 dB gain contour by introducing the aperture efficiency η. That is

$$\hat{\theta}_t = \text{transverse extent of the 3 dB gain contour}$$

$$= \frac{\theta_t}{\eta} = \frac{\tau}{2\eta\gamma_t T_\Delta(\Delta_o, h_o)} \sin\Delta_o \tag{2.9}$$

For a uniform amplitude weighting of equally spaced elements η is unity. For other amplitude weightings smaller values of η will result.

2.5 RADIAL EXTENT OF THE ARRAY CONTOUR

Shown in Figure 2.4 is the geometry pertinent to the calculation of the radial extent of gain contour, θ_r. The arc $\overline{BD}$ represents the equivalent linear array. The array is steered to the focus at point S. In this case the main beam of the radial pattern is not broadside to the equivalent linear array. In fact, $\Delta\tau_s$ will be equal to the differential travel times from the point S to the end elements at points B and D. Let $T(\Delta_Q, h_Q)$ be the travel time from the focus at point S to the array center at point Q. Hence

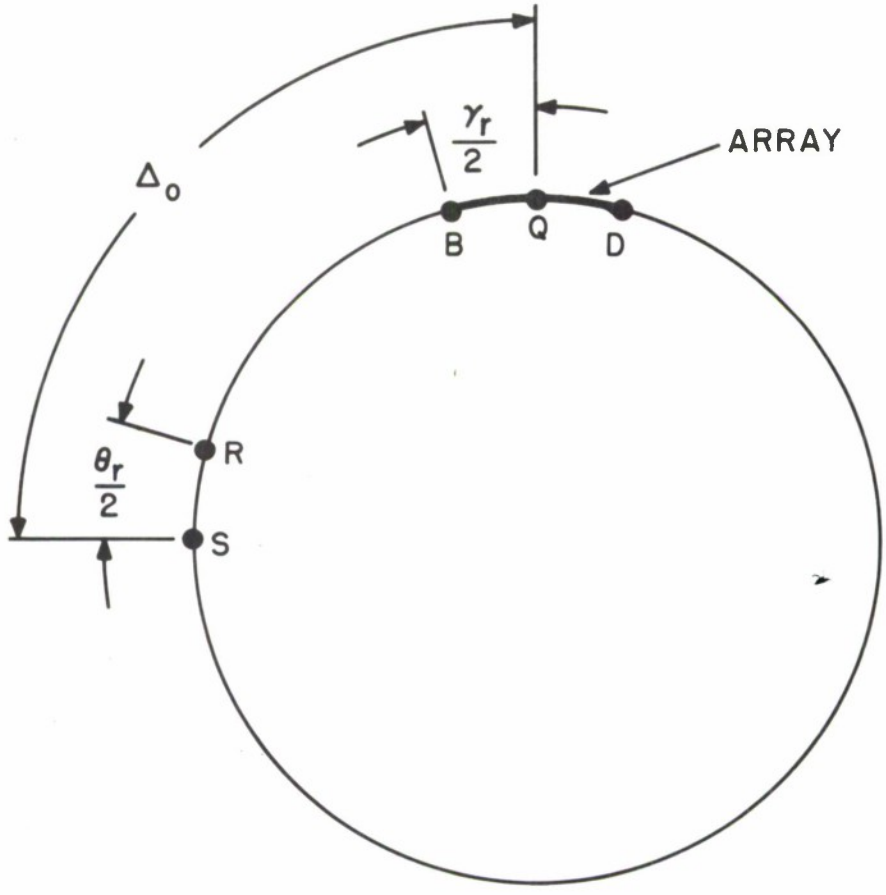


FIGURE 2.4

GEOMETRY FOR THE COMPUTATION OF θ_r

$$\frac{\Delta\tau_s}{2} = T(\Delta_o,h_o)-T(\Delta_o-\frac{\gamma_r}{2},h_o) \simeq \frac{\gamma_r}{2} T_\Delta(\Delta_o,h_o) \qquad (2.10)$$

where γ_r is the radial extent of the array $\overline{BD}$ in radians.

Point R is one of the points of intersection of the cone of the main beam with the earth's surface. Hence the radial extent θ_r is just twice $\overline{RS}$ measured in radians. Based on our definition of beamwidth, the differential travel time from R to the array elements located at points B and D will be $(\tau/4+\Delta\tau_s)$. Hence

$$\frac{\tau}{4} + \Delta\tau_s = 2\{T(\Delta_o - \frac{\theta_r}{2},h_o)-T(\Delta_o - \frac{\theta_r}{2} - \frac{\gamma_r}{2},h_o)\} \qquad (2.11)$$

Combining Equations 2.10 and 2.11, we obtain

$$\frac{\tau}{8} = \frac{\gamma_r}{2} T_\Delta(\Delta_o - \frac{\theta_r}{2},h_o) - \frac{\gamma_r}{2} T_\Delta(\Delta_o,h_o) \qquad (2.12)$$

$$\simeq \frac{\gamma_r}{2} \cdot \frac{\theta_r}{2} T_{\Delta\Delta}(\Delta_o,h_o)$$

where $T_{\Delta\Delta}$ is the second partial derivative of travel time with respect to distance, with source depth held constant.

The radial extent of the gain contour is obtained directly from Equation 2.12.

$$\theta_r = \frac{\tau}{2\gamma_r T_{\Delta\Delta}(\Delta_o,h_o)} \qquad (2.13)$$

Again we can obtain an expression for the extent of the corresponding 3 dB contour by introducing the aperture efficiency η, i.e.,

$$\hat{\theta}_r = \text{radial extent of the 3 dB gain contour}$$

$$= \frac{\tau}{2\eta\gamma_r T_{\Delta\Delta}(\Delta_o,h_o)} \qquad (2.14)$$

2.6 APPLICATION OF BEAM THEORY TO LASA

For system considerations, it is convenient to deal with the 3 dB contour dimensions in terms of kilometers and the array dimensions in terms of degrees. Thus, corresponding to Equations 2.9 and 2.14, we have

$$S_t = \text{3 dB transverse extent in km}$$

$$= R_e\hat{\theta}_t = \frac{c\sin\Delta_o}{T_\Delta(\Delta_o,h_o)} \frac{\tau}{2} \frac{1}{\eta\gamma_t^o} \qquad (2.15)$$

$$S_r = 3 \text{ dB radial extent in km}$$

$$= R_e \hat{\theta}_r = \frac{c}{T_{\Delta\Delta}(\Delta_o, h_o)} \frac{\tau}{2} \frac{1}{n\gamma_r^o} \qquad (2.16)$$

where γ_t^o and γ_r^o are the transverse and radial extents of the array in degrees, R_e is the radius of the earth, and c is a constant equal to $180R_e/\pi$. Figure 2.5 contains smoothed plots of the factors $\alpha \sin\Delta/T_\Delta$ and $c/T_{\Delta\Delta}$ versus the range Δ°(in degrees). The values for the curves were calculated using P-phase travel times obtained from the Jeffreys-Bullen travel time tables (3).

In Section III, LASA array patterns are presented for three different ranges. Although those patterns were computed using a transient, the beamwidths obtained will be compared with those predicted by the theory developed in this section for a 1 Hz signal in order to infer the approximate value of the aperture efficiency n.

The 3 dB transverse extents for LASA obtained in Section III are 800 km, 1000 km, and 1100 km for ranges of 48°, 64° and 84°, respectively. The value of n that leads to these beamwidths using the expressions of this section is approximately 0.5. A similar comparison with the patterns presented in Section IV for a random array with 525 elements and a two-degree diameter leads to a value of the aperture efficiency of approximately 0.65.

It can be observed that LASA having a greater concentration of elements near the center than the random array considered in Section IV, has a smaller aperture efficiency.

2.7 SUMMARY AND CONCLUSIONS

A measure of the beamwidth of teleseismic arrays has been derived in terms of the aperture of the array and the range to the focus point. This derivation is based on several simplifying assumptions: 1) a 1 Hz continuous signal is assumed; 2) a convenient measure of beamwidth which involves differential time delay of the signal at the extremes of the aperture is used; 3) simple spherical geometry is employed and 4) the J-B travel time tables are used to obtain travel time as a function of range. The results of the derivations have been compared with calculated array patterns for LASA and for a random array of LASA dimensions, and reasonable agreement has been observed. This derivation was originally intended to provide a rough estimate of the extent of the array pattern that would result with a given range and aperture. As it is now relatively easy (by means of the appropriate computer program) to calculate patterns for specific arrays, and for more realistic signals, we do not anticipate any further use of the results of this derivation. Several of these computer-aided pattern calculations are presented in the next section.

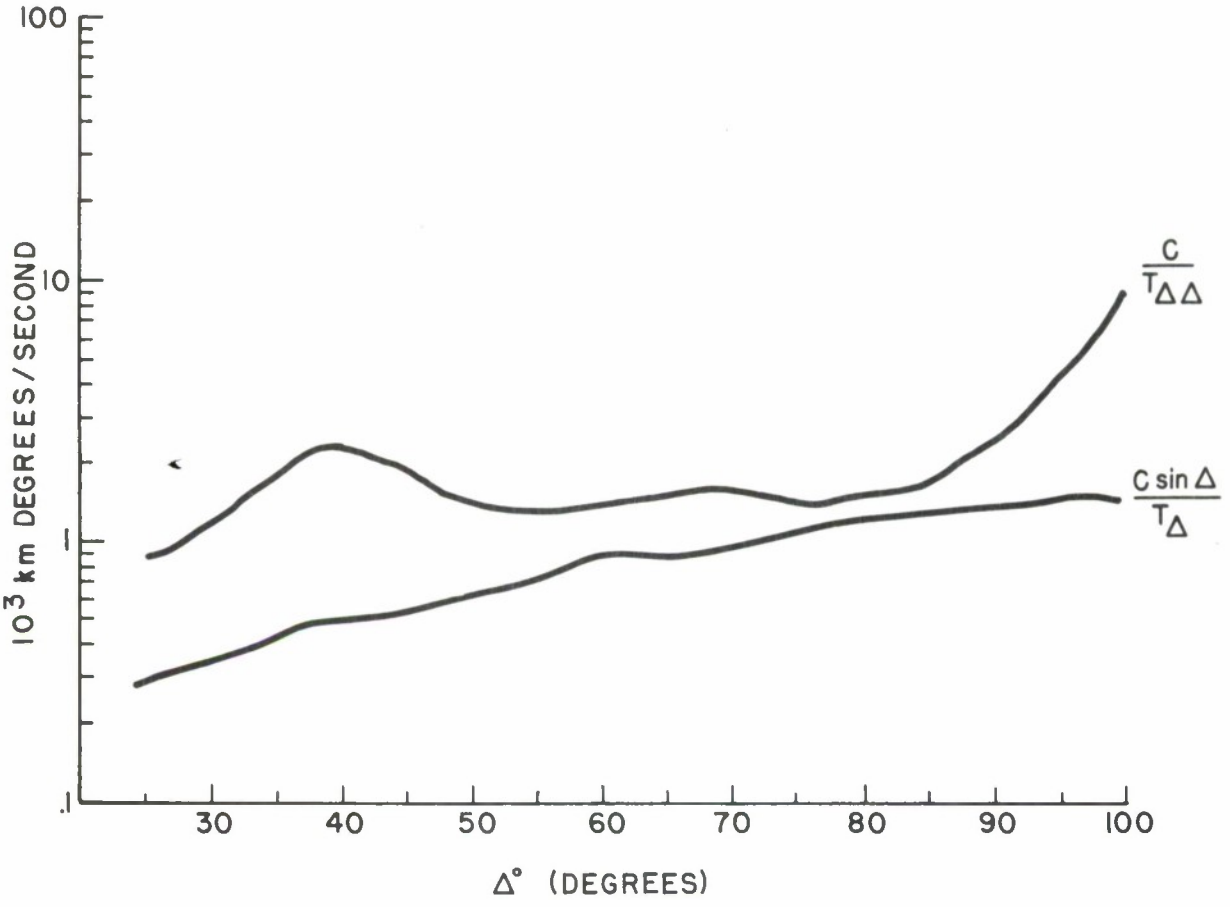


FIGURE 2.5

SMOOTHED DERIVATIVES OF THE P PHASE TRAVEL TIME RELEVANT TO THE TELESEISMIC BEAM DIMENSIONS

SECTION III

ARRAY PATTERN COMPUTATIONS

The array characteristics of LASA have in the past been principally studied in terms of gain patterns in frequency wave number space (see,e.g., reference 4). Generally, these K-space patterns are based on a straight summation of the array seismometer outputs with no filtering applied prior to summing. The seismometers themselves are assumed to be frequency independent. Under these conditons, the response in two-dimensional wave number space is sufficient to describe the properties of the array. Such K-space patterns are particularly useful for examining the noise discrimination properties of seismic arrays.

From a systems point of view certain array performance parameters assume importance. These include the dimensions of the 3 dB gain contour at the array focal point (see Section II), the array sidelobe structure in the radial and transverse planes, etc. Usual array patterns are calculated on the basis of received sinewave signals. In practice, transient signals are received by the array and hence it is of interest to examine the effect on array performance caused by the reception of wideband signals rather than sinewaves. Lastly, it is instructive to include range dependent factors such as spreading loss and attenuation in the array computations.

Since the above quantities are not readily derivable from K-space patterns, we have directly calculated the radial and transverse array patterns for LASA focused at each of these locations. These calculations are based on the following: 1) only the 21 center elements are used, since the cluster dimensions are on the order of one wavelength of the seismic signals; 2) the LONGSHOT transient as recorded at the center element of A0 is used for the received signal at each element; 3) unsmoothed J-B travel-times are employed.

3.1 RADIAL AND TRANSVERSE BEAM PATTERNS

Figure 3.1 illustrates the geometry applicable to the beam pattern calculations, and shows qualitatively the appearance of a radial and transverse beam pattern. The array consists of N identical seismometers spread over a plane area as indicated by the circular boundary in Figure 3.1. The array is focused at a point S. The great circle Λ_r represents the axis of the main beam of the array. As shown in Figure 3.1, the distance in radians from the array center (located at point Q) to the focus S is defined as Δ_o, and the azimuth of the focal point measured at the center of the array is defined as Az_o. The great circle Λ_t is normal to Λ_r at the focus and defines the axis of the transverse beam of the array pattern.

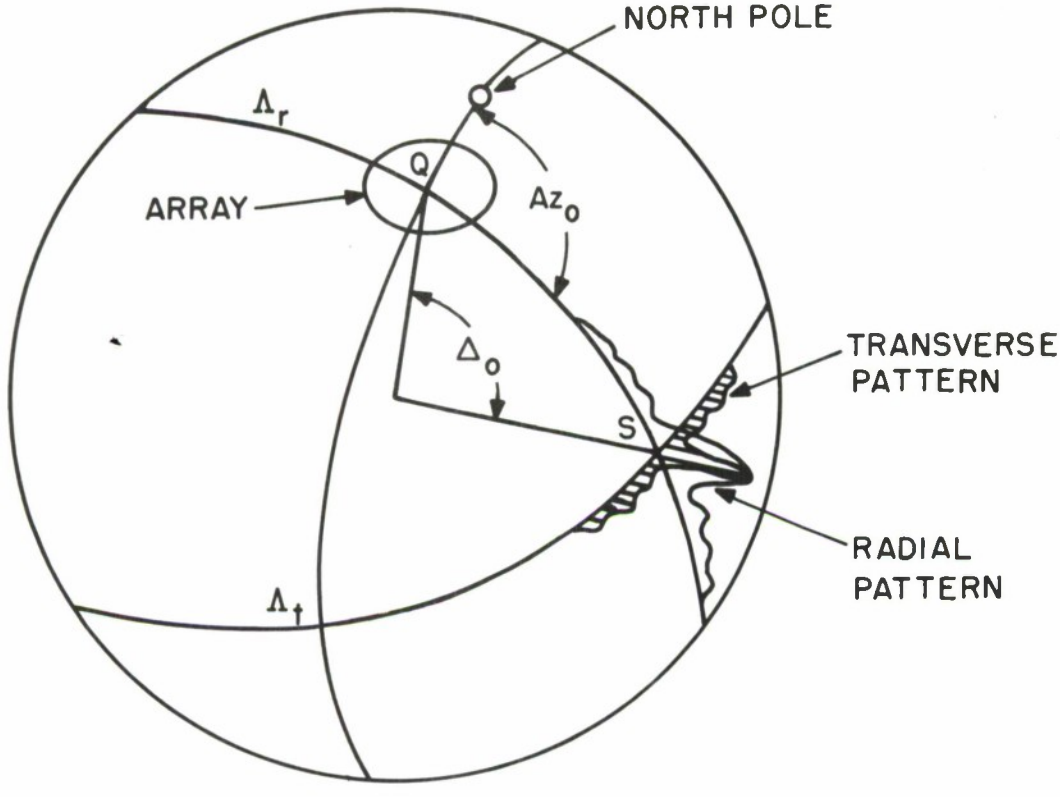


FIGURE 3.1

GEOMETRY FOR ARRAY PATTERN COMPUTATIONS

The positions of the various seismometers in the array are defined by the position vectors $\vec{r}_k$ (k=1,2,...,N), which are vectors from the array center to the various seismometers. Thus the output of the k^{th} seismometer is given by

$$x_k(t) = s(t-\vec{\alpha}\cdot\vec{r}_k) \qquad (3.1)$$

where s(t) is the received waveform at the array center, and $\vec{\alpha}$ is the delay vector per unit distance. The vector $\vec{\alpha}$ characterizes the phase velocity of the seismic signal and its angle of arrival with respect to the array. That is, for a given array location, every point at teleseismic distance can be characterized by a single delay vector $\vec{\alpha}$. As is evident, the above statements are based on far field assumptions.

Let $\vec{\alpha}_o$ be the delay vector associated with the focus at point S. If we delay all seismometer outputs by an amount $\vec{\alpha}_o\cdot\vec{r}_k$ (k=1,2,...,N) and sum the delayed outputs we will obtain a beam focused at point S. Thus, for a source at the focus, the array output, $V_o(t)$, will be Ns(t). If the source is located at a point other than the focus the array output takes on a value

$$V_o(t) = \sum_{k=1}^{N} s(t-(\vec{\alpha}-\vec{\alpha}_o)\cdot\vec{r}_k) \qquad (3.2)$$

For $\vec{\alpha}\neq\vec{\alpha}_o$ the output given by Equation 3.2 will be a distorted version of Ns(t), and will be of lower peak amplitude.

The following will briefly outline the computational steps involved in the computer program for determining the basic array beam pattern. The basic inputs to the program are the seismometer locations, focal point coordinates, a table of travel times appropriate for the P-phase arrival, and a set of sample values which specify the transient s(t). Then for a given source location, the value for $\vec{\alpha}$ is computed by taking derivatives of the appropriate travel times, and the results are used to form the sum given by Equation 3.2. The peak value of the sum is selected and normalized with respect to the peak array output obtained at the focus. This normalized output then represents the array output corresponding to the chosen source location.

To obtain the transverse pattern of the array the above computation is iterated for a series of source points located along Λ_t (see Figure 3.1). Similarly, the radial array pattern is obtained by locating sources along the great circle Λ_r.

The actual computations used for the transient s(t), the P-phase signal of the LONGSHOT event as recorded at the center element of the LASA AO cluster. The curves labeled

"a" of Figures 3.2, 3.4, and 3.6 show the result of this calculation for the radial pattern for focal points at distances of 48°, 64°, and 84° respectively. These curves do not include the effect of range loss. Figures 3.3, 3.5, and 3.7 show the corresponding transverse array patterns. Since for the transverse case the distances from the various source points to the array is practically constant, there is no need for range loss corrections.

3.2 RANGE LOSS CORRECTIONS

It is evident that for the case of the radial pattern the actual value of the array output will increase for source points along Λ_r with ranges less the Δ_o and will decrease for source points with ranges greater than Δ_o, when compared to the patterns obtained in Section 3.2. To account for this the computer program was also designed to provide plots of the radial pattern corrected to include the effects of range loss.

Range loss is composed of two components: one due to the spreading of the seismic energy as it leaves the source point, and the other due to an actual energy loss due to absorption. Spherical spreading was assumed and hence the array output as defined in Section 3.2 was scaled by a factor $\frac{\Delta_o}{\Delta}$ for an event at distance Δ from the array center.

The absorption loss $L_A(\omega,\Delta)$ is both frequency dependent and range dependent. The functional form assumed for $L_A(\omega,\Delta)$ is given below (see Section XIII).

$$L_A(\omega,\Delta) = \exp\left(-\frac{\omega\Delta}{2cQ}\right) \tag{3.3}$$

where

ω = angular frequency of the seismic wave

c = velocity of propagation

Q = ratio of energy stored to energy lost per cycle

Thus the necessary correction factor to account for absorption is given by

$$\frac{L_A(\omega,\Delta)}{L_A(\omega,\Delta_o)} = \exp\left\{-\frac{\omega(\Delta-\Delta_o)}{2cQ}\right\} \tag{3.4}$$

That is, the array output corresponding to an event at a distance Δ from the array is scaled by the factor given by Equation 3.4. In utilizing the values for the absorption scale factor given by Equation 3.4, a value of 2000 for Q was assumed

and the frequency was taken as 1 Hz. This choice of frequency corresponds to the dominant period contained in the LONGSHOT P-phase signal.

The curves labeled "b" of Figures 3.2, 3.4 and 3.6 are the resulting radial patterns obtained by applying the range correction factors discussed above to curves labeled "a."

3.3 SUMMARY OF LASA BEAM PATTERN RESULTS

Some discussion is necessary to describe the array configuration that was utilized in the array pattern calculation, since it is a simplified version of the actual LASA configuration. The actual LASA configuration consists of 21 clusters, each containing 25 seismometers. For a frequency of 1 Hz (the predominant P-phase signal frequency) the cluster dimensions are on the order of a wavelength. Thus, for the signals of interest, the pattern of a single cluster is quite broad. Based on this fact, it was assumed that the array patterns for LASA could be closely approximated by considering the 21-element array formed by the center seismometers of each cluster. This simplification greatly reduces the amount of computer computation necessary for beam calculations.

As mentioned previously, Figures 3.2 through 3.7 display the results of the beam pattern computations for a simulated LASA receiving the LONGSHOT signal. Array focal points were chosen at Amchitka, the Kurile region and Kazakh. The 3 dB extent of the radial and transverse patterns obtained for each of the above focal points are summarized in the following table.

Δ	3 dB Extent of Transverse Pattern	3 dB Extent of Radial Pattern
48°	7°	12°
64°	9°	13°
84°	10°	10°

There are negligible differences in the 3 dB extent of the radial pattern for the range corrected and uncorrected patterns. As expected, the radial beamwidths are generally larger than the corresponding transverse beamwidths, since the derivative of the angle of incidence with respect to range is less than unity at teleseismic distances.

A few general comments about the array patterns are in order. Some of the minor kinks in the array patterns are due to the fact that unsmoothed versions of the travel-time derivatives were used in the computations. The sidelobe level of the

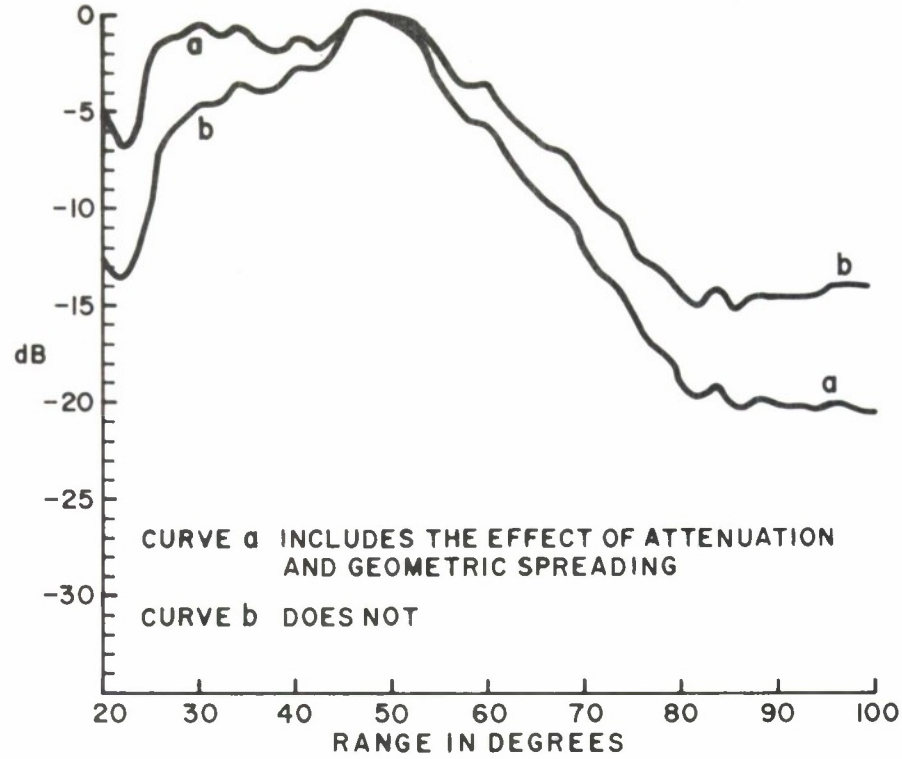


FIGURE 3.2
RADIAL PATTERN FOR LASA
FOCUSED AT AMCHITKA

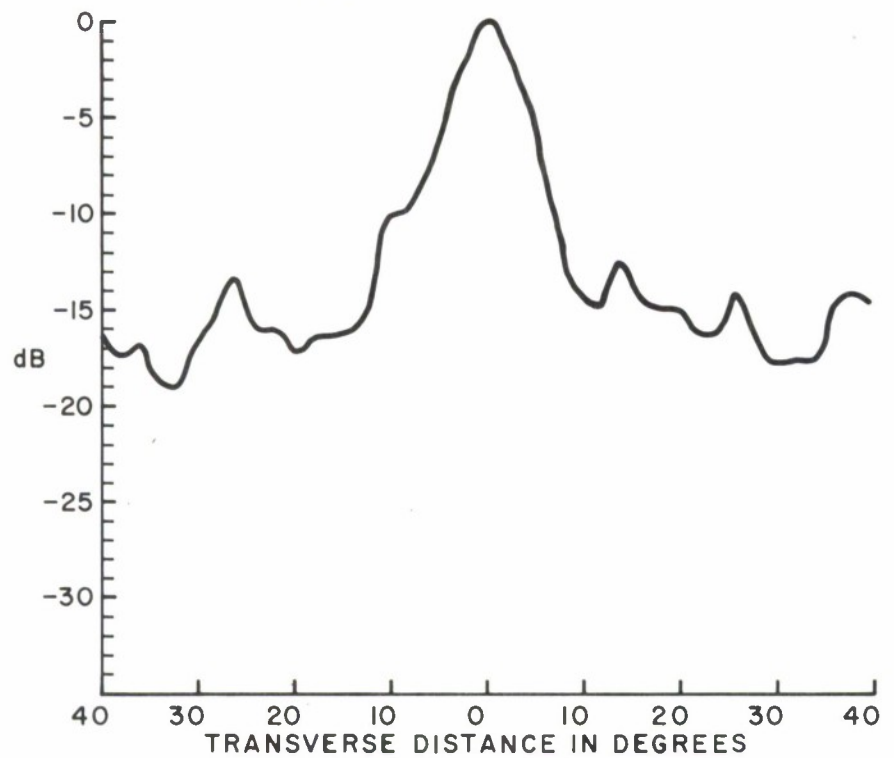


FIGURE 3.3
TRANSVERSE PATTERN FOR LASA
FOCUSED AT AMCHITKA

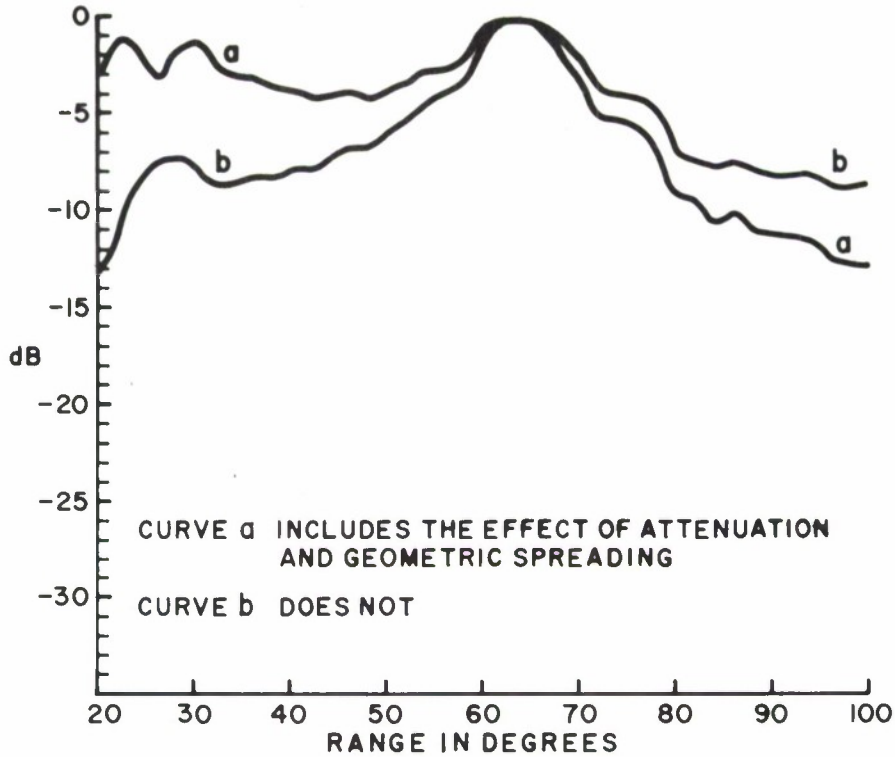


FIGURE 3.4
RADIAL PATTERN FOR LASA
FOCUSED AT KURILES

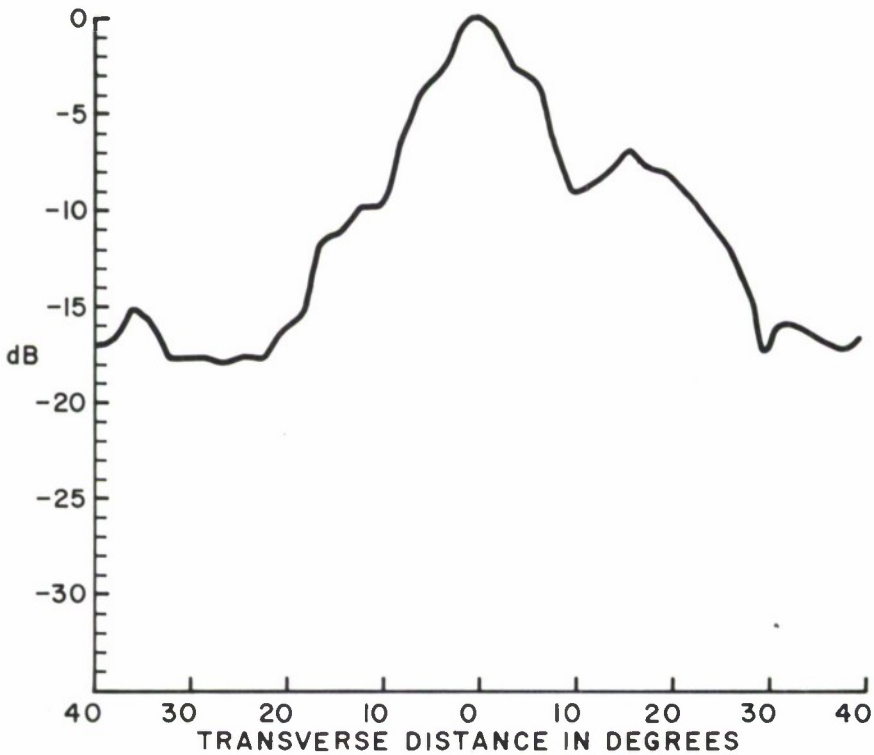


FIGURE 3.5
TRANSVERSE PATTERN FOR LASA
FOCUSED AT KURILES

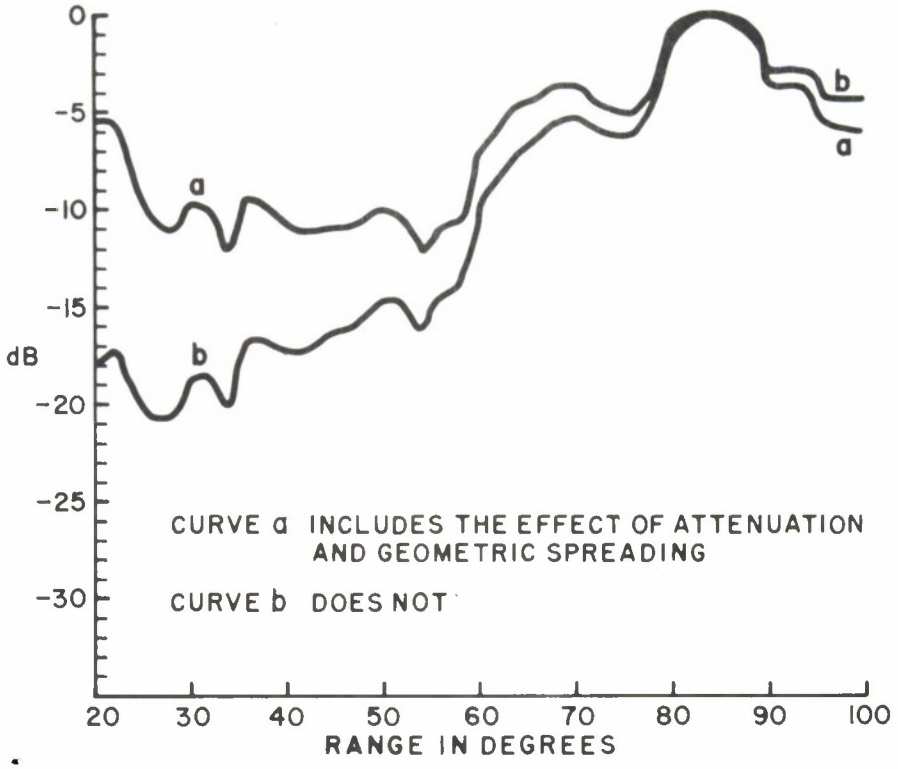


FIGURE 3.6
RADIAL PATTERN FOR LASA
FOCUSED AT KAZAKH

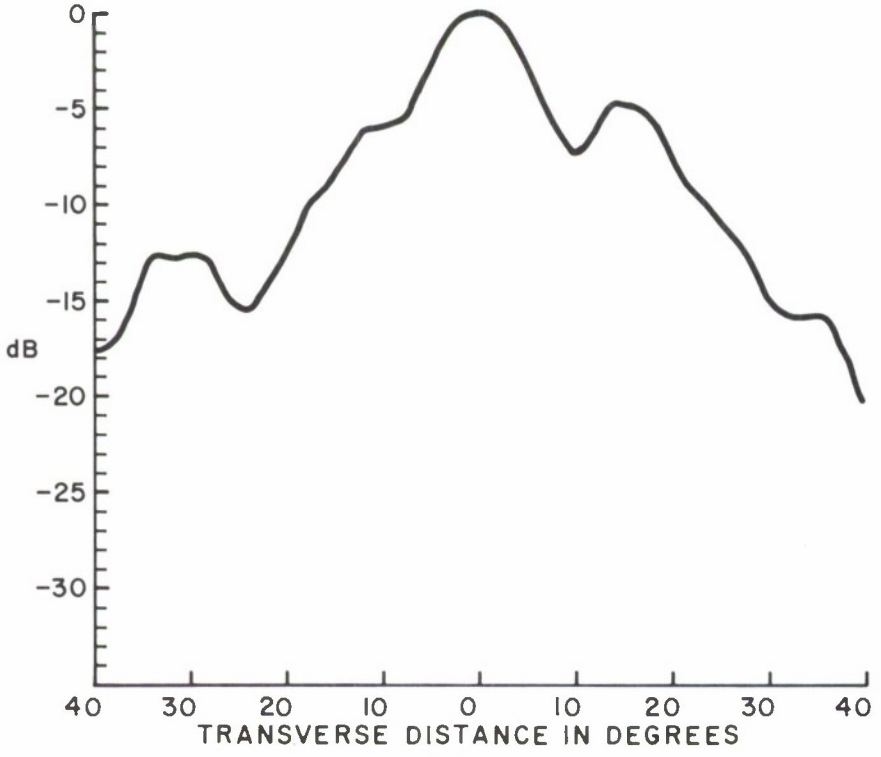


FIGURE 3.7
TRANSVERSE PATTERN FOR LASA
FOCUSED AT KAZAKH

transverse pattern is significantly lower than that of the corresponding uncorrected radial pattern. This is due to the fact that in the radial plane the angular extent of a ray bundle at the source is compressed when it reaches the array. The sidelobes of the radial pattern degrade even further when the range correction factors are applied to the pattern. In Section IV randomization of array elements is investigated as a means of improving the sidelobes.

SECTION IV

RANDOM ARRAY THEORY AND SIMULATION

The beam pattern calculations of Section III indicate that the sidelobe performance of LASA-Montana (as simulated by considering a 21 element array with elements located at the cluster centers) leaves much to be desired. The major cause for the poor sidelobe performance is the fact that the array is thin. One method of improving array sidelobe performance under such conditions is to randomize the location of the array elements. This section considers a random array of 525 elements whose extent approximates that of LASA-Montana. It is realized that there are many practical difficulties which mitigate against randomizing the entire LASA array. However such an analysis will bound the improvement in sidelobe performance obtainable from array element randomization.

In the analysis of the random array the x-y coordinates of each of the array elements are assumed to be independent Gaussian random variables with identical variances and zero means. The origin of the coordinate system is located at the array center. A closed-form expression for the average radial beam pattern is developed. The results of a computer simulation of a 525 element random array are presented so that comparisons can be made with the theoretical results. The simulated beam patterns are shown to compare favorably with the average pattern predicted by theory. Consideration is also given to the dependence of the beam dimensions and teleseismic sidelobe level on the number of array elements.

4.1 RADIAL BEAM OF AN ARRAY WITH RANDOM ELEMENTS.

In analyzing the beam pattern of a random LASA a number of simplifying assumptions will be made. Arrays with large numbers of elements will be considered, truncation effects will be ignored, and the incoming wave will be assumed to be narrowband. The coordinates which locate the array elements will be independent, zero mean, normal random variables. With the above simplifications, it will be shown that the resulting radial array pattern of the random array is essentially the Fourier transform of the probability density function of the random variable R, defined as the projection of the element locations onto the radial meridian (defined in Section III). Hence, for the assumed normal distribution of array elements, the expected array pattern will have a Gaussian shape.

In the following, the density function of a zero mean, normal, random variable with variance σ^2 will be denoted by N(o σ). In practice, due to the finite size of the array, the elements will follow a truncated normal distribution rather than a true normal distribution. Two parameters define a symmetrical truncated zero mean normal distribution: the variance, σ^2, and the truncation point, R_{max}.

In our case R_{max} corresponds to the maximum distance from the array center at which an array element can be located.

In determining the radial array pattern at an angle θ (see Figure 4.1), it is first necessary to project the array elements onto the radial line. Hence the length of the projection of the array element with coordinates (x,y) is given by

$$R = x\sin\theta + y\cos\theta \qquad (4.1)$$

If x and y are independent, random normal, variables with zero means, then R will also be a zero mean, normal random variable, since it is a linear combination of normal random variables. Also, because of the sine-cosine coefficients, the variance of R will be the same as that of x and y.

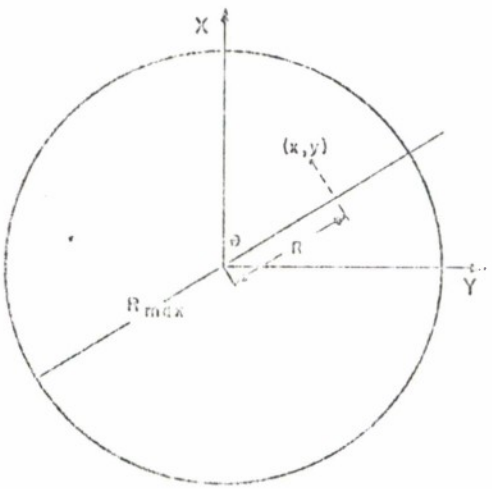


FIGURE 4.1
GEOMETRY FOR RANDOM ARRAY SIMULATION

Hence for normally distributed elements, the expected array patterns are independent of Az_o, the azimuth of the focus.

For a narrowband signal the radial pattern is given by:

$$\psi(\alpha)=\left|(1/N)\sum_{i=1}^{N} \exp(j2\pi f\alpha R_i)\right| \qquad (4.2)$$

where

f = frequency of the incoming wave
N = number of array elements
α = relative delay per unit distance along the radial meridian
R_i = the projection of the i^{th} element onto the radial meridian

For a large number of elements

$$\frac{1}{N}\sum_{i=1}^{N} \exp(j2\pi f\alpha R_i)\rightarrow E\{\exp(j2\pi f\alpha R)\} \qquad (4.3)$$

Hence for large N

$$\Psi(\alpha)\approx\left| E\{\exp(j2\pi f\alpha R)\}\right| \qquad (4.4)$$

where E is the expectation operator.
The characteristic function of a zero mean Gaussian random variable has a real Gaussian form. That is,

$$\Psi(\alpha) = \exp(-2\pi^2\alpha^2 f^2\sigma^2) \qquad (4.5)$$

Hence $\Psi(\alpha)$ has a Gaussian shape and a "width" that is inversely proportional to the standard deviation of the element locations and to the frequency, f.

4.2 RANDOM ARRAY SIMULATION

4.2.1 Comparison with Clustered LASA

A 525-element array with randomly located elements was simulated. A standard deviation of .5 degrees and a maximum distance to the array center (R_{max}) of one degree were chosen. The array obtained is shown in Figure 4.2. The standard deviation was chosen to be one-half of the maximum distance to avoid strong sidelobe generation due to truncation of the density function. For $\sigma > \frac{1}{2} R_{max}$ the actual array beamwidth will be smaller than computed, but the truncation effect will start to become important. No attempt has been made to find an "optimum" σ for a given R_{max}.

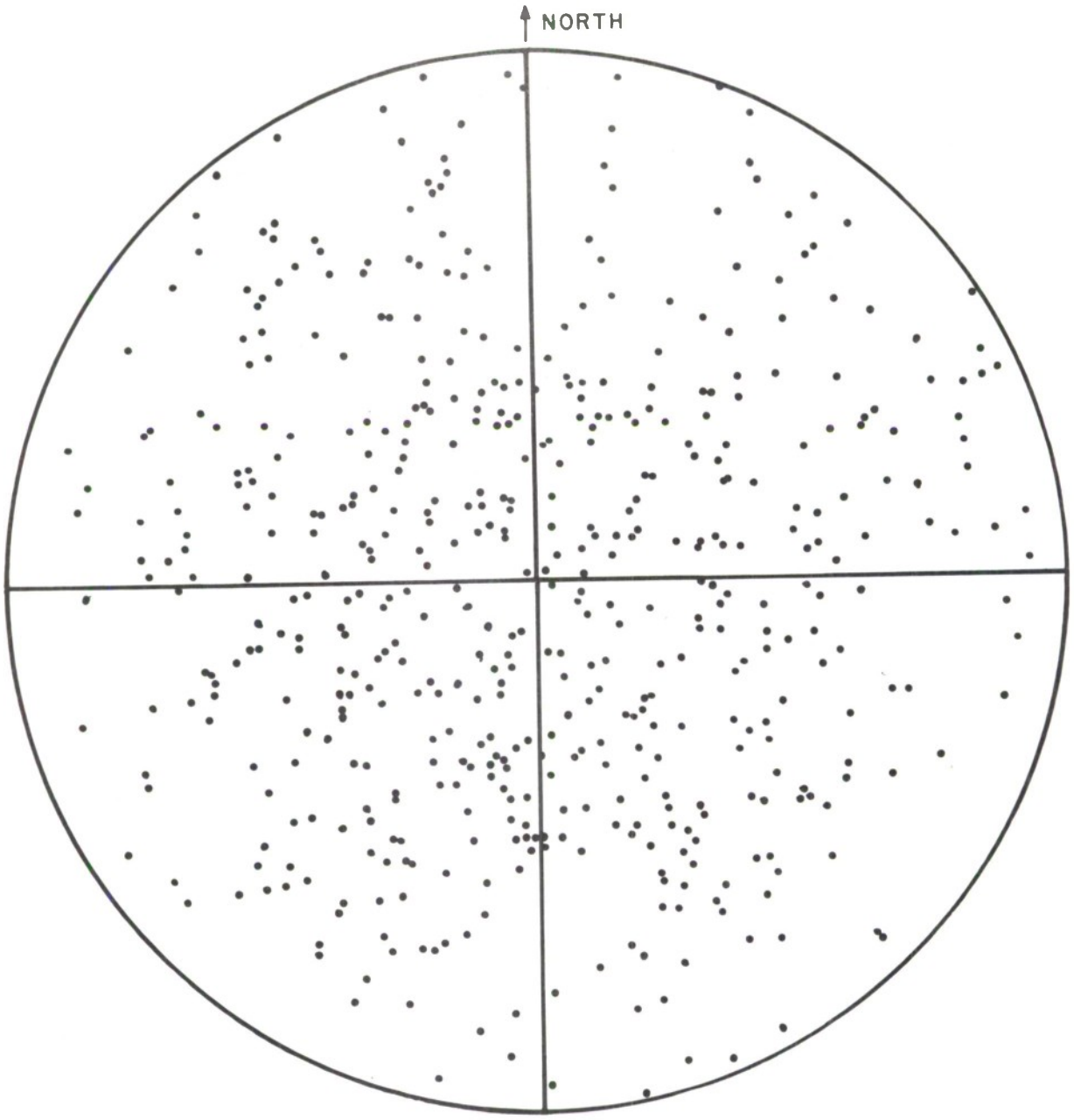


FIGURE 4.2
RANDOM ARRAY

The patterns obtained are shown in Figures 4.3-4.8, and correspond to the same focuses used in Section III for LASA. The corresponding LASA patterns appear in these figures as dashed lines, and all radial patterns indicate the effect of attenuation and geometric spreading as described in Section III. It can be observed that the teleseismic sidelobes for the computed random array are 10-15 dB lower than a clustered LASA with the same number of seismometers. The main lobe is somewhat narrower for this particular set of parameter values. For comparison purposes, Figure 4.5 includes the theoretically derived average radial pattern for a random array with a $\sigma=0.5$. This average radial pattern is derived from Equation 4.5 by converting α to range in degrees using the J-B travel time tables, and correcting the resulting radial pattern to include the effect of spreading and attenuation. The average theoretical pattern compares favorably with the computed pattern for the random array of Figure 4.2.

4.2.2 Effect of Number of Elements

Arrays with different numbers of elements were simulated, and the corresponding patterns are shown in Figures 4.9 and 4.10. The same parameter values as in Section 4.2.1 were used. Four different choices for the number of elements were considered: 525, 263, 132, and 66. The resulting radial patterns are presented in Figure 4.9 with the LASA pattern as a reference. The corresponding transverse patterns can be found in Figure 4.10.

It may be observed that the main beam dimensions are not very sensitive to the number of elements in the array considered. The transverse patterns show a similar teleseismic sidelobe level for the three largest numbers of elements studied. With only 66 elements, the sidelobe level is somewhat higher, but still less than that of LASA-Montana. Similar observations apply to the radial patterns. It may be concluded that in sites with a high teleseismic noise level, unclustered seismic array of some 100 elements are likely to outperform clustered arrays of geometries similar to LASA when delayed sum processing is employed.

4.3 SUMMARY AND CONCLUSIONS

Random arrays were studied as a means of improving the sidelobe performance of a clustered LASA. A theoretically derived average array pattern was obtained for the random array. The derived array pattern indicated that much improved sidelobe performance could be expected from the random array on the average. The question then arises as to how well will the array pattern of a specific random array (out of the ensemble of random arrays) compare with the theoretically derived average pattern. We expect

that with high probability most members of the ensemble will yield an array pattern which compares favorably with the average pattern associated with the ensemble. A specific random array consisting of 525 elements was simulated and its pattern calculated. For this case, the actual pattern of the simulated random array yielded results similar to the theoretically derived average array pattern. Further, the calculations indicated that the 525 element random array resulted in a teleseismic sidelobe level some 10-15 dB less than that calculated for LASA-Montana.

Since it is impractical to randomize all the elements of LASA, random arrays with fewer elements than 525 were examined. In particular random arrays having 66, 132, and 263 elements were simulated and the resulting array patterns calculated. It was observed that the array beamwidth was not significantly altered when the number of array elements was reduced. The sidelobe performance was observed to gradually degrade as the number of array elements was reduced. However, even in the case of the 66 element random array the sidelobe performance was usually at least 6 dB better than that calculated for LASA-Montana.

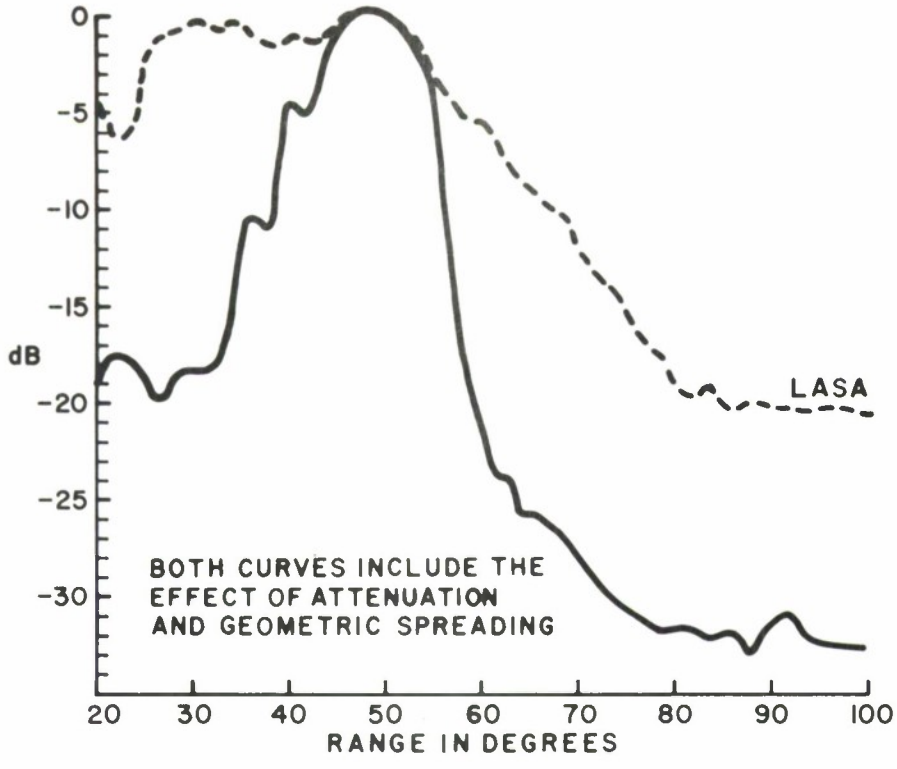


FIGURE 4.3
RADIAL PATTERN FOR RANDOM ARRAY
FOCUSED AT AMCHITKA

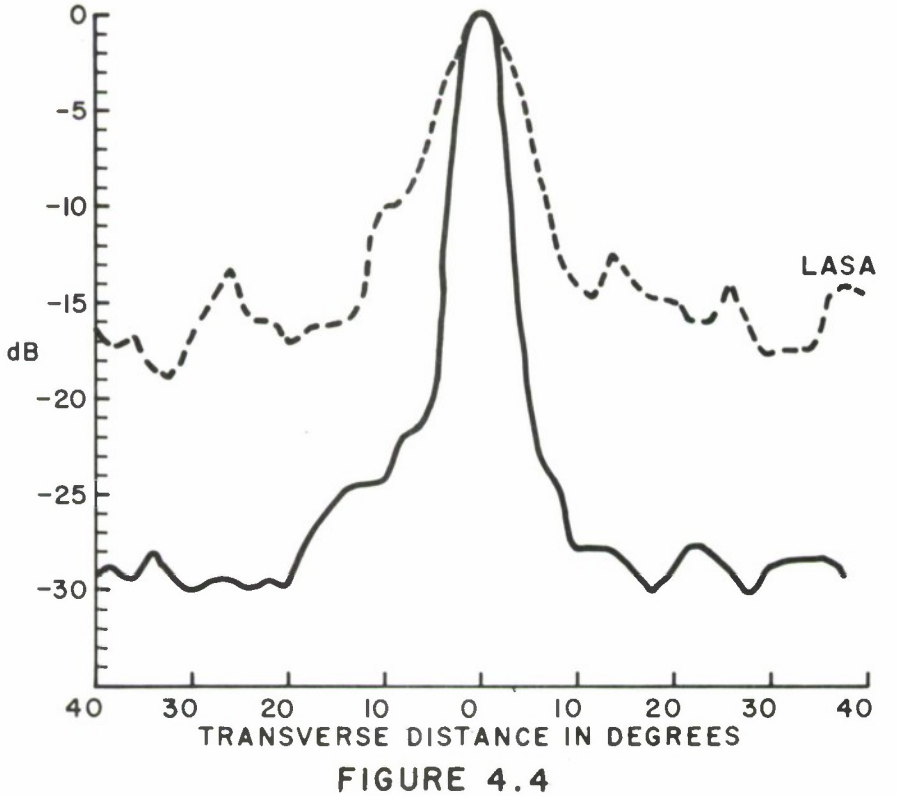


FIGURE 4.4
TRANSVERSE PATTERN FOR RANDOM ARRAY
FOCUSED AT AMCHITKA

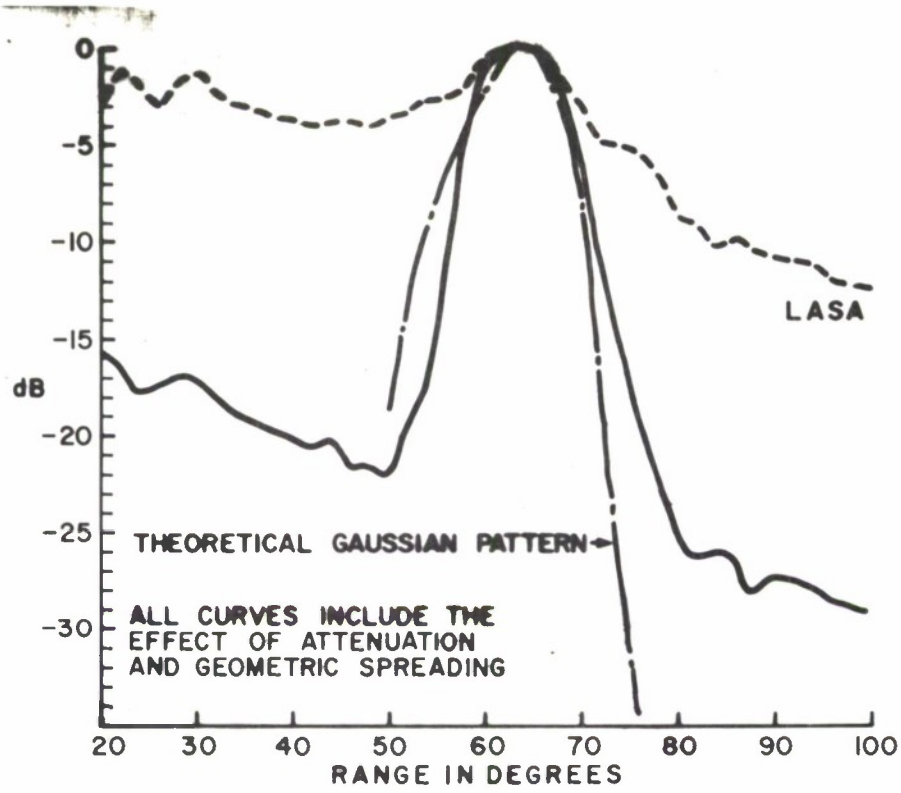


FIGURE 4.5
RADIAL PATTERN FOR RANDOM ARRAY
FOCUSED AT KURILES

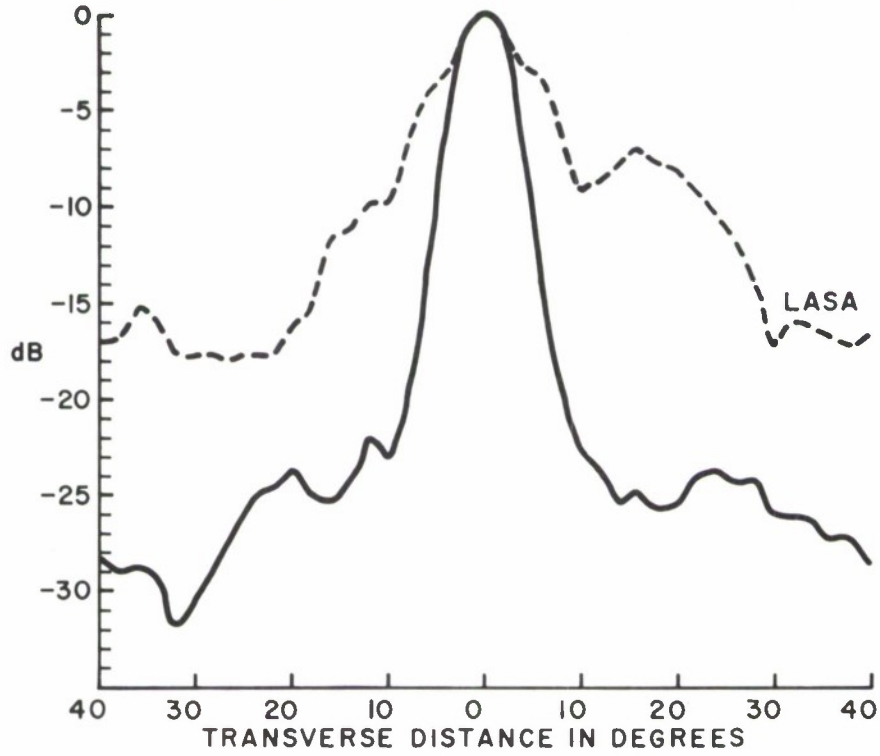


FIGURE 4.6
TRANSVERSE PATTERN FOR RANDOM ARRAY
FOCUSED AT KURILES

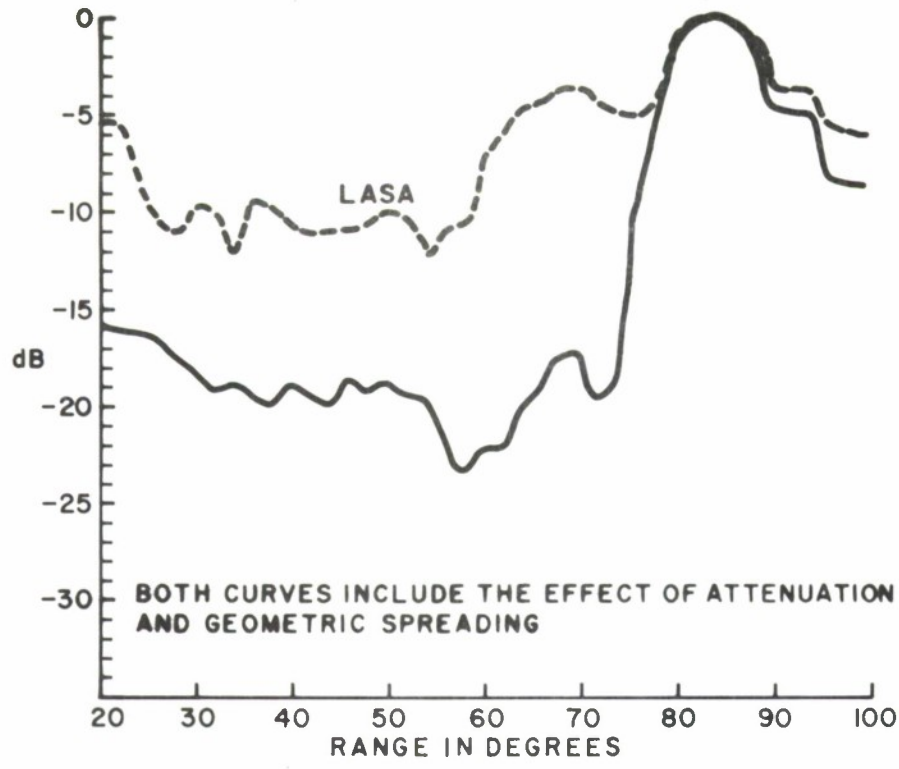


FIGURE 4.7
RADIAL PATTERN FOR RANDOM ARRAY
FOCUSED AT KAZAKH

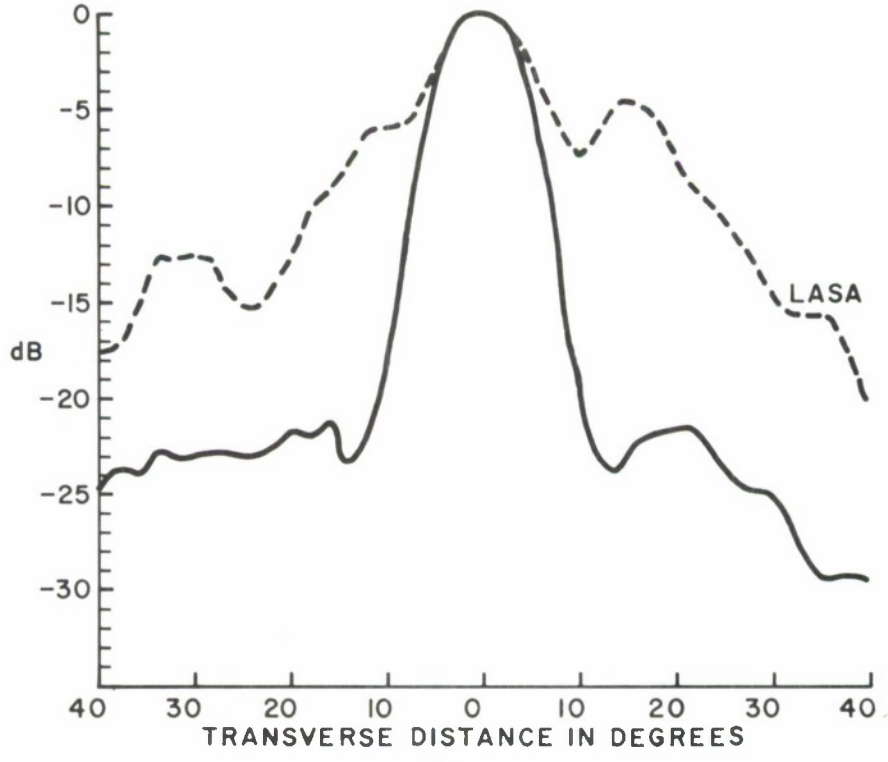


FIGURE 4.8
TRANSVERSE PATTERN FOR RANDOM ARRAY
FOCUSED AT KAZAKH

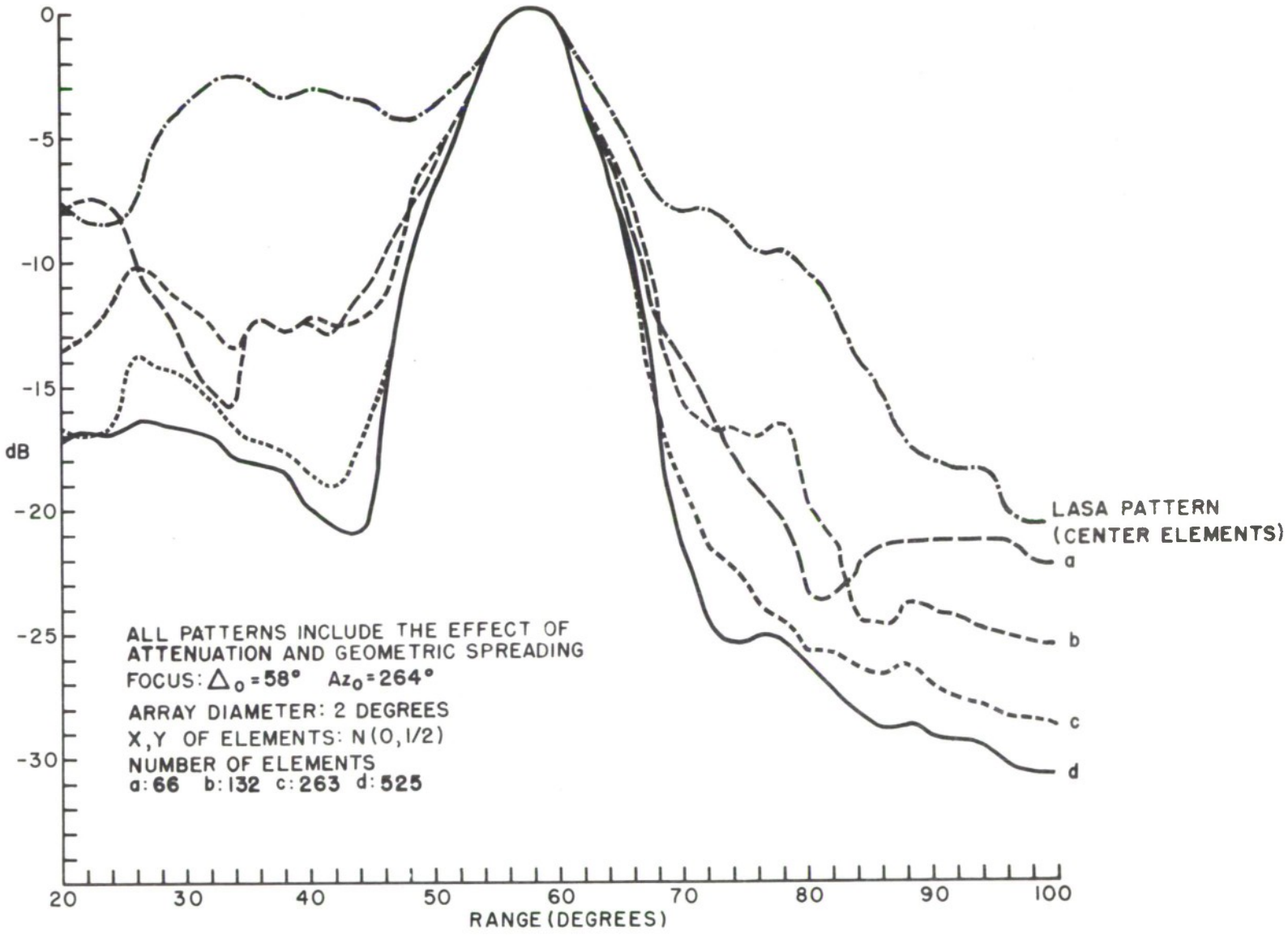


FIGURE 4.9

EFFECT OF THE NUMBER OF ELEMENTS
ON THE RADIAL PATTERN OF A RANDOM ARRAY

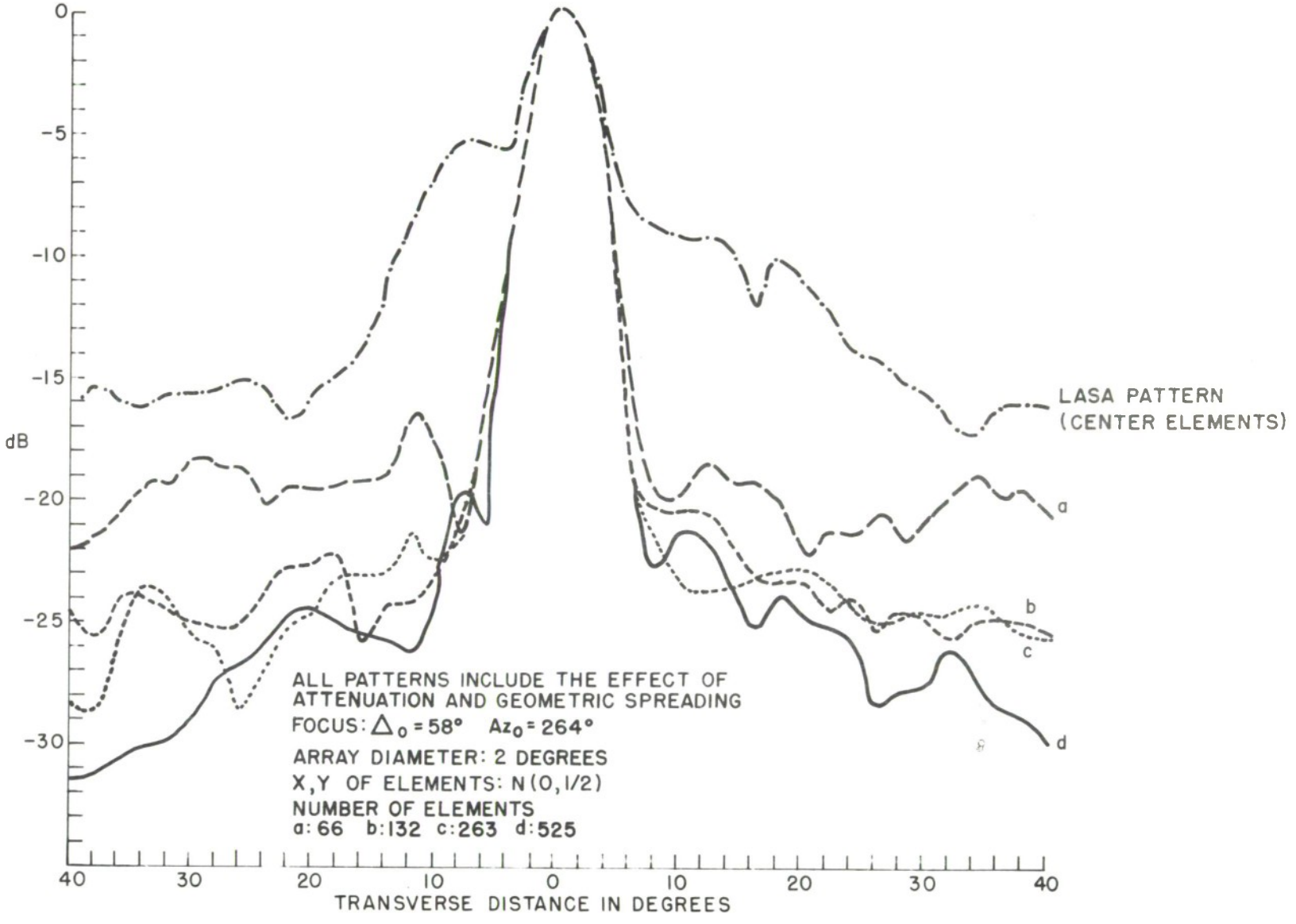


FIGURE 4.10

EFFECT OF THE NUMBER OF ELEMENTS
ON THE TRANSVERSE PATTERN OF A RANDOM ARRAY

SECTION V

DETECTION OF NUCLEAR EXPLOSIONS IN THE PRESENCE OF LARGE NATURAL EVENTS

If a country decided to violate an underground test ban treaty, one of the strategies that it would be likely to choose is selecting an area of high seismicity for the test. There are two reasons for such a selection: the nuclear test might not be detected at all if its signal arrives at the monitoring stations simultaneously with one from a large earthquake, and, if it is detected, it might be mistaken for an earthquake.

Large events produce signals of considerable duration at the receiving instruments. A magnitude-six earthquake, for example, is likely to last many minutes before its power decreases by the equivalent of one magnitude unit. This slow decay rate of the power at the receiver is a serious limitation on monitoring capabilities. Certain array and signal processing techniques can be used to advantage for reducing the interference of the earthquake. Two of these techniques are discussed in this section; both of them are strongly related to the directional characteristics of arrays. In both approaches to detecting underground nuclear tests in the vicinity of natural earthquakes four considerations are of interest: the relative magnitudes of the two events, the relative geometry of the two, the relative time of occurrence of the two, and the geometrical distribution of receiving stations about the epicenters of the two events.

The first approach consists of "steering" one or more nulls of the array pattern in the direction of the earthquake. The limitations that these nulls place on searching nearby regions for test explosions will be discussed together with the quality of nulls which might be obtained. This discussion begins with the introduction of the simple concept of a seismic dipole. This is followed by a discussion of the patterns of a seismic dipole. The characteristics of an array of LASA dimensions that is formed by combining these dipoles is also discussed. Finally the effect of the sampling rate on the effectiveness of a nulling array is briefly discussed.

The second approach to the suppression of earthquake signals consists of steering the main lobe of an array pattern toward the suspected test site; this approach requires a narrow main beam and a low sidelobe level so that an earthquake near the shot epicenter would not contribute significantly to the array output when the array is "steered" to the shot. The 3 dB

beamwidth of LASA-Montana, for example, is on the order of 10^{o} at teleseismic ranges - far too large for the purpose intended here. Thus, continental-size arrays would be necessary in order to search for test explosions detonated in seismically active areas. We shall present four calculated patterns for continental-size arrays in order to give some indication of the patterns that might be achieved. Unfortunately, due to some difficulties in obtaining data in proper format, we have not yet been able to study experimentally the effectiveness of such an array in suppressing earthquake signals.

5.1 SEISMIC DIPOLES

A pair of seismometers, the outputs of which are delayed according to some rule and then subtracted, will be referred to as a seismic dipole.

The response of such a dipole to a plane wave can be expressed as a function of one angle measured on the plane determined by the axis of the seismic dipole and the direction of propagation of the wave. This angle θ is formed by the normal to the dipole axis and the direction of propagation of the plane wave.

5.1.1 Seismic Dipole Response in Terms of the Angle θ

Let us consider such a dipole as is shown in Figure 5.1. The array possesses a null in the direction $\theta=0$ (broadside), for $\varepsilon=o$; the angle θ_m where the dipole response is maximum is given by:

$$\theta_m = \sin^{-1}\left(\frac{\lambda}{2d}\right) \qquad \lambda = \text{fundamental wavelength } (\sim 14 \text{ km}) \qquad (5.1)$$

We can see that a seismic dipole of length d of approximately 60 km would possess a first maximum in its output for an angle θ as close as 7 degrees to the null. This high slope of the pattern can be of great help in the problem we are analyzing.

If we choose a delay τ so as to have a null in the direction θ_o, the angle θ_{m_1}, (angle of maximum output closest to θ_o), will be given by:

$$\theta_{m_1} = \sin^{-1}\left(\pm \frac{\lambda}{2d} + \sin \theta_o\right) \qquad (5.2)$$

There are many angles where the conditions for maximum output are satisfied, and they are given by the general expression

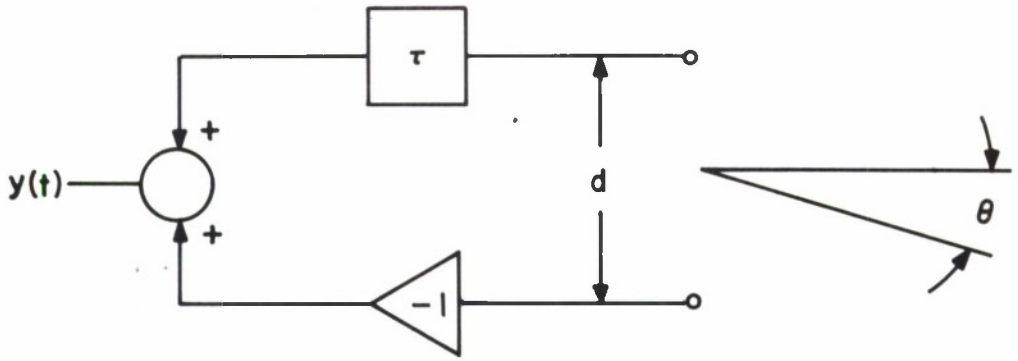


FIGURE 5.1
SEISMIC DIPOLE

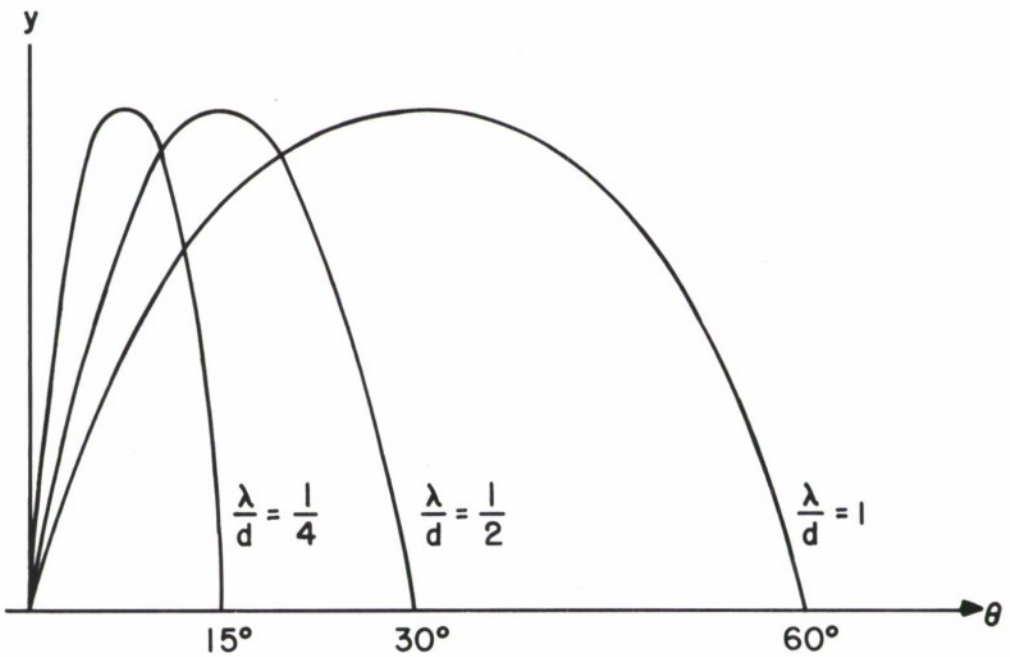


FIGURE 5.2
SEISMIC DIPOLE OUTPUT

$$\theta_{m_j} = \sin^{-1}\left(\pm \frac{2j+1}{2}\frac{\lambda}{d} + \sin\theta_o\right) \quad j=0,1,2... \qquad (5.3)$$

The angles for which the output is zero (a null in the pattern) are given by:

$$\theta_{n_j} = \sin^{-1}\left(\pm \frac{j\lambda}{d} + \sin\theta_o\right) \quad j=0,1,2... \qquad (5.4)$$

The angle θ will be a function of range and azimuth.

The characteristics of the pattern are not greatly affected by the introduction of a delay, the null is just placed at the corresponding θ_o; for small θ_o, the shape of the pattern will remain very close to the corresponding pattern for $\theta_o=0$ shown in Figure 5.2.

5.1.2 Response of a Seismic Dipole in Geographical Coordinates.

Consider a seismic dipole formed with two of LASA's elements. We shall steer a null to a certain point on the surface of the earth and compute the response of the dipole for events coming from the region of the null. Figure 5.3 presents a schematic diagram of the configuration under consideration.

In order to steer the null to N, a delay τ_o is introduced and then the two signals are subtracted.

$$\tau_o = k_{\Delta_o} d\sin\theta_o$$

$$\text{where } k_{\Delta_o} = \frac{1}{v_{\Delta_o}} = \text{slope of the travel-time curve in sec/deg} \qquad (5.5)$$

d = length of the dipole in degrees

The expected pattern is shown in Figure 5.4.

The locus of the first null is obtained by setting the relative delay between arrivals equal to τ_o. Therefore,

$$dk_\Delta \sin\theta = dk_{\Delta_o} \sin\theta_o \qquad (5.6)$$

(Equation of locus 5 in Figure 5.4)

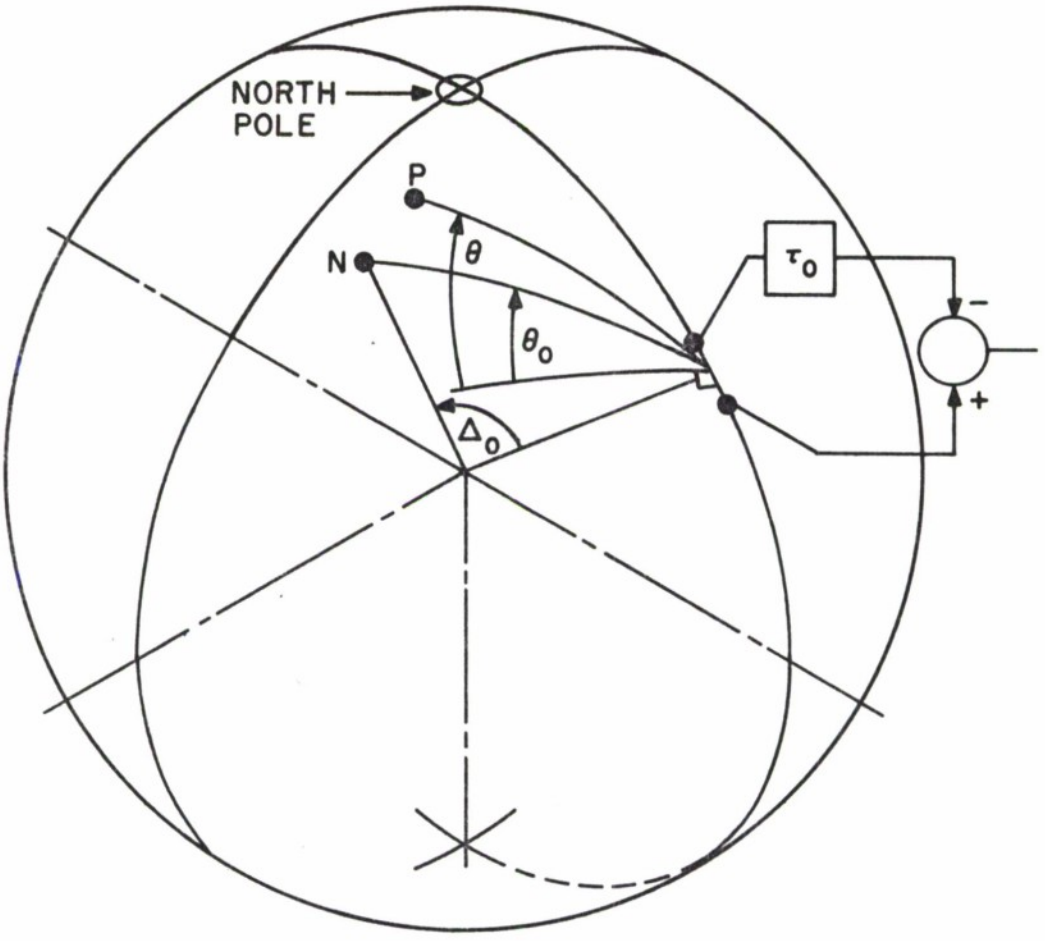


FIGURE 5.3
SEISMIC DIPOLE LOCATION FOR PATTERN COMPUTATION

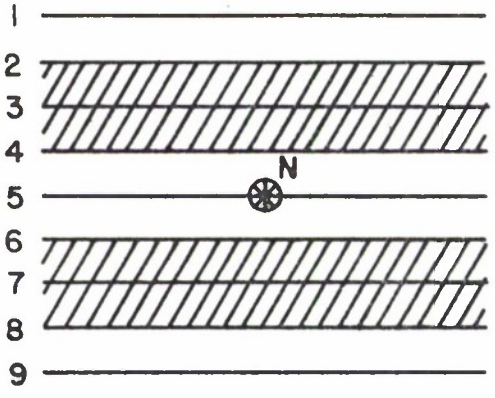


FIGURE 5.4
EXPECTED PATTERN FOR SEISMIC DIPOLE

In order to have the maximum output, the difference between the actual delay in arrival and the "built in" delay τ_o should be equal to ½T where T is the period of the dominant frequency.

$$d|k_\Delta \sin\theta - k_{\Delta_o} \sin\theta_o| = T/2 \tag{5.7}$$

In a similar fashion, the conditions for the rest of the contours may be obtained. The following parameter values have been used:

$$\begin{aligned} T &= 1 \text{ sec} \\ d &= 64 \text{ km} \\ \Delta_o &= 62^o \\ Az_o &= 320^o \end{aligned} \tag{5.8}$$

The resulting dipole response is plotted in Figure 5.5; the corresponding region of the total pattern of the dipole is indicated in Figure 5.6. Observe that if a null is steered at a point O in Figure 5.6 (broadside to the dipole), then all points lying on the great circle that joins O and the array center, C will also produce a zero response. On the other hand, if the null is steered to a point M (on the axis of the dipole), the great circle joining M and C will show alternating maxima and minima.

The radial beamwidth is considerably greater than the transverse beamwidth for a null placed at M. As a matter of fact, a dipole of approximately 200 km would have the second null at about 20^o from the first null.

It can be observed that the response at two dipoles such as shown in Figure 5.7 is going to show regions of maximum output such as indicated by the shaded areas in Figure 5.7.

In order to have circular symmetry about the null, N, d_2 needs to be larger than d_1. A distance d_2 on the order of 200 km is required.

We expect that having the freedom to choose elements from a very large array, a pattern that has a central null surrounded by a region of high response could be obtained. The dipoles are required to have different lengths and orientations. Obviously, the width of the region of high response depends on the size of the dipoles.

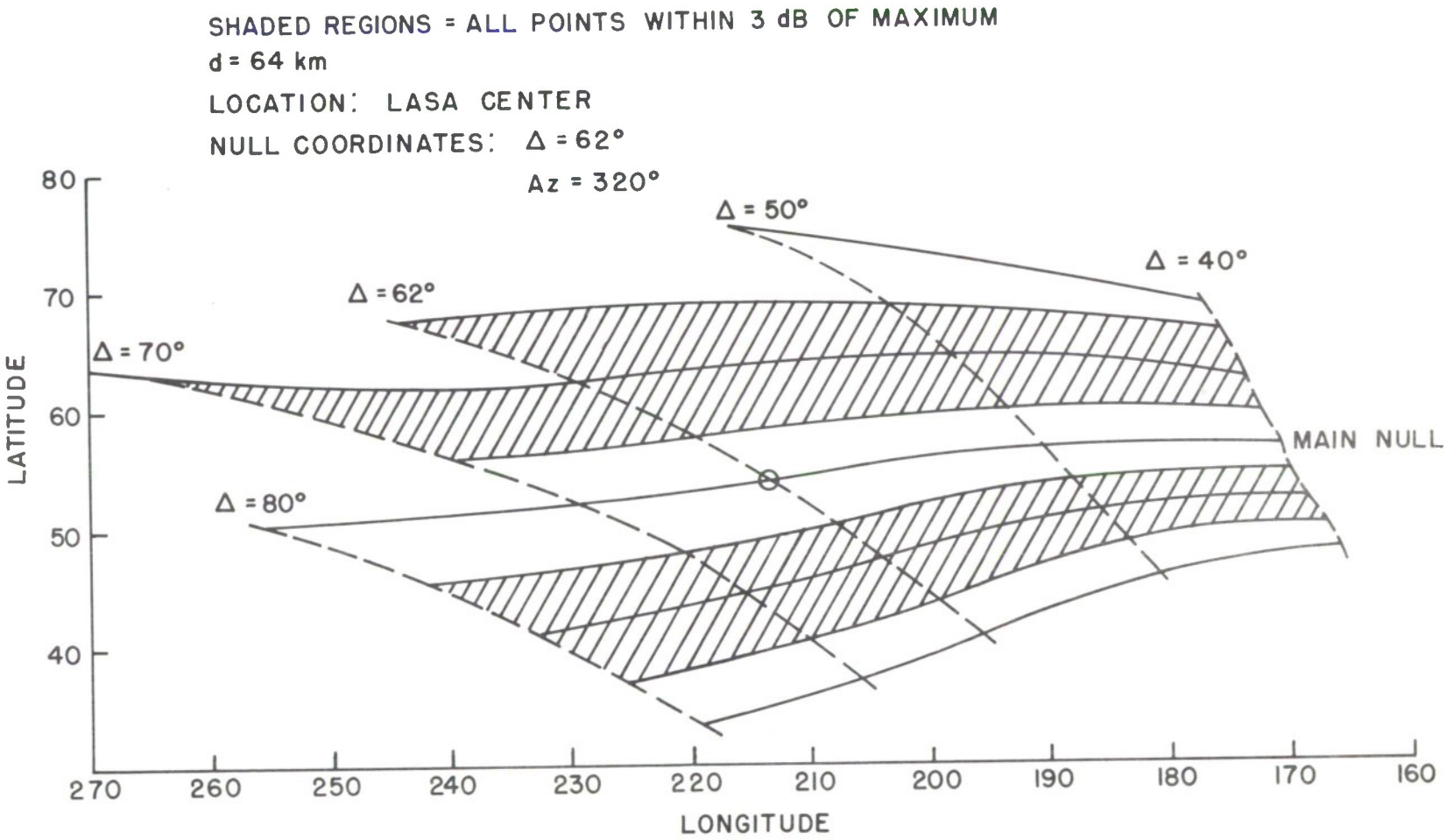


FIGURE 5.5
DIPOLE PATTERN

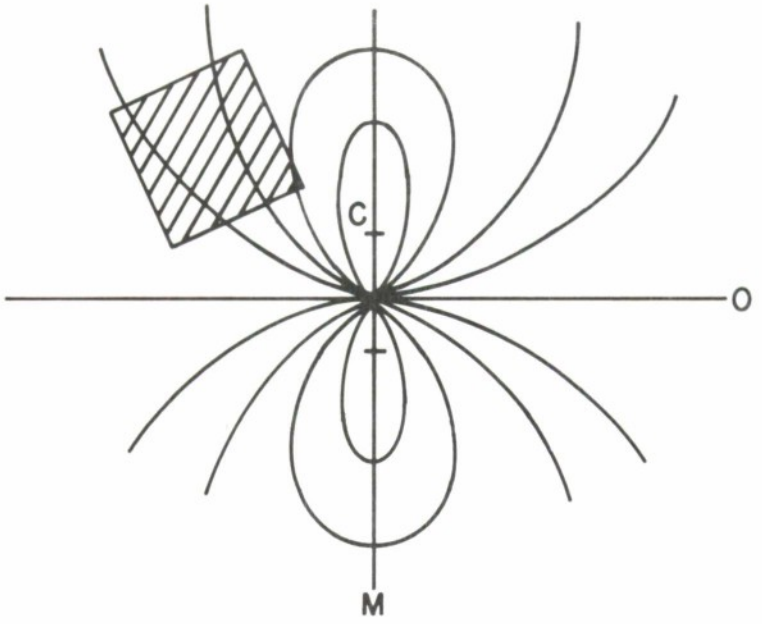


FIGURE 5.6
REGION OF THE TOTAL PATTERN OF THE DIPOLE
ILLUSTRATED IN FIGURE 5.5

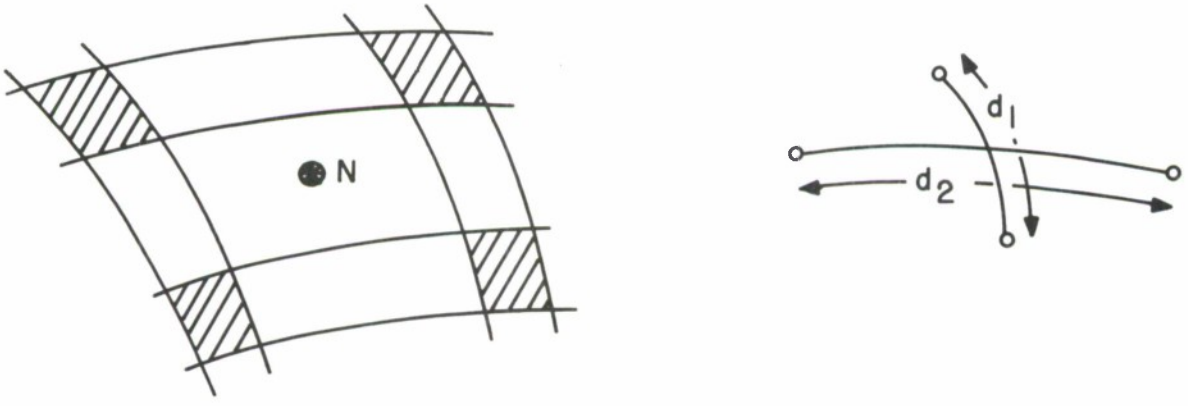


FIGURE 5.7
PATTERN OF AN ARRAY OF TWO DIPOLES

5.1.3 Effect of Time Sampling Rate on Efficiency of Nulling

In order to be able to steer a complete null ($-\infty$ dB), two conditions have to be satisfied: the signals in the elements have to be identical and the steering delay has to align both signals exactly. The first condition is met fairly well by the first second of the P-arrival but not by the P-coda (and we were not successful at extending the useful region into the P-coda by employing calculations designed to remove local reverberations). The second condition cannot be met using discrete time records without interpolation, since the desired time resolution is less than the sampling period. Using a 1 Hz sinewave for illustration, it can be shown that the relative suppression will be given by:

$$G = \sqrt{2-2\cos 2\pi\delta} \quad \text{where } \delta = \text{misalignment in seconds}$$

Three sample values of suppression, corresponding to three possible values of δ are tabulated below:

δ [Sample points for 20 s.p.s.]	δ sec	G	G(dB)	G (Seismic magnitude)
0	0	0	$-\infty$	$-\infty$
½	.025	.155	-16	-.5
1	.05	.285	-10.5	-.3

From this table it is clear that the obtainable suppression is seriously deteriorated by timing errors. In order to improve the suppression capabilities, a higher sampling rate or an interpolation between the sample points is required.

5.2 CALCULATED PATTERNS FOR CONTINENTAL-SIZE ARRAYS

A continental-size array will be necessary if an array pattern with a narrow enough main beam and low enough sidelobes to allow searching for a nuclear test in the vicinity of a natural earthquake is desired. Figures 5.8 and 5.9 present calculations of array patterns that might result from continental size arrays. For these calculations two different arrays (one with 27 stations and one with 17 stations) and two different focus points were used. These choices correspond to stations and epicenters for which we have requested data.

Two patterns were obtained for each array: the "latitude cut" and the "longitude cut." These patterns were obtained by calculating the maximum value of the array output that would occur with the source placed at different points on the focus meridian (the latitude cut) and on the focus parallel (the longitude cut). For all of these calculations it is

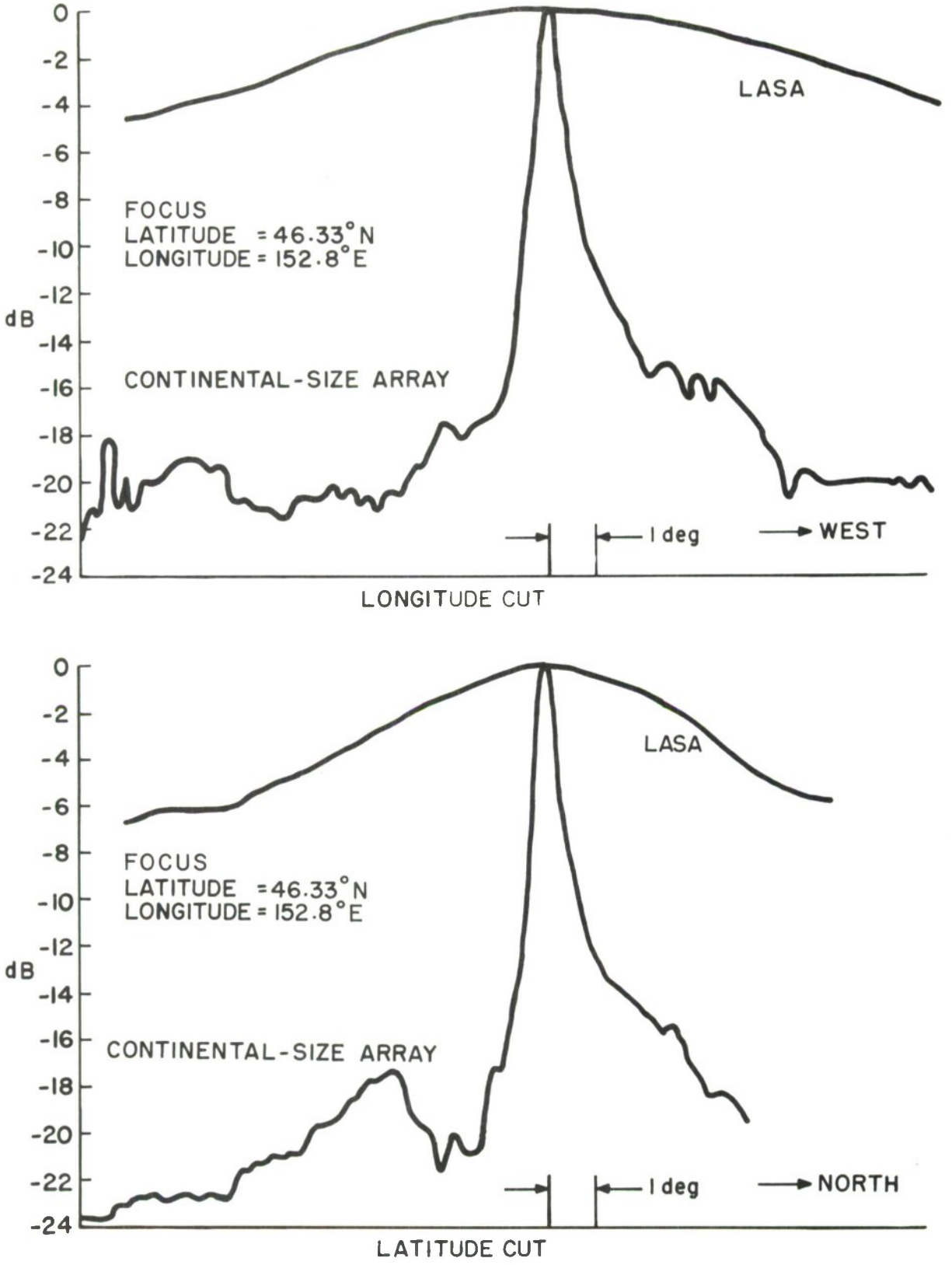
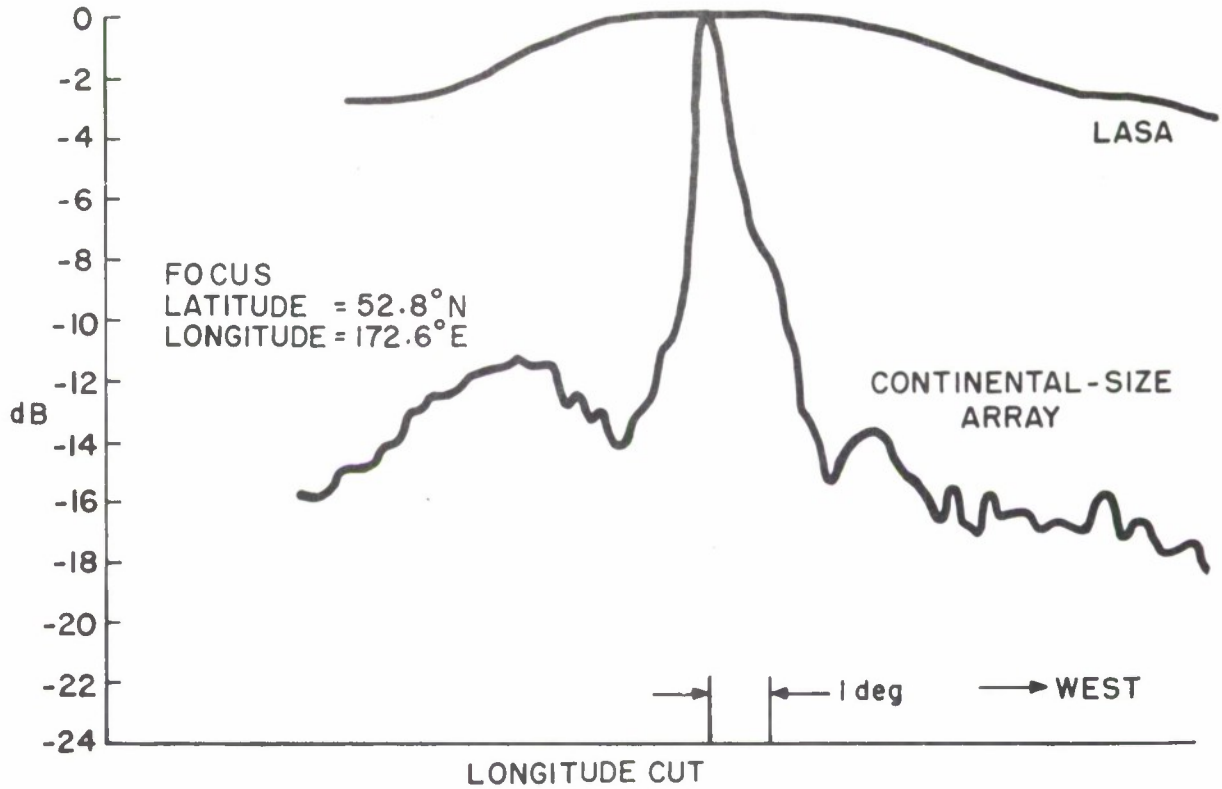


FIGURE 5.8

CONTINENTAL-SIZE ARRAY PATTERNS (27 ELEMENTS)



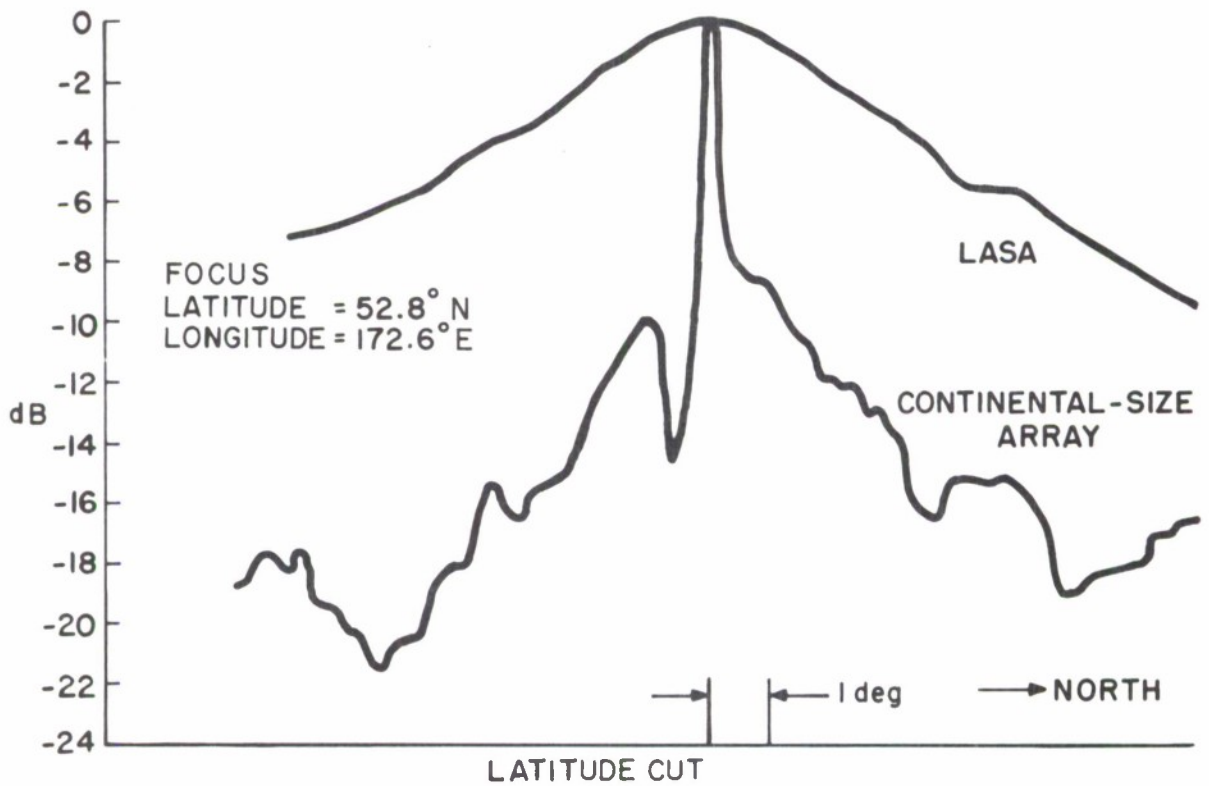


FIGURE 5.9

CONTINENTAL-SIZE ARRAY PATTERNS (17 ELEMENTS)

assumed that the seismic records consist of one period of a 1 Hz sinewave. It should be noted that this method of calculating the pattern must lead to a pattern that is never smaller in amplitude than the reciprocal of the number of elements in the array, when the maximum of the pattern is normalized to unity. Furthermore,these patterns apply only to that portion of the coda of the earthquake which is correlated. The uncorrelated component of the coda should not be sensitive to the aiming point of the array. This portion of the energy should be reduced by the number of elements in the array at all angles.

For purposes of comparison, patterns calculated on the same basis for an array consisting of the center elements of the LASA-Montana clusters are also presented in Figures 5.8 and 5.9. Figure 5.8 presents the two patterns for the array described in Table XV. From this figure it is clear that the beamwidth for the continental-size array is one order of magnitude smaller than that of LASA-Montana. The same observation may be made from Figure 5.9, which is based on the array described in Table XVI.

These calculations indicate that very narrow beamwidths (less than 1 degree) and relatively low sidelobes might be obtained from continental-size arrays. Several qualifications should be placed on this conclusion. First of all, in making this calculation it was assumed that the seismic signal could be replaced by one period of a 1 Hz sinewave. Actual earthquake signals, where the rate of decay of the signal after its initial peak is relatively slow, may lead to quite different beam patterns. Even if this is not the case, the practical problems of implementing such an enormous array are, of course, considerable. Most obvious of these is the communications problem of getting all of the seismic records together for further processing.

5.3 SUMMARY AND CONCLUSIONS

This section has presented some early considerations and calculations relating to the problem of detecting covert nuclear tests in the presence of natural earthquakes. The calculated array patterns for continental-size arrays indicate that such arrays may be very useful in searching for nuclear tests in the vicinity of earthquakes since beamwidths on the order of 1° appear possible. It should be stressed at this point that these array patterns must eventually be considered in the context of a detection system that consists of more than a single continental-size array. Until these more general considerations are understood, it is not possible to reliably estimate parameters of a potential operational system such as search times or minimum magnitude of a nuclear test in order to

be detected under a given set of circumstances. If, for example, a detection system consisted of a circle of seismometers surrounding the region of interest, plus a continental-size array, many suspected test sites could be eliminated (for a specific detonation time) on the basis of single seismic records, and the region that must be "searched" by the array would thereby be reduced. Continued work on this problem will include considerations of possible detection systems employing continental-size arrays plus single seismometers, as well as further study, employing actual seismic data, of continental-size arrays themselves.

SECTION VI

LOCATION OF EVENTS USING A SINGLE LASA

This section deals with the location of events using a single LASA. The discussion will be limited to a consideration of teleseismic events with direct P-phase arrivals at the array. Within this limitation we shall discuss the differences between event location by conventional triangulation methods and by measurements of the parameters of the ray connecting the source of the seismic energy and the array. Also discussed will be the effects of noise- and time-errors on this single array measurement. Finally, the results obtained to date will be presented. Except for two Kurile Island earthquakes, where large errors in the determination of range are believed to result from errors in the J-B travel-time tables, the results are encouraging: epicenter location errors are on the order of one-half degree.

6.1 CONVENTIONAL AND ARRAY LOCATION TECHNIQUES

The hypocenters of seismic events are conventionally located by the process of triangulation. That is, from a knowledge of velocity of propagation of seismic signals and the arrival times of these signals at a number of seismic stations, it is possible to infer the epicenter of an event, the depth of occurrence of the event, and also the origin time of the event. Since each event is characterized by four parameters, latitude, longitude, depth, and time of occurrence, at least four seismic stations are required to perform these computations. Obviously, the greater the number of stations detecting the event, the finer will be the determination of its location. Geometry also plays an important role in the accuracy with which events can be located. When the detecting stations completely surround the event to be located, the accuracy of location is superior to the case when the detecting stations are all located so as to lie on nearly the same bearing from the event to be located. When attempting conventional location of events with a single LASA, it is this latter limitation on accuracy which is dominant, for the total collection of sensors contained in a single LASA subtends at most a few degrees in azimuth as viewed from any epicenter of an event at teleseismic ranges. Experiments at Lincoln Laboratory with data from LASA-Montana bear this out, since the location accuracy achieved by treating the clusters as individual seismic stations is on the order of 310 km. This error, determined from the distance between LASA and C&GS epicenters for 39 teleseismic events, agrees quite well with a first order estimate of the standard deviation in event location for timing errors on the order of tenths of a second (private communication from Dr. E.J. Kelly, Jr., Lincoln Laboratory).

Because the seismometers of a LASA can be operated as an array rather than a collection of individual stations, it is possible, in principle, to achieve far more precise location information from a single LASA than is indicated above. Location of events by array techniques takes an altogether different form than location by triangulation. The array is used to measure the direction from which the seismic signals arrive (azimuth and angle of incidence) by coherent combination of the signals at all sensors of the array. The locus of the intersection of the 3 dB level of a LASA beam with the surface of the earth can be as large as 10° for teleseismic events. This does not mean that the accuracy of location with such a beam is limited to this magnitude of precision, however, for in the absence of interfering noise, etc., there is no limit to the accuracy with which angles may be measured with an array of any size. Thus, the array is used to determine the parameters of the seismic ray connecting the array and the seismic source. The hypocenter of the event must lie somewhere along this ray -- presumably near the point at which the ray intersects the surface in the teleseismic region. Obviously, a knowledge of the depth of focus of the event is required to determine precisely its hypocenter.

Approximately 50% of the teleseismic events observed at LASA-Montana can be sorted for depth by pP measurement at Montana alone (5). For these events, a definite hypocenter location can be determined. Where no pP depth determination can be made with the single LASA, prior seismicity information concerning the region in which the ray intersects the surface may be of some value. Even here, the relatively normal angles of incidence of teleseismic signals at the surface of the earth introduce quite small errors in location. For example, if an event is known to lie somewhere between the surface and a depth of 200 kilometers, the maximum error in location introduced for ranges of approximately 90° would be 25 kilometers. For closer ranges, approximately 40°, this maximum error would be only 50 kilometers. Of course, it should be possible to combine information from the LASA with that obtained from other stations (single instrument stations as well as arrays) to obtain better depth estimates from the normal computer solutions for epicenters. However, our interest at this time is centered on what can be done with a single LASA. As a result, for the following, we shall concentrate on the location of either surface-focus events or those earthquakes with known depths. The effects of additive noise and timing errors will be considered, and the experimental results will be described.

6.2 LIMITATION OF ANGULAR ACCURACY BY ADDITIVE NOISE

If one attempts to measure the angle of arrival of a plane wave with a pair of sensors, the accuracy of the measurement depends on the accuracy of the measurement of the following three quantities: the time of arrival at the individual sensors, the spacing between the sensors (the base line), and the velocity of propagation of the wave. When the sensors are spaced no farther apart than the maximum dimensions of LASA, the uncertainty in the separation of the sensors can produce at most a secondary effect on the accuracy of the angular measurement. For the present, we shall assume that the travel-time table from which the velocity of propagation is obtained is perfect. This leaves for discussion only the determination of the arrival time of the wave at the sensors.

To see how additive noise will affect the measurement of arrival time of the seismic signals, let us consider the measurement of times of a zero crossing of a sine wave of frequency f, corrupted by additive Gaussian noise. The standard deviation of this measurement can be shown, for the case of moderate signal-to-noise ratios, to be:

$$\sigma_t = \frac{1}{2\pi f(S/N)} \tag{6.1}$$

where S/N is the ratio of peak-signal-to-rms-noise. For the two-element array hypothesized at the beginning of this section, it is possible to make use of the above expression together with the assumption of independent noise at the two sensors to compute the standard deviation in angular measurement with this array for signals arriving from a direction nearly perpendicular to the line of the array. This quantity is given approximately by the following expression:

$$\sigma_\theta \simeq 1.4 \frac{c}{D} \sigma_t \simeq \frac{1.4c}{2\pi fD(S/N)} \tag{6.2}$$

where c is the velocity of propagation, and D is the spacing between elements. By way of illustration, for events located at a range of 80° from the two-element array, the velocity of propagation is approximately 0.2 degrees/sec. If we choose the spacing of these elements to represent the diameter of LASA, two degrees, and take the frequency as 1 Hz, which is typical for teleseismic signals, this standard deviation becomes:

$$\sigma_\theta\Big|_{80°} \simeq \frac{0.025}{(S/N)} \text{ radians} \tag{6.3}$$

This figure strongly suggests that noise would not introduce serious errors for events with sufficient S/N to be detected on a single seismometer. For smaller events, however, the accuracy available from the two-element array would be smaller than desired -- particularly in estimating range, since there is an angular compression of some eight-to-one in the relation-

ship between incidence angle and range. Here, we should note that when the signals from a large number of seismometers (the center elements of the LASA clusters, for example) are used to form an array, the angular accuracy stated above can be materially improved if additive noise is the only interfering element.

For a multi-element array, estimates of the angular accuracy which can be achieved are nowhere near as simple as for the two-element array. This is because the computations must take into account not only the actual locations of the elements within the array, but also the type of signal processing employed to combine the outputs of the various sensors of the array. The particular geometry of the Montana array proved a difficult one to handle analytically, and estimates of LASA's performance have been made using a linear array with equally-spaced elements (see Appendix B). For a 20-element array, a lower bound on the standard deviation in angular measurement (for conditions similar to that for the two-element array, independent noise at each element, and two-degree array dimensions) is given by:

$$\sigma_\theta = \frac{0.019}{(S/N)_T} \quad \text{radians} \tag{6.4}$$

where $(S/N)_T$ is the square root of the power signal-to-noise ratio at the output of the array. It is interesting to note that, if one takes into account the fact that sinusoidal signals were assumed, this expression can be rewritten in terms of the ratio of the peak-signal-to-rms-noise out of the array, $(S/N)_o$, as follows:

$$\sigma_\theta = \frac{0.027}{(S/N)_o} \tag{6.5}$$

Since there were two elements in the first array, and 20 in the second, the increase in performance is almost identical with the array gain in signal-to-noise ratio. This suggests that the spacing of the elements may not be as important as originally hypothesized, provided the noise is independent at the various elements of the array. Further, it appears likely that events with sufficient S/N to be detected with the array can be located with adequate precision when additive noise is the sole corrupter of the signals. Unfortunately, another source of error, more serious than that produced by additive noise, appears to dominate the location problem. This is the problem of timing errors which will be discussed in the next section.

6.3 EFFECT OF TIMING ERRORS ON ANGULAR ACCURACY

As just mentioned, the most serious problem affecting the location of events with a single LASA appears to lie in timing errors which result from a number of sources. At the moment, only two such sources that could have first order effects have been identified. These are differential travel time anomalies and errors in the travel-time derivatives. A third source of error, the quantized nature of the delays introduced in scanning a beam of the array, is of only secondary importance. Both of the primary sources of error appear to have about the same magnitude of possible effect on location accuracy. Ways of separating these effects are available . As of this report, however they have not been applied to the experimental data. An empirical approach, which infers the magnitude of the time errors by measuring the maximum value of the beam pattern, suggests that the errors in angular measurement are not inconsistent with the time errors that are present. To simplify the discussion, each of the primary sources of timing errors will be considered separately, and then the measure of consistencey will be described. Finally, the experimental results will be presented.

6.3.1 Differential Local Travel-Time Anomalies

Travel-time anomalies, in the form of station corrections, have long been accounted for in the determination of event location. These station corrections were assumed to be zero in the preceding noise discussion. In practice, however, local travel-time anomalies amounting to substantial fractions of a second exist across the Montana array. Moreover, these anomalies (deviations from the plane wave assumption introduced above) vary with both bearing and range of the event from the array. While these anomalies have been estimated from the arrival times of many events located in different portions of the earth (6), good estimates are available only for relatively active seismic areas. Further, there exists considerable variance in the estimates of the anomalies for events in some of the regions already calibrated.

The magnitude of these time uncertainties is perhaps best illustrated by way of the data presented in Table I. Here the standard deviations in determination of local travel-time anomalies are presented for the center elements of the B, C, D, E, and F ring clusters of LASA for three regions of interest. These regions are Amchitka, Kazakh, and the Kurile Islands. Two facts are immediately obvious from this table. First, the mean values of these standard deviations, for all three regions, are substantial (0.06 to 0.08 seconds). Second, for the Kuriles and Amchitka regions, where the bulk of the data were obtained from earthquakes, the individual anomaly standard deviations are, in general, at least twice as large as those for Kazakh. Presumably this is because the Kazakh events, all surface-focus events, occurred within an exceedingly small geographic region.

TABLE I

STANDARD DEVIATION OF LOCAL ANOMALY ESTIMATES
FOR LASA CLUSTERS FOR THREE REGIONS

CLUSTER	KURILE (sec)	AMCHITKA (sec)	KAZAKH (sec)
B1	0.06	0.06	0.06
B2	0.09	0.07	0.02
B3	0.06	0.06	0.05
B4	0.06	0.06	0.06
C1	0.05	0.08	0.04
C2	0.07	0.09	0.10
C3	0.09	0.09	0.02
C4	0.05	0.08	0.05
D1	0.05	0.12	0.02
D2	0.07	0.08	0.01
D3	0.07	0.05	0.03
D4	0.09	0.06	0.06
E1	0.05	0.08	0.06
E2	0.07	0.07	0.06
E3	0.07	0.13	0.09
E4	0.07	0.06	0.10
F1	0.10	0.10	0.09
F2	0.07	0.07	0.12
F3	0.07	0.07	0.07
F4	0.08	0.12	0.07
Mean Values	0.07	0.08	0.06

NOTE: All anomalies referred to AO

At this time, it is not possible to state whether the spread in measurements indicated by Table I results from microstructural differences in the earth, is a function of perturbation of the measurements, or simply the result of too few measurements to date. Suffice it to say that it is these anomalies which were used for the position measurements decribed later on.

While the observed standard deviations in travel-time anomalies are not large enough to produce substantial loss in S/N gain for an array (providing the mean values of these anomalies are removed), they are large enough to produce substantial beam pointing errors. This will be discussed further in Section 6.4. Before proceeding further, however, it is instructive to note that the mean values of the spread in the local anomalies indicated in Table I can result in rms pointing errors of some 5-10% of the 3-dB beamwidth of the array. For those ranges at which the LASA beam is approximately 10°, this implies a beam pointing error on the order of 50 to 100 km.

6.3.2 Errors in Travel-Time Table Derivatives

Earliest location computations were performed using the J-B tables. It was soon discovered that these tables led to considerable problems. First, since the tables were not smoothed, flat areas appeared in the beam patterns produced when these tables were used to scan the array. Second, we have learned that the time derivatives of these tables can be in error by as much as some 10% (private communication, E. Herrin). This latter fact could account for an error of some one or two degrees when attempting to infer range from a measurement of the angle of incidence at certain ranges. It is just this source to which we attribute the large errors in range for the two Kurile earthquakes studied. We understand that Dr. Eugene Herrin of SMU will soon be publishing a new set of travel-time tables. Unfortunately, these tables were not available at the time these calculations were performed, and the older J-B tables were used instead.

The problems evidenced by the flats in the array patterns were removed by smoothing of the travel-time table derivatives, in a manner suggested by Herrin, so that there existed only a constant term and even powers of range in the polynomial fit. While this expedient helped, it did not remove the errors in the derivatives. Thus, even though the correct range might be chosen for an event, the velocity associated with this range, and hence the time delays associated with scanning the beam in azimuth could be in error by some 10%. For an event at a range of 80° where the velocity is approximately 20 km/sec, a 10% error in velocity could result in a timing error of some 0.02 seconds for the elements in the F-ring. Of course, the error decreases for those elements in the center of the array, but it also increases with decreasing range. As a result, this source of time errors requires further study. The Herrin tables should be very useful in resolving this problem.

6.4 RELATIONSHIP BETWEEN TIMING ERRORS, ARRAY GAIN, AND ARRAY POINTING ERROR

In the previous section, two sources of timing error which could affect angular measurement accuracy were introduced. We shall now assume that the travel-time anomaly errors are the largest of the two, and concentrate our attention on these. In this manner we shall avoid the problem of separating the two sources of error. Let us assume then that there exists a set of travel-time anomalies which are correct for any event we wish to study. Next, we must note that our knowledge of the anomalies is imperfect: there is some difference between our estimates of these anomalies and the actual ones. Let us further assume that these differences are random, in fact, normally distributed with zero mean. The mean pointing error will be zero, and we may estimate the standard deviation of the pointing error of the array (error in angular measurement) in terms of the beamwidth of the array and the standard deviation of the anomaly errors (7).

$$\sigma_\Theta = \frac{\sqrt{6}\ \sigma_\varepsilon \Theta_B}{\pi\ \sqrt{N}} \text{ radians} \qquad (6.6)$$

where σ_ε is the rms phase error in radians

Θ_B is the beamwidth in radians

N is the number of elements

Because the spread in estimates of the local travel-time anomalies is, in general, of the same order of magnitude as the difference between the mean values and those measured for any one event studied, it is impossible to state that the anomalies are well-known. Thus, comparisons of the mean catalogued values and those measured for any single event do not adequately describe the time errors for that event, and the effect of these errors must be estimated by other means.

Because it has been impossible to make direct measurements of the anomaly errors, we have resorted to an indirect method of estimating their contribution to the beam pointing error. If, in fact, there are random errors in the time alignment of the outputs from the sensors of an array, there will be a loss in signal gain for the array. Thus, if the peak outputs of each of the sensors of an array are normalized to unity, and the array scanned so as to point directly at the energy source, with no time errors the output of the array should be equal to the number of sensors in the array. Where there are timing errors, the output of the array will be less than the number of sensors. If these time errors have zero-mean, normal distributions, the loss in gain can be related to the number of sensors and the standard deviation of the time errors (8).

$$G = e^{-\sigma_\varepsilon^2} + (1/N)(1-e^{-\sigma_\varepsilon^2}) \simeq e^{-\sigma_\varepsilon^2} \quad \text{(for N large)} \tag{6.7}$$

where G is the normalized power gain, i.e., G = 1 with no phase errors. This is precisely the case at hand, for we assume that by taking into account the mean value of the catalogued, local travel-time anomalies, remaining time errors have the required distribution. It is possible to combine this expression with that for the pointing error in such a manner as to eliminate the standard deviation in travel-time anomalies. We can thus obtain an expression for the rms pointing error in terms of the array beamwidth and the loss in signal gain -- both directly measurable quantities.

$$\sigma_\theta = \theta_B \sqrt{12 \ln(N/A)/N\pi^2} \tag{6.8}$$

where A is the maximum of the array output. Assuming a predominant period of 1 Hz for the seismic signals, we can also infer the rms time errors from the loss in gain.

$$\sigma_T = \sqrt{\ln(N/A)/2\pi^2} \tag{6.9}$$

By way of illustration, the ratio of the standard deviation of the beampointing error to the array beamwidth, and the standard deviation of the time errors are both plotted as a function of peak signal out of the array in Figure 6.1, where the number of elements in the array is taken to be 17 (center elements of all subarrays except the F-ring).

In summary, a method has been found which will serve to estimate the errors in beam pointing which result from time errors in choosing local travel-time anomalies. Experimental results will be compared with this estimate in a later section.

6.5 COMPUTATIONAL PROCEDURES

A number of surface-focus events and two Kurile earthquakes were chosen for study (events 42 through 47). Seismograms from the center elements of the LASA clusters represented the input data. As a first step in the procedure, each seismogram was passed through a filter to increase the S/N of the records. (This filter is discussed in Section X, and its response is described by Equation 10.5.) The records were also interpolated to increase the number of effective sample points from 20 per second to 100 per second. This step was taken to minimize errors resulting from the quantized delay steps available in scanning the beam. Next, each record was normalized so that the peak signal in the first second after onset was unity.

The C&GS epicenters were taken as a trial epicenter for the calculations, and travel-time anomalies relative to AO were chosen for this epicenter from published tables (6). Each of

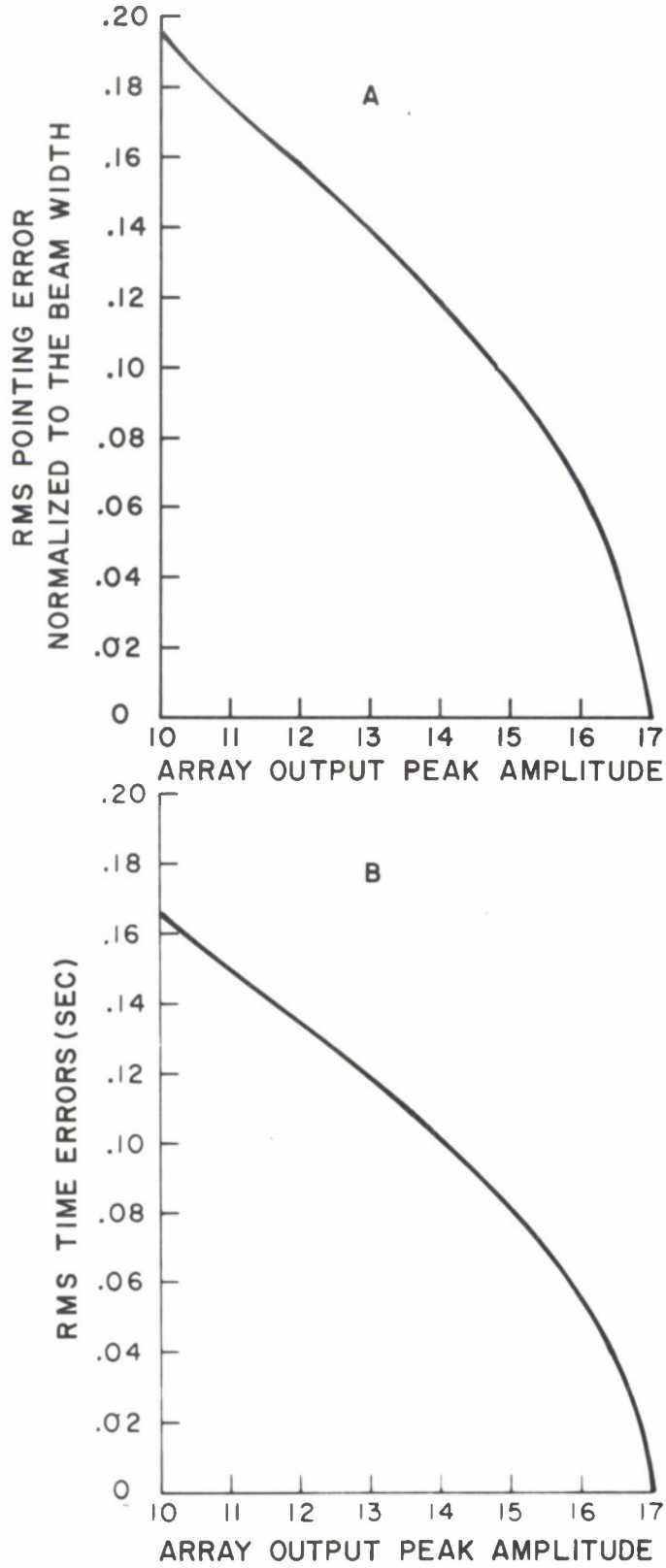


FIGURE 6.1
RMS POINTING AND TIME ERRORS VS.
PEAK ARRAY OUTPUT

the seismic records was then offset by a time equal to the appropriate anomaly. For the bulk of the calculations performed, a pair of beams -- offset both left and right or greater and lesser in range -- was formed, and the two beams scanned in small steps (0.02° or 0.04°) about the trial epicenter. The first scan was in azimuth, and the second in range. Outputs of the two beams were subtracted, and the event location indicated by a null in this difference beam (peak signal in a two-second window surrounding the onset time for AO). This nulling technique is similar to techniques used in passive sonar systems and was chosen as a first approach since it was believed that microstructure of the beam patterns caused by the quantized delays would make it easier to smooth the patterns to find this null than to find the peak of the unsquinted pattern. Because the LASA patterns, particularly in radial scan, are not symmetrical (see Section III), the squint angles could not be equal, as in the sonar case, but had to be determined from CW pattern computations for the trial epicenter. The amount of squint chosen was that which caused the two beams to lap at the 2 dB point, thereby avoiding occasional flats in the main lobe pattern in the vicinity of the 3 dB point.

Initial computations attempted to use all 21 clusters of the array. In the main, this was accomplished; however, occasional bad seismograms (extremely poor signal-to-noise ratio or badly spiked records) made it necessary to work with less than the complete array. At a later date, it was suspected that time errors for the F-ring elements of the array were excessive, and that removal of these elements, despite the decrease in array aperture, would improve location accuracy. As will be shown below, this supposition proved false, for removal of the F-ring elements from the array substantially increased the errors in measurement.

Finally, several spot checks were made to compare the angular location indicated by the difference beam with the peak of the unsquinted beam; for these, the unsquinted beam was smoothed with a local average of 9 points. Here, the majority of these checks showed angular differences of only some 0.04°, a negligible amount. For two events, however, substantial differences were noted. In one case the error of measurement was approximately halved, while in the second it was nearly doubled. These differences have not been explained.

6.6. EXPERIMENTAL RESULTS

As described earlier, angular measurements were made using the difference between two squinted array beams. Figures 6.2 through 6.5 show, respectively, the unsquinted azimuth beam, the azimuth difference beam, the unsquinted radial scan, and the difference beam radial scan for the 7 May 1966 Kazakh event. These figures are representative of the beam patterns for all events studied. Thus, no other array patterns need be illustrated.

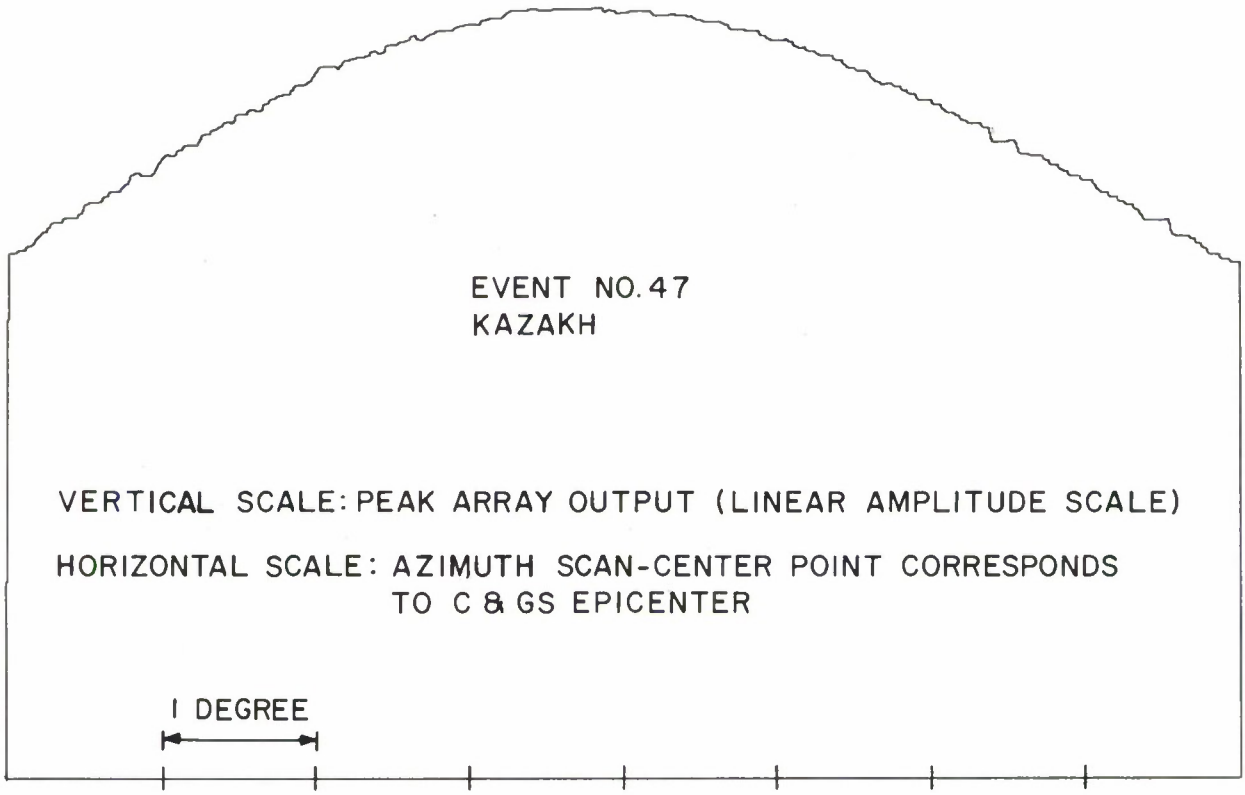


FIGURE 6.2
UNSQUINTED AZIMUTH BEAM

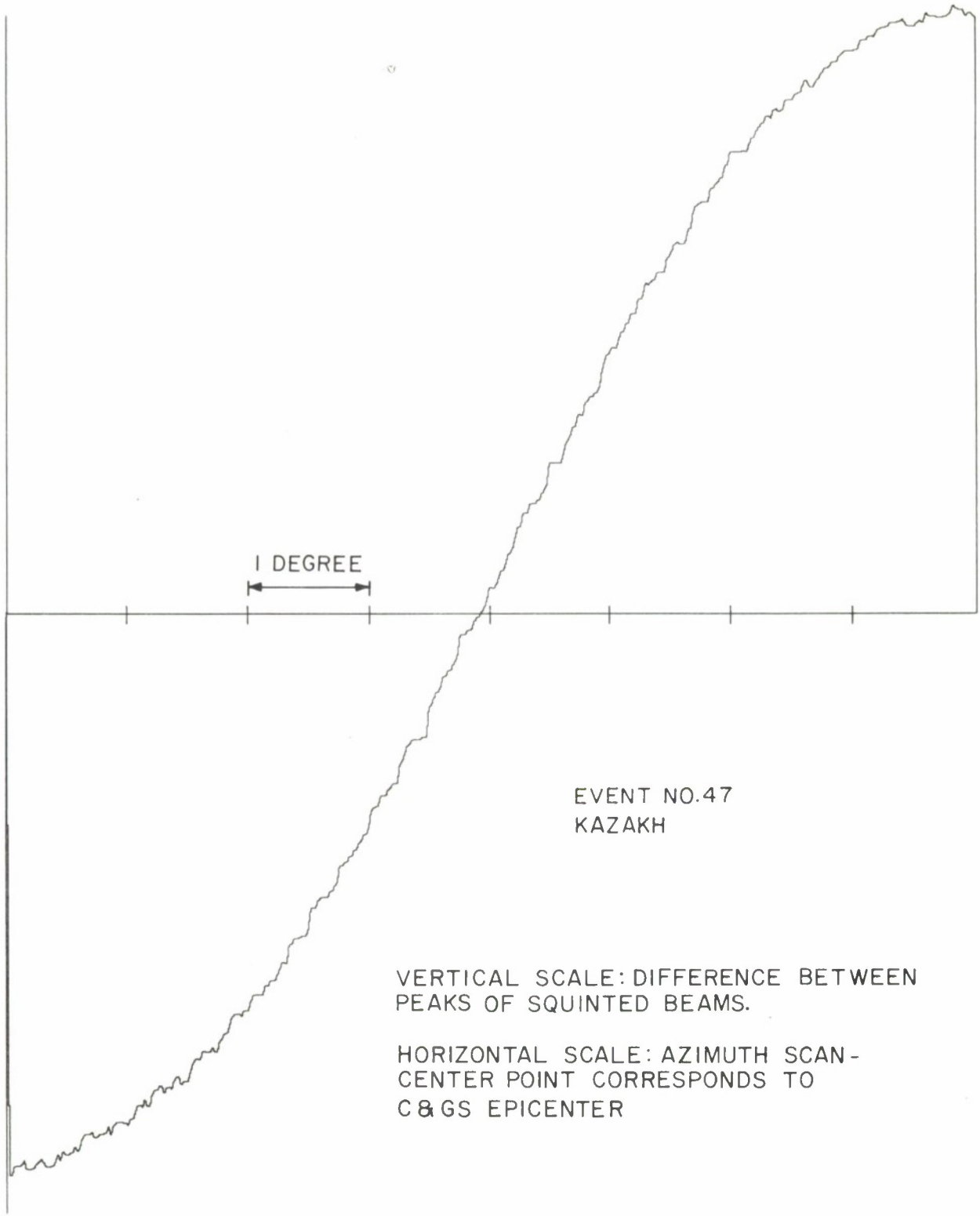


FIGURE 6.3

AZIMUTH DIFFERENCE BEAM

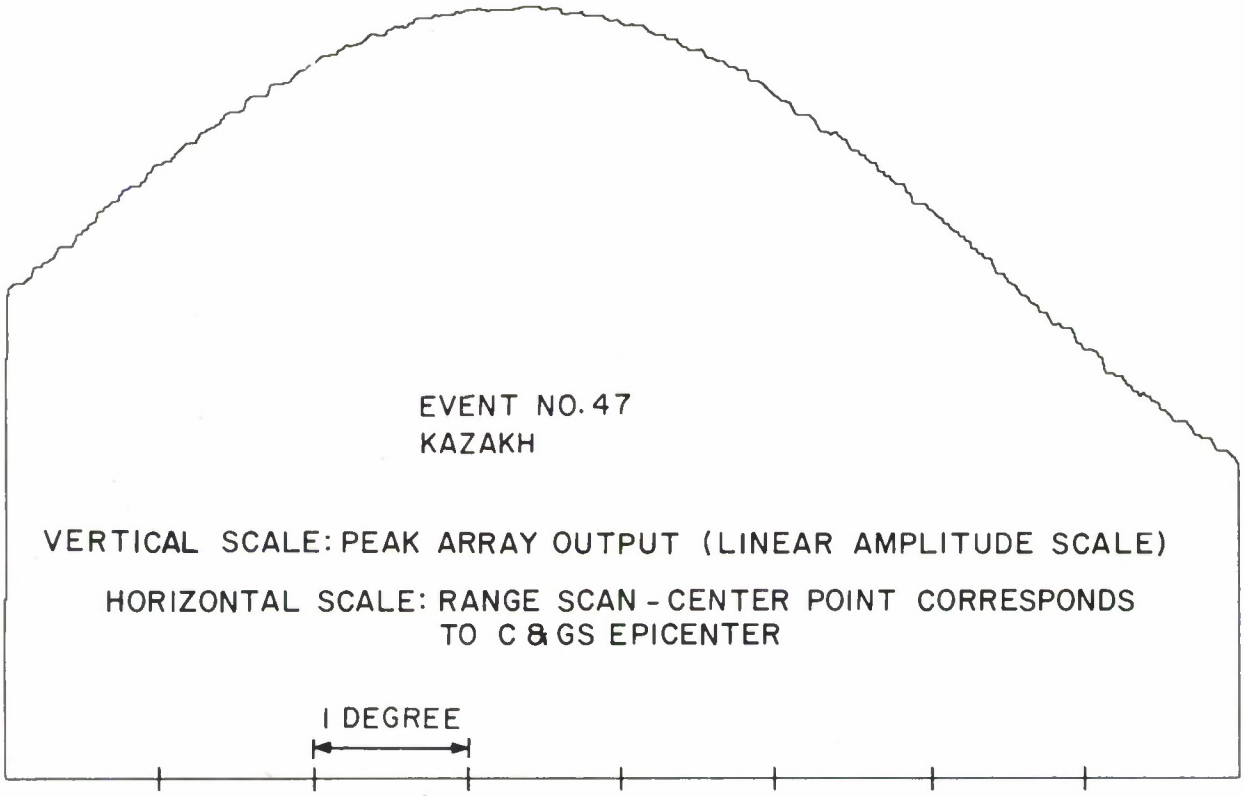


FIGURE 6.4
UNSQUINTED RADIAL BEAM

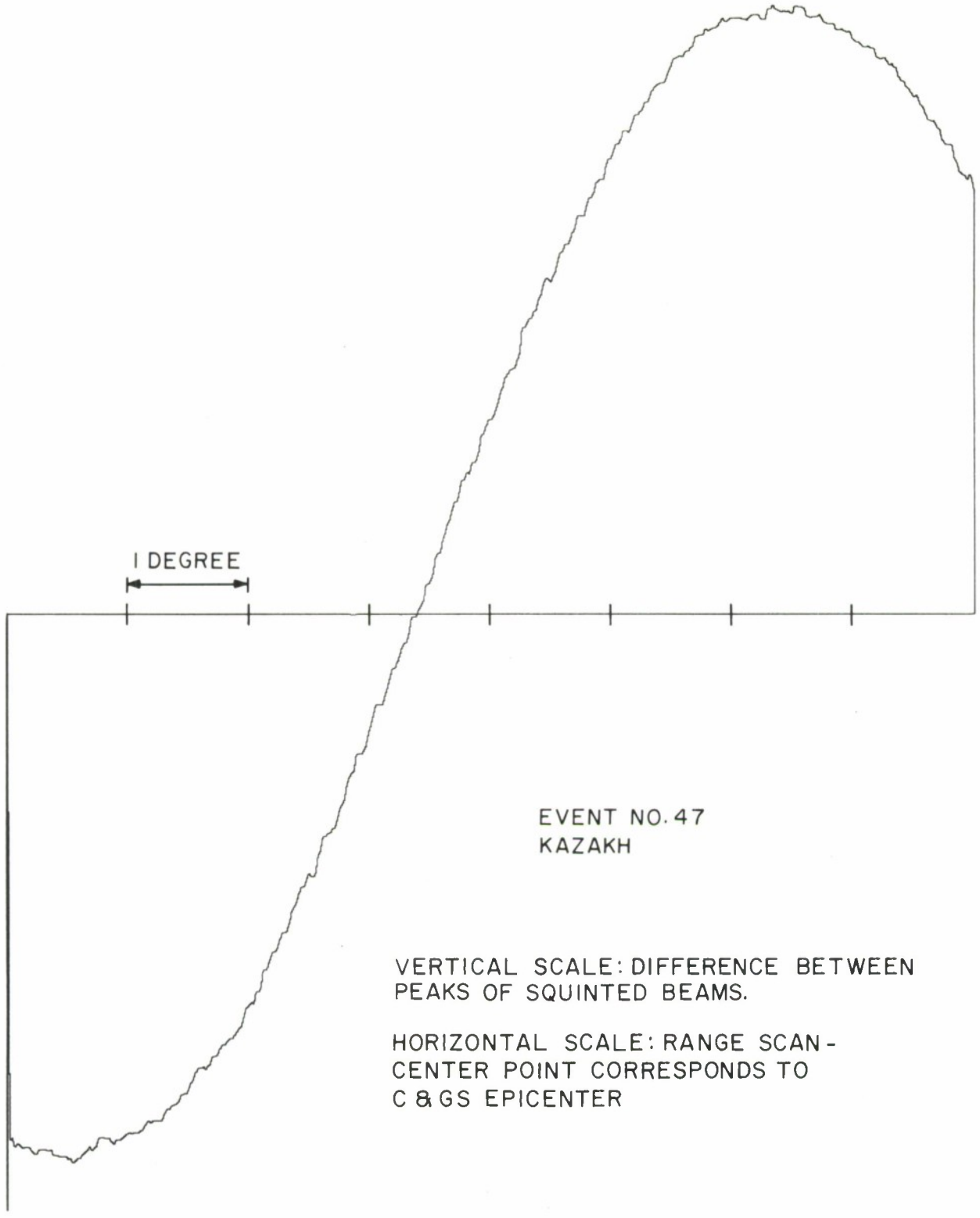


FIGURE 6.5
RADIAL DIFFERENCE BEAM

Results of the measurements with the full array (21-cluster center elements) are given in Tables II and III. Table II gives the C&GS epicenters, the computed epicenters, and the distance between the two for each of the events studied with the full array. Table III gives the C&GS azimuth and range, the computed azimuth and range, the differences between the C&GS and computed values, and the standard deviation of the computations resulting from noise interference alone. Figures 6.6A through 6.6F present graphic illustrations of the differences in epicenter locations for these events.

Tables IV and V give the same information for events studied with the F-ring eliminated from the array. As stated earlier, it was believed that this elimination of the F-ring from the calculations would produce improved results; however, as is obvious from these tables, the reverse is true. The implication here is that the most distant elements of the array, despite substantial time errors, are more critical for the measurement of angles than had been supposed.

Tables VI and VII give the array peak output, the array beamwidth, the standard deviation of the beam pointing error and the actual error for azimuth measurements on several of the events studied. Table VI gives results for the complete array, while Table VII gives results for the reduced array. As can be seen from these tables, the empirical errors in azimuth determination are well within the standard deviation expected for these measurements as a result of the time errors inferred from the measured degradation in signal gain.

From the results presented above, it can be seen that the bearing measurements are generally better than those for range. This fact may be attributed to two sources. First, the compression of approximately 8:1 in the angle of incidence necessarily causes greater errors in the range determination. Second, it is known that the smoothed J-B travel-time tables have substantial errors. Substitution of the Herrin tables, when they become available, should eliminate much of the latter error; however, there is no way of eliminating the first. The substantial range errors for the two Kurile events should be materially reduced with these new tables, but we expect that range estimates will always be poorer than those of azimuth. The only conclusion that can be reached at this time is that it appears possible to make epicenter estimates with errors of no more than some 50 kilometers. Further work in reduction of the errors in local travel-time anomalies may be able to improve these results so as to have location errors no greater than some 25 kilometers, but this remains to be proven.

TABLE II

COMPARISON OF C&GS AND COMPUTED EPICENTERS FOR LASA

EVENT NO.	DEPTH	MAG.	C&GS LAT.	COMP. LAT.	C&GS LON.	COMP LON.	DIST. DEG.
47	0	4.9	49.700N	50.306N	77.900E	78.093E	0.619
42	0	6.0	51.438N	51.957N	179.182E	179.146E	0.521
45	0	6.3	49.800N	50.312N	78.100E	78.536E	0.585
43	0	5.8	49.800N	50.295N	78.100E	78.390E	0.530
44	33	4.7	48.400N	45.971N	154.700E	150.766E	3.619
46	33	4.5	45.600N	43.340N	150.100E	147.597E	2.884

TABLE III

COMPARISON OF C&GS AND COMPUTER BEARINGS AND RANGES FOR LASA

EVENT NO.	C&GS AZ	COMP. AZ	DIFF.	ST.DEV. NOISE	C&GS RANGE	COMP. RANGE	DIFF.	ST.DEV. NOISE
47	357.310	357.215	0.094	0.045	83.930	83.319	0.612	0.141
42	304.600	305.257	0.658	0.007	47.150	49.949	0.199	0.037
45	357.180	356.930	0.254	0.006	83.820	83.297	0.527	0.018
43	357.180	357.024	0.161	0.006	83.820	83.319	0.505	0.020
44	311.850	311.784	0.070	0.013	62.070	65.690	3.619	0.050
46	311.830	311.423	0.409	0.024	66.280	69.143	2.859	0.092

TABLE IV

COMPARISON OF C&GS AND COMPUTED EPICENTERS FOR LASA WITHOUT THE F-RING

EVENT NO.	DEPTH	MAG	C&GS LAT	COMP LAT	C&GS LON	COMP LON	DISTANCE
42	0	6.0	51.438°	52.118°	-179.182°	-179.121°	0.682°
43	0	5.8	49.800	50.160	- 78.100	- 76.681	0.985
45	0	6.3	49.800	49.619	- 78.100	- 77.028	0.719
44	33	4.7	48.400	42.220	-154.700	-150.051	3.841
46	33	4.5	45.600	43.457	-150.100	-146.604	3.292

TABLE V

COMPARISON OF C&GS AND COMPUTED BEARINGS AND RANGES FOR LASA WITHOUT THE F-RING

EVENT NO.	C&GS AZ	COMP AZ	DIFF	ST.DEV. NOISE	C&GS RANGE	COMP RANGE	DIFF	ST.DEV. NOISE
42	304.599°	305.466°	0.867°	0.010°	47.148°	46.896°	0.252°	0.058°
43	357.184	358.121	0.937	0.011	83.824	83.504	0.321	0.033
45	357.184	357.875	0.691	0.010	83.824	84.038	0.213	0.030
44	311.854	312.355	0.501	0.029	62.072	65.886	3.815	0.114
46	311.833	312.060	0.227	0.096	66.284	69.570	3.286	0.358

TABLE VI

AMPLITUDE-INFERRED AND MEASURED POINTING ERRORS FOR LASA

EVENT NO.	ARRAY PEAK	BEAMWIDTH	ST.DEV. POINTING ERROR	ACTUAL POINTING ERROR
45	18.26	7.92°	0.713°	0.254°
43	17.28	7.44°	0.781°	0.161°
44	15.55	5.74°	0.724°	0.070°

TABLE VII

AMPLITUDE-INFERRED AND MEASURED POINTING ERRORS FOR LASA WITHOUT THE F-RING

EVENT NO.	ARRAY PEAK	BEAMWIDTH	ST.DEV. POINTING ERROR	ACTUAL POINTING ERROR
42	13.44	8.04°	1.04°	0.867°
43	15.00	22.40°	2.2°	0.837°
45	15.65	27.24°	2.1°	0.691°

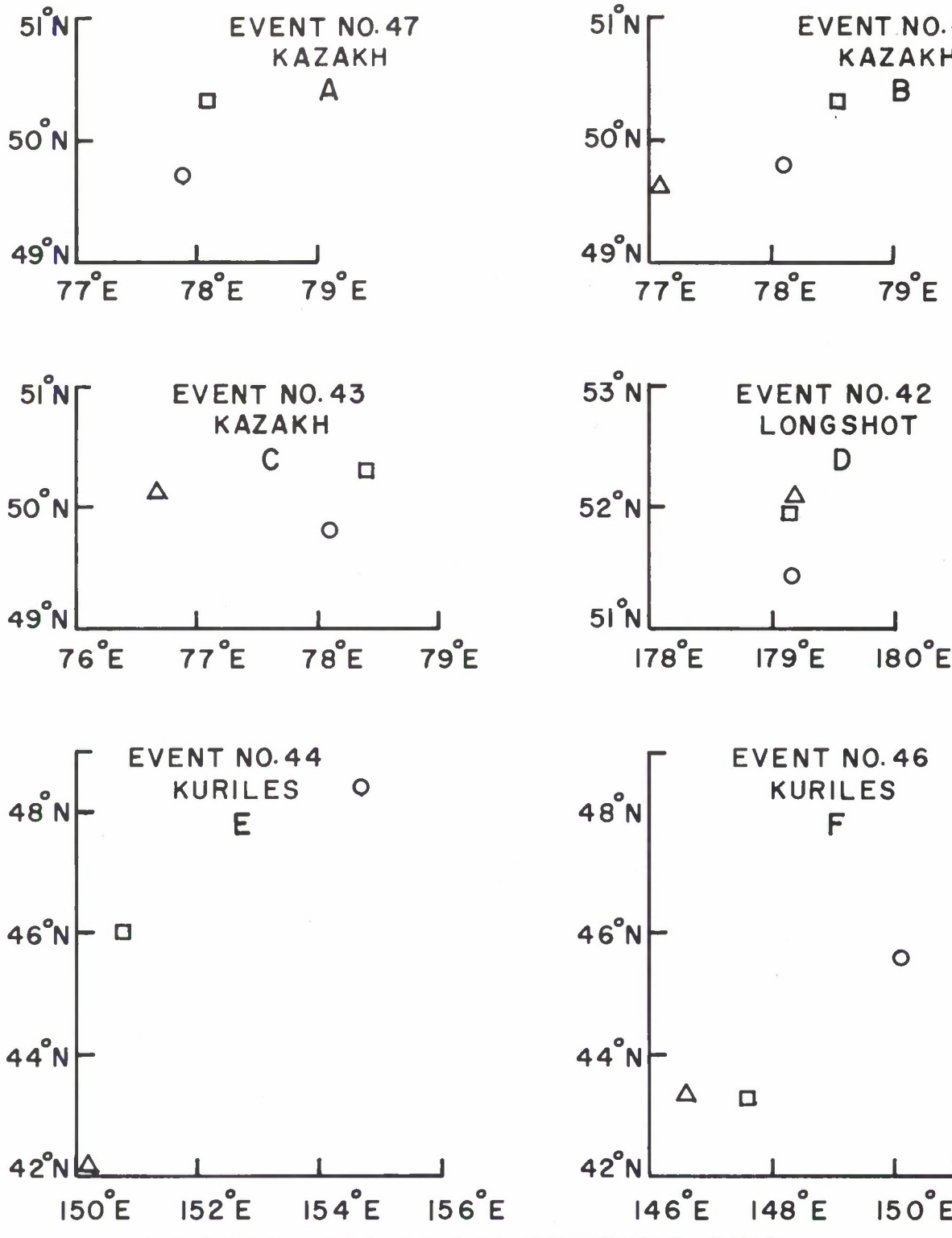


FIGURE 6.6
MAPS OF COMPUTED EPICENTERS

SECTION VII

ARRAY PROCESSING FOR SIGNAL-TO-NOISE ENHANCEMENT

One of the principal objectives in processing the outputs of seismic arrays is the enhancement of the signal-to-noise ratio over that available from a single seismometer. Three general methods of array processing currently in use are, in order of increasing complexity, delayed sum (DS), weighted delayed sum (WDS), and filter and sum (FS). The FS processing, which is also called maximum-likelihood processing, is usually superior to the other two, but it is also considerably more complex to implement. The DS processing is by far the simplest of the three but is degraded by the coherence of the noise across array elements. The FS processing (and to a lesser extent the WDS processing) is able to use this noise correlation across elements to advantage. These processing techniques have been extensively studied by other laboratories (see, for example, reference 9). Lincoln Laboratories has concluded that the FS processing can be very useful within a subarray of diameter between 7 and 20 km but that for larger apertures simpler schemes might well be adequate. As already indicated, the principal consideration in determining the relative performance of these processing schemes is the degree of noise correlation across the array. In this section we shall be principally concerned with the simplest of the processing schemes, the delayed sum processing. Two simple formulas that relate the available processing gain to the degree of noise and signal correlation across the array will be derived. As these formulas indicate the functional dependence of processing gain on correlation across the array, they will be of value in examining data in other sections of this report. The formulas are not intended to answer the question of what is the best or most practical processing scheme for a given array (this question has been extensively studied by others), but rather they relate to the question of how well the simple DS processing will perform.

There are several parallels between the problem of processing the outputs of the seismic array and the collection of problems in communication theory related to diversity combining; there are also some very important differences between these two classes of problems. By considering the similarity of these two problems it is possible that some additional insights may be available and that some relevant results may be carried over from the communication context to that of seismic array processing. This topic will be briefly discussed below and, in particular, a diversity combining rule that is used in the automatic pP test that is discussed in Section X will be cited.

7.1 DS PROCESSING GAIN AS A FUNCTION OF SIGNAL AND NOISE COHERENCE

In this section, the processing gain available from a seismic array is expressed in terms of a quantity called the "average paired correlation coefficient." Before proceeding with this derivation, several definitions are needed. Let the output of the i^{th} seismometer in a seismic array be given by

$$z_i(t) = x_i(t) + n_i(t) \tag{7.1}$$

where $x_i(t)$ is the "signal" and $n_i(t)$, the "noise." Let T be the integration interval of interest for the calculations. In particular, T is the integration interval over which the signal-to-noise ratio is defined. The signal-to-noise ratio for the i^{th} element is given by

$$(S/N)_i = \frac{\frac{1}{T}\int_0^T x_i^2(t)dt}{\frac{1}{T}\int_0^T n_i^2(t)dt} \tag{7.2}$$

In calculating the average power of the summed signal, the crosscorrelations of the various time functions become important. For convenience, we shall define these correlations by

$$\overline{x_i x_j} = \frac{1}{T}\int_0^T x_i(t)x_j(t)dt \Big/ \sqrt{\frac{1}{T}\int_0^T x_i^2(t)dt \; \frac{1}{T}\int_0^T x_j^2(t)dt} \tag{7.3}$$

$$\overline{n_i n_j} = \frac{1}{T}\int_0^T n_i(t)n_j(t)dt \Big/ \sqrt{\frac{1}{T}\int_0^T n_i^2(t)dt \; \frac{1}{T}\int_0^T n_j^2(t)dt} \tag{7.4}$$

$$\overline{x_i n_j} = \frac{1}{T}\int_0^T x_i(t)n_j(t)dt \Big/ \sqrt{\frac{1}{T}\int_0^T x_i^2(t)dt \; \frac{1}{T}\int_0^T n_j^2(t)dt} \tag{7.5}$$

Note that with these definitions,

$$\overline{x_i x_i} = 1 \qquad \text{and} \qquad |\overline{x_i x_j}| \leq 1 \tag{7.6}$$

Throughout this discussion it will be assumed that the signal and noise powers are the same at all elements and that all of the signal terms are uncorrelated with all of the noise terms. These assumptions are summarized in Equations 7.7 through 7.9, where symbols for the signal power and the noise power at each element are also defined.

$$\frac{1}{T}\int_0^T x_i^2(t)dt = S^2 \qquad \text{all } i \tag{7.7}$$

$$\frac{1}{T}\int_0^T n_i^2(t)dt = N^2 \qquad \text{all } i \tag{7.8}$$

$$\overline{x_i n_j} = 0 \qquad \text{all } i,j \tag{7.9}$$

Finally, it is assumed that the array consists of M elements.

With all of these assumptions it is clear that the average power in the summed seismogram is simply the sum of the power due to the signal and the power due to the noise, since by virtue of Equation 7.9 all of the crossterms will be zero. The power in the signal contribution is given by

$$\frac{1}{T}\int_0^T \Big(\sum_{i=1}^{M} x_i(t)\Big)^2 dt = \sum_{i=1}^{M}\sum_{j=1}^{M} \frac{1}{T}\int_0^T x_i(t)x_j(t)dt = S^2 \sum_{i,j} \overline{x_i x_j}$$

$$= MS^2 + S^2 \sum_{i\neq j} \overline{x_i x_j} = MS^2 + M(M-1)S^2 \overline{\rho_x} \qquad (7.10)$$

where the quantity $\overline{\rho_x}$, which is called the average paired correlation coefficient for the signal, has been defined. This definition is stated explicitly in Equation 7.11 and the corresponding definition for the average paired correlation coefficient for the noise is given in Equation 7.12.

$$\overline{\rho_x} = \frac{1}{M(M-1)} \sum_{i\neq j} \overline{x_i x_j} \qquad (7.11)$$

$$\overline{\rho_n} = \frac{1}{M(M-1)} \sum_{i\neq j} \overline{n_i n_j} \qquad (7.12)$$

Note that the normalization for these correlation coefficients is chosen in such a way that their maximum possible value is 1. By analogy with Equation 7.10, the noise power in the output of the summed seismogram is given by Equation 7.13.

$$\frac{1}{T}\int_0^T \Big(\sum_{i=1}^{M} n_i(t)\Big)^2 dt = MN^2 + M(M-1)N^2 \overline{\rho_n} \qquad (7.13)$$

Finally, then, the processing gain is given by the ratio of the signal-to-noise ratio of the summed output to that of the single elements.

$$G = \frac{(S/N)_{out}}{(S/N)_{in}} = \frac{1+(M-1)\overline{\rho_x}}{1+(M-1)\overline{\rho_n}} \qquad (7.14)$$

If the signal were perfectly correlated across the array and the noise completely uncorrelated between array elements, Equation 7.14 would simply indicate a (power) gain of M. As the average paired correlation coefficient for the noise is strongly dependent upon the relative contribution of local and teleseismic noise, it is useful to try to separate these contributions in the gain expression. This is done with a few simplifying assumptions in the next section.

7.2 DS PROCESSING GAIN -- CONTRIBUTIONS OF LOCAL AND TELESEISMIC NOISE

In this section we consider a LASA such as LASA-Montana which is divided into several subarrays, each one consisting of the same number of elements. It is assumed that the noise contribution at each element consists of two components, local and teleseismic, and that these two components behave independently. It is assumed that the teleseismic noise contribution is characterized by perfect correlation across the dimensions of the subarray, but zero correlation between elements of different subarrays. It will be assumed that the local noise contribution is also totally uncorrelated between subarrays but has an average paired correlation coefficient for each subarray given by $\overline{\rho_L}$. Finally, it is assumed that each subarray consists of k seismometers and that, therefore, there are M/k subarrays. As before, it is assumed that the signal power and the noise power are the same at each seismometer and it is now further assumed that the signal is perfectly correlated across the entire array (ρ_x=1). Since local and teleseismic noise contributions are assumed to be independent, the noise power at each seismometer may be written as the sum of the noise powers due to each contribution.

$$N^2 = N_L^2 + N_T^2 \tag{7.15}$$

One final parameter that will be convenient for this derivation is the ratio of the local to the teleseismic noise contributions at each seismometer.

$$R = N_L^2/N_T^2 \tag{7.16}$$

Referring to Equation 7.14 of the previous section, we have assumed that ρ_x is equal to unity and it remains only to calculate ρ_n. This is easily done by making the following observations.

1. There are M(M-1) pairs in the entire array.
2. There are (M/k)(k-1)k pairs which have a nonzero contribution to the average paired correlation coefficient and each one of these contributes on the average

$$\frac{\overline{\rho_L}\, N_L^2 + 1N_T^2}{N^2} = \frac{R\,\overline{\rho_L} + 1}{1+R} \tag{7.17}$$

to the total. Therefore, the average paired correlation coefficient for the entire array is given by

$$\overline{\rho_n} = \frac{(K-1)}{(M-1)} \frac{1+R\overline{\rho_L}}{1+R} \tag{7.18}$$

Substituting this expression into Equation 7.14 yields, after a little simplification,

$$G = \frac{M(1+R)}{[(k-1)\overline{\rho_L}+1]R+k} \qquad (7.19)$$

In the case of LASA-Montana this equation would specialize to

$$G = \frac{525(1+R)}{(24\overline{\rho_L}+1)R+25} \qquad (7.20)$$

Equation 7.20 is plotted in Figure 7.1 for five values of R. The dotted line indicates the gain that could be achieved if the noise between elements were completely uncorrelated ($\overline{\rho_L} = 0$). The curves show the degradation in gain as $\overline{\rho_L}$ increases or R decreases.

7.3 THE SEISMIC ARRAY AS A DIVERSITY SYSTEM

The subject of diversity combining has been pursued in considerable detail in the context of communication systems (see, e.g., reference 10). A typical problem is that of high frequency radio communication by means of ionospheric reflection in which the same information is sometimes transmitted over more than one "channel." The problem of receiver design is how best to combine the information available from two or more "channels" in order to recover the original information. "Channels" in this context might refer to different frequencies at which the information is modulated or might simply be separate receivers that are sufficiently separated that they receive somewhat different signals. In this communication context several combining techniques have been developed and studied. Some of them are linear; some of them assume a perfect measurement of the current channel characteristics; many of them are designed to maximize the signal-to-noise ratio of the combined signal; and most of them assume that the noise on the separate channels is independent.

The similarities between the diversity combining problem of communications and the seismic array processing for the purpose of maximizing signal-to-noise ratio are fairly apparent. In both cases similar information is available on several records and the question is how best to combine them. In some cases (one of which will be cited below) the results from the communication context are directly available to the seismic array processing problem. However, in general,there are several qualifications which must be placed on any attempt to relate these two subjects. In the first place, it is not always the case with the seismic array that the noise on the separate sensors is independent. Secondly, many of the diversity combining techniques assume a perfect measurement of the channel. In the communication context this is sometimes achieved by

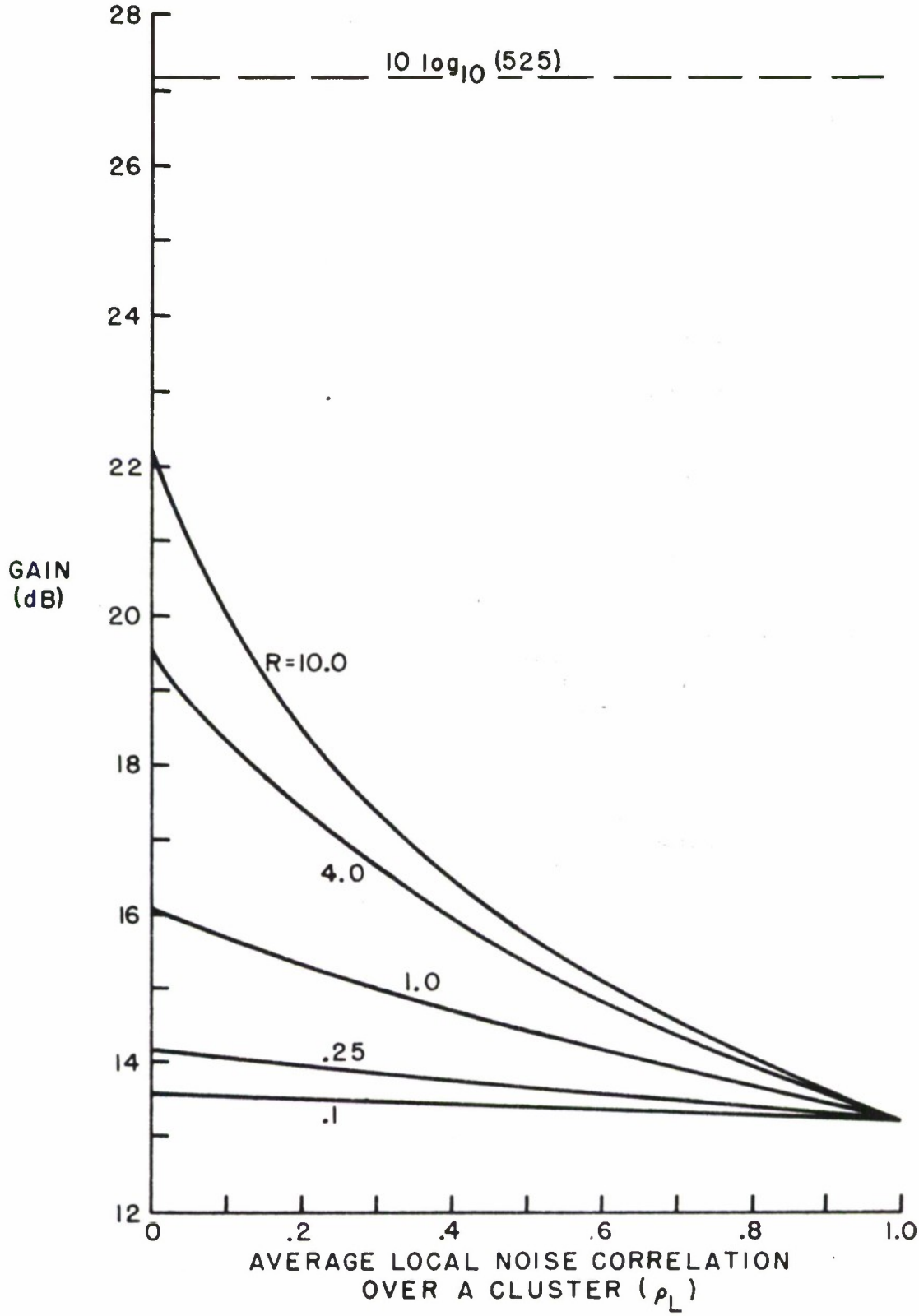


FIGURE 7.1
DS GAIN OF LASA
VS AVERAGE LOCAL NOISE CORRELATION

sending a pilot tone strictly for the purpose of measuring the channel. In the seismic situation a directly parallel measurement is not obvious.

There has been one instance in which we have had occasion to employ directly a well-known technique in diversity combining. The technique is often called "maximal-ratio diversity combining." This processing, which is often used in a communication context, assumes that the noise on the separate channels is independent and that the levels of the signal and the noise on each channel are known. If these assumptions hold, the optimum rule for combining the signals in order to maximize the signal-to-noise ratio of the combined signal is to weight each signal by a factor equal to the signal amplitude divided by the noise power and add them. If this is done, the resulting signal-to-noise ratio is simply the sum of the signal-to-noise ratios available on the individual channels. In general, this technique is not directly applicable to the seismic situation because an independent measurement of the signal amplitude (other than the signal itself) is not always available. However, in the case of the automatic test for pP that is discussed in Section X, an indirect measurement of the desired signal amplitude is available. In that context it is desired to maximize the signal-to-noise ratio of a combined seismogram in which the signal is considered to be the pP phase. Assuming that the amplitude of this phase on the individual records is proportional to the amplitude of the main P phase, which can be measured, and treating the coda which surrounds pP as "noise," the maximal-ratio combining technique does become relevant and, in fact, has been applied in this processing problem.

7.4 SUMMARY AND CONCLUSIONS:

Several formulas have been presented that relate signal-to-noise-ratio gain for an array to various correlations across the array and to the relative contributions of local and teleseismic noise. The correlation measure that is important for these formulas is the "average paired correlation coefficient" for the array. This coefficient is defined for noise, P phase and coda. The formulas that give the array gain in terms of the average paired correlation coefficient for "signal" and "noise" are based on several simplifying assumptions, and therefore cannot be regarded as precise. They do, however, suggest what correlation statistics are important in terms of array gain, and thereby suggest the measurements that are reported in Section VIII, where the dependence of these various correlation coefficients on the separation of the seismometers is examined. It has developed that the average paired correlation coefficient for the coda is of some interest in itself, since data from continental-size arrays indicate that this

statistic may be a useful discriminant for distinguishing between surface focus events and earthquakes with depths in the 10-40 km region. This calculation is discussed in some detail in Section IX. Another test for distinguishing between 10-40 km is the automatic pP test that is presented in Section X. One step of the processing in this test involves a weighted summation of several appropriately aligned seismograms. The weighting rule used in this test is one that is borrowed from the collection of topics in communication theory known as diversity combining. The similarities and differences between the problems that occur in the seismic context were briefly discussed above and the weighting rule used in Section X described.

SECTION VIII

SPATIAL CORRELATION ACROSS AN ARRAY

Section VII contains a simple formula relating array processing gain with DS processing to various average paired correlation coefficients. Section IX presents data indicating that the average paired correlation coefficient for the coda may be a useful statistic for discriminating between surface-focus events and earthquakes with depths between 10 and 40 km. The majority of those data are based on very large arrays. Both for the coda correlation discriminant and for the question of DS processing gain it is of interest to study the dependence of various correlation coefficients on the separation of seismometers.

We have employed data from LONGSHOT to study the dependence on separation of P-phase, noise, and coda correlation. These calculations are summarized in this section. Also summarized in this section are data obtained for continental-size arrays on P-phase and noise correlation.

8.1 SPATIAL CORRELATIONS OBSERVED ACROSS LASA FROM LONGSHOT

The basic calculations described in this section are the correlation coefficients between corresponding portions of pairs of records and the average of this coefficient over various ensembles. The correlation coefficient was defined (in the usual way) in Section VII as

$$\overline{x_i x_j} = \frac{\int_o^T x_i(t) x_j(t)\, dt}{\sqrt{\int_o^T x_i^2(t) \int_o^T x_j^2(t)\, dt}} \qquad (8.1)$$

where the $x_i(t)$ and T could correspond to the P phase, the preceding noise, or the P-coda. In Sections VII and IX, these coefficients are averaged over all pairs in an M-element array to yield an average paired correlation coefficient defined by

$$\bar{\rho} = \frac{1}{M(M-1)} \sum_{i \neq j} \overline{x_i x_j} \qquad (8.2)$$

In order to explore the dependence of the various $\overline{x_i x_j}$ on distance, we shall perform a somewhat different average in this section. With each $x_i x_j$ we associate the separation of the i^{th} and j^{th} seismometers. We then average all of the $\overline{x_i x_j}$ that correspond to a given range of separations. It is easy to see that the average will not necessarily involve

all possible pairs of any set of stations. For example, station pairs 1-2 and 1-3 might have separations in the desired range while pair 2-3 does not.

The seismometers used in these calculations are the center elements of each of the clusters in LASA rings B,C,D,E and F, a total of 20. Thus there are 20(20-1)/2=190 paired correlation coefficients.

8.1.1 P-Coda Correlation

The mean and standard deviation of the 190 coda correlation measurements are 0.24 and 0.25. The distribution of P-coda correlation clearly exhibits distance dependence. Figure 8.1A shows the mean values in the 10 km intervals. Table VIII lists the means, standard deviations, and the number of correlation coefficients in each interval.

Although the variation with separation between the elements is erratic, a general diminution with separation is apparent. The mean correlation drops toward zero in the neighborhood of 100-150 km. The separation or distance dependence becomes clearer in Figure 8.1B, in which the range scale is made logarithmic. Here the same data are replotted with the distance interval one octave in size. The decrease in the erratic nature (compare with Figure 8.1A) is due to the larger number of sample points in each interval.

These results are quoted in the discussion of the coda correlation discriminant (Section X), and a few calculations that were suggested by these data are presented.

8.1.2 P-Phase Correlation

The cross-correlation of main-P is large. The mean value is 0.97, and the standard deviation is 0.04. No distance dependence is observed in the data, contrary to the expected tendency for correlation to fall off with separation between seismograms. The smallest cross-correlation coefficient, which is 0.72, is obtained from seismometers in C3 and D4, which are only about 40 to 45 km apart. All C3 values are low compared to the rest of the cross-correlation matrix. The mean correlation of C3 with all the rest is 0.87, possibly due to an error in picking the arrival time of the event. Dropping C3 on this assumption raises the mean to 0.98 and reduces the standard deviation to 0.02. The distribution of the correlation coefficients (minus C3) is plotted in Figure 8.2.

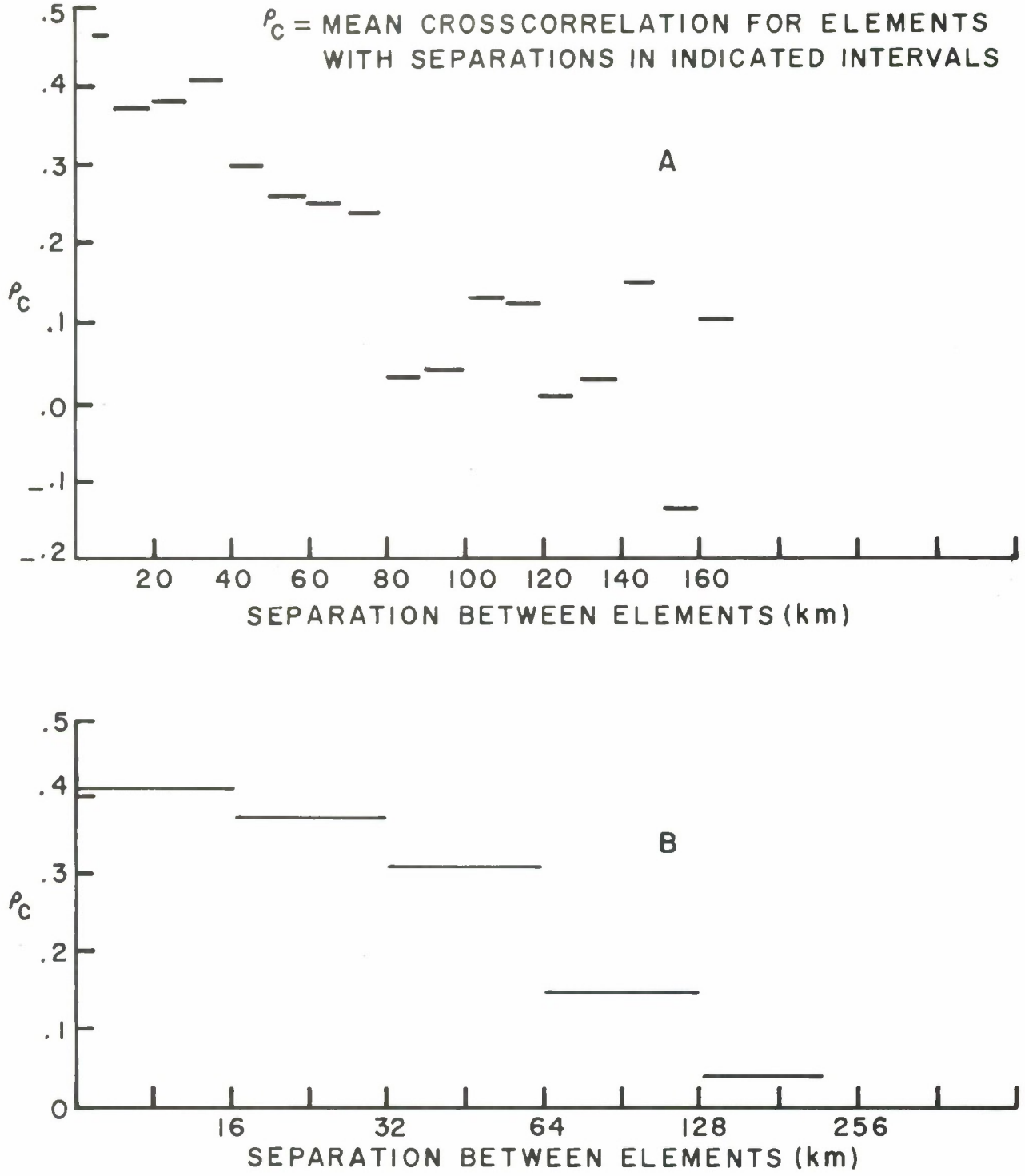


FIGURE 8.1
LONGSHOT CODA CORRELATION ACROSS LASA

TABLE VIII CODA CORRELATION ACROSS LASA

DISTANCE INTERVAL (km)	ρ_c	σ	N
8-	.47	.26	2
10-	.37	.24	18
20-	.39	.21	24
30-	.40	.15	20
40-	.29	.24	14
50-	.26	.16	14
60-	.25	.19	16
70-	.24	.20	16
80-	.04	.19	11
90-	.05	.33	14
100-	.13	.20	9
110-	.12	.19	10
120-	.01	.04	3
130-	.03	.21	4
140-	.16	.17	5
150-	-.13	.27	3
160-	.10	--	1
8-15	.40	.26	11
16-31	.37	.19	35
32-63	.31	.19	52
64-127	.14	.24	76
128-210	.03	.22	14

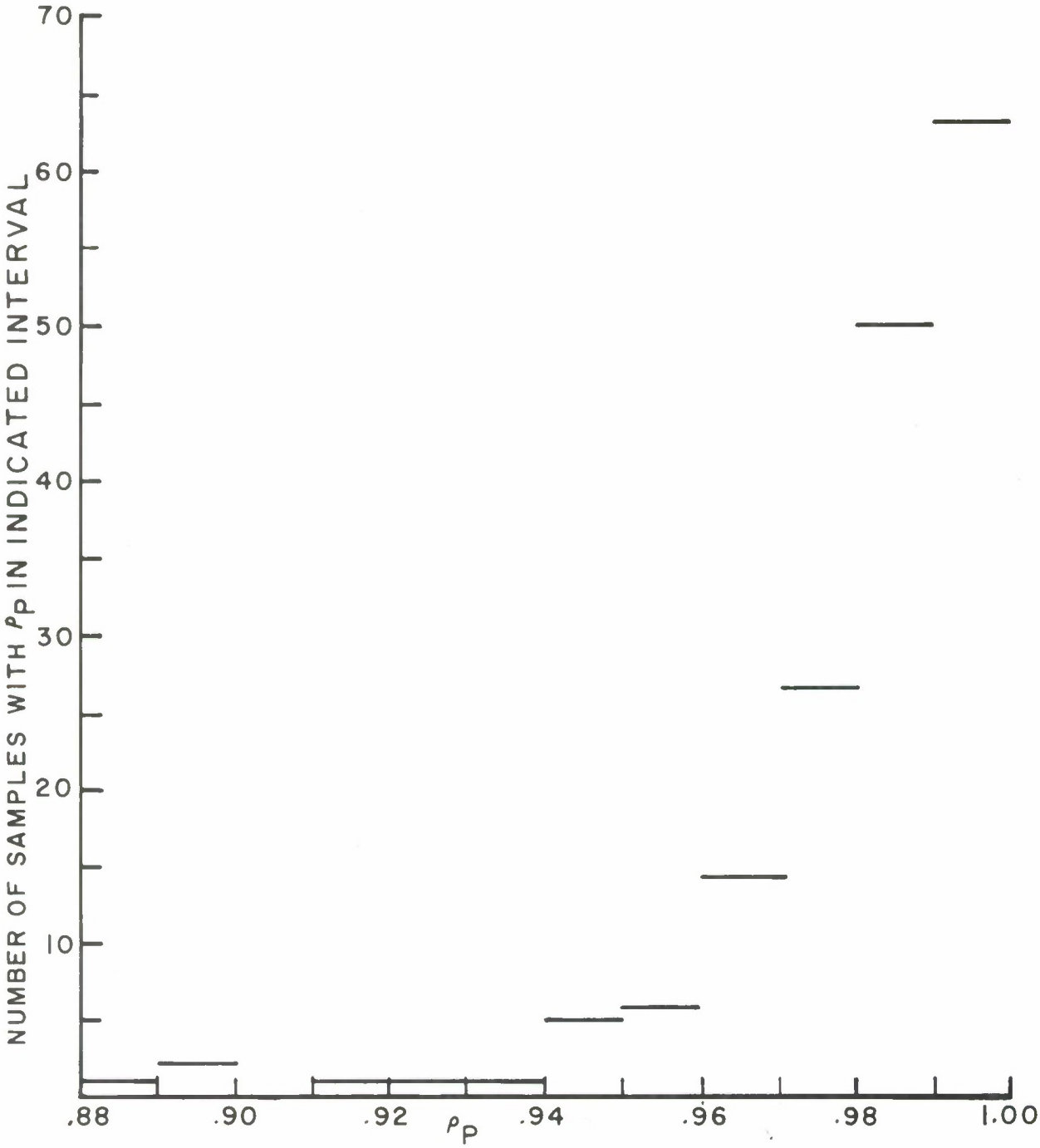


FIGURE 8.2

LONGSHOT P-WAVE CORRELATION ACROSS LASA

8.1.3 Noise Correlation

With arrays having distances between seismometers on the order of thousands of kilometers, the mean noise cross-correlation appears unbiased and reasonably symmetrical. It was of interest to determine if the same was true when the distance between elements shrank drastically. Across LASA the minimum spacing is about 8 km. The noise on the seismic records just prior to the LONGSHOT event permitted such a test. Figure 8.3 shows the cumulative distribution plotted on probability paper (dashed curve). The mean and standard deviation are 0.009 and 0.35.

A test for independence of the noise between elements may be made by comparing this distribution with the theoretical cumulative distribution for the cross-correlation coefficient between two independent Gaussian sources when the sample size is comparable to the estimated number of independent samples in the noise records from the seismograms. This quantity is

$$N = 2TW \tag{8.3}$$

where T is the length of the noise record and W is the noise bandwidth. The length of the record T = 10 seconds. From other spectral measurements of other records (see Section XII)

$$1/4 < W < 1 \text{ Hz}. \tag{8.4}$$

Thus the estimated number of independent noise samples in each record is about 5 to 20 samples.

Shown in Figure 8.3 are the theoretical curves for the cross-correlation coefficient between two independent Gaussian sources for a range of sample size which brackets the estimated number of independent samples in each record (11). It is apparent that the measured distribution is consistent with N = 9, except at the tail, where it deviates markedly. It is believed that this departure is attributable to the limited number of correlation coefficients from which the distribution was calculated. That is, the experimental distribution had a very small number of extreme values. These results are consistent with the hypothesis that the noise at each cluster is independent of that of every other cluster.

8.1.4 Comment on Detection Efficiency

As derived in Section VII, the gain in signal-to-noise power ratio for a teleseismic array is a first order function of three quantities. These are the number of elements M, the mean spatial correlation of signal $\overline{\rho}_p$, and the mean spatial corre-

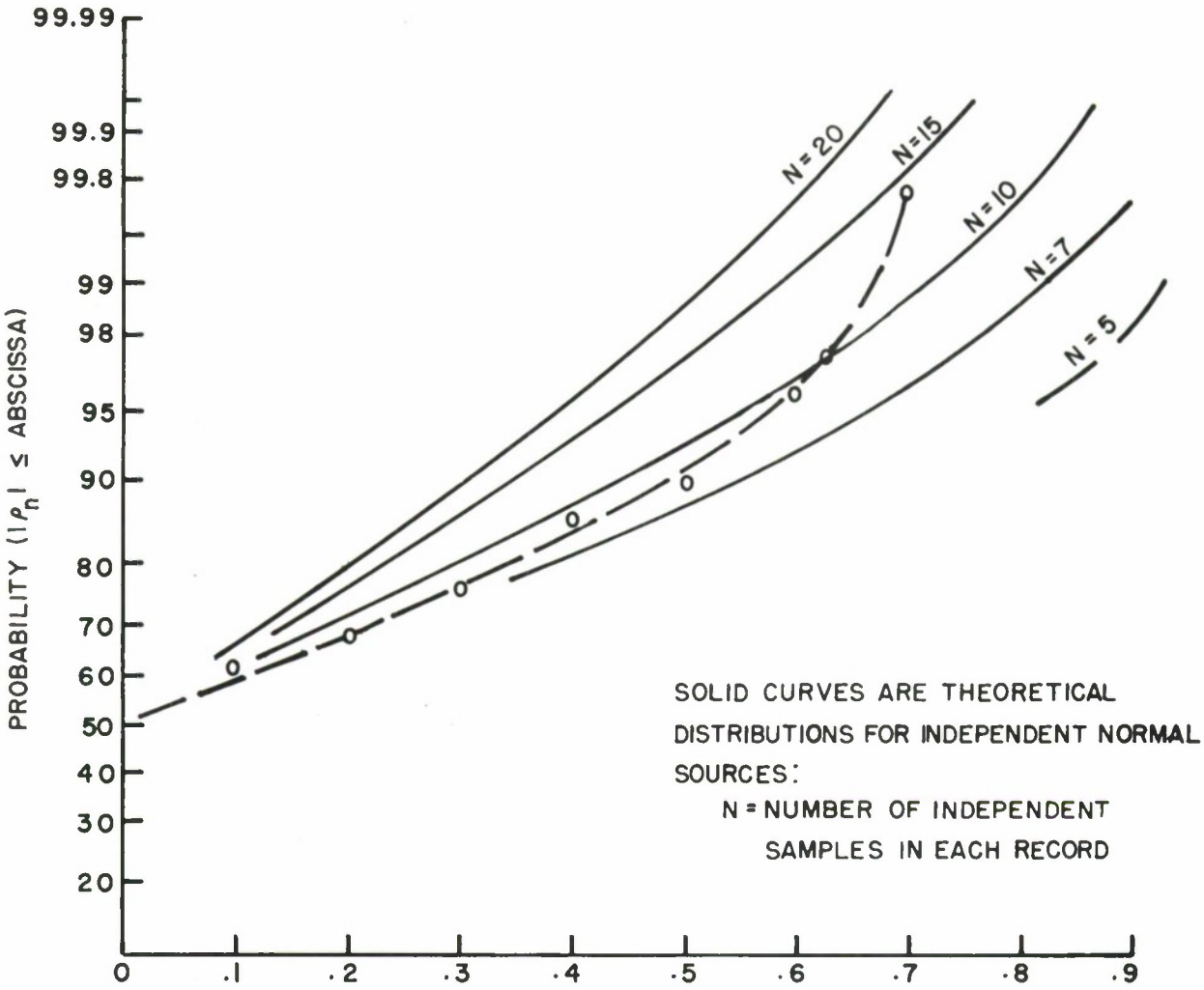


FIGURE 8.3
LONGSHOT NOISE CORRELATION ACROSS LASA

lation of noise $\bar{\rho}_n$. The relation is

$$G = \frac{\bar{\rho}_p (M-1)+1}{\bar{\rho}_n (M-1)+1} \qquad (8.5)$$

In this expression, M is the number of clusters or subarrays rather than the total number of seismometers. This is because the dimension of each subarray is only the order of a wavelength. The ideal asymptotic enhancement is obtainable when $\bar{\rho}_p = 1$ and $\bar{\rho}_n = 0$. The limiting gain in this case is M, the number of subarray clusters.

It is to be expected that as the separation between elements increases, both mean correlations $\bar{\rho}_p$ and $\bar{\rho}_n$ will decrease. Thus, to maximize detection efficiency an optimum array size is one which is not so large that $\bar{\rho}_p$ departs greatly from unity, while it is large enough so that $\bar{\rho}_n$ is near zero. The LONGSHOT experiment reported above suggests that the LASA dimension may be large enough to accomplish the latter while not so large as to cause significant degradation in the signal correlation. Thus for detection of main-P in microseismic noise, 200 kilometers may well be within the broad optimum array size range.

8.2 SPATIAL CORRELATION OBSERVED ACROSS CONTINENTAL-SIZE ARRAYS

Continental-size arrays have been used to study the coda correlation discriminant and the automatic pP test that are discussed in Sections IX and X. These calculations were based on 43 different seismic events, and the results are summarized in Tables XI through XIII. Of interest here are the columns labeled $\bar{\rho}_n$ and $\bar{\rho}_p$, which contain the measured average paired correlation coefficient for the first 1 sec of the P-phase and for a 30 sec sample of noise preceding the event. These statistics are defined in Section VII and are the same statistics that are reported in Section 8.1 for LASA recordings of LONGSHOT.

A review of the numbers in these columns indicates that $\bar{\rho}_n$ is close to zero and $\bar{\rho}_p$ is close to unity, as would be desired for signal-to-noise enhancement. More specifically, the following table gives two averages of these statistics over the ensemble of 43 events.

	MEAN	STANDARD DEVIATION
$\overline{\rho_p}$	.87	.28
$\overline{\rho_n}$	.01	.14

The fact that the noise is uncorrelated is not surprising, since the elements of these arrays are widely spaced. The fact that the P-phase is apparently correlated over these large distances is a little more surprising. In considering this correlation, nowever, it should be noted that all of the records were aligned according to the first motion and that a one-second integration interval was used. If the P-phase had a dominant 1 Hz component, as is often assumed, this method of calculating $\overline{\rho}_P$ would be expected to yield values close to unity. The real problem in trying to achieve a large processing gain from an array of these dimensions, is, of course, the correct alignment of the various records. Errors in alignment would decrease $\overline{\rho}_P$ and, hence, the gain of the array.

8.3 SUMMARY AND CONCLUSIONS

The behavior of the paired correlation coefficients for various portions of the seismogram has been studied as a function of the separation of the seismometers. The first set of calculations was based on LASA-Montana data from LONGSHOT. These calculations suggest that 1) separations greater than 100 km are necessary to get a coda correlation coefficient close to 0; 2) P-phase correlation coefficients (based on 1 sec) are very close to unity and do not appear to fall off with separations, for the separations that occur in LASA-Montana; 3) the noise statistics are consistent with the hypothesis that the noise is independent from cluster to cluster; 4) the 200 km aperture of LASA-Montana is within the broad optimum array size range for detection of main P in microseismic noise.

Similar calculations performed on continental-size arrays indicate, as expected, that the noise correlation is very small. These calculations also indicate an average paired correlation coefficient for the P phase of 0.87, which is larger than might be expected, given the very large separations involved in these arrays. It was noted, however, that before these calculations were performed the various seismograms were essentially aligned by eye so that first motions agreed, and, furthermore, the integration interval over which the P-phase correlation coefficient is calculated is only 1 sec. Given that this procedure was used and the seismograms typically have a dominant period near 1 Hz, it is not surprising that such a large correlation coefficient has been observed. This result does suggest that very large aperture seismic arrays could lead to good signal-to-noise ratio enhancement if the alignment problem could be solved. There is nothing in this chaper, however, that deals directly with the very important problem of alignment.

SECTION IX

CODA CORRELATION AS A DISCRIMINANT

The previous two sections discuss the correlation of various portions of the seismic record across arrays, and the implications of this correlation in terms of processing gain for the array. In this section the correlation of coda across the array is studied as a possible discriminant between surface-focus events and earthquakes with depths between 10 and 40 km. The basic calculation under consideration is the averaged paired correlation coefficient that was defined in Sectior VII. Data will be presented below that show that these calculations applied to the coda portions of the seismic record reveal a higher coda correlation across the array with earthquakes in the 10-40 km depth region that with surface-focus events. Based on results from 30 earthquakes and 12 surface-focus events, this correlation measurement appears to have considerable value as a discriminant.

The calculations presented in this section and those presented in Section X have the same principle objective: discrimination between surface focus events and "moderate-depth" earthquakes. The structure of the calculation, however, is quite different. The calculation presented in Section X (the "automatime pP test") results first in a depth estimate for the event, whereas the calculation presented in this section yields only a correlation as a discriminent was "discovered" during the development of the pP test. In retrospect, there are some good reasons that the higher correlation between codas of moderate depth earthquakes might be expected. For one thing, for earthquakes in the 10 to 40 km depth region, the pP phase will be in the region we are calling coda, and if the "move-out" of this phase across the array is not too much, this phase itself will contribute considerably to the apparent coda correlation. A second reason for expecting higher coda correlation from earthquakes than nuclear tests is that, in general, earthquake sources appear to be longer in time, and aftershocks and reverberations that are local to the source will propagate along the same path as the P phase. These should lead to a coherent section of the coda waveform.

The organization of this section is as follows. The discussion begins with a description of the coda correlation calculation. This is followed by a presentation of results based on 30 earthquakes and 12 surface-focus events. These results are presented in terms of the cumulative distribution function for the test statistic for each of three populations: 24 earthquakes with depths between 10 and 40 km; 6 earthquakes with depths either less than 10 km or greater than 40 km; and 12 surface-focus events. These cumulative distribution functions show that the earthquakes of moderate depth separate very clearly from the other two populations. Finally the implications of these results are briefly discussed in terms of the reliability of this test as a discriminant.

9.1 METHODS

The basic calculation was already introduced and defined in a somewhat different context in Section 7.1.

For convenience that definition is repeated in Equations 9.1 and 9.2. For the purposes of this calculation, the coda portion of each seismic record is considered to be the portion contained in the interval from 3 to 13 sec following the first motion. Let the coda portion of the i^{th} seismometer be given by $x_i(t)$. Define the paired correlation coefficient between the i^{th} and j^{th} seismometers as $\rho_{i,j}$

$$\rho_{i,j} = \frac{\int_o^T x_i(t)x_j(t)dt}{\sqrt{\int_o^T x_i^2(t)dt \int_o^T x_j^2(t)dt}} \qquad (9.1)$$

where T is 10 sec, the integration interval used in determining the coda correlation. Note that this correlation coefficient is defined in such a way that its maximum value is 1. We now calculate the average of this correlation coefficient over all possible pairs of seismometers. If there are M seismometers in the array, then the number of pairs is M (M-1), and the average paired correlation coefficient for the coda, $\bar{\rho}_c$, is given by

$$\bar{\rho}_c = \frac{1}{M(M-1)} \sum_{i \neq j} \rho_{i,j} \qquad (9.2)$$

where the indices i and j run between 1 and M.

The seismic events that were used to explore the behavior of this statistic are summarized in Tables XI through XIII. Most of the data appearing in these tables applies to the automatic pP test that is discussed in Section X. The same set of events was used for that test as for the coda correlation test discussed in this section. In fact, both the coda correlation calculation and the automatic pP test were implemented by the same computer program so that the same preparation of the data was involved for both tests. As discussed in more detail in Section X, various numbers of stations were involved with each event; some of the seismic records were bandpass filtered; the seismograms were aligned by eye according to the first motion of the P phase; and, as indicated in the tables, the elements of the seismic array were spread over a very large range.

9.2 RESULTS

The results of the coda correlation calculation appear in the column labeled $\bar{\rho}_c$ of Tables XI through XIII. In the case of the earthquakes, these numbers appear to come from two populations: most of the earthquakes in the 10-40 km depth range have coefficients larger than 0.2,

and most of the other earthquakes have coefficients less than 0.1. Most of the surface-focus events also have coefficients less than 0.1. These observations suggest that the coda correlation statistic, $\bar{\rho}_c$, may be useful in distinguishing between surface-focus events and earthquakes in the 10-40 km depth range. In order to study this possibility, we have separated these events into three categories and plotted cumulative distribution functions of $\bar{\rho}_c$ for each category. The first category is the surface-focus events, and it consists of 12 events. The second category (the "moderate depth" earthquakes) consists of all earthquakes for which our best estimated depth is in the 10-40 km. These estimates are based primarily on the pP test (Section X), and in most cases they are consistent with the listed depth. The third category consists of the remaining earthquakes. (Not included in any of these categories is one deep earthquake (Event No. 17) which has a listed depth of 134 km. As discussed in Section 10.4, there are some indications that this is either a shallow event or the P phase was incorrectly identified).

The second category includes 24 events. Of these, 18 have listed depths between 10 and 40 km. There are only 2 earthquakes in the third category with listed depths between 10 and 40 km; both have listed depths of 40 km, and in both cases the pP test (see Section X) indicates a depth greater than 40 km. There are a total of 7 earthquakes that are listed as "shallow." With two of these, the pP test (Section X) indicates a depth of less than 10 km; these two are in the third category. The remaining 5 "shallow" earthquakes show a depth between 10 and 40 km on the pP test, and all 5 are in the second category. Finally, there is one event with a listed depth of 60 km, which shows a depth of 19 km on the pP test; this event is in the second category.

In Figure 9.1 the cumulative distribution function for the test statistic $\bar{\rho}_c$ is plotted for each of the three categories of events. This plot is on probability paper, so that the tendency for these points to fall on a straight line suggests a normal distribution for the statistic. It is clear from this figure that there is a very good separation between the earthquakes of moderate depth and the other events. Roughly speaking, the moderate-depth earthquakes have a mean coefficient of approximately .285 and the other events have a mean correlation coefficient of approximately .025. The fact that there is very little overlap between the cumulative distribution function for the moderate-depth earthquakes and the other cumulative distribution functions indicates that this discriminant should be very effective in separating these classes of events.

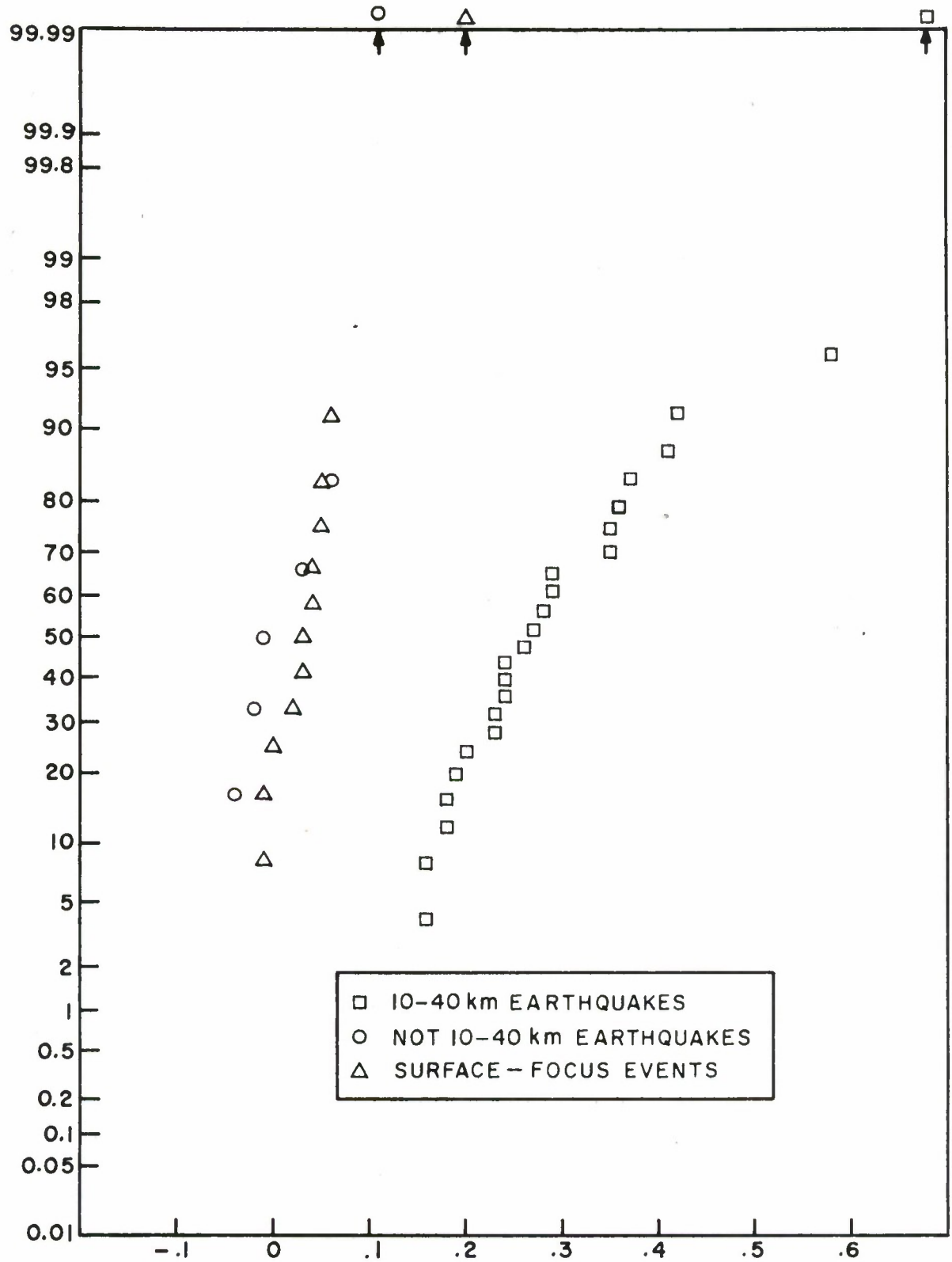


FIGURE 9.1
CODA CORRELATION CUMULATIVE DISTRIBUTION FUNCTIONS

9.3 DISCUSSION

The values of $\bar{\rho}_c$ for the surface-focus events and the earthquakes that are not in the 10-40 km depth region are almost entirely confined to the interval 0±0.05. A rough idea of how much apparent correlation might be expected if there were no correlated component in the coda at the various seismometers may be obtained by examining the column labeled $\bar{\rho}_n$ in Tables XI through XIII. This column lists the averaged paired correlation coefficient for the noise preceding the events. Presumably the noise waveforms at these (widely spaced) seismometers are independent, so that the calculation indicates how much apparent correlation might be expected on purely statistical grounds. Since the noise calculations employed a 30 sec interval, and the coda calculation only a 10 sec interval, the $\bar{\rho}_n$ would be expected to vary somewhat less than would the $\bar{\rho}_c$ if the codas were truly uncorrelated. Comparing the $\bar{\rho}_n$ with the $\bar{\rho}_c$ that are calculated from surface-focus events and earthquakes that are not in the 10-40 km depth region suggests that the observed $\bar{\rho}_c$ are consistent with the hypothesis that the codas are uncorrelated for these events.

In order to understand the statistical significance of the results presented in Figure 9.1, it may be instructive to make some additional assumptions about the behavior of the test statistic $\bar{\rho}_c$. If we assume that the distribution of this test statistic is in fact normal across the population of events for all three populations of events, and replace the scatter of points of Figure 9.1 by rough straight-line fits to those points, we may then quote a few classification probabilities that may be relevant in evaluating this test.

A rough straight line fit to the curves suggests the following parameters:

	MEAN	STANDARD DEVIATION
surface-focus events	0.025	0.015
moderate depth earthquakes	0.285	0.045

If a decision threshold is arbitrarily set at $\bar{\rho}_c = 0.1$, then these numbers suggest the following: if a surface-focus event occurs, the probability that it will be classified as a moderate depth earthquake is $3 \cdot 10^{-7}$; if a moderate depth earthquake occurs, the probability that it will not be classified correctly is $2 \cdot 10^{-5}$. These numbers are summarized in the following equations:

$$\Pr\{\bar{\rho}_c > 0.1 \mid \text{surface-focus event}\} = 3 \cdot 10^{-7} \quad (9.3)$$

$$\Pr\{\bar{\rho}_c < 0.1 \mid \text{moderate depth earthquake}\} = 2 \cdot 10^{-5} \quad (9.4)$$

It should be stressed that these numbers are based on several very strong assumptions, and should only be regarded as an alternate summary of the curves of Figure 9.1. These curves summarize the distribution of $\bar{\rho}_c$ over a limited number of events; the number and location of stations that are involved vary considerably. For these reasons, it would be premature to conclude that this level of performance would apply to a specific set of stations for all events of some minimum magnitude.

9.4 DEPENDENCE ON ARRAY CHARACTERISTICS

A few experiments have been performed to study the dependence of the coda correlation discriminant on the specific characteristics of the array. Specifically, we have examined the dependence on the number of stations for a continental-size array and the possibility of employing the test with an array as small as LASA-Montana.

9.4.1 Number of Stations

Three of the above calculations were tested on arrays consisting of fewer elements, by dividing the original array into two sets of stations and repeating the calculation. The results of these calculations appear in Tables XII and XIII. In the case of two surface-focus events (Number 35 and 36), $\bar{\rho}_c$ was small for the entire array and remains small with each of the smaller (in number of elements) arrays. In the case of the earthquake (Event No. 32) $\bar{\rho}_c$ was .19 for the entire array and .15 and .22 for the smaller arrays. None of these calculations indicate a strong or consistent dependence on the number of stations, but it should be noted that the "smallest" array used had 6 stations, and there was a considerable range spread for the stations.

9.4.2 Dependence on Separation of Stations

All of the calculations presented above are based on very large arrays. The usefulness of the discriminant would, of course, be considerably enhanced if it would function satisfactorily with an array the size of LASA-Montana. A few experiments have been performed to explore the possibility.

Several correlation measurements have been performed with the LASA recordings of LONGSHOT. These calculations are presented in Section VIII. Among the calculations performed were some that measured the dependence of $\bar{\rho}_c$ on the separation of the array elements. These calculations indicated a value of $\bar{\rho}_c$ of .03 if the minimum cluster separation was 128 km. However, for smaller values of cluster separation this number

increased appreciably. For example, for cluster separations between 64 and 127 km, $\bar{\rho}_c$ = .14; for cluster separations between 32 and 63 km, $\bar{\rho}_c$ = .31. These results suggest that a minimum separation on the order of 100 km would be necessary to avoid confusing shots with moderate depth earthquakes.

We have performed a few calculations with an array consisting of the center elements of the AO subarray and the four F-ring subarrays. (For this 5-element array, the minimum separation is 98 km.) The results of these calculations are summarized in the following table.

Event No.	Depth	$\bar{\rho}_c$
43	0	.11
45	0	.12
42	0	-.06
44	33	.40
46	33	.15

These numbers suggest that the test is seriously degraded by using a LASA-size array but it may still provide sufficient separation between shots and moderate-depth earthquake to be of some value. This question merits further study.

9.5 SUMMARY AND CONCLUSIONS

Data have been presented to indicate that the average paired coda correlation coefficient may be a very useful discriminant for distinguishing between "moderate depth" (10-40 km) earthquakes and surface-focus events. For the purposes of calculating this statistic, the coda is taken to be the interval from 3 to 13 seconds after the first motion on each seismogram. For every pair of seismograms the cross correlation coefficient for this interval is calculated. The average of all of these correlation coefficients is taken as the test statistic, $\bar{\rho}_c$.

Calculations based on data from a continental-size array for 12 surface-focus events and 24 "moderate depth" earthquakes indicate an approximately normal distribution for the test statistic $\bar{\rho}_c$ with the following parameters for the two classes events:

	MEAN	STANDARD DEVIATION
surface-focus events	0.025	0.015
moderate depth earthquakes	0.285	0.045

As yet, the dependence of this calculation on the characteristics of the array (number of stations, ranges to each station, etc.) has not been thoroughly studied. Preliminary calculations suggest that 6 stations may be essentially as good as 12, provided that the spread of ranges is comparable in both cases. Calculations based on LASA-Montana data lead to results that are clearly inferior to those of a larger array, but may be useful.

The results presented above are very encouraging in that they indicate the coda correlation coefficient may be a very useful discriminant for identifying earthquakes of moderate depth. In its present form the test is very simple to describe and implement, except for the fact that it typically involves records from stations spread over a considerable range. To date we do not have a very good understanding of the dependence of this test on certain of the parameters such as range-from-the-epicenter, spread-of-ranges across the array, and number of stations. We also do not know how much of the correlation coefficient that occurs with earthquakes of moderate depth is due to the pP phase being in the coda interval and how much is due to the fact that the earthquake source is relatively extensive in time. A better understanding of the relative contributions of these two items might lead to some insights into ways in which the coda correlation discriminant could be improved.

SECTION X

AUTOMATIC pP TEST FOR SHALLOW EARTHQUAKES

The most powerful diagnostic aid for discrimination between earthquakes and nuclear explosions is the measurement of the depth of the source. The only certain method for observing this depth is the measurement of the difference in arrival times of the P phase and the pP phase. Often this method cannot be applied for shallow earthquakes because the pP phase is masked by the coda of P. In this section an automatic test for extracting the pP arrival information from the outputs of a seismic array of continental dimensions (3000 to 7000 km) is presented. Basically the method consists of assuming a "test depth," aligning all of the seismograms in such a way that if the "test depth" were correct, the pP phase would add up coherently, and then looking for a peak in energy at the appropriate place in the summed seismogram. The test depth which yields the largest peak in energy (relative to the surrounding coda) is selected as the estimated source depth. While the basic concept is fairly easy to state, there are several details of implementation and one important modification of the technique that merit further discussion.

The objectives in developing this test are twofold. The first is simply to automate what might in some cases be done manually. More importantly, however, it is hoped that the test will in many cases yield correct test depths that would otherwise be unavailable or difficult to obtain. It should also be noted at this time that there are some clear limitations on the applicability of this test. The test is designed to identify depths between the (approximate) limits of 10 and 40 km. The 10 km limit is imposed to prevent confusion between the pP and P phases. The upper limit is imposed by an assumption that will be discussed in more detail below. Basically, the assumption is that an average crustal velocity of 6.34 km/sec can be used in calculating the difference in arrival times of P and pP. This assumption becomes quite inappropriate when the test depths approach the depth of the Moho, which in some continental regions is as small as 30 km. Finally, the test is designed for use with continental-size arrays. Having a large variation in range-from-the-epicenter across the array is desirable because it reduces the probability that other phases will add up coherently when the seismograms are aligned to allow coherent addition of pP. Some appreciation for the parameters involved may be obtained by examining travel-time tables for the various phases (see, e.g., reference 12).

This section begins with a detailed description of the structure of the automatic test for pP. Details such as window lengths are omitted from the first description, but are included in the immediately following discussion of the specific parameter

choices that have been made in implementing this test and of the potential sources of error that are involved. Following these details,the results of applying this test to 31 earthquakes and 12 surface-focus events will be presented and discussed. For all of the surface-focus events the test indicated that the depth was not within the 10-40 km region. For earthquakes with depths between 10 and 40 km, the results of this test agreed with the "listed" depths on approximately 75% of the trials. (The sources of these "listed" depths are indicated in Section 10.3.) In some of the cases of disagreement, examination of the original seismograms leads us to question the "listed" depth. However, we have not yet systematically studied these cases.

10.1 DESCRIPTION OF THE AUTOMATIC pP TEST

As indicated above, this test consists of aligning the outputs of seismometers in a continental-size array in such a way that the pP phases will add coherently if the assumed "test depth" is correct, and examining a "combined" seismogram for a peak in energy at the pP location determined by the assumed test depth. The appropriate delay to be applied to each seismometer in order to carry out the test depends on the "test depth" of the source and the range from the epicenter to each sensor. The functional dependence on these two parameters will be derived on the basis of some simple ray tracing arguments, and an assumed "average crustal velocity."

Once the seismograms have been properly aligned for a specific test depth the problem is how best to combine them. The maximal-ratio combining technique, which is often employed in communication problems,has been used, and will be briefly discussed below. The final step in the pP test is the calculation of the energy in a time window corresponding to the summed pP phases and the comparison of this energy with the energy in the surrounding coda. The test depth that yields the largest ratio of these two energies is selected as the estimated source depth. It turns out this technique can yield misleading results in the case where one of the several seismic records has a very large signal-to-noise ratio compared to the others. This problem will be discussed together with a modification of the pP test that was designed to correct for this difficulty. Most of the calculations presented in this section are based on the modified test.

10.1.1 Time Delay Between P and pP Phases

Figure 10.1 indicates the appropriate ray paths and geometry for determining the time delay between the arrivals of the P and pP phases. In this figure h is the assumed test depth of the source and i is the angle of incidence for the P ray going from the source to a particular seismometer. As indicated in the figure the ray path for the pP phase is longer than the ray path for the P phase by an amount 2h cos i. If an average

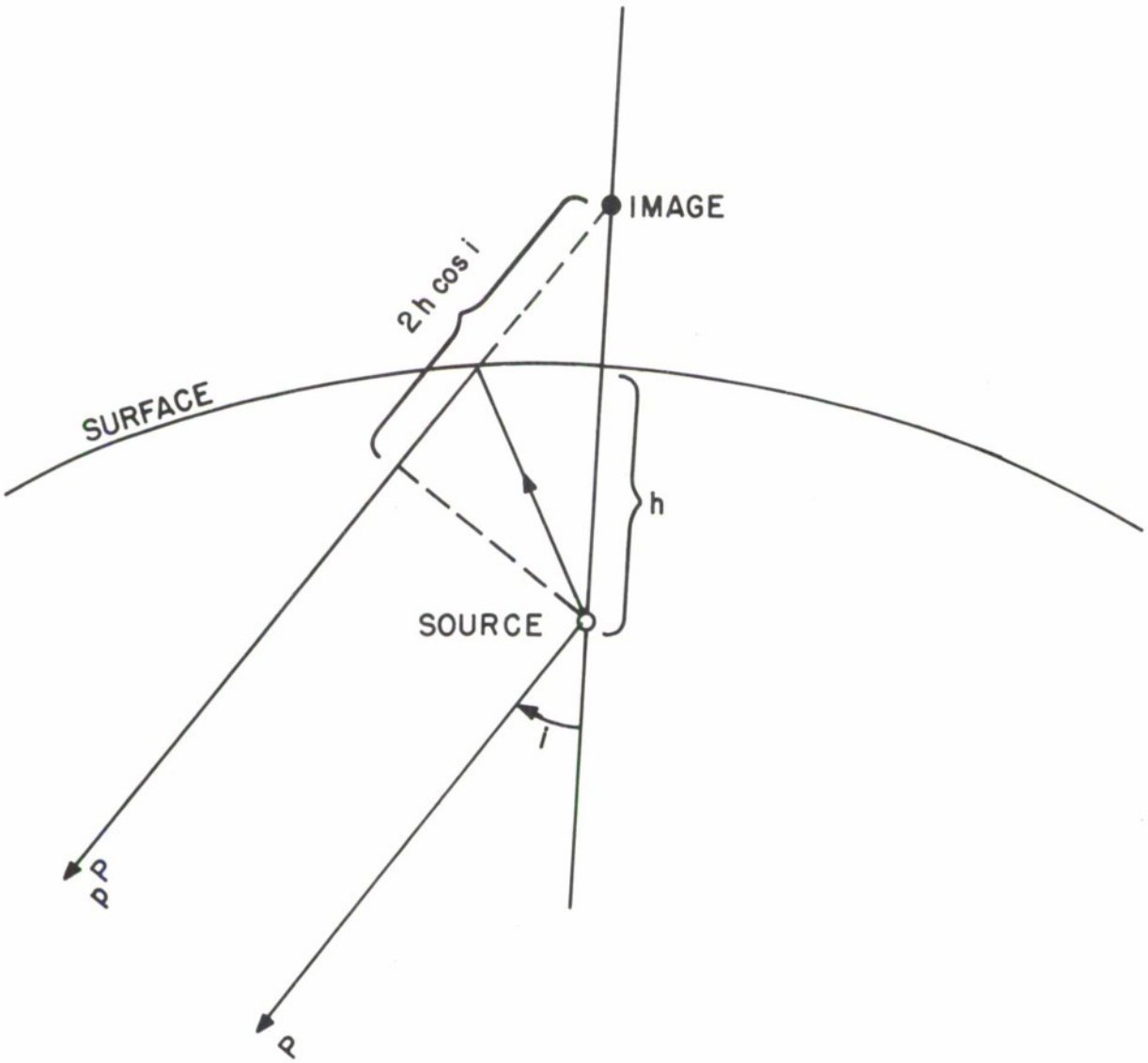


FIGURE 10.1
GEOMETRY OF SURFACE REFLECTION

crustal velocity for the P phase c is assumed, the expected differential arrival time is given by

$$\tau = \frac{2h}{c} \cos i \qquad (10.1)$$

In applying this test it is necessary to consider several different test depths and several different seismometers; these will be identified by the subscripts j and i, respectively. It is trivial to modify Equation 10.1 to include these subscripts.

$$\tau_{ij} = \frac{2h_j}{c} \cos i_i \qquad (10.2)$$

This equation gives the expected differential arrival time between P and pP for the j^{th} test depth and the i^{th} seismometer.

10.1.2 Combining of Seismometer Outputs

The question of the appropriate alignment of the various seismic records for a given test depth was discussed above. The problem now is how best to combine these various seismograms. Since the objective is the enhancement of the pP phase in the combined seismogram, relative to the surrounding waveform, and since the seismometers are typically widely spaced, we have chosen to borrow a combining rule from the diversity-combining techniques that have been applied in communication problems. More specifically the maximal-ratio combining rule has been used. This rule is briefly described in Section VII of this report. Under certain conditions in communication problems, this rule is optimum in the sense that it maximizes the signal-to-noise ratio of the combined output. In order to apply this rule, we have assumed that the amplitude of the pP phase on a given seismic record is proportional to the amplitude of the P phase for that record and that, therefore, the P phase may be taken as a reliable measure of the "signal" strength. We have tried two different choices as to what we consider "noise" for the purpose of this diversity combining technique. In one case, we have assumed that the major interference in identifying the pP phase of the summed seismogram is simply teleseismic noise and we therefore have taken the average power in the teleseismic noise (measured from a record of the noise preceding the seismic event) as the "noise" parameter in the diversity combining rule. Probably a more appropriate definition of the interfering signal is the coda that results from the P phase. With this in mind we have also defined "noise" as the coda that follows the P phase and have calculated our combining weights by estimating the coda energy. As might be expected, we have found in general that the weighting based on the coda as the interfering signal leads to somewhat better results than the weighting based on the teleseismic noise being the interfering signal. However, in many cases the difference is not significant. The various choices of window lengths used in calculating the energy of the P phase, the coda, and the noise will be discussed below.

10.1.3 The Test Statistics ε_j and η_j

The alignment of the various seismograms according to an assumed test depth and the combining rule for adding up the various aligned seismometers have now been discussed. If the assumed test depth is the correct one, the combined seismic record should have a relatively large pP phase appearing at a specific location. The expected location for this phase is of course known in terms of the test depth.

If the test depth is incorrect, the pP phase should not add up coherently (though this effect may not be large), and, more importantly, the time window where the pP phases would add up if the test depth were correct should consist only of coda. It only remains then to devise a statistic to measure whether or not the combined pP phases do occur in the time window corresponding to each test depth.

We have made a fairly simple choice for this statistic. A one second time window is placed at the location where the pP phases should appear if the assumed test depth is correct, and the energy in this one second interval is calculated. Also calculated is the energy in the coda surrounding this one second window normalized to the integration interval. The ratio of these two normalized energies is defined as the test statistic ε_j. Recall that j is the parameter by which the various test depths are indexed. In implementing this test the ε_j's are calculated for each test depth h_j and the depth corresponding to the maximum value of ε_j is selected as the estimated depth of the source.

As suggested above,this technique can yield spurious peaks in the value of ε_j when one of the several seismic records used in the test has a very large signal-to-noise ratio compared to the others. One reason this problem can develop is that the maximal-ratio combining used in this test tends to emphasize the records with very good signal-to-noise ratio. For this reason, even a spurious peak in the coda of a single record with a very good signal-to-noise ratio can contribute quite strongly to the combined record that is used in this test. In order to try to avoid this possibility of a spurious peak in one or two records leading to an incorrect depth estimate, we have rather arbitrarily selected the following modification of this test. Roughly speaking,this modification is intended to allow only legitimate peaks in the summed seismogram to be counted. The modification consists of simply weighting each ε_j by an average paired correlation coefficient for all of the records. This average paired correlation coefficient depends upon the test depths being considered. For each assumed test depth the one second interval that would contain the pP phase if the test depth were correct is considered. Based on this one second interval of each seismogram,all possible paired correlation coefficients are calculated

and the average of these numbers is what is used to multiply the ε_j statistic. The objective in employing this additional weighting is to eliminate the problem mentioned above of a spurious peak in one strong record contributing unduly to the ε_j statistic. The reasoning is that if a peak in one record does occur and it legitimately represents a pP phase, it should be highly correlated with the appropriate time window in the other records, whereas a spurious peak occurring in a single record would have a relatively low correlation coefficient with the appropriate time windows in the other records.

In summary, the majority of the calculations to be presented below are based on the modified automatic pP test. This modified test consists first of calculating the statistic ε_j for each test depth h_j. Also calculated for each test depth will be the average paired correlation coefficients based on the pP time window that corresponds to the assumed test depth. The final output of the automatic pP test is the product of these two statistics, η_j. If the statistic η_j has a clear peak at a value of j corresponding to values of h_j that are between 10 and 40 km, that h_j is selected as the estimated depth of source.

10.2 PARAMETER CHOICES

Several choices of parameter values must be made in order to carry out the automatic pP test described above. The parameter values that have been used to date are described in this section.

10.2.1 Lengths of Integration Intervals

Several time windows or integration intervals are used in these calculations. For both the P phase and the pP phase calculations,a one second time window was used throughout these calculations. In the case of the P phase calculations this integration interval was used in order to infer the amplitude of the pP phase, which was needed for the weighting coefficients in the maximal-ratio combining. The one second integration interval for the pP phase was used in order to calculate the numerator of the test statistic ε_j. When the maximal-ratio combining weights were determined by the noise preceding the seismic event, a 30-second time window was used in order to estimate the average power in the noise. When these weights were determined by the coda energy the coda interval was considered to run from 2 to 17 seconds after the first motion of the P phase. The integration interval for the coda energy,calculation that determines the denominator for ε_j was based on the same 15-second interval, except that the one second region which is the trial location of the pP phase was excluded.

We would expect that these calculations are fairly sensitive to the choice of a one second time window for examining the pP phase. The reason for this choice is that it is felt that one

second is the interval over which good coherence of the P and the pP phase may be expected across the array. We would expect that the test would not work as well with a longer time window than the one second value used to date,but this expectation has not been explored experimentally. We do not feel that these calculations are very sensitive to the choice of integration interval for determining either the noise or the coda energy.

10.2.2 Choice of Test Depths, h_j

In all of these calculations, the following test depths were used.

$$h_j = \frac{c}{2} \cdot \frac{1}{2} \cdot (j+6) \qquad j = 0,1,\ldots,20$$

$$= \frac{6.34}{4} (j+6) \text{ km} \tag{10.3}$$

As can be seen from the above equation, the increment in test depth is approximately 1.6 km. Referring back to Equation 10.2, the increment in delay time for the i^{th} seismometer is

$$\Delta\tau_{ij} = \frac{1}{2} \cdot \cos i_i \text{ sec} \tag{10.4}$$

For the ranges we will be considering, i_i might vary between 15° and 32°, and the cosine factor between 0.96 and 0.85. For a single continental-size array, the spread in ranges, and hence in angles of incidence, will typically be somewhat less.

Since, by Equation 10.4, the increment in τ_{ij} for consecutive test depths will be less than 1/2 sec, consecutive 1-sec integration intervals for the pP phase will overlap by at least 50%. For this reason, we doubt that there would be any value in taking smaller increments in test depth.

10.2.3 Number and Location of Stations

In the data to be presented below,the number of stations involved in the automatic pP test varies from 4 to 20. We would expect that the quality of this automatic test might be very sensitive to the number and distribution of stations. To date, only very preliminary experiments have been performed to explore this dependence, and these will be discussed below. Specifically, on three events the total collection of stations has been divided into two groups, and these treated separately as seismic arrays. The results from these two calculations have been compared with each other and also with the predicted source depth that would result from using the entire array. One of the more important characteristics of a seismic array used for these calculations would be that it have a considerable spread in range to the epicenter. This is desirable in order to allow for "move-out" of the pP phase (or of the P_cP phase) across the array. Without

the "move-out," there is the danger that when the seismograms are aligned in such a way that pP adds coherently, the P_cP phase will also add coherently.

10.2.4 Average Crustal Velocity

In calculating the appropriate time delay in order to align the seismograms for coherent addition of the pP phase, an average crustal velocity of 6.34 km/sec is assumed. It should be noted that several different velocity profiles for the crust have been reported, and, in general, these profiles vary with location on the earth. The most important variation in these profiles is that the Moho depth varies with location on the earth, and at the Moho there is a very significant change in velocity. For this reason, the technique presented in this section cannot be expected to work satisfactorily for earthquakes that are deeper than the Moho. Even for earthquakes shallower than the Moho the calculation is approximate in the sense that an average crustal velocity is used, rather than the detailed velocity profile that might be appropriate for a specific region. Examination of typical velocity profiles (see, for example, reference 13) indicates that using an average crustal velocity rather than the profile itself will tend to make shallow earthquakes appear somewhat shallower than they really are and earthquakes near the maximum depth for the test seem somewhat deeper than they are.

10.2.5 Angle of Incidence

The expression for the appropriate time delay to be applied to each seismometer involves the angle of incidence of the P wave traveling from the source to that seismometer. In the automatic pP test this angle is determined from the values given by Richter (14). A straight-line interpolation between the points of this table has been used. We estimate that the maximum error due to this interpolation is on the order of a 20^{th} of a second, or one sample point of the digital seismogram. This value is probably small compared to other sources of error.

10.2.6 Filtering of Seismic Records

In the case of the smaller magnitude events the seismic records were all filtered before performing the automatic pP test. This filtering was for the purpose of enhancing signal-to-noise ratio and made it somewhat easier to determine the arrival time of the P phase. The filter used in these calculations is similar to the filter used in calculations presented elsewhere in this report. (See Section 12.2.) It has a frequency response which is real and given by

$$H(f) = \begin{cases} 0 & |f| \leq 0.25 \text{ Hz} \\ \frac{1}{2}\left[1-\cos\frac{2\pi(|f|-0.25)}{1.0}\right] & 0.25 \leq |f| \leq 0.75 \\ 1 & 0.75 \leq |f| \leq 2.0 \\ \frac{1}{2}\left[1+\cos\frac{2\pi(|f|-2.0)}{3,0}\right] & 2.0 \leq |f| \leq 3.5 \\ 0 & 3.5 \leq |f| \end{cases} \qquad (10.5)$$

The (time domain) impulse response of this filter is an even function about the origin and hence introduces no delay in the seismogram. A 513-point filter was used in these calculations. We would not expect that the quality of the pP test would be very sensitive to the details of the filter that is employed; however, this question has not been systematically studied.

10.3 EXPERIMENTAL RESULTS

Results obtained to date from applying the pP test to data from 31 earthquakes and 12 surface-focus events are summarized below. Data are first presented on 11 earthquakes using the ε_j test statistic of the pP test. Except for the 3 earthquakes that are deeper than the 40 km limit of the test, the pP test yielded close to the correct test depth on all trials. As was indicated in the description of the test, the test was modified to include a new test statistic, η_j. Data are presented which indicate that the η_j test statistic can be significantly better than the ε_j test statistic for surface-focus events and slightly better for earthquakes. Following this comparison, the remainder of the data presented are in terms of the test statistic η_j. Depth estimates based on this statistic for 20 additional earthquakes are presented. In 5 of these 20 trials the estimate conflicts with the listed depth. In 7 of the trials the estimate from other sources of the depth of the event is listed simply as "shallow" and the results of the pP test seem to be consistent with this designation. Data will then be presented of the η_j calculation based on 12 surface-focus events. In all of these trials the test succeeds in the sense that no apparent pP phase is indicated. Finally, three sets of calculations are presented to give some indication of the dependence of the pP test on the number of stations employed. These calculations are based on one earthquake and two surface-focus events. In all three cases, the pP test was applied to the entire set of seismograms and to two nonoverlapping subsets of the entire set. The resulting curves vary somewhat in character. In the case of the earthquake, however, the depth estimate changes only negligibly. In the case of the surface-focus events, it is clear in all cases that no depth estimate is appropriate.

The data presented in this section are summarized in Tables XI to XIII. Table XI lists the 11 earthquakes for which the ε_j calculation was performed. Table XII lists the

20 additional earthquakes on which the η_j calculation was performed (the ε_j calculation was also performed but only data from the η_j calculations are presented here). Finally, Table XIII summarizes the data from the 12 surface-focus events. The information on the vast majority of the earthquake data used for the pP test was provided by Vela Seismological Center. We understand that the word "shallow" indicates that no depth estimate was possible by identifying the pP phase on separate traces and that the computer solution (based on main P arrivals) indicated a shallow depth. We presume that shallow could mean anything in the range 0-15 km. The last 6 events listed in Table XII (which occupy the last 8 lines) have depths that are based on the C&GS estimates. There are three columns of correlation coefficients listed in Tables XI to XIII that are not discussed in this section. The contents of the last three columns of these tables are discussed in Sections VIII and IX.

10.3.1 Automatic pP Test (ε_j) - Earthquakes

Figure 10.2 summarizes the ε_j calculations that were performed on a set of 11 earthquakes. The depth estimates based on these figures, which were obtained by simply choosing the tallest bar of the histogram, are listed in Table XI. With the exception of the very deep earthquakes, which correspond to parts A, B and I of the figure, the pP test yielded a depth estimate very close to the listed estimate in all cases. These results are considered as very encouraging since the test was not designed to estimate depths of earthquakes deeper than 40 km.

10.3.2 Comparison of the ε_j and η_j Test Statistic

Figure 10.3 presents calculations of ε_j and η_j based on the same events. One earthquake and one surface-focus event are involved. In the case of the surface-focus event, the ε_j shows a very clear peak at about 15 km but the η_j does not show any clear peak. In fact, no amplitudes are above 1.0, and based on experience with these statistics this figure would be sufficient to indicate very clearly that the depth was not in the 10-40 km range. In the case of surface-focus events, then, using η_j rather than ε_j provides a more useful test. In parts C and D of Figure 10.3 the ε_j and η_j calculations are presented for an earthquake. In this case the shape of the curve changes somewhat but the location of the peak is essentially unchanged. The peak is slightly clearer in the case of the η_j than in the case of the ε_j plot but the difference is not important. These data suggest that for earthquakes the η_j statistic is slightly superior to the ε_j statistic, but the difference between these two test statistics may not be important. These comparisons between the two statistics have been performed on a number of earthquakes and surface-focus events and the data presented in Figure 10.3 may be regarded as representative.

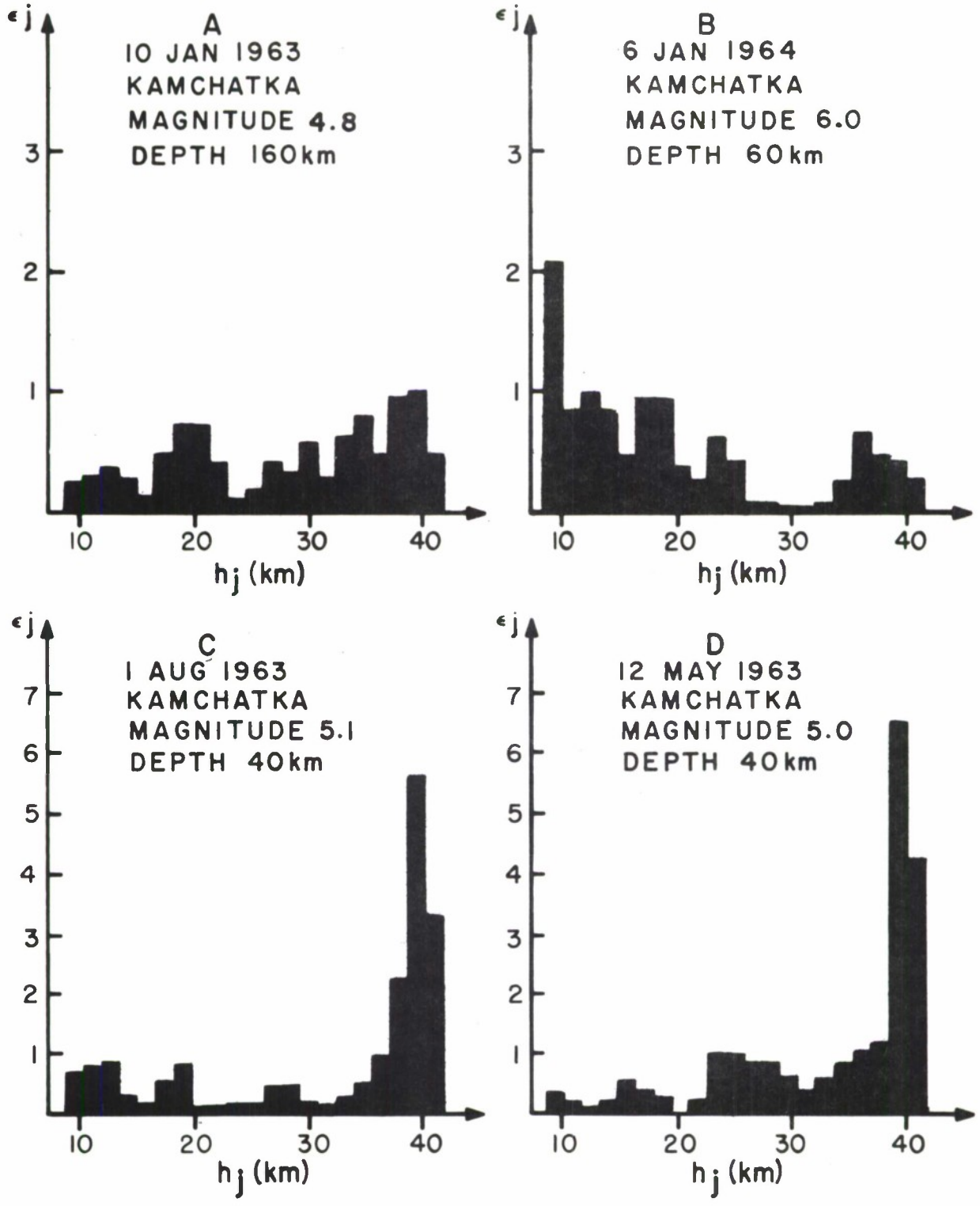


FIGURE 10.2 (A-D)
AUTOMATIC pP TEST (ϵ_j)
EARTHQUAKES

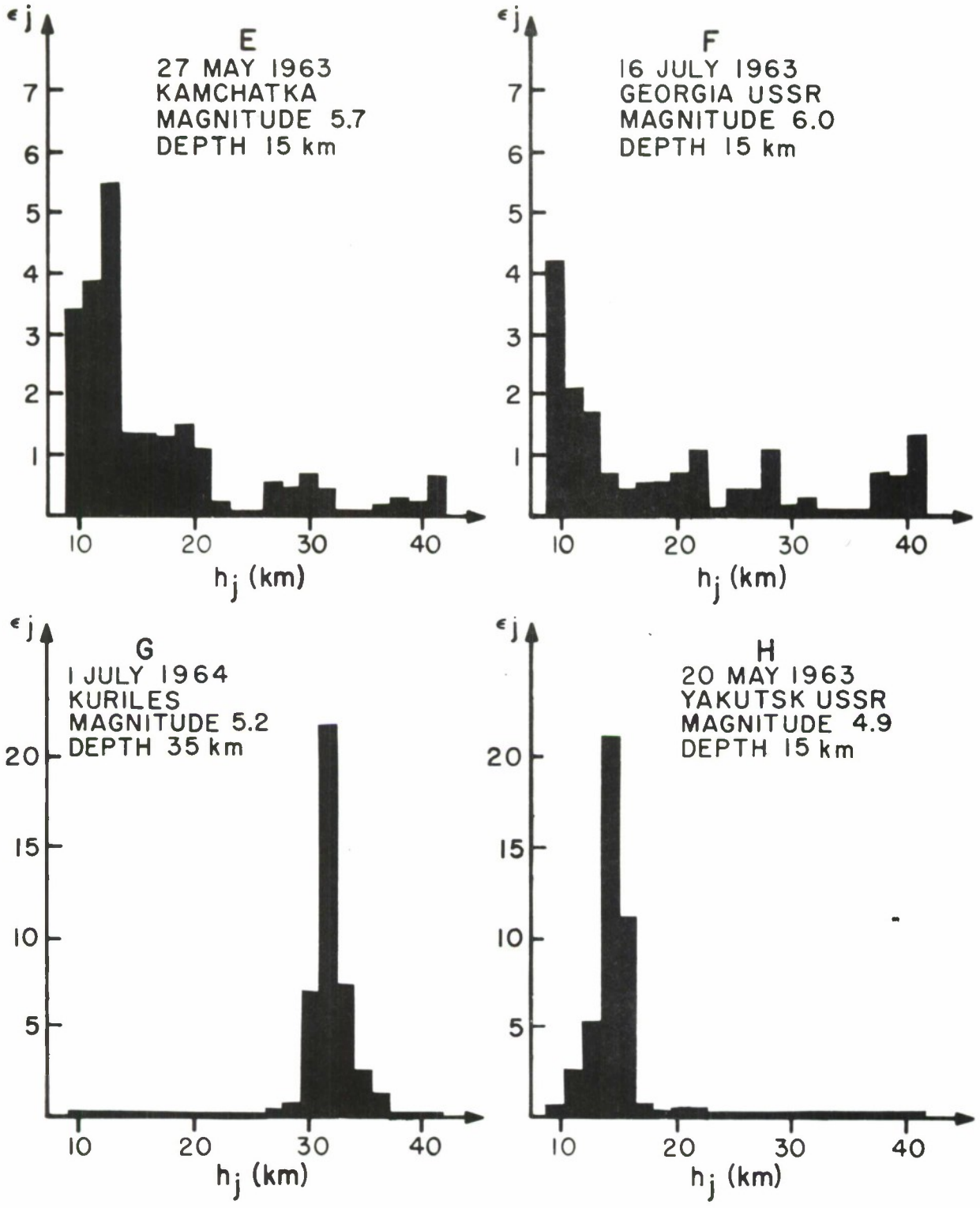


FIGURE 10.2 (E-H)
AUTOMATIC pP TEST (ϵ_j)
EARTHQUAKES

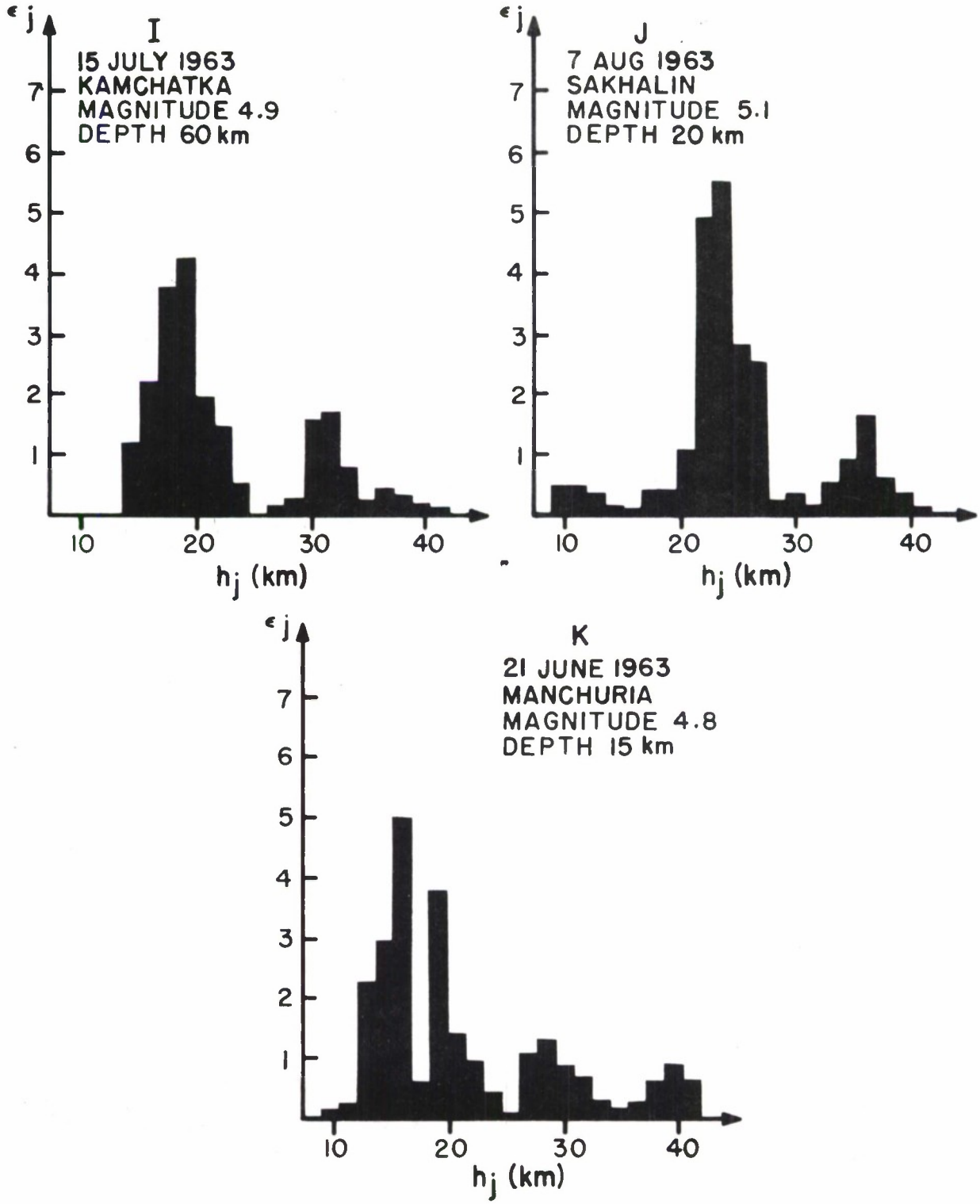


FIGURE 10.2 (I-K)
AUTOMATIC pP TEST (ϵ_j)
EARTHQUAKES

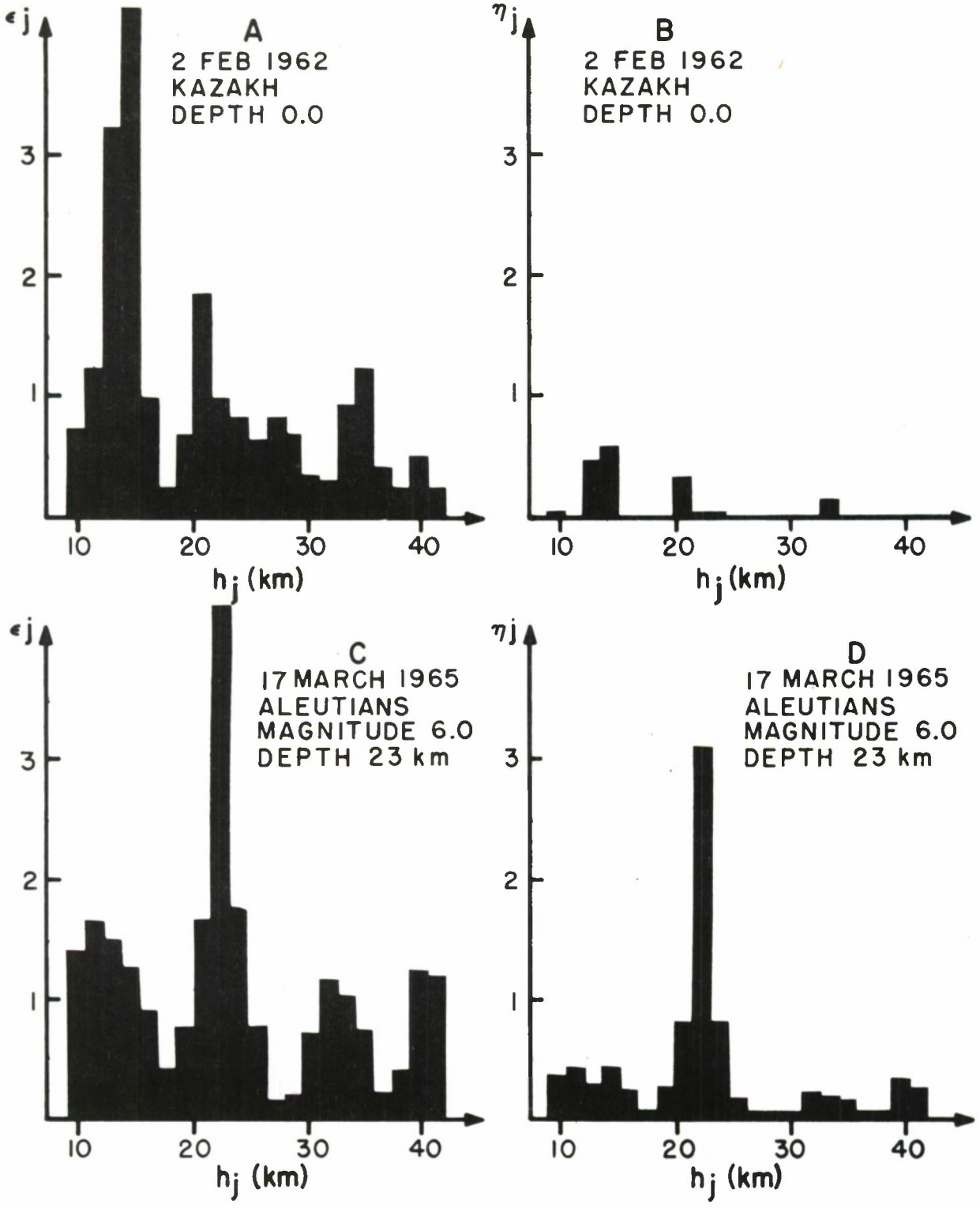


FIGURE 10.3 (A-D)
AUTOMATIC pP TEST
COMPARISON OF ϵ_j AND η_j

10.3.3 Automatic pP Test (n_j) -- Earthquakes

Calculated n_j for 20 earthquakes are presented in Figure 10.4 and the estimated depths based on this calculation are summarized in the appropriate column of Table XII. Table XII indicates that in general the test agrees well with the listed depths, but there are some clear disagreements. For example, part E of the figure indicates a very clear peak at about 13 km whereas the listed depth of that event is 25 km (it should be noted, however, that the C&GS depth for this event is 10 km); similarly, part S peaks at 16 km rather than the listed 25 km; part N of the figure has a listed depth of 15 km but there are two peaks in the figure that are larger than the peak at 15 km; parts Q and R of the figure,which have listed depths of 25 and 23 km,show no significant peaks in the n_j plots; part T shows three peaks, the largest being at 13 km whereas the listed depth is 134 km.

Parts I through L of this figure illustrate some of the rules we have developed for estimating depths by examination of n_j plots. In the case of parts I and J the only peak in the plot is at the last bar to the right. When this occurs,we estimate the depth as greater than 40 km. Part L of the figure has the tallest bar as the first one of the figure. When this occurs, and the bar is less than 3 in height, we estimate the depth at less than the corresponding depth of 9 km. Part K shows no clear peak, and if the true depth of that event were in the region of 10 to 40 km, this figure would have to be regarded as a failure. However, the listed depth for this event is only "shallow" so it may well have been less than the 9 km, in which case this test could not be expected to show the true depth.

10.3.4 Surface-Focus Events

Figure 10.5 presents the n_j calculations for 12 surface focus events. As none of the graphs in this figure show any clear peaks, the test is considered to have worked satisfactorily on all 12 events. Two possible exceptions to this conclusion are parts B and H of the figure where there exist small peaks with amplitudes of approximately unity. In general, the peaks that "legitimately" occur with the earthquake data are a good deal larger than this, but the data of Figure 10.4, H and L for example, suggest that sometimes the peaks occurring with earthquakes can be on the order of 1.0. However, both of these examples involve "shallow" earthquakes and so may involve pP phases outside of the test range.

10.3.5 Dependence on Number of Stations

A few calculations have been performed to date to explore the question of how sensitive the results of the pP test is to the number of stations involved. We have not yet explored the dependence on the spread of ranges between epicenter and

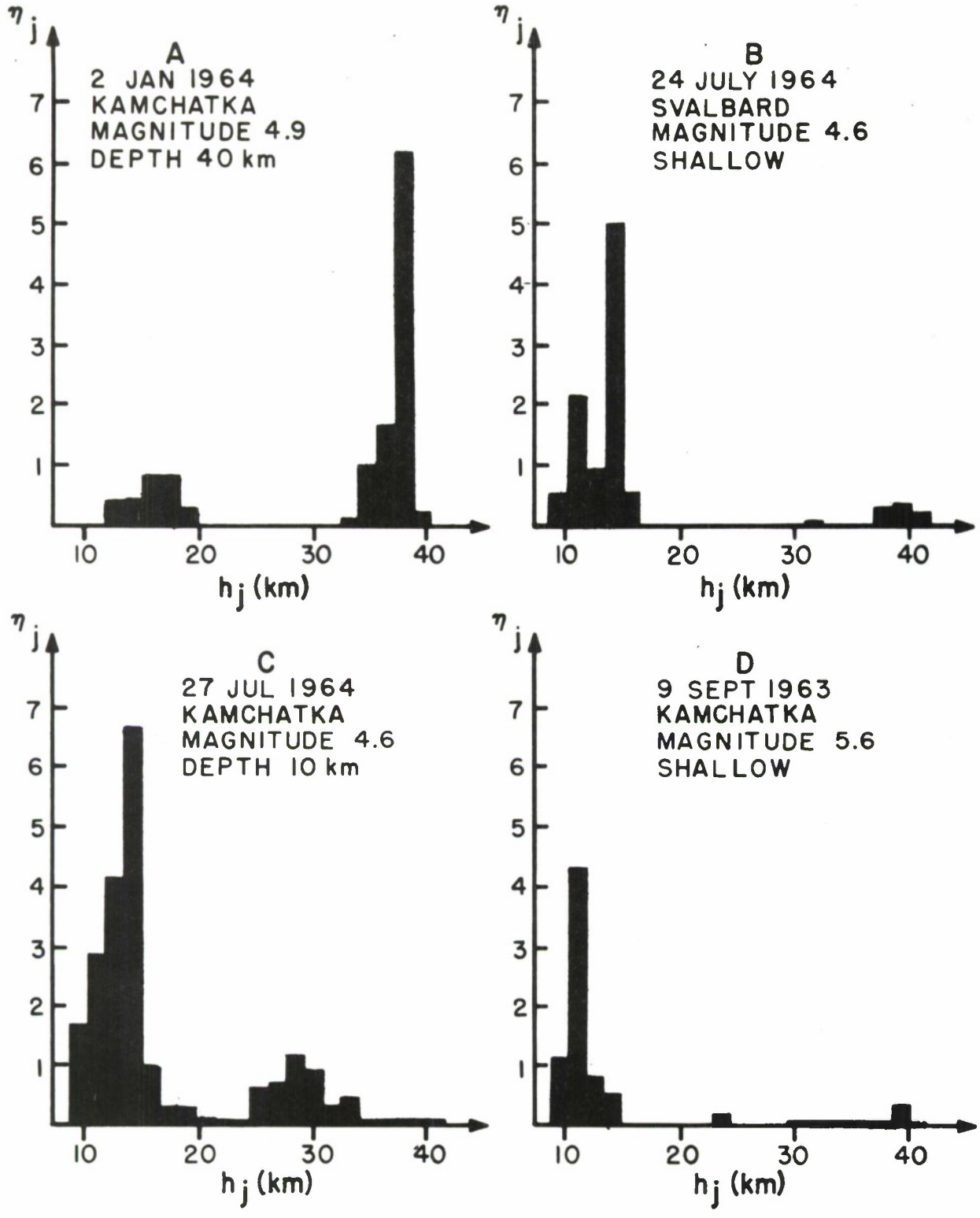


FIGURE 10.4 (A-D)
AUTOMATIC pP TEST (η_j)
EARTHQUAKES

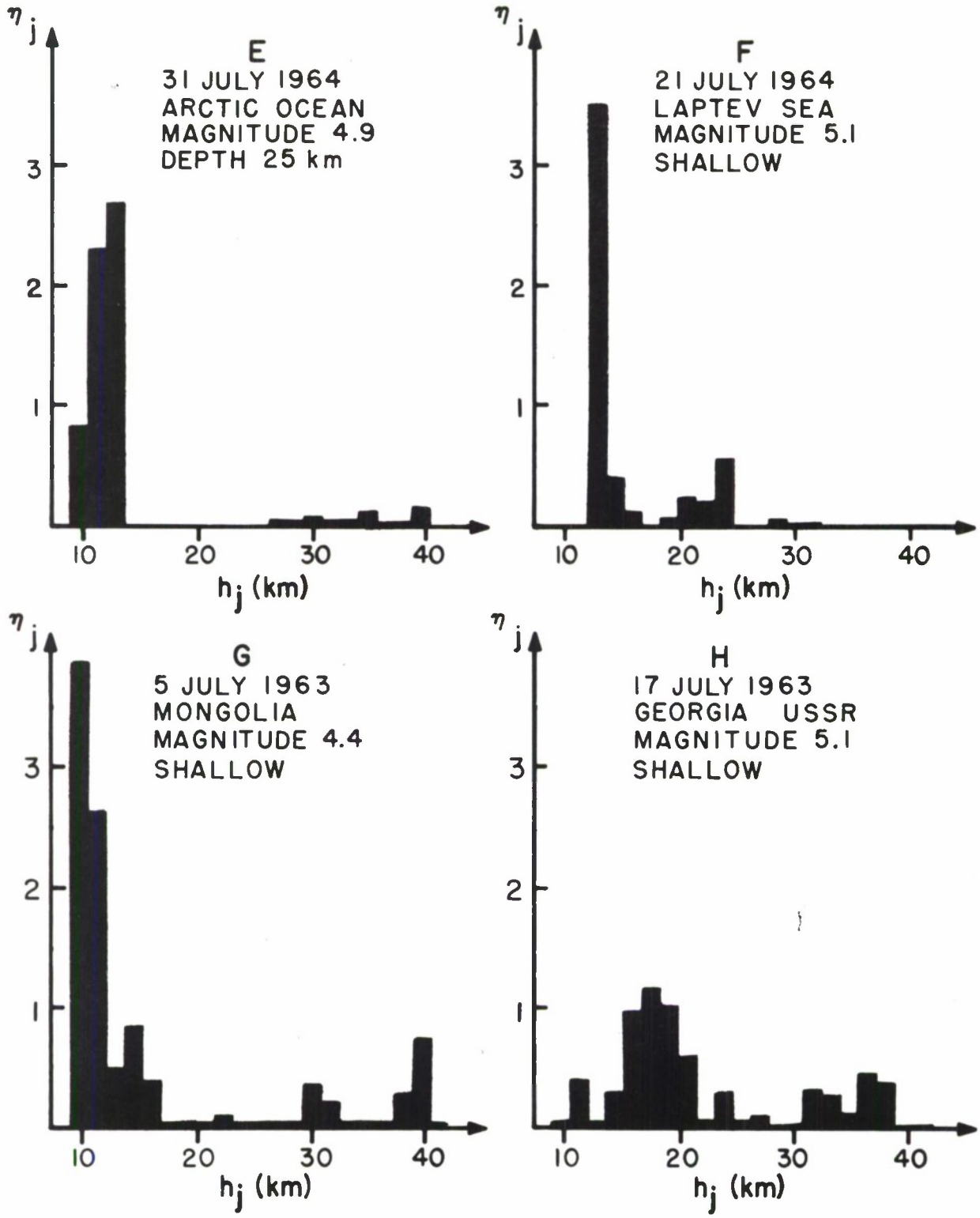


FIGURE 10.4 (E-H)
AUTOMATIC pP TEST (η_j)
EARTHQUAKES

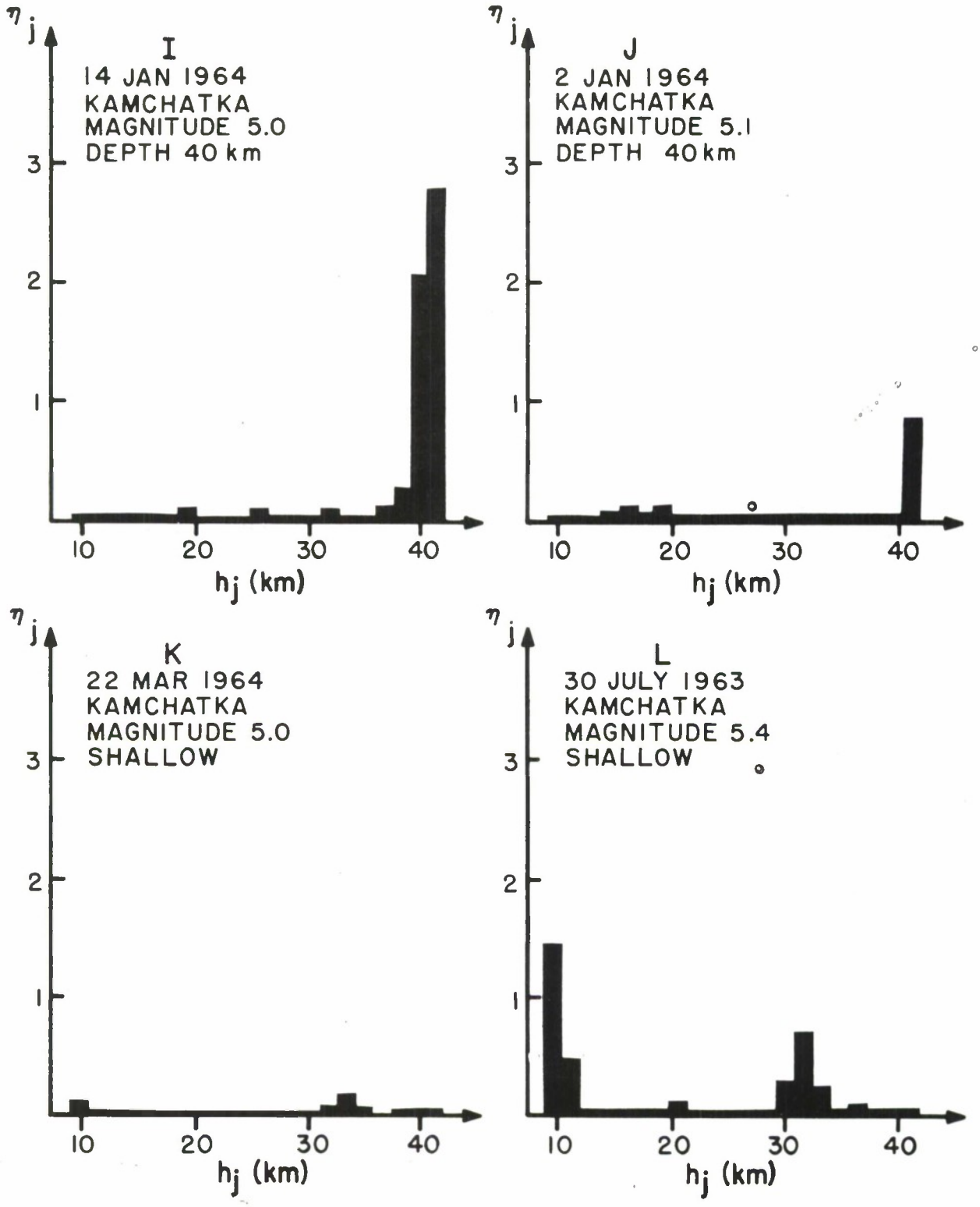


FIGURE 10.4 (I-L)
AUTOMATIC pP TEST (η_j)
EARTHQUAKES

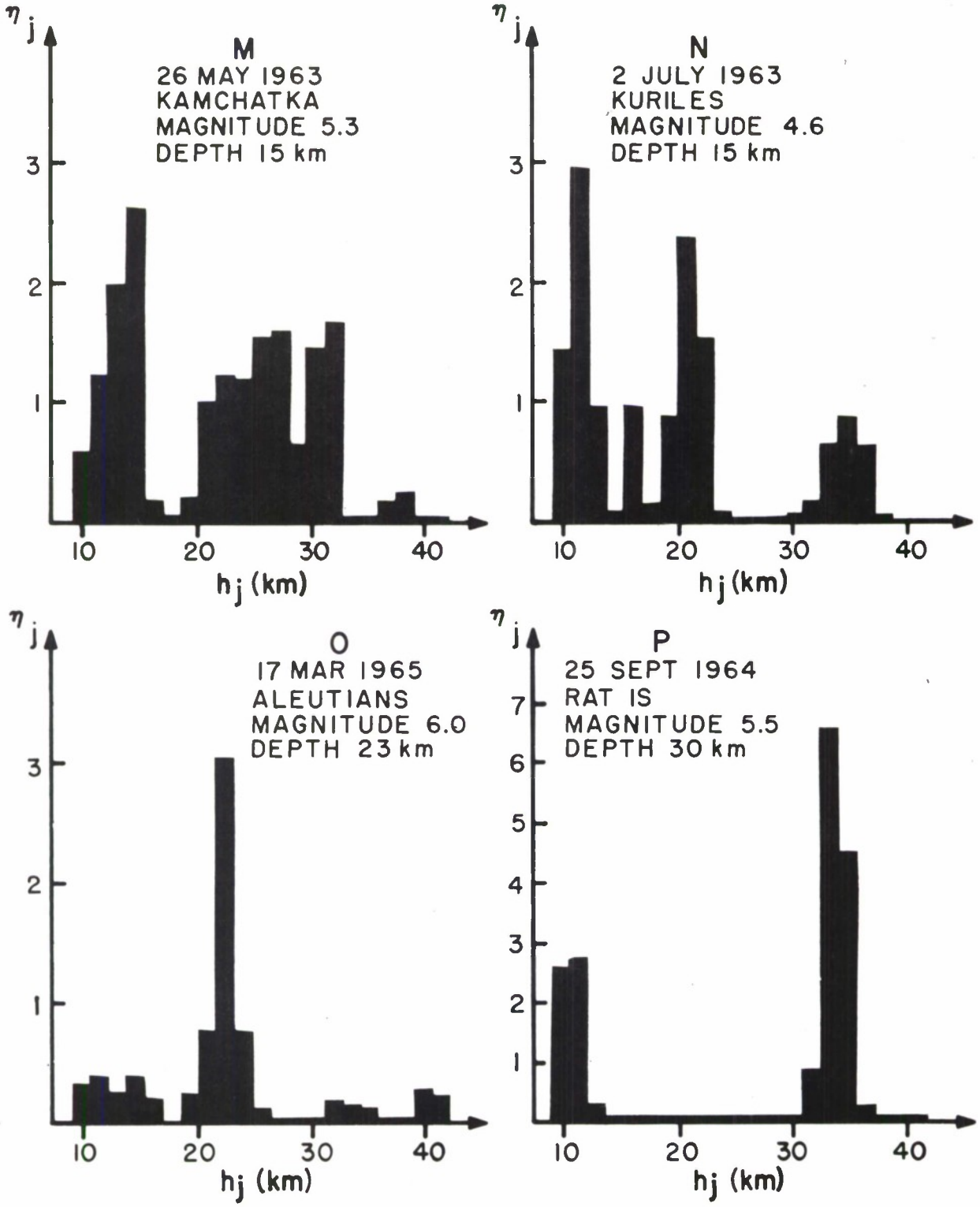


FIGURE 10.4 (M – P)
AUTOMATIC pP TEST (η_j)
EARTHQUAKES

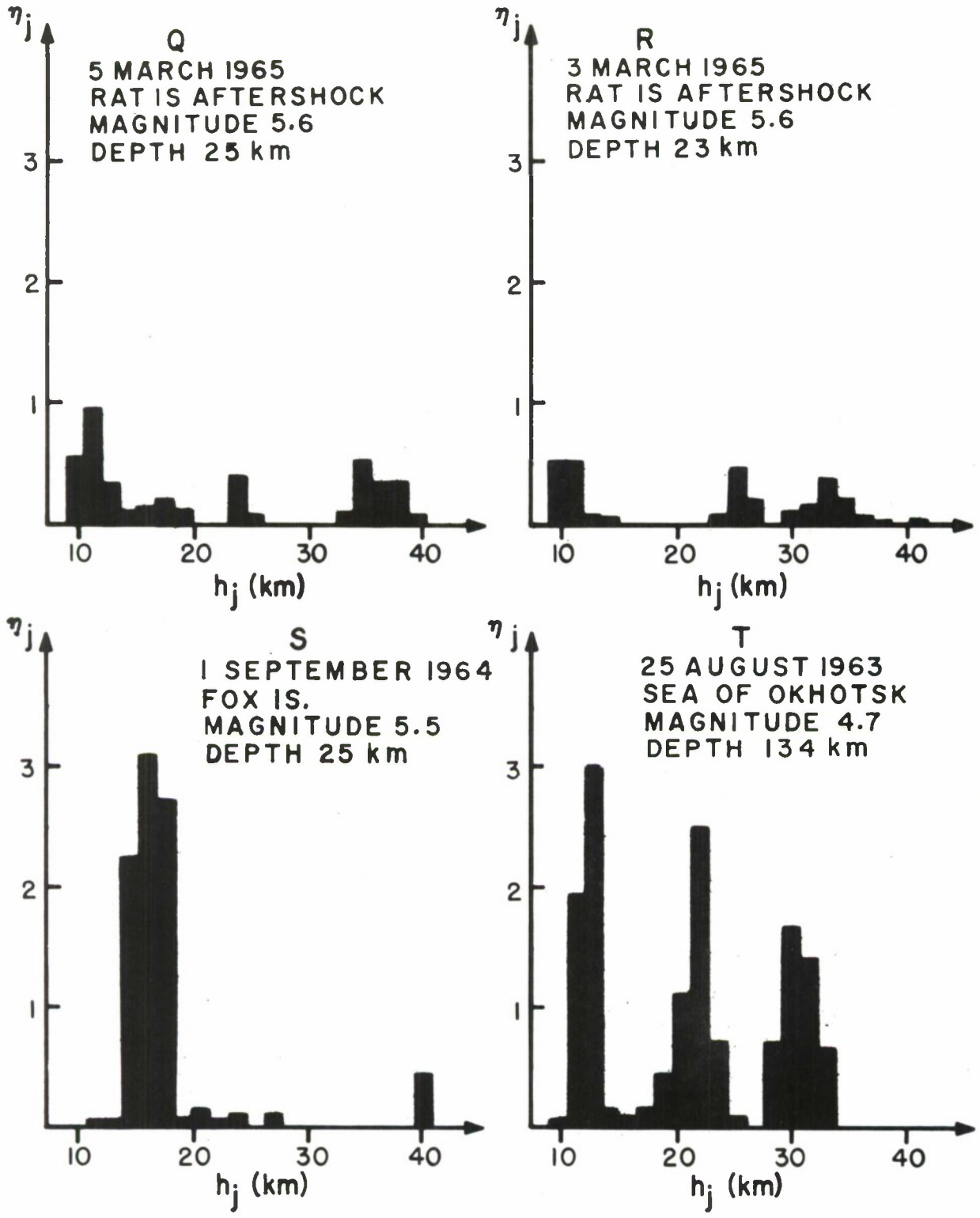


FIGURE 10.4 (Q-T)
AUTOMATIC pP TEST (η_j)
EARTHQUAKES

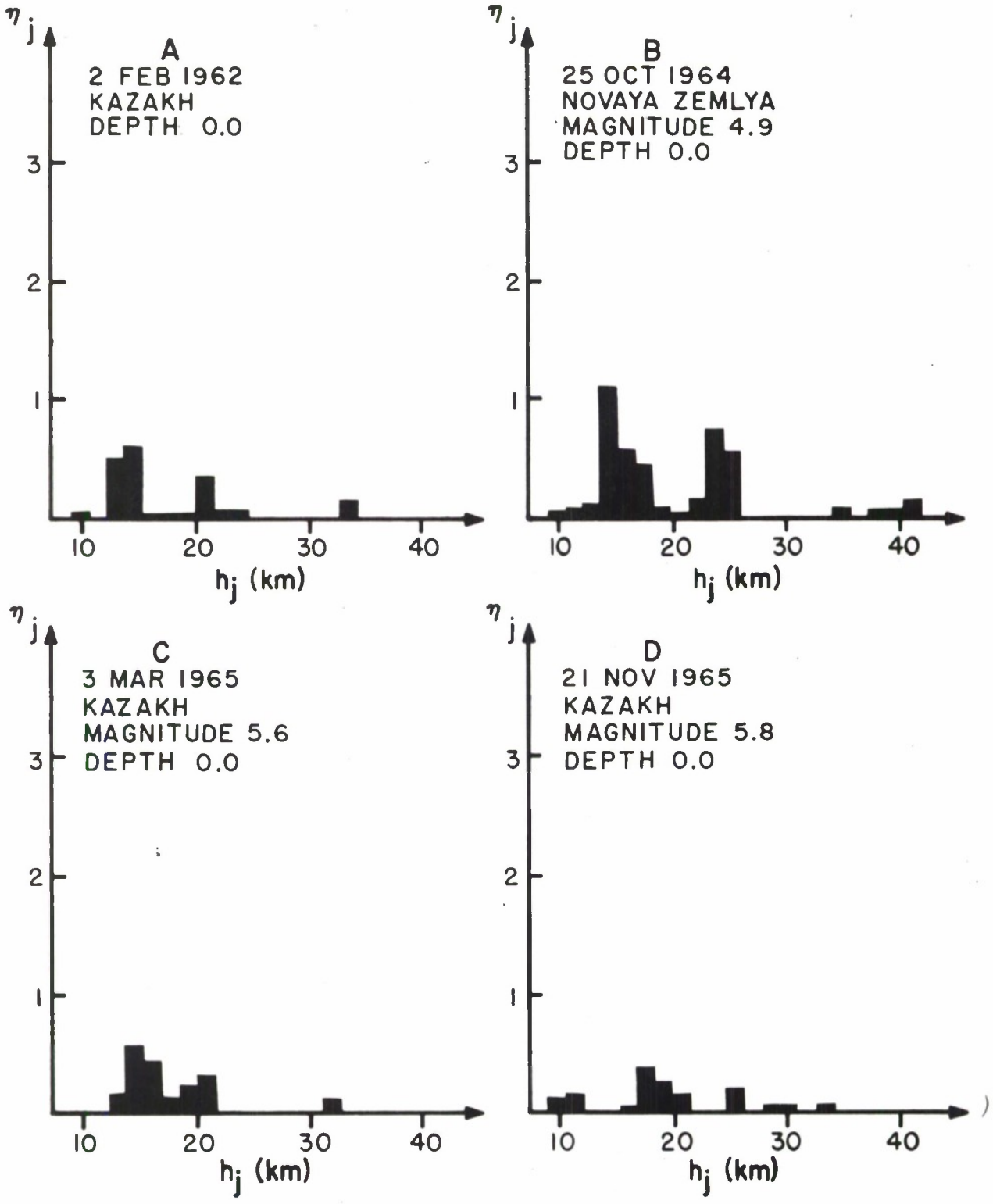


FIGURE 10.5 (A-D)
AUTOMATIC pP TEST (η_j)
SURFACE FOCUS EVENTS

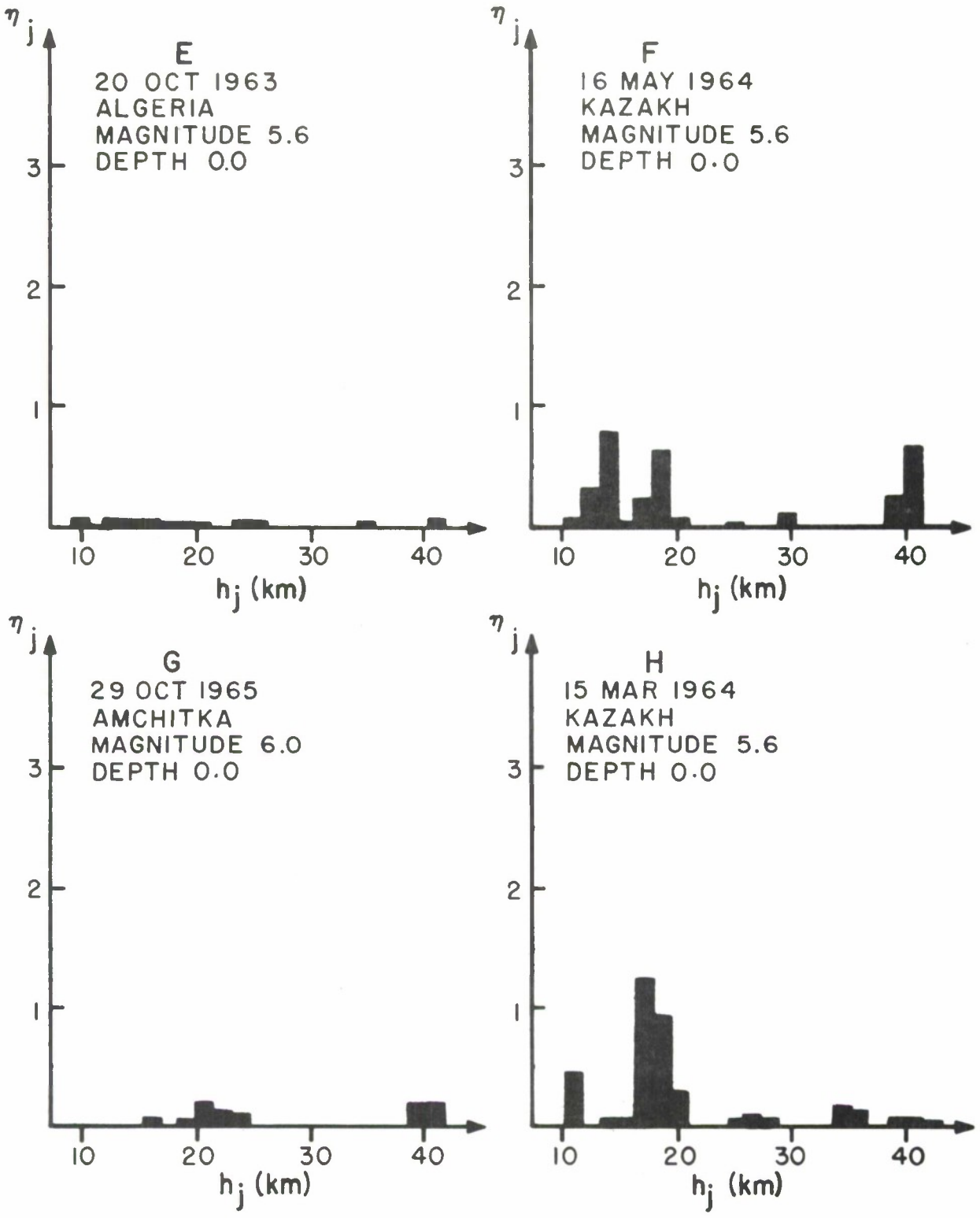


FIGURE 10.5 (E–H)
AUTOMATIC pP TEST (η_j)
SURFACE FOCUS EVENTS

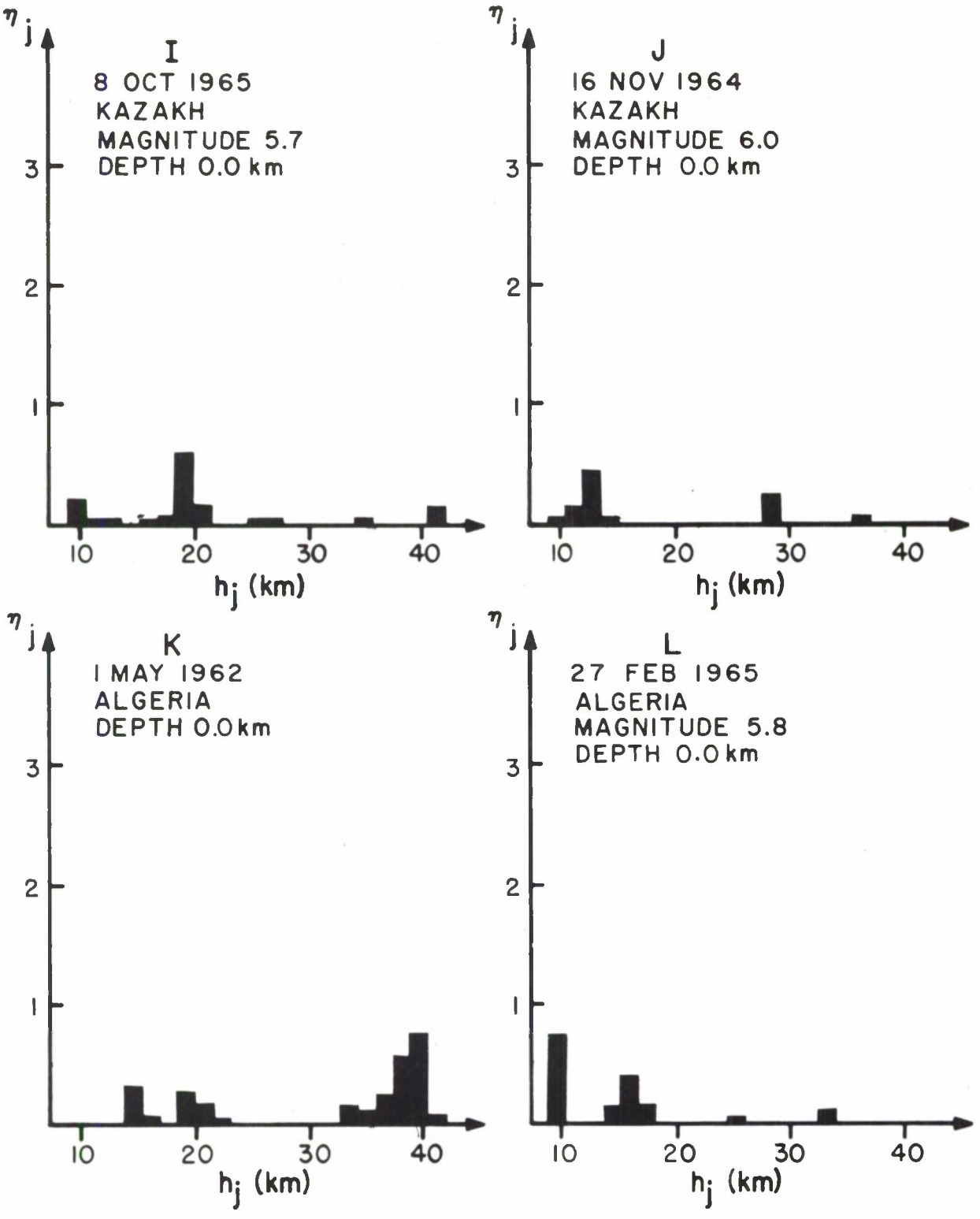


FIGURE 10.5 (I-L)
AUTOMATIC pP TEST (η_j)
SURFACE FOCUS EVENTS

stations, which we expect may be very important. To examine the dependence on the number of stations we have simply repeated calculations performed for the entire array of stations on subsets consisting of roughly 1/2 of the array and compared the results from each subset with themselves and with the calculations based on the entire array. These results indicate the dependence on number of stations may not be too severe in the sense that the depth estimate does not change significantly for the earthquake, and with the surface-focus events no spurious peaks arise that would be confused with "legitimate" depths. The data comparing the number of stations are presented in Figure 10.6 and are based on a single earthquake and two surface-focus events.

10.4 SUMMARY AND CONCLUSIONS

An automatic pP test has been described and tested on 31 earthquakes and 12 surface-focus events. The test has been used primarily with continental-size arrays; very preliminary calculations have also been performed using only LASA-Montana data. The test may be roughly described as follows. Twenty "test depths" between approximately 10 and 40 km are considered. For each test depth the seismograms are aligned in such a way that if the test depth were correct the pP phase on all of the seismograms would add coherently. A weighted sum of all of the seismograms is calculated, the energy in a 1 sec time window located where the pP phase would be if the test depths were correct is calculated, the energy in the surrounding coda is calculated, and the ratio of these two energies for the j^{th} test depth is defined as ε_j. The idea in calculating this ratio is that if the test depth is correct, the pP phases should add coherently and the region of the summed seismograms containing the summed pP phases should have more energy than the surrounding coda. For an incorrect test depth, the pP phases may not add coherently, and, perhaps more importantly, not all of the pP phases will contribute to the 1 sec time window corresponding to the assumed depth. The original version of the test took the largest value of ε_j as corresponding to the correct test depth. It was found that in some cases, due to the weighting used in combining seismograms, a random fluctuation in a single record that had a large S/N ratio could lead to a spurious peak in the ε_j plot. To alleviate this problem, the ε_j's were multiplied by a weighting factor equal to the average paired correlation coefficient for the region of interest. The reasoning behind this modification was that a spurious peak on a single record would not be accompanied by a large average paired correlation coefficient, whereas the legitimate pP phase would be because it would show up on all records.

The first output of the pP test is a plot of ε_j vs j, or test depth. If there is a clear peak in the 10-40 km region covered by the plot the depth of source is estimated to be the corresponding test depth. If no clear peak is present the result of the test is interpreted as "not in the 10-40 km region." It should be noted that no final rules for interpreting the ε_j plots have been developed. These rules are still developing and the criterion for developing these rules has been a combination of simplicity and accuracy, where accuracy is determined by the "listed depths" for the events processed to date. As additional data become available these rules will probably change (the test may also change); however, the rules that seem to lead to the highest performance on the existing set of data may be stated as follows: (all of the following refer to the η_j (not the ε_j) plots).

1) if all bars are less than 1.0 the estimate is "not in 10-40 km region"
2) if at least one bar is greater than 1.0, choose the tallest bar:
   a) if the bar is not at either horizontal extreme, estimate the depth as the value corresponding to the location of the bar;
   b) if the tallest bar is at the right hand extreme, estimate the depth as greater than 40 km;
   c) if the tallest bar is at the left hand extreme,
      i) if the bar is less than 3 in height, estimate depth as less than 9 km;
      ii) if the bar is greater than 3 in height estimate the depth as 10 km.

The automatic pP test has been tested on 31 earthquakes and 12 surface-focus events using data from continental-size arrays. Of the 31 earthquakes tested, 4 were deeper than 40 km. On two of these (see Figures 10.2 I and J) the ε_j plot failed to indicate any clear peak corresponding to a depth of source between 10 and 40 km. On another of the earthquakes deeper than 40 km the ε_j plot indicates a fairly clear peak at 19 km. The fourth earthquake that was deeper than 40 km (134 km) showed three peaks in the η_j plot. We suspect that the "time pick" may have been in error, since what appear to be at least two separate phases may be observed in the first 10 sec following what was thought to be the P phase. Of the remaining 27 earthquakes 7 were listed as "shallow." The pP test yielded a depth estimate of 14 km or less on 6 of the 7 shallow earthquakes and an estimate of 17 km on the last. All of the 20 remaining earthquakes have listed depths between 10 and 40 km. The pP test yielded depth estimates close to the

listed depths on all but 5 of the 20 earthquakes. These 5 disagreements were discussed in Section 10.3.3. In summary, considering only earthquakes with depths between 10 and 40 km, we may say that the pP test agrees with listed depths on between 75% and 80% of these events, depending upon how we count the "shallow events.

While we regard the above results as encouraging we feel that there are many detailed issues yet to be resolved with respect to this test. The question of dependence upon number of stations and variation of range-to-the-epicenter of the various stations has not yet been throughly explored, but would certainly have to be resolved before any operational use of this test could be considered. The question of whether or not the maximal ratio combining that is used in this test is really the most satisfactory combining rule also has yet to be resolved. Finally, the test as it now stands is a fairly complicated calculation. We do not at this point know what, if any, of the complexity of the test could be removed without seriously degrading the performance. If this test were ever to be considered for operational applications this issue should certainly be resolved.

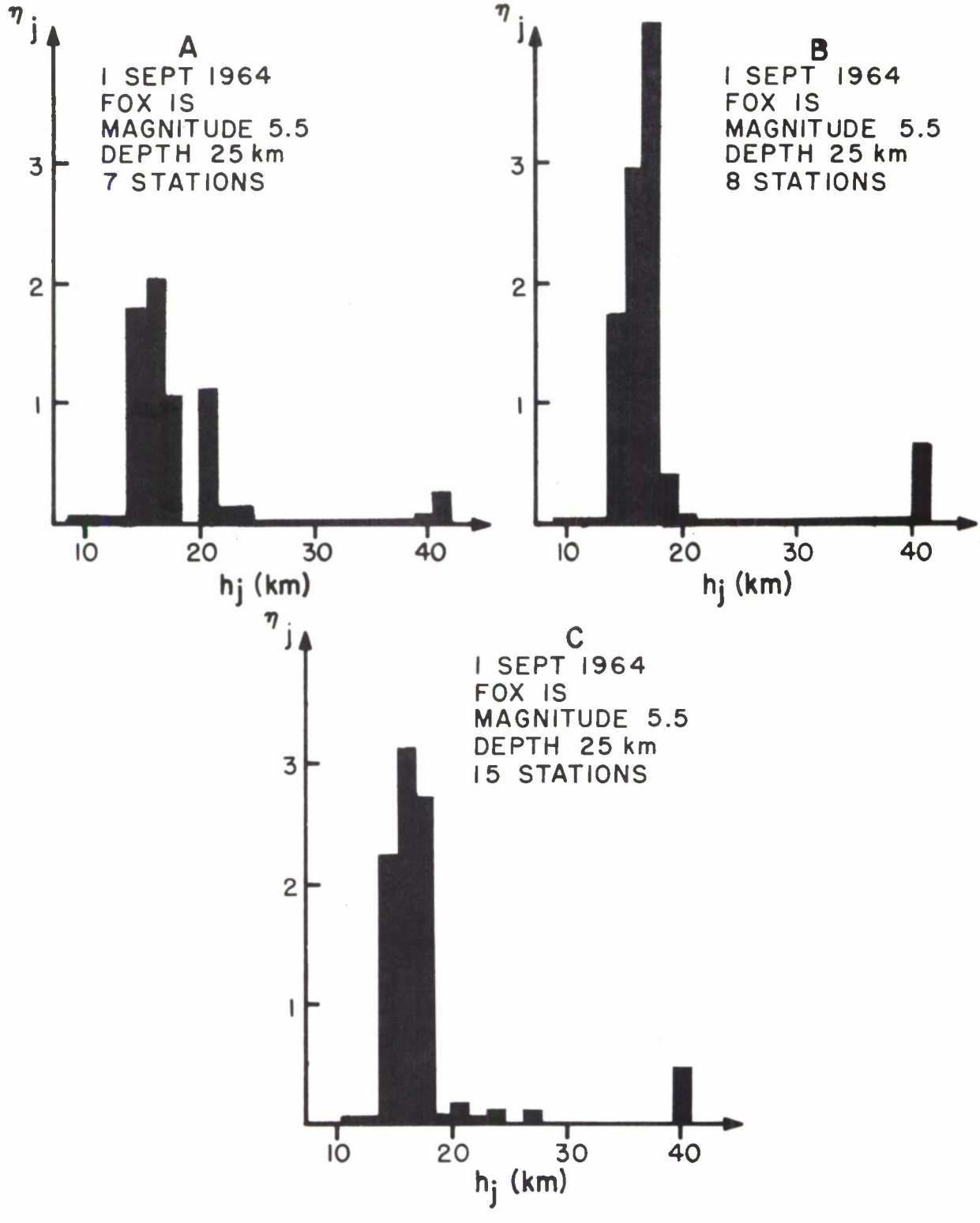


FIGURE 10.6 (A-C)
AUTOMATIC pP TEST (η_j)
DEPENDENCE ON NUMBER OF STATIONS

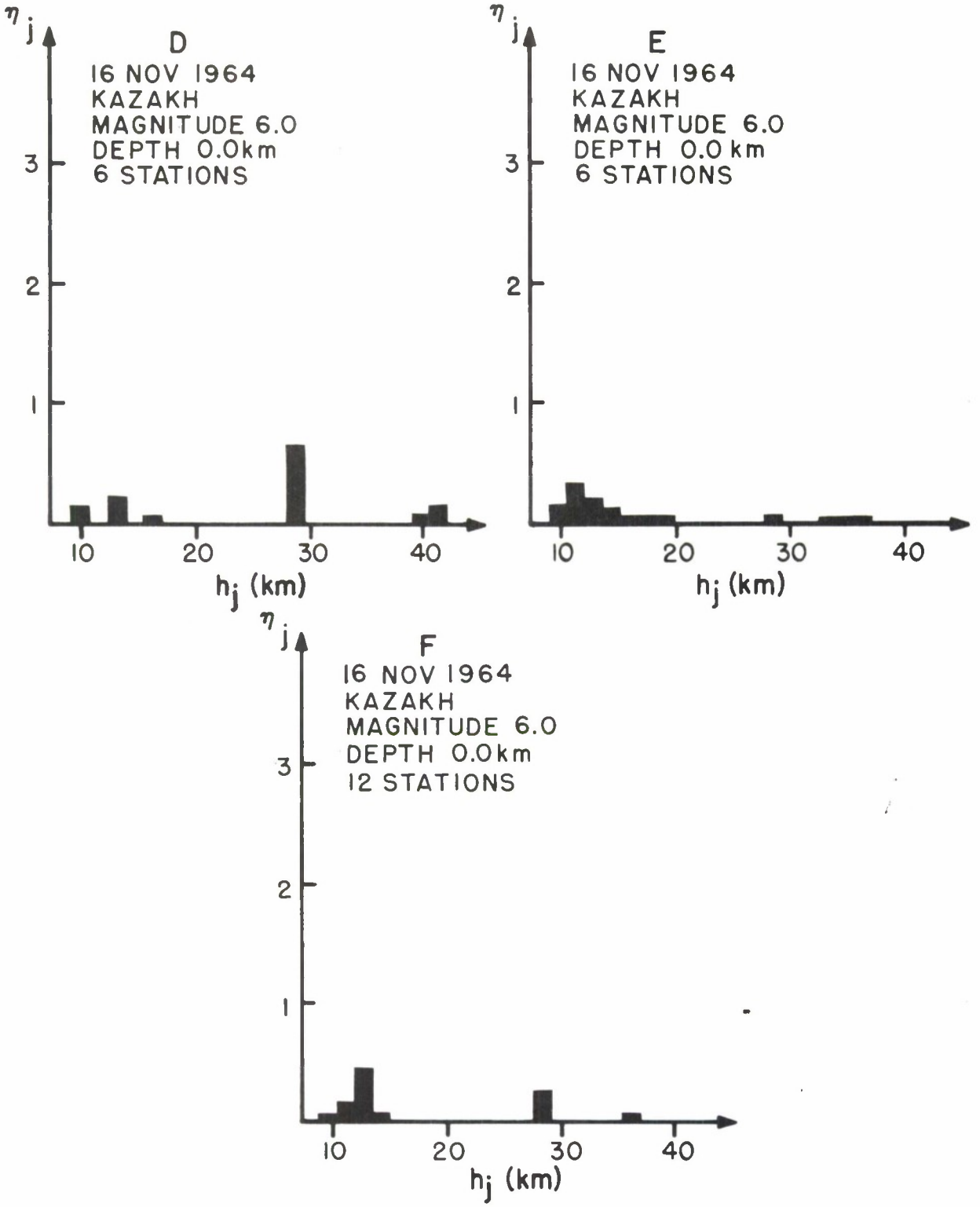


FIGURE 10.6 (D-F)
AUTOMATIC pP TEST (η_j)
DEPENDENCE ON NUMBER OF STATIONS

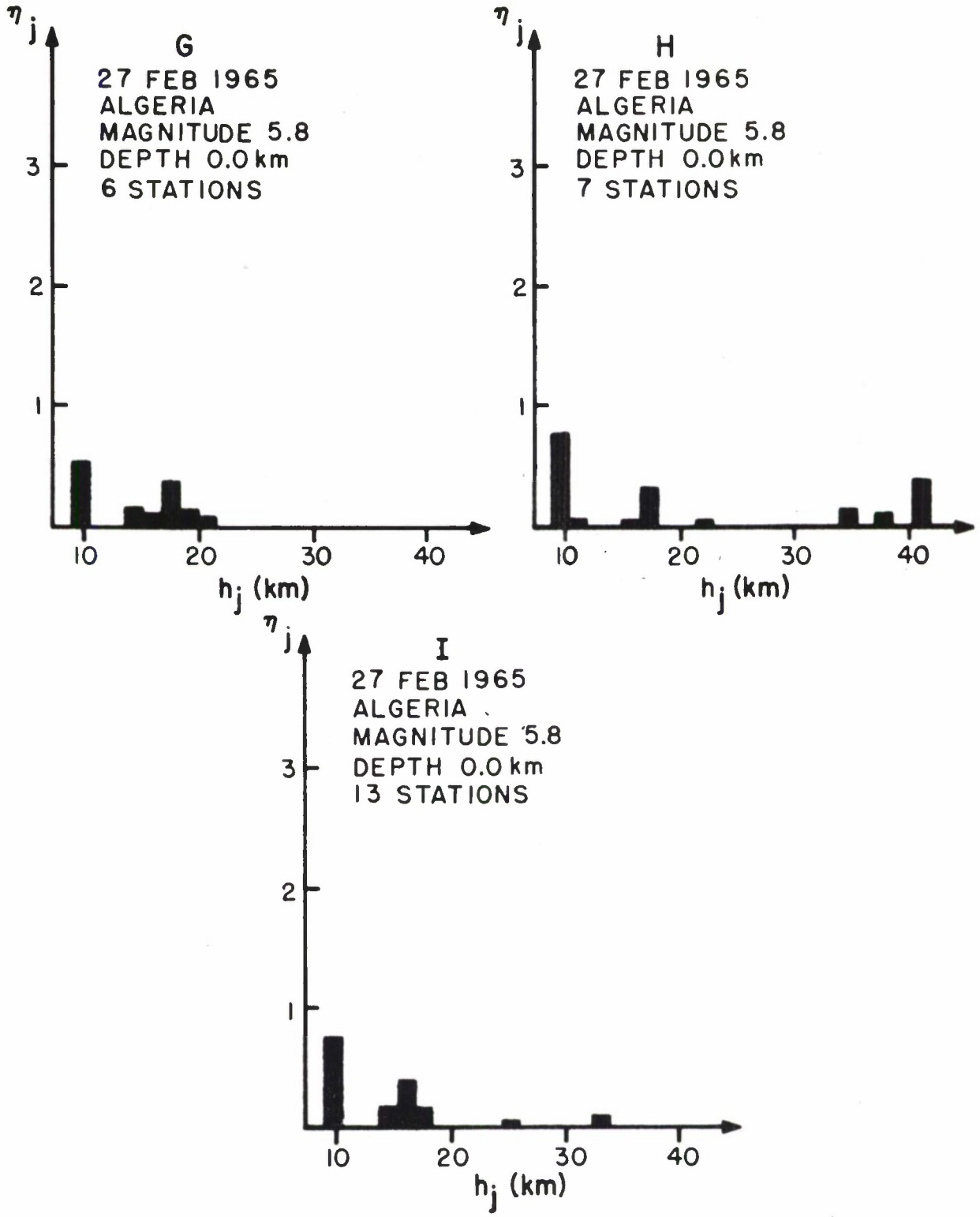


FIGURE 10.6 (G – I)
AUTOMATIC pP TEST (η_j)
DEPENDENCE ON NUMBER OF STATIONS

SECTION XI

DIMUS ARRAY PROCESSING

Many investigators have treated the case of clipped (use of zero crossing information only) processing of signals in the presence of noise. The motivation for resorting to clipped processing include: simplification of processing equipment; reduction in the amount of data which must be handled and/or stored; normalization of the noise output, i.e., the output-noise intensity is independent of the input-noise intensity. The penalties incurred by using clipped processing (when compared to the corresponding linear processing) are a loss in output signal-to-noise ratio, and a loss of signal fidelity.

Anderson of Scripps Oceanographic Institute applied the technique of clipped processing to array signal processing and coined the name DIMUS (digital, multiple steered) for the resulting array processor (15). DIMUS processing amounts to hardlimiting the output of each sensor, sampling the hardlimited signals, and feeding the sampled signals into a bank of shift registers which act as array delay elements. The outputs of the various shift register taps are combined to form a beam.

Let us define the gain G of an array as the ratio of the output signal-to-noise ratio to the input signal-to-noise ratio appearing at each array element. For a large number of array elements, and for the case of independent noise at each array element, the gain of the DIMUS array is given by

$$G = k N \qquad (11.1)$$

where N is the number of array elements, and k is a loss factor which represents the loss in signal-to-noise ratio due to hardlimiting.

A number of investigators have studied the signal-to-noise performance of hardlimiters. Typically, the analyses have been based on the assumption that the input noise is stationary and Gaussian, and that the limiter input signal-to-noise ratio is small. Various values for the loss in output signal-to-noise ratio have been developed. These loss factors range from $k = \frac{\pi}{4}$ (~ 1 dB)(16) to $k = \frac{2}{\pi}$ (~2 dB)(17). The variation is due to the particular definition chosen for output signal-to-noise ratio. For the case of large input signal-to-noise ratio the loss factor can be expected to increase over the values quoted above. In addition to signal-to-noise calculations, Remley (18) has considered the problem of loss in signal fidelity.

One other loss in processing gain found in DIMUS is the loss due to time quantization. The time quantization errors arise because of the discrete steps in time delay available in the shift registers,which act as delay elements for the array. These time quantization errors result in imperfect time alignment of the signals from the individual array elements and, hence,a loss in array gain. This loss in array gain decreases as the sampling frequency is increased. Anderson (19) shows that this loss is negligible (0.5 dB) if the sampling rate is at least five times the highest signal frequency present at the input.

11.1 DIMUS APPLICATION TO SEISMIC ARRAYS

In considering the use of DIMUS signal processing for the seismic detection of underground nuclear explosions,the problem of loss in signal fidelity becomes critical because of the necessity of providing a classification capability as well as a detection capability. Hence, a study of DIMUS processing must be undertaken from two distinct points of view: detection and classification.

Before proceeding further with a discussion of DIMUS processing itself, let us consider the potential gains that may be achieved through its use in implementing a large aperture seismic array. Most obvious is the reduction in the amount of data which must be handled and/or stored. Since in DIMUS each sample conveys one bit of information, there is available an immediate reduction of some 15 to 1 in the data handled over that necessary in the current design of the LASA-Montana system. Furthermore, if we might limit our attention to seismic frequencies below 2 Hz, the sampling rate itself could be reduced to about 10/sec, rather than the 20/sec value in use at LASA-Montana. The net result of such changes would be a data rate some thirty times less than current practice. One result of such a reduction in data rate would be the possibility of storing an entire day's output of a LASA on only four ten-inch recording tapes. Perhaps more important, for a 250-seismometer array, the total output data rate (taking each seismometer separately) would be approximatley 2.5 kilobits per second. Such a rate is clearly low enough to permit the transmission of the total raw data from such a site to a central data processing facility over a single telephone circuit in real time. As noted previously, DIMUS will result in significant simplification of the beamforming equipment. Finally, if such a drastic reduction in data rate from individual instruments proves completely satisfactory, it may be realistic to consider arrays where the seismometers need not be clustered. Rather, each instrument could be self-powered by a fuel cell or solar battery, and the instrument output relayed to the array center by means of very simple communication equipments located

at the instrument sites. So much for the potential advantages of DIMUS processing itself. As stated above, we will consider such processing from two standpoints: detection and identification.

11.2 DETECTION ASPECTS OF DIMUS BEAMFORMING FOR LASA

As stated earlier in this section, previous studies of the detection capabilities of DIMUS beamforming systems have predicted a one to two dB loss in processing gain for such systems when compared to analog systems. In analyzing the performance of the DIMUS array, the microseismic noise is assumed to be Gaussian noise which is independent from array element to array element. For this kind of noise, one would expect that the DIMUS processing would be 2 dB poorer than analog processing, given low-input signal-to-noise ratios. To test this hypothesis, a continental-size seismic array was formed using the five continental U.S. array stations and NPNT as clusters. Each of the clusters was summed without delay, and the phased sum of the cluster outputs was calculated. The event used for the experiment was a surface-focus event of low magnitude, with epicenter located in Algeria. Differential delays for the clusters were determined from another, larger, surface focus event located in the same general vicinity.

Figure 11.1 is the record from a single seismometer located in the WMO "cluster." This record is typical of those for each instrument in the large array. From this figure, it is easy to see that the criterion of low signal-to-noise ratio at each seismometer was met for this test. Figure 11.2 shows the analog sum of the seismometers for the array focused at the event under study, the sum of the hardlimited seismometer outputs, and also the same two signals after band pass filtering (0.75 to 1.5 Hz). This filter served the dual purposes of removing out of band interference and harmonic distortion introduced by the limiting process. The event in question is clearly visible on each of the two filtered traces; however, the final signal-to-noise ratio leaves something to be desired.

Since the peak outputs of both kinds of array processing have been normalized in the traces shown, it was easy to compute the rms value of the noise for both array outputs immediately preceding the arrival of the event. The ratio of clipped noise to unclipped noise was found to be 2.1 or about the expected loss in DIMUS processing. While the length of the noise record available for analysis on each of these records was small (approximately 15 sec), and only one experiment was performed, the results agree so well with theoretical expectations that one may assume that the theoretical predictions of DIMUS detection performance can be used directly for the seismic case.

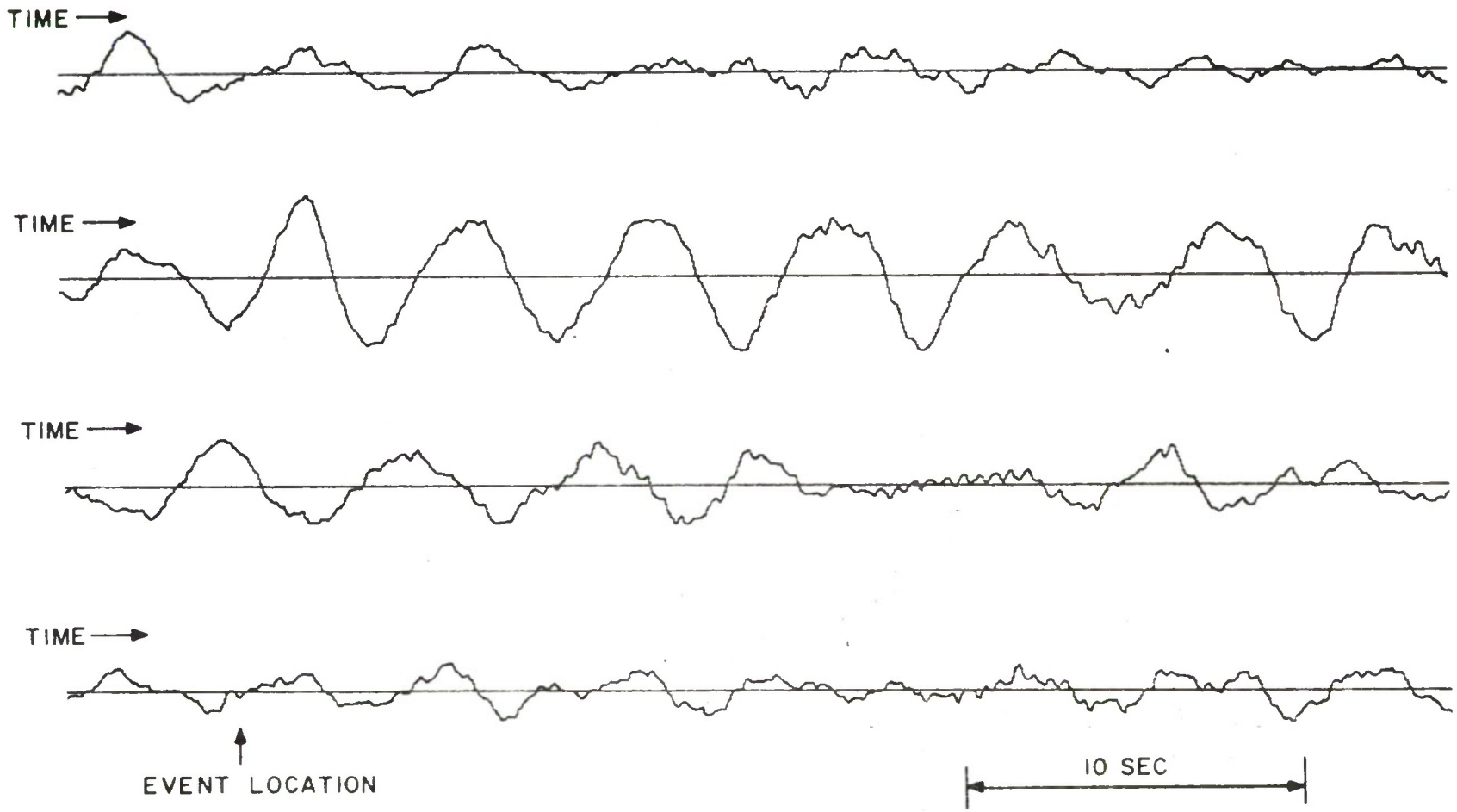


FIGURE II.1
ALGERIAN EVENT – SINGLE SEISMOMETER WMO

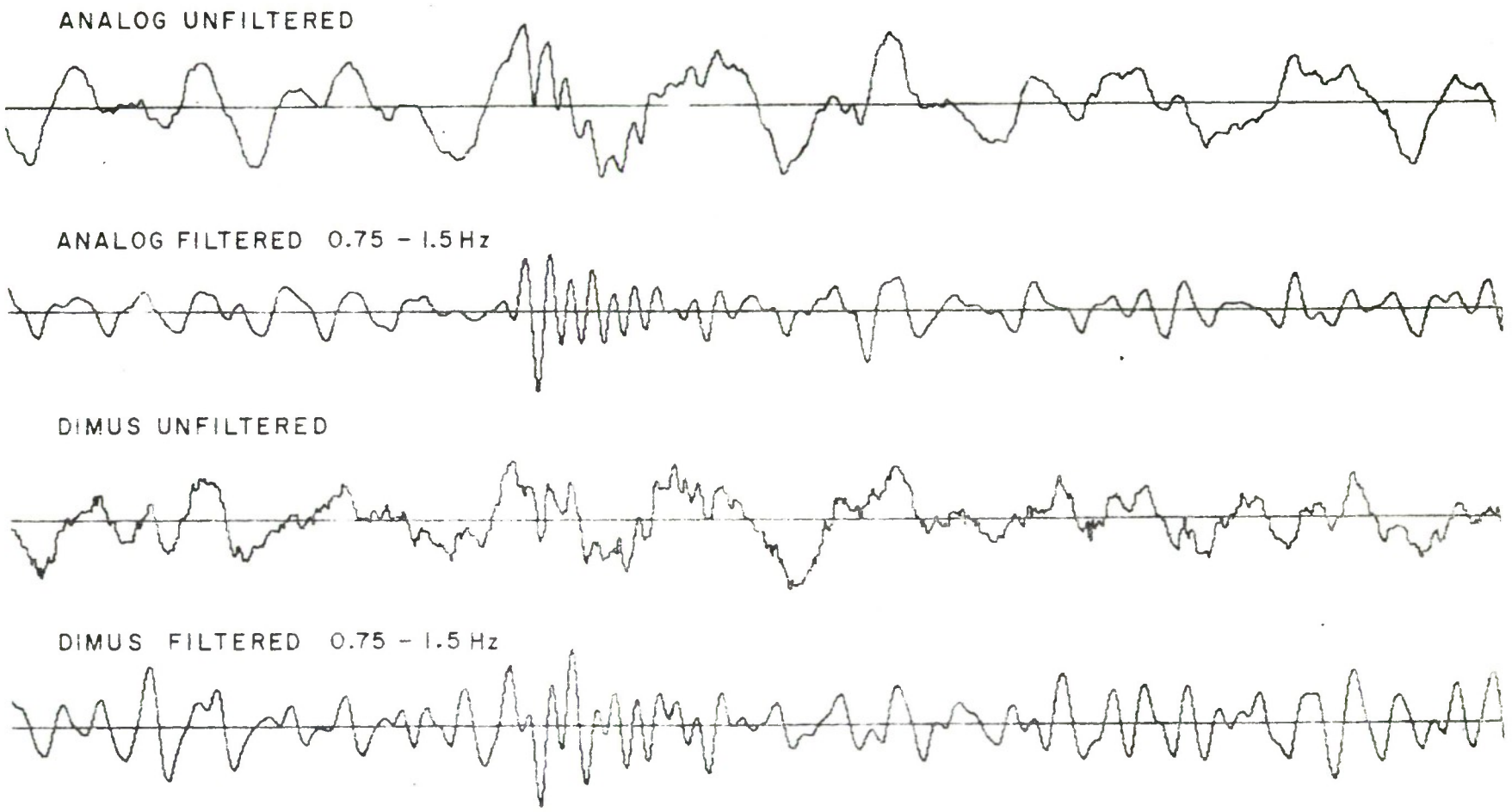


FIGURE II.2
ANALOG AND DIMUS BEAMS

Before leaving the detection aspects of the DIMUS, it is interesting to note that such beamformers make possible CFAR (constant false alarm rate) automatic detectors without the usual problems of automatic gain-controlled amplifiers. To see why this is the case, first consider that the noise input to each of the seismometers is independent and has zero mean. Then, the sum of N hard-limited instrument outputs will range from -N to +N and possesses a binomial probability distribution with zero mean - no matter what the strength of the noise at each of the seismometers. This is the noise normalization property referred to earlier. It is easy to see, then, that a constant threshold set at the array output will give a constant and predictable false alarm rate.

To determine the probability of detection for such a system, first consider a constant signal at the input to each seismometer. Then,in the absence of noise, all of the hard-limiters following the seismometers would have the same polarity, and the magnitude of the output of the summer of the system would be exactly N. When sufficient noise is present at the inputs to the seismometers, not all of the hard-limited outputs will be of the same polarity. Here the magnitude of the output of the array summer can take values less than N, the exact value being a function of the signal-to-noise ratio at the inputs to the individual seismometers.

Figure 11.3 illustrates how it is possible to determine the probability distribution of the magnitude of the summed output as a function of the input signal-to-noise ratio. The figure shows the probability density of signal plus noise at the input to a single sensor as a normal distribution with mean value E_s, where E_s is the signal voltage. This results from the assumption that the noise is normally distributed with zero mean. From the figure, it is easy to see that the probability that noise will cause the limiter output to be of different polarity than would be true in the noiseless case is simply the area of the probability density for negative values of the variable. Thus, given the input signal-to-noise ratio at the individual seismometers, it is possible to compute the probability of noise producing an incorrect polarity for a single seismometer output. One can,in fact,compute what this signal-to-noise ratio must be for a given probability that no more than m of the N outputs will be so reversed. If the threshold is set at a value N-m, this probability will be the probability of detection. Figure 11.4 gives several illustrations of the detection performance (probability of detection versus input signal-to-noise ratio for a given false alarm rate) for a DIMUS CFAR detector. The illustrations are for a 21 element array and a 49 element array; the first is chosen to illustrate what LASA performance would be if hard-limiting takes place after analog summation of the individual seismometers of the clusters. Typically the array parameters would be chosen to provide a false alarm probability on the

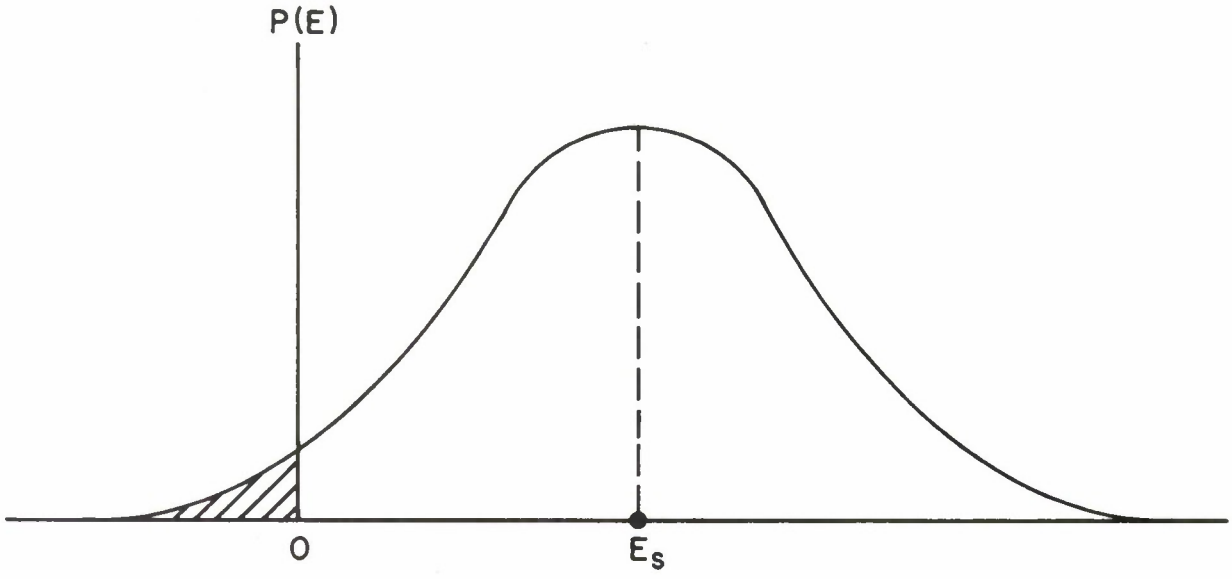


FIGURE 11.3
PROBABILITY DENSITY FOR SIGNAL PLUS NOISE

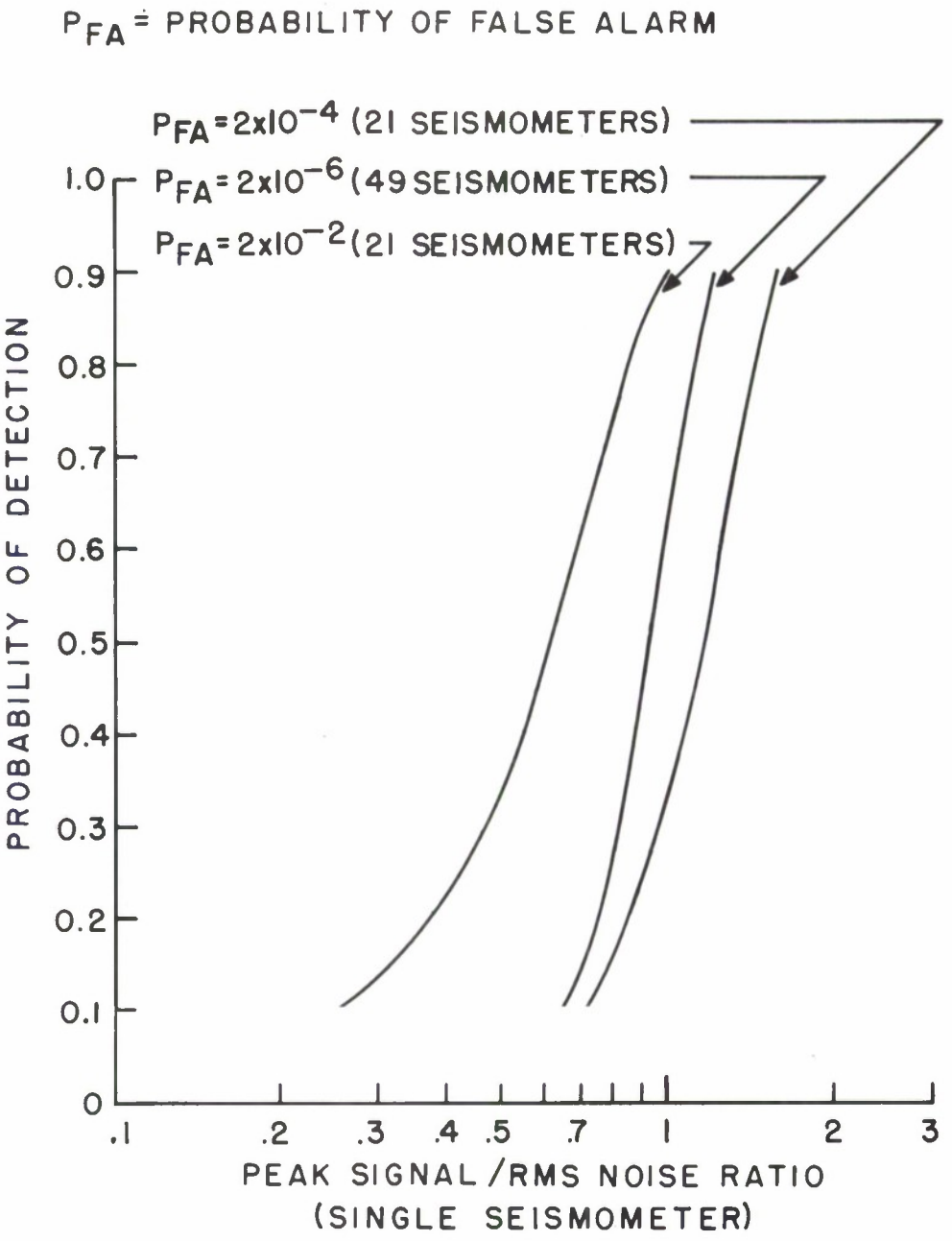


FIGURE 11.4
REPRESENTATIVE DIMUS DETECTION CAPABILITY

order of 10^{-6} and a detection probability on the order of 0.9 for the minimum signal. For example, for a single seismometer signal-to-noise ratio of unity, about 70 seismometers would be required in the DIMUS array to provide the above levels of performance.

11.3 IDENTIFICATION WITH A DIMUS ARRAY PROCESSOR

As stated at the beginning of this section, the DIMUS beamformer is inherently a nonlinear device. A recent paper by Remley (20), presents the first derivation of the transfer function for such a processor. This transfer function is given in Figure 11.5, where the average output signal voltage is as a function of the input signal voltage at each limiter. As can be seen from the figure, when the signal-to-noise ratio is on the order of unity or less, the output signal waveform is expected to be linearly related to the input waveform. Where the number of elements in the array is large, not only will the output signal be a faithful representation of the input signal, but the output signal-to-noise ratio may also be large, even for low input signal-to-noise ratios. Here, the DIMUS output may be used exactly as the analog output is in the determination of the source of the seismic signals. Of course, the output signal-to-noise ratio for the DIMUS will be approximately 2 dB less than that for the corresponding conventional array; however, only minor distortion of the waveshape will have been introduced by the nonlinear processing.

When the input signal-to-noise ratio is high, however, considerable distortion of the seismic waveform may take place. To discover the magnitude of such effects, the records of some 13 teleseismic events (both earthquakes and underground explosions) were processed with both conventional and DIMUS techniques. At least 10 widely spaced seismometers were used to form beams focused at each event. The signal-to-noise ratio was high in all cases. Thus the differential time delays could be picked by eye from the individual seismograms. The fidelity measure chosen to determine the similarity between the analog and DIMUS outputs was the zero offset correlation coefficient for the P-coda signals of these events. That is, the corresponding signals in the P-coda region of the analog channel and the DIMUS output are multiplied and integrated over the P-coda interval and the result is normalized by dividing by the square root of the product of the energies of the two signals. The resulting coefficient is thus always less than or equal to one. Here P-coda was taken to be that portion of the seismogram from three to thirteen seconds following the onset of the P-phase. The choice of this fidelity measure was based on the hypothesis that the identification of source mechanism would be based mainly on the waveforms found in this time interval of the seis-

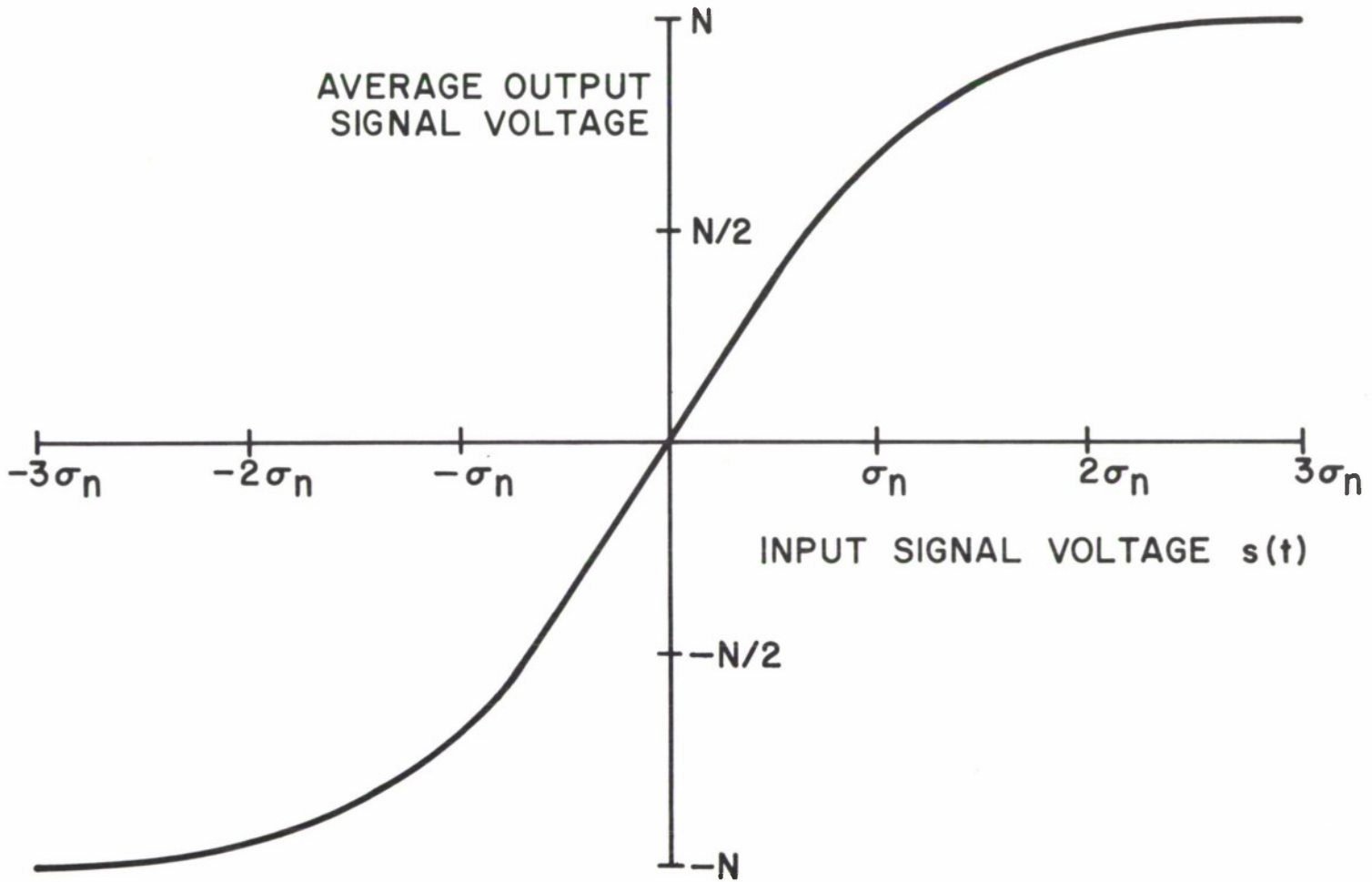


FIGURE 11.5
STATISTICAL EQUIVALENT OF DIMUS FOR GAUSSIAN NOISE WITH RMS VALUE σ_n

mogram, although it was recognized that most complexity criteria employed to date required a measurement of the ratio of main P energy to energy in specific portions of the P-coda. Undoubtedly this choice of fidelity measure was strongly affected by the interesting results of study of the P-coda correlation coefficient as a discriminant (see Section IX).

Results of these computations were much as expected. P-coda was emphasized with respect to main P, and the general noise level increased. These two effects are illustrated by Figure 11.6, which shows the filtered (0.75 to 1.50 Hz) analog and DIMUS beam outputs (14 seismometers) for a typical earthquake. What is somewhat unexpected is the remarkable similarity of the coda waveforms for the two signals. In fact, the coda correlation coefficient is 0.96. Of the 13 events studied, this coda correlation coefficient ranged from 0.97 to 0.59, with only two events showing correlation coefficients lower than 0.76. With this high correlation, it is hypothesized that the coda correlation discriminant discussed in Section IX could be satisfactorily employed with conventional DIMUS processing. There are, however, a number of ways by which the nonlinear transfer function of the conventional DIMUS may be linearized.

To date, one test of the simplest modification of DIMUS processing has been made. Recognizing that only events with large singal-to-noise ratios will be distorted by the conventional DIMUS, it was hypothesized that the output of a single seismometer of the array should be a good estimate of the desired output signal - particularly for the largest portions of the record. Thus, in addition to the hard-limited outputs of the individual seismometers, one analog channel is used to estimate the output of a conventional analog array. The modified array output is then computed in the following manner. At the first point in time that all hard-limited signals possess the same polarity (presumably that time for which the input signal entered the region of severe distortion in the transfer function), the corresponding value of the single analog channel is noted. Let the analog channel output at this time be called V_L. The analog channel is then adjusted so that its value at the noted point is equal to the number of seismometers making up the array (21 for the case studied). The remaining portion of the analog output is scaled by a factor $21/V_L$. Now, the value of the DIMUS output is retained as long as it has a value of 20 or less. However, when its value reaches 21 its value is replaced by the corresponding value of the scaled analog channel.

Results of this simple "fix" are illustrated in Figure 11.7. Shown in the figure are the analog beam output, the modified DIMUS beam output, and the conventional DIMUS beam output. In each case, the outputs have been passed through a bandpass filter centered at 1.125 Hz. The filter bandwidth is approximately 1.25 Hz. From the figure, it is easy to see that this simple "fix" (combined with bandpass filtering) has eliminated nearly all of the distortion introduced by conventional DIMUS processing. Some minor distortion still exists for the main P arrival and the first second of the coda; however, the

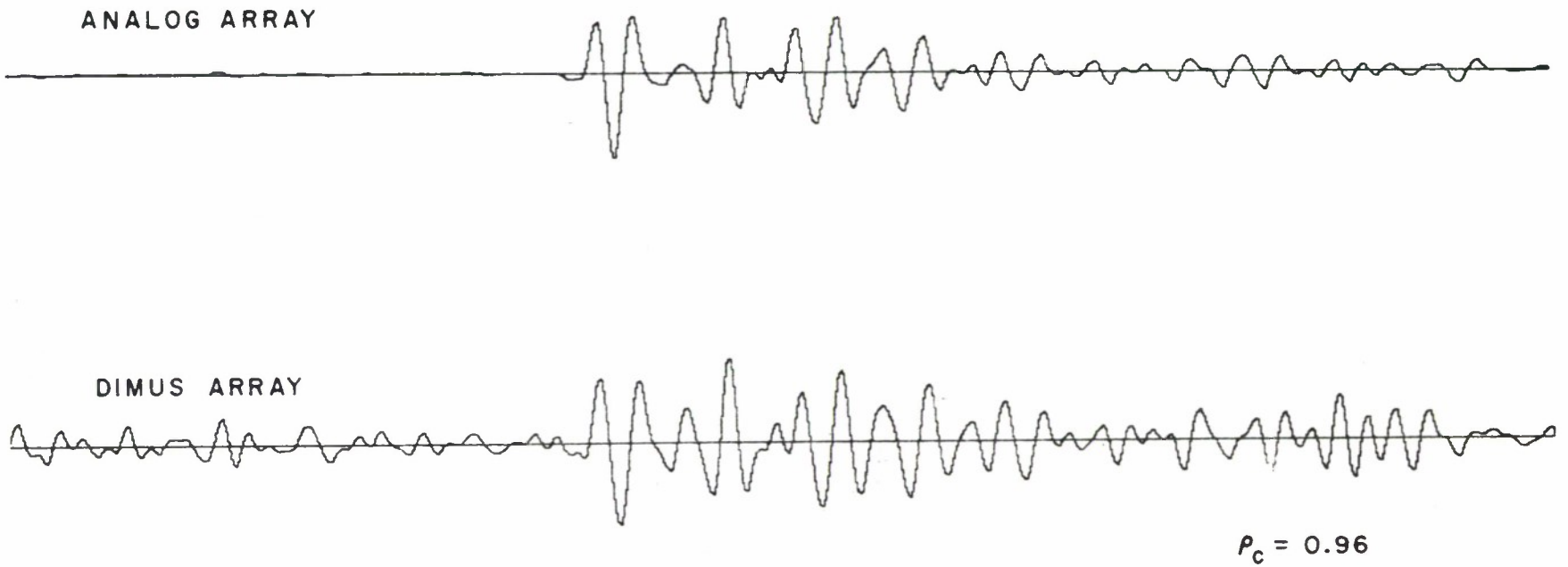


FIGURE 11.6
COMPARISON OF ANALOG AND DIMUS PROCESSING

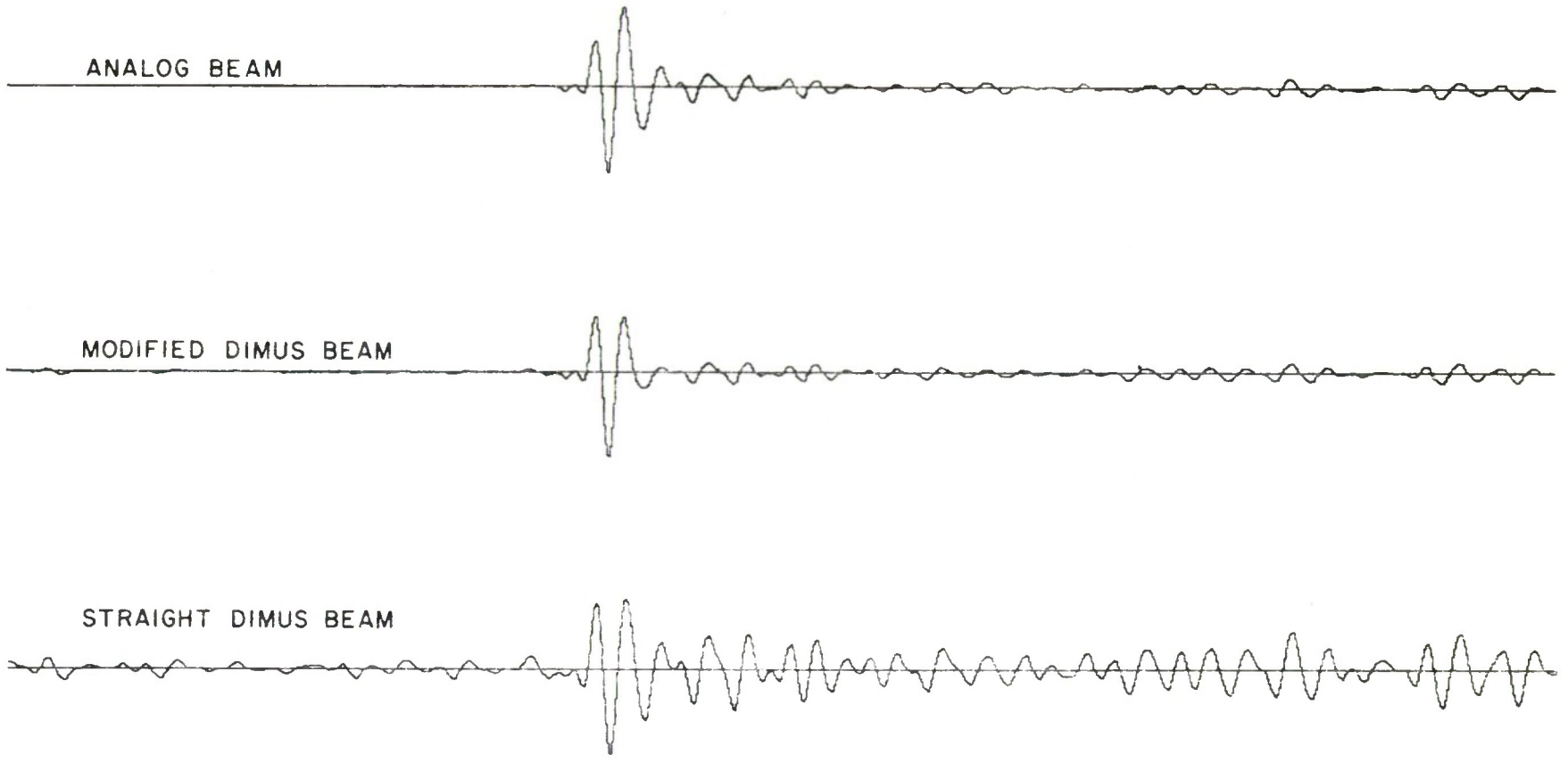


FIGURE II.7
COMPARISON OF BEAM PROCESSING TECHNIQUES

remaining portion of the modified array output is as nearly identical with the corresponding portion of the analog processor as could be desired. In addition, it can be seen from the figure that the level of the noise in the modified record is reduced over that for the conventional DIMUS. This is to be expected, as it will be the ratio of low energy coda to noise which is expected to remain unchanged by this processing technique. As a result, when the coda level is reduced to its proper relationship with respect to main P, the noise should also shrink with respect to P. Other, more sophisticated modifications of the DIMUS technique are currently under study with a view toward correcting the distortion in the first three seconds noted above. Even without such further modifications, the work to date suggests that the inclusion of a single analog channel with a DIMUS processor may be able to provide all of the information possible with an analog array, and it can do so with far greater simplicity.

11.4 SUMMARY AND CONCLUSIONS

The analyses of DIMUS processing performed thus far may only be regarded as a first step at studying this problem. The motivation for studying DIMUS processing is the potential savings in system data rate and equipment complexity. DIMUS processing results in a loss in system signal-to-noise ratio, and distortion in the output waveform. Loss in signal-to-noise ratio affects detection performance and is most important for the case of low signal-to-noise ratios at the array seismometer imputs. It has been concluded that the detection performance of a LASA (which employs DIMUS processing) will be negligibly affected under such low signal-to-noise ratio conditions. Specifically, DIMUS will result in less than a 2 dB loss in signal-to-noise ratio at the output of the array.

Any distortions of the output seismic waveform which are introduced by DIMUS processing could severely limit the ability of a LASA-DIMUS to discriminate between an underground nuclear explosion and an earthquake. It has been shown that on the average the output of the DIMUS array will be linearly related to the input signal under conditions of low seismometer input signal-to-noise ratio. For large signal-to-noise ratios the DIMUS signal output will be severely distorted.

Nonlinear distortion caused by DIMUS has only been studied thus far in a very qualitative manner. For a selected seismic waveform both DIMUS processing and analog array processing were simulated (under conditions of high signal-to-noise ratio) for a 21 element array. The resulting array outputs

were compared and certain evident distortions were noted. An ad hoc modification of DIMUS processing (see Section 11.3) was examined as a means of reducing the observed distortion. For the case considered, the DIMUS modification appeared to reduce the distortion.

Such qualitative observations of distortion do not provide detailed results concerning the effect of DIMUS processing on discrimination capabilities. In order to perform such a detailed analysis it is necessary to consider the specific discriminant rules (which will be used to effect a classification of an unknown seismic event) and the effect of DIMUS distortion on each of the discriminants. Such an approach may yield an appropriate criterion for evaluating the effect of DIMUS distortion on the ability of the system to classify seismic events.

SECTION XII

SPECTRAL ESTIMATES OF SEISMIC EVENTS

It has been suggested that earthquakes and underground nuclear tests may result in seismograms that differ significantly in their spectral energy content. If this is the case, the analysis of the spectral distribution of energy might provide useful statistics for discriminating between these two kinds of events. More specifically, it has been suggested that the impulsive nature of nuclear explosions might lead to more "high frequencies" than would occur with earthquakes. "High frequencies" in this context might be considered as any significant energy at frequencies above 2 or 3 Hz. If,in fact,high frequencies are present in these seismograms,it would be despite the characteristics of the propagation medium and the recording system (specifically, the aliasing filter), since the attenuation of both becomes especially severe with increasing frequency. It should be noted, however, that if the noise is teleseismic in origin,it also would be affected by both sources of attenuation, so that the real signal-to-noise ratio problem would be caused by local seismic noise and the noise internal to the recording system. In this section the theoretical problem of estimating the energy density spectrum of a transient from a record consisting of that transient plus additive noise is considered. Data from five seismic events are presented and analyzed in ways suggested by the theoretical discussion. From these data it does appear that high frequencies are present in many seismograms but it is too early to tell whether or not there are characteristic differences between the spectra resulting from earthquakes and nuclear tests that might be useful for discrimination purposes.

The organization of this section is as follows. First, the theoretical problem of estimating the energy density spectrum of a transient in noise is discussed. Two general considerations are important in analyzing this problem: 1) What is the variability in the spectral estimate that results from the noise? (This will depend, among other things, on the shapes and relative magnitudes of the power density spectrum of the noise and the spectrum of the signal); and 2) What is the distortion in the spectral estimate? (For example, loss of frequency resolution that results from efforts to reduce this variability.) Following this theoretical discussion,a brief description of the details of the computer implementation of these calculations is presented, in order to illustrate the dependence of the spectral estimate on the length and shape of the time window and also the effect of high-pass filtering the seismic records before performing these calculations. Several sample calculations on the same seismic event are next presented. Following these sample calculations,a single spectral calculation is presented for each of fifteen seismic records. These records consist of the outputs of three

seismometers (center elements of LASA clusters A0, B1 and F4) for each of three surface-focus events and two earthquakes. These data indicate a definite high-frequency content for all but one of the surface-focus event calculations and some of the earthquake calculations. Following this presentation of spectral calculations, the assumptions used in the analysis of these data and the potential sources of errors in carrying out these calculations are summarized. Finally, conclusions are presented together with recommendations for continued work on this project.

12.1 THEORETICAL ANALYSIS

For the purposes of this analysis it is assumed that the seismic record consists of the desired transient plus stationary Gaussian noise. It is further assumed that the onset time of the transient is fairly clear and that the appropriate duration (for these calculations) is on the order of a few seconds. The stationarity of the noise is necessary in applications so that the power density spectrum of the noise may be reliably estimated from a long record of the noise preceding the transient. The statistics of the spectral estimate of the transient will, of course, depend in part on this power density spectrum. With these assumptions stated, the remaining problem is how best to estimate the energy density spectrum of the transient. As was suggested above, there will be two kinds of considerations in analyzing this problem. One is the variability in the spectral estimate that results from the noise, and the other is the distortion in the spectral estimate that results from efforts to reduce this variability. There is a considerable literature relating to the problem of estimating the power density spectrum of a stationary random process. Probably the most cited reference is that of Blackman and Tukey (21), which first appeared in 1958. This book provides a rather thorough discussion of the problem, with an emphasis on applications, and it has served as almost a handbook for many people. The problem considered in this section differs fundamentally from the one considered by Blackman and Tukey. While their methods remain relevant, they are not directly applicable, as will be demonstrated shortly.

There are a few obvious guesses for possible ways to estimate the energy density spectrum. One way would be to apply the Blackman and Tukey calculation to the portion of the record containing the transient. As will be discussed below, this does not appear to be a very satisfactory procedure. Another possibility would be simply to calculate the magnitude-squared of the Fourier transform of the portion of the record containing the transient. The statistics of a slight generalization of this calculation will be discussed in some detail. Still another possibility would be to pass the record through a bank of narrow-band filters and examine the envelopes of the outputs at the appropriate time. It is easy to show that this can be equivalent to the generalized Fourier transform operation that will be analyzed, and, for digital computer applications, at least, it is less flexible. (This might not be the case if the location of the transient were not at least approximately known.)

12.1.1 Definitions

Let the available record be given as $x(t)+n(t)$, where $n(t)$ is a stationary Gaussian process with power density spectrum (double-sided) $S_n(f)$, and $x(t)$ is the transient of interest. Let $a(t)$ be the "time window" (the choice of which will be discussed momentarily). Then, defining

$$z(t) = a(t)[x(t)+n(t)] \tag{12.1}$$

$$Z(f) = \int_{-\infty}^{\infty} z(t)e^{-j2\pi ft}\, dt \tag{12.2}$$

The function of interest is $|Z(f)|^2$. For convenience, let

$$Z(f) = Z_x(f) + Z_n(f) \tag{12.3}$$

where the transforms correspond to the obvious time functions. Then, using ⊛ to denote convolution,

$$Z_x(f) = A(f) \circledast X(f) \tag{12.4}$$

12.1.2 The Time Window

Perhaps the simplest choice of a time window would be a rectangular pulse that is a constant in the interval thought to contain the signal and zero elsewhere. However, there are at least two reasons for a more rounded choice; one of these reasons is illustrated by the two examples in Figure 12.1. The second time window (sometimes called the Hanning window) has the same duration as the rectangular window, but the sidelobes of its transform are considerably smaller, and its main lobe is somewhat wider. In general, the second time window would be expected to introduce less distortion in the convolution operation of Equation 12.4. (There is at least one special case where this would not be the case: the case where the transient is strictly time-limited and completely contained within the time window.) The other reason for a rounded window is roughly stated as follows. In the analysis of seismic records, the duration of the transient is somewhat uncertain. Presumably $a(t)$ should be "turned off" when $x(t)$ becomes small compared to the noise. Not knowing exactly when that is, a reasonable compromise is to turn it off gradually.

In the equations that follow it will be useful to have an approximate value for the width of $A(f)$ in terms of the duration of $a(t)$. For this it will be assumed that

$$A(f) = 0 \qquad |f| > 1/T \tag{12.5}$$

where T is the duration of $a(t)$. Of course, this cannot hold exactly, but Figure 12.1 gives some indication of the degree of approximation involved.

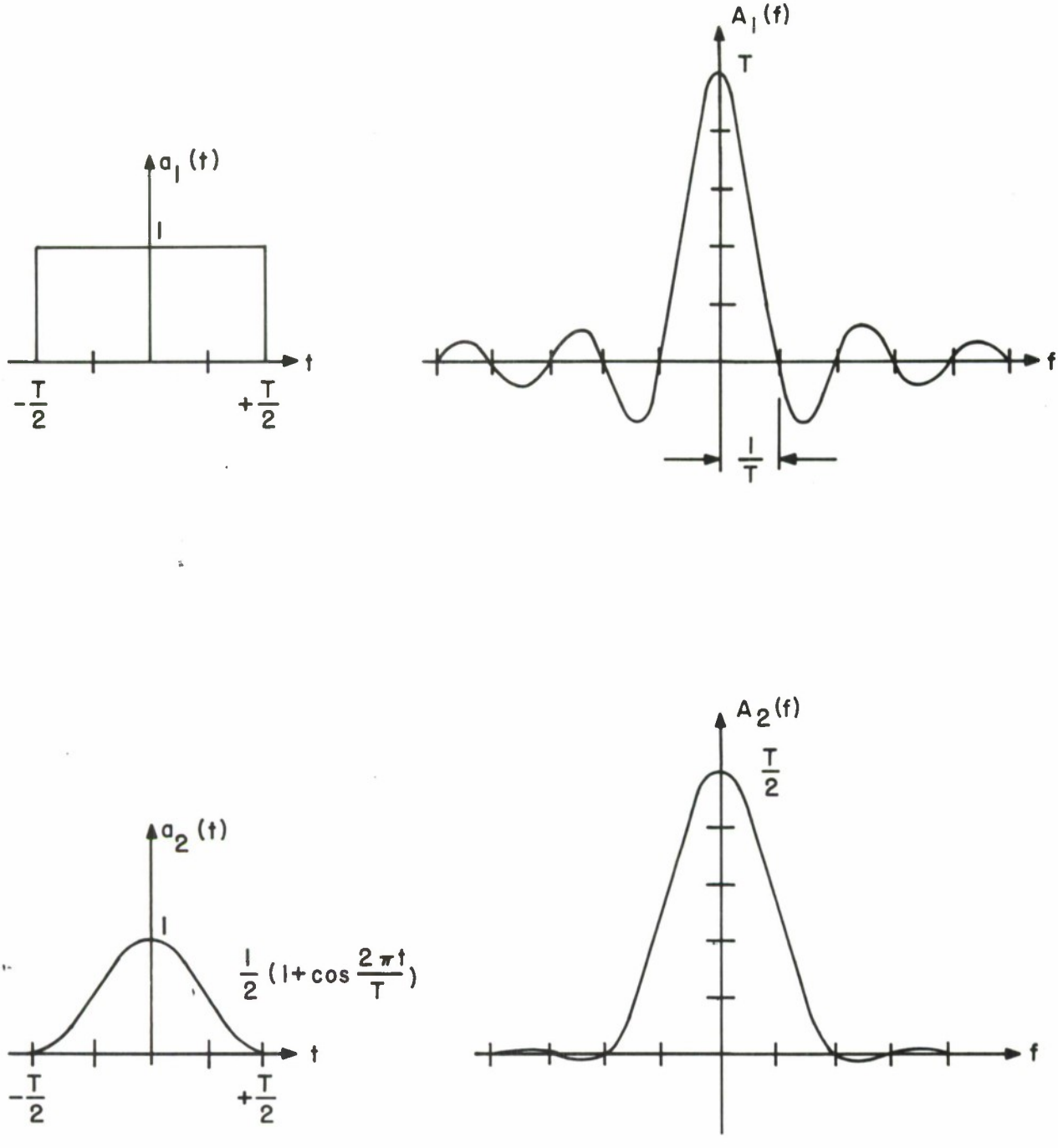


FIGURE 12.1
EXAMPLES OF TWO TIME WINDOWS AND THEIR TRANSFORMS

12.1.3 Noise Alone Case

In analyzing the statistics of $|Z(f)|^2$, it is convenient to analyze first those of $|Z_n(f)|^2$, or, equivalently, to assume that x(t) is zero. Considering this "noise-alone" case yields

$$|Z_n(f)|^2 = \int d\alpha \int d\beta \; a(\alpha)a(\beta)n(\alpha)n(\beta)e^{-j2\pi f(\alpha-\beta)} \quad (12.6)$$

which, taking expectations, interchanging orders of integration and expectation, and recognizing convolutions in one domain as products in the other, leads to

$$\overline{|Z_n(f)|^2} = S_n(f) \circledast |A(f)|^2 \quad (12.7)$$

Thus the expected value of $|Z_n(f)|^2$ is a "smoothed" version of the true power density spectrum, $S_n(f)$, where the smoothing is accomplished by a convolution in the frequency domain. (Clearly if $S_n(f)$ changes slowly relative to 2/T, the expected value of $|Z_n(f)|^2$ will have essentially the same shape as $S_n(f)$.)

Similar calculations, which employ the convenient property of zero-mean Gaussian variates,

$$\overline{n(t)n(\tau)n(\alpha)n(\beta)} = \overline{n(t)n(\tau)}\;\overline{n(\alpha)n(\beta)} + \overline{n(t)n(\alpha)}\;\overline{n(\tau)n(\beta)} + \overline{n(t)n(\beta)}\;\overline{n(\tau)n(\alpha)} \quad (12.8)$$

lead to

$$\mathrm{cov}[|Z_n(f_1)|^2, |Z_n(f_2)|^2] = \left|\int du S_n(u)A^*(u-f_1)A(u+f_2)\right|^2 + \left|\int du S_n(u)A^*(u-f_1)A(u-f_2)\right|^2 \quad (12.9)$$

which specializes to

$$\mathrm{var}|Z_n(f)|^2 = \underbrace{\left|\int du S_n(u)|A(u-f)\right|^2}_{\overline{|Z_n(f)|^2}}\Bigg|^2 + \left|\int du S_n(u)A(u+f)A^*(u-f)\right|^2 \quad (12.10)$$

This last equation is a generalization of the standard periodogram result (see, e.g., reference 22), which may be obtained from the above by choosing

$$a(t) = 1/\sqrt{T} \qquad 0 < t < T \quad (12.11)$$

$$= 0 \qquad \text{elsewhere}$$

The important observation from Equation 12.10 is that, no matter what a(t) is chosen,

$$\mathrm{var}[|Z_n(f)|^2] \geq (E[|Z_n(f)|^2])^2 \quad (12.12)$$

In particular, using longer and longer observation times would never reduce the variance to less than the square of the mean. Clearly, this calculation by itself would not be a very satisfactory way of estimating the power density spectrum (PDS) of a stationary random process. To see how this calculation could lead to a good PDS estimate, it is useful to resort to the approximation suggested earlier for the width of A(f). If Equation 12.5 were true, then Equations 12.9 and 12.10 could be simplified to state that

$$\overline{|Z_n(f_1)|^2 |Z_n(f_2)|^2} = \overline{|Z_n(f_1)|^2}\ \overline{|Z_n(f_2)|^2}$$

$$\text{for } ||f_1|-|f_2|| > 2/T \qquad (12.13)$$

$$\text{var}[|Z_n(f)|^2] = (E[|Z_n(f)|^2])^2 \qquad \text{for } |f| > 1/T \qquad (12.14)$$

The fact that the values of $|Z_n(f)|^2$ separated by more than 2/T in frequency are uncorrelated provides the means of achieving statistically satisfactory estimates of the PDS of a stationary random process. To illustrate, suppose that $S_n(f)$ varies only slightly over frequency intervals of several times 2/T. Then the samples $|Z_n(2K/T)|^2$ would have the same expectation for several consecutive values of K, and a local average would be an appropriate estimate of this expectation. Since successive values of $|Z_n(2K/T)|^2$ are approximately uncorrelated, the local average would be statistically superior to any of the individual samples. A convenient measure of the variability of a single statistic is the "coefficient of variation," which is defined as the ratio of the standard deviation to the mean. It is easy to show that adding together M uncorrelated random variables with identical means and variances results in a new random variable with a coefficient of variation that is $1/\sqrt{M}$ times that of the original variables.

To summarize, for K>0, $|Z_n(2K/T)|^2$ has a coefficient of variation of unity. If T is large enough that $S_n(f)$ is essentially constant over frequency regions of length 2M/2T, then the local averages taken over M of the samples $|Z_n(2K/T)|^2$ will yield spectral estimates with coefficients of variation equal to $1/\sqrt{M}$. The calculation just described -- smoothing of the magnitude squared of the Fourier transform -- could be a perfectly satisfactory method of estimating the PDS of a stationary random process, provided it were possible to choose T large enough to achieve a low coefficient of variation for the spectral estimates. This method is essentially equivalent to the "indirect" method of Blackman and Tukey, as will be discussed below. A more careful and thorough discussion may, of course, be found in Blackman and Tukey (23).

An operation similar to that of adding M adjacent values of $|Z_n(2K/T)|^2$ would be convolving $|Z_n(f)|^2$ with Q(f), where Q(f) is a pulse of width 2M/T located at the origin of the frequency

domain. Because this operation does in a sense combine M uncorrelated samples, one would expect it to result in a coefficient of variation of roughly $1/\sqrt{M}$. Defining the result of this further smoothing as P(f) yields

$$P(f) = |Z_n(f)|^2 \circledast Q(f) \tag{12.15}$$

and, therefore,

$$\begin{aligned} \overline{P(f)} &= \overline{|Z_n(f)|^2} \circledast Q(f) \\ &= S_n(f) \circledast |A(f)|^2 \circledast Q(f) \\ &\approx c\, S_n(f) \circledast Q(f) \end{aligned} \tag{12.16}$$

where the last approximate equality is based on $|A(f)|^2$ being narrow compared to Q(f), which will be the case if Q(f) is sufficiently wide compared to 2/T that a low coefficient of variation results. P(f) is sometimes called a "smoothed periodogram."

This smoothed periodogram calculation can be made equivalent to the standard "indirect method" of Blackman and Tukey. The "indirect method" consists of three steps: 1) estimate the autocorrelation function of the noise, $\phi_n(\tau)$; 2) multiply this estimate by a "lag window," $q(\tau)$; 3) calculate the Fourier transform of the result.

Defining

$$\begin{aligned} \phi_n(\tau) &= \frac{1}{T}\int_0^{T-|\tau|} n(t)n(t+|\tau|)\, dt && |\tau| < T \\ &= 0 && |\tau| > T \end{aligned} \tag{12.17}$$

$$\begin{aligned} a(t) &= 1/\sqrt{T} && 0 < t < T \\ &= 0 && \text{elsewhere} \end{aligned}$$

leads to

$$\Phi_n(f) = |Z_n(f)|^2 \tag{12.18}$$

and

$$P(f) = \int_{-\infty}^{\infty} d\tau e^{-j2\pi f\tau}\, q(\tau)\phi_n(\tau) = |Z_n(f)|^2 \circledast Q(f) \tag{12.19}$$

where $q(\tau)$ and Q(f) are Fourier transforms of each other. Earlier, it was observed that the coefficients of variation of P(f) were proportional to the square root of the ratio of the widths of A(f) and Q(f). It can now be observed that this ratio is proportional to the ratio of the widths of $q(\tau)$ and a(t). Typically $q(\tau)$ is an even function of τ that is zero for τ larger in

magnitude than the "maximum lag." As an example of representative parameter values for the application of the indirect method of PDS estimation, a maximum lag of about T/10 would be used to achieve an rms fluctuation of one-third of the mean value. At the time the Blackman and Tukey paper appeared, the indirect route was the most efficient for use on a digital computer. Since the development of the Cooley-Tukey algorithm for computing Fourier series (24), however, the frequency domain calculations have become very much faster, and it is now usually fastest to compute power spectra by the more direct route leading to the smoothed periodogram.

12.1.4 Signal Plus Noise Case

Returning now to the original problem, which included both signal and noise, and still assuming the noise is Gaussian, it can be shown that, as before, the estimates are uncorrelated for frequencies separated by more than the width of A(f), and that the following equations describe the mean and variance of the spectral estimates.

$$\overline{|Z(f)|^2} = |Z_x(f)|^2 + \overline{|Z_n(f)|^2} \tag{12.20}$$

$$\begin{aligned}\mathrm{var}[|Z(f)|^2] = {} & \mathrm{var}[|Z_n(f)|^2] + 2|Z_x(f)|^2\ \overline{|Z_n(f)|^2} \\ & + 2\mathrm{Re}Z_x^{\,2}(f) \int du S_n(u)A^*(u+f)A(u-f)\end{aligned} \tag{12.21}$$

Expressions for the mean and variance of $|Z_n(f)|^2$ were given in Equations 12.7 and 12.10. Equation 12.20 states that the expected value of the spectral estimate is equal to the sum of the signal and noise contributions. The expression for the variance (Equation 12.21), however, involves not only the contributions from the noise, but also the interaction terms. Continuing the assumption that A(f) has a width of 2/T (Equation 12.5) implies that the last term of Equation 12.21 is zero for $|f| > 1/T$. For f=0 the last two terms of Equation 12.21 are equal.

To summarize these results, it is convenient to concentrate on the samples of the spectral estimates spaced at intervals of 2/T. Defining

$$y_K = |Z(\tfrac{2K}{T})|^2 \tag{12.22}$$

The above results may be summarized as follows:

$$\overline{y_K} = |Z_x(2K/T)|^2 + \overline{|Z_n(2K/T)|^2} \tag{12.23}$$

$$\mathrm{cov}(y_k, y_\ell) \simeq 0 \qquad \text{for } |k| \neq |\ell| \tag{12.24}$$

$$\mathrm{var}\ y_K = (\overline{|Z_n(2K/T)|^2})^2 + 2|Z_x(\tfrac{2K}{T})|^2\ \overline{|Z_n(\tfrac{2K}{T})|^2}(1+\delta_K) \tag{12.25}$$

$$\text{where } \delta_K = 1,\ K=0; \qquad \delta_K = 0,\ k\neq 0 \tag{12.26}$$

12.1.5 Comments on Applications

In applying these calculations, the $\overline{|Z_n(2K/T)|^2}$ would be determined by a smoothed periodogram (or the equivalent Blackman-Tukey) calculation on a sufficiently long run of noise preceding the transient. (Typically, two minutes of noise on the seismic records has been used.) For this calculation Q(f) would be chosen to equal the $|A(f)|^2$ used with the transient, in order to obtain the appropriate numbers. Once this is done, the $\overline{|Z_n(2K/T)|^2}$ in Equations 12.23-12.25 are assumed known, and the remaining statistical problem is to estimate the $|Z_x(2K/T)|^2$ from the y_K. One interesting aspect of this problem is that not only the means of the y_K but also their variances depend on the $\overline{|Z_x(2K/T)|^2}$. Thus, for example, a value of y_K much larger than $\overline{|Z_n(2K/T)|^2}$ suggests a signal contribution at that frequency in two related ways: a larger mean value and a larger variance.

At frequencies where the signal-to-noise ratio -- perhaps defined as $|Z_x(2K/T)|^2 / \overline{|Z_n(2K/T)|^2}$ -- is relatively large, there should be little difficulty in estimating the $|Z_x(2K/T)|^2$. However, where this is not the case, some further smoothing may be necessary. This smoothing would reduce the resolution in order to increase the signal-to-noise ratio at those frequencies where it is necessary. Exactly what smoothing is "best" would depend not only on the details of $|Z_x(f)|^2$ and $\overline{|Z_n(f)|^2}$ but also on the objectives of the particular application.

It should be noted that the application of the Blackman-Tukey methods with the customary choice of parameters would correspond to smoothing equally over all frequencies in such a way that the standard deviation of the noise contribution is a small fraction (e.g., 1/3) of the mean of the noise contribution. In many applications this smoothing would be more severe than necessary except at those frequencies where the signal-to-noise ratio is very small, since the appropriate criterion here is that the standard deviation of the spectral estimate be small compared to the signal contribution. At a frequency where the signal contribution is relatively large, for example, it matters not at all if the standard deviation of the noise contribution equals the mean of the noise contribution (as it will with no smoothing).

In applying these calculations there are several choices to be made, such as what shape and duration of time window to be used and where to locate it. No general rules for making these decisions are presented here, but data are presented for two lengths of time windows and two shapes in order to give some indication of the dependence of the estimate on these parameters. For most of the seismic records used to date, the choice of the onset time is fairly clear. The rectangular time windows are defined to begin a point or two before the initial motion of the event; the Hanning windows are defined to begin 1/2 second earlier.

Since the seismic spectra do fall off quite rapidly with frequency, there is the possibility, which was discussed above, that the sidelobes of A(f) together with the large low frequency energy might contribute more apparent energy at the high frequencies than is actually there. To provide against this possibility, the seismic records have all been high-pass filtered and the spectral calculations repeated. Since the principal concern in this section is with the high-frequency content of the seismograms, most of the calculations that are presented will be based on the high-pass filtered records.

The possibility of reducing the variability of the spectral estimates, by subtracting from the observed record an estimate of the noise that is based only on the noise preceding the time window, has been considered. The few theoretical predictions that are workable suggest that this procedure might be useful in applications where the correlation time of the noise is comparable to the length of the transient. In application, however, results have been rather disappointing, and it is thought that this is due to the lack of stationarity of the noise, and also to the fact that rather artificial assumptions were used in the theoretical analyses in order to yield "paper and pencil" results. Even if the noise prediction were to significantly reduce the variability of the spectral estimate, the value of this reduction would have to be weighed against the cost of the relatively long computation times necessary to implement these calculations.

12.2 COMPUTER IMPLEMENTATION OF SPECTRAL CALCULATIONS

Implementing the calculations discussed in the previous section on a digital computer is relatively straightforward. The fundamental difference between the computer implementation and the calculations discussed in the preceding section is that a discrete rather than continuous representation is used in the computer handling of the data. (The continuous formulation is somewhat more convenient for the theoretical discussion.) The results that were presented in continuous form in the previous section can easily be transcribed to an appropriate discrete formulation. A few examples will illustrate how closely the discrete formulation parallels the continuous. By analogy with Equation 12.1 we have

$$z_i = a_i[x_i+n_i] \tag{12.27}$$

where the x_i and n_i are the signal and noise contributions to the observed samples, the a_i form the time window and the z_i are the samples to be transformed. In the case of rectangular time windows the a_i may be written as

$$a_i = \begin{cases} 1/\sqrt{N} & 0 \leq i < N-1 \\ 0 & \text{elsewhere} \end{cases} \tag{12.28}$$

where N is the length of the time window. In the calculations to be presented below, both rectangular and Hanning windows of two lengths have been used. In all cases, the normalization constants are chosen such that

$$\sum_{1}^{N} a_i^2 = 1 \tag{12.29}$$

This normalization is chosen because it is the normalization which yields comparable power density spectra for the noise.

The Fourier series based on the z_i is given by

$$Z_k = \sum_{i=1}^{N} z_i e^{-j\frac{2\pi ki}{N}} \tag{12.30}$$

and the spectral estimates are simply $|Z_k|^2$. By analogy with the previous discussion (or by direct calculation) the expected contribution of the noise to the spectral estimates, P_k, for the case of rectangular time windows may be written as

$$P_k = \sum_{s=-(N-1)}^{+(N-1)} (1 - \frac{|s|}{N})\rho_s e^{-j\frac{2\pi sk}{N}} = \rho_0 + 2 \sum_{s=1}^{N-1} (1 - \frac{s}{N})\rho_s \cos\frac{2\pi sk}{N} \tag{12.31}$$

where the ρ_s are the correlation coefficients estimated from a long run of the noise preceding the event (that is, $\overline{n_i n_j} = \rho_{|i-j|}$). Equation 12.31 is simply the smoothed periodogram that corresponds to the choice of time window given in Equation 12.28. A similar expression may be derived for the case of Hanning windows and is, of course, implemented in those calculations. The spectral calculations will be presented below in the form of plots of $|Z_k|^2$ and P_k vs. k, or frequency. In all cases, the smoothed periodogram shown with an energy density spectrum will be the one corresponding to the choice of time window used for the energy density spectrum.

Some programming was necessary in order to carry out the calculations reported in this chapter. In writing these programs, considerable use was made of subroutines available from the staff of the Seismic Data Laboratory, Earth Sciences Division, Teledyne Industries, Inc. The subroutine COOL, which calculates Fourier series by means of the Cooley-Tukey algorithm (25) and the subroutine COOLVOLV, which convolves two waveforms by calculating and multiplying their Fourier series and then calculating the corresponding time series, were used extensively throughout these calculations. (Descriptions of these subroutines may be found in reference 26.) To carry out the filtering a subroutine was written which calculates the (time-domain) impulse response from a desired frequency-domain response. Filtering was effected by using COOLVOLV to convolve the impulse response of the filter with the entire seismic record. For the number of sample points

used in these calculations, it was not necessary to segment the waveforms, as suggested for some filtering applications by Stockham (27).

As suggested earlier, spectral calculations have been performed on both the raw seismic data and on high-pass-filtered seismograms. The high-pass filtering was employed in order to be sure that the apparent signal energy at high frequencies is not an artifact resulting from the sidelobes of the time window's transform, but is in fact due to high frequencies in the seismogram. In all cases where high-pass filtering was employed the same filter was used. The frequency response, H(f), of this filter is given by

$$H(f) = \begin{cases} 0 & |f| < 2.5\text{Hz} \\ 1/2\,(1-\cos(\frac{2\pi(|f|-2.5)}{2.5})) & 2.5\text{Hz} < |f| < 3.75\text{Hz} \\ 1 & 3.75\text{Hz} < |f| \end{cases} \quad (12.32)$$

Data will be presented below for spectral calculations on both unfiltered and high-pass filtered seismograms. In viewing these data it should be recalled that in both cases the LASA recording system includes an aliasing filter that is flat to approximately 5 Hz and provides 30 dB of attenuation at 10 Hz. This filter precedes the sampling and quantizing that form the digital records.

When parity errors occur in the digital recording of the seismic records a value of zero is substituted. This also occurs when parity errors occur in transcribing digital tapes. In order to avoid misleading results in the spectral calculations, it is necessary to remove these spurious zeroes from the seismic records. For this purpose we have used the following simple rule: whenever a zero or a string of zeroes occurs, the polarity of the samples immediately preceding and following the zeroes is checked; if the polarity changes, it is considered a "legitimate" zero; if the polarity does not change, the zero is replaced by the straight-line interpolation of the surrounding values. The removal of the spurious zeroes precedes any other processing of the seismic record in the spectral calculation. At the time these zeroes are removed, a count is printed out that indicates the total number of spurious zeroes and the number of these that occur singly so that data containing an excessive number of parity errors may be discarded.

Following the removal of the spurious zeroes the seismic record is normalized in such a way that the noise portion of the record has zero mean and unity standard deviation. That is, the mean value of the noise portion is removed from the entire record, and the entire record is divided by the rms

level of the noise. The noise autocorrelation function is then estimated by using COOLVOLV to convolve either a two or three minute sample of the noise with itself reversed in time. Because of the just mentioned normalization, the value of the autocorrelation function at the origin will be exactly unity. When high-pass filtering is employed the new noise autocorrelation function is estimated in the same way using the output of the high-pass filter. The output of the filter is not renormalized. In interpreting the spectral data there are several statistics of the data that are of interest. For the calculations presented in this section these statistics are summarized in Table IX. The first column of this table gives the peak deflection in the unfiltered seismogram, and is expressed in terms of "counts." The digital representation of these data consists of 14-bit samples. For convenience in this discussion each quantizing level is referred to as a "count." The next column of the table gives the calibration factor (in counts per millimicron) as measured for that seismometer on the appropriate day or in one case, on the preceding day. The third column contains the ratio of the first two, which is the peak deflection measured in millimicrons. The next column, labeled "Noise Reduction Factor," gives the factor by which the rms value of the noise is reduced by the high-pass filtering operation. The column following that is the rms value of the unfiltered noise in terms of the original quanitzing levels, or counts. The next column contains the product of these last two columns, which is the rms value of the filtered noise in terms of the original quantizing levels. Finally, the last column of the table references the figure in which the corresponding spectral calculations appear.

12.3 SAMPLE CALCULATIONS ON ONE EVENT

All the calculations presented in this section are based on a Kazakh surface-focus event of magnitude 4.9 as recorded at the center element of LASA cluster D4. The calculations presented here are spectral calculations with 64- and 128-point time windows, with rectangular or Hanning shapes, and with high-pass filtered or unfiltered records. The objective in presenting so many calculations for a single event is to give some indication of the dependence of these calculations on the parameter choices such as shape and duration of the time window. In the next section only a single spectral calculation -- the one employing the 128-point Hanning window -- will be presented for each recorded event.

Figure 12.2 presents a portion of the seismogram used in the sample calculations presented in this section. Indicated on this figure is the origin time that was used in

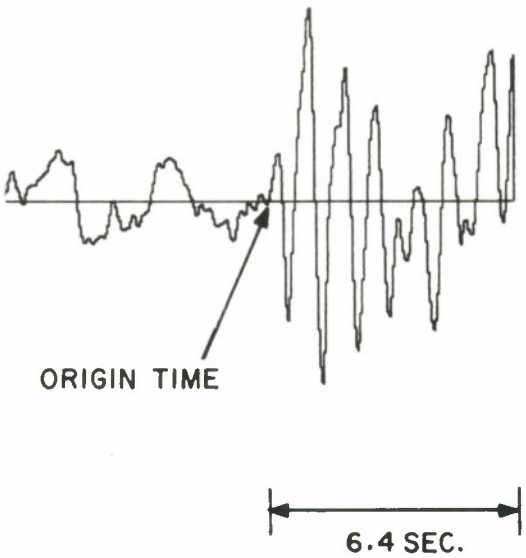


FIGURE 12.2
SEISMOGRAM FOR SAMPLE SPECTRAL CALCULATION

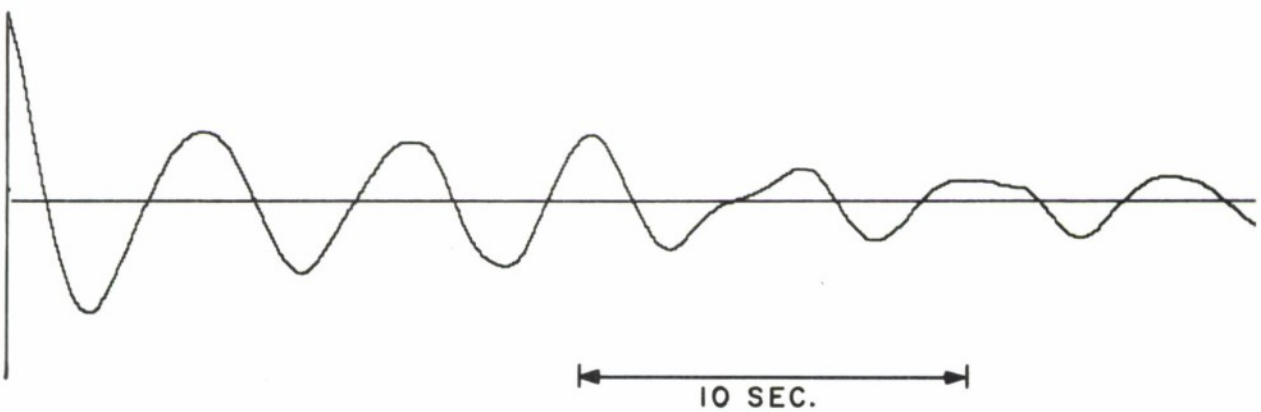


FIGURE 12.3
AUTOCORRELATION FUNCTION FOR
SAMPLE SPECTRAL CALCULATION

these calculations. The rectangular time windows begin at this time. The length of the 128-point time window, 6.4 seconds, is indicated on the figure. In the case of the Hanning windows the origin time for the time window was moved 10 points earlier. The autocorrelation function estimated from 3 minutes of noise preceding this event is given in Figure 12.3. The spectral calculations performed on the unfiltered seismogram are presented in Figure 12.4 the same calculations performed on the filtered seismogram are presented in Figure 12.5. From Figure 12.4 the rapid decrease in spectral energy with increasing frequency may be observed. The presence of good signal-to-noise ratios over a wide range of frequencies may be observed and some inferences may be made about the relative amounts of smoothing caused by the various time windows. Figure 12.5, which presents the same calculations performed on the filtered seismogram, indicates that the signal-to-noise ratios observed in the 4 to 5 Hz region are "legitimate," and not simply a sidelobe artifact resulting from the transform of the time window. The effect of the various widths of the transforms of the time windows are somewhat clearer in Figure 12.5 than Figure 12.4. Comparing the various spectra of Figure 12.5 it may be concluded that the 128-point time windows has a narrower transform than the corresponding 64-point time widnows and that both Hanning windows are narrower in their transforms than the rectangular windows. For our purposes the most imporatnat observation to be made from this figure is that even after the high-pass filtering there still appears to be a significant amount of signal energy at the higher frequencies.

In order to consider the statistical significance of the high frequency content, let us consider the results of the calculation based on the 64-point Hanning window. At a frequency of approximately 4 Hz, the energy density spectrum has a value of approximately 0.3 while the smoothed periodogram at that point is approximately 0.03. If in fact there were not signal energy at this frequency, the expected value of the energy density spectrum calculation would be 0.03, and this would also be the standard deviation of the result of this calculation. Thus the observed value is more than nine standard deviations away from the expected value that would apply if there were not signal energy present at this frequency. For this reason, it is concluded that a significant amount of signal energy is present at this frequency. The problem of devising a good estimate for just how much signal energy is present is not entirely trivial. The reason, which was suggested in the previous section, is that both the mean and the variance of the spectral estimates depend upon the signal contribution.

There are several features of the curves presented in these figures that deserve additional comment, since they will also appear in one form or another in the figures to be

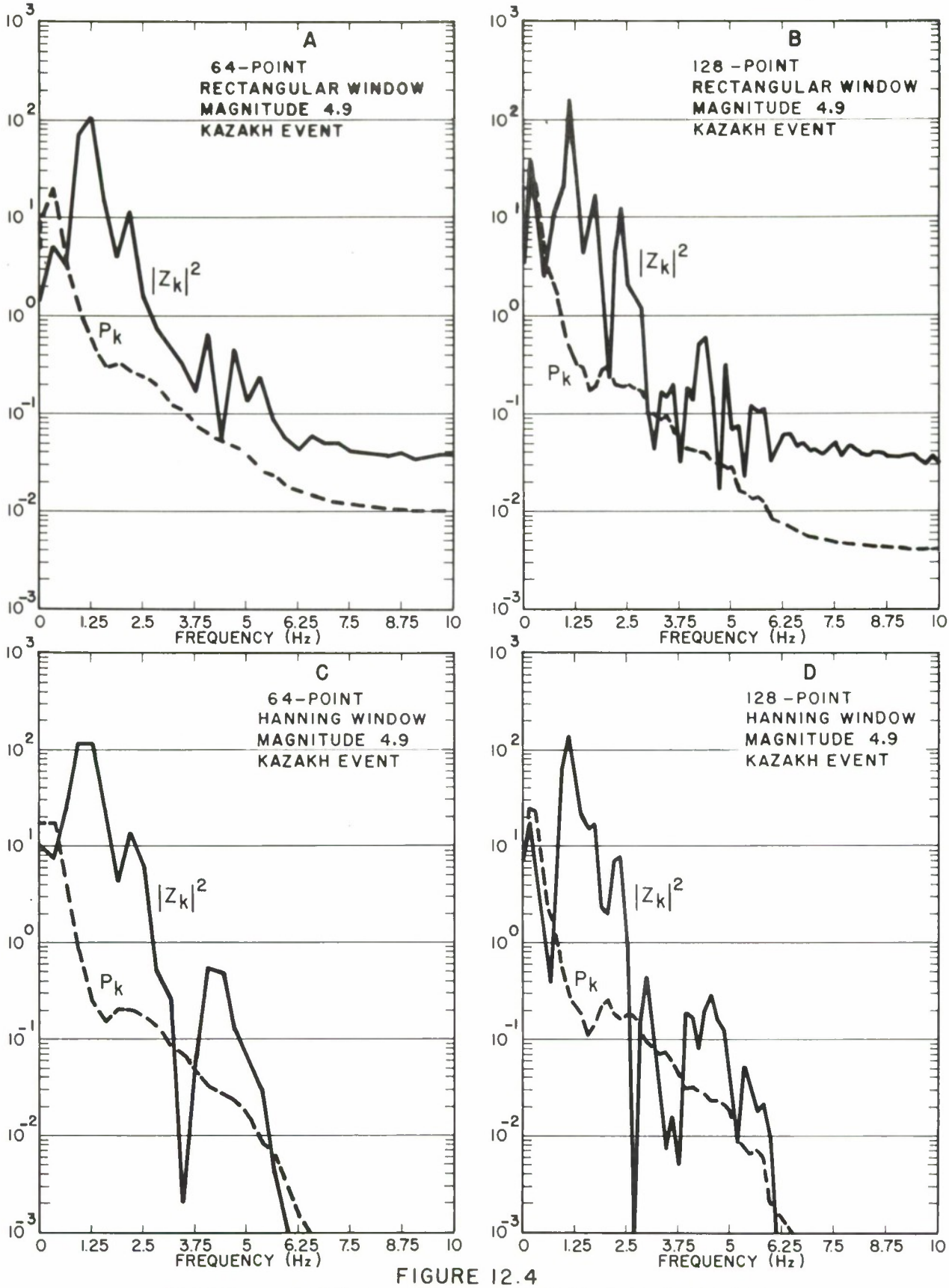


FIGURE 12.4
SAMPLE SPECTRAL CALCULATIONS - UNFILTERED

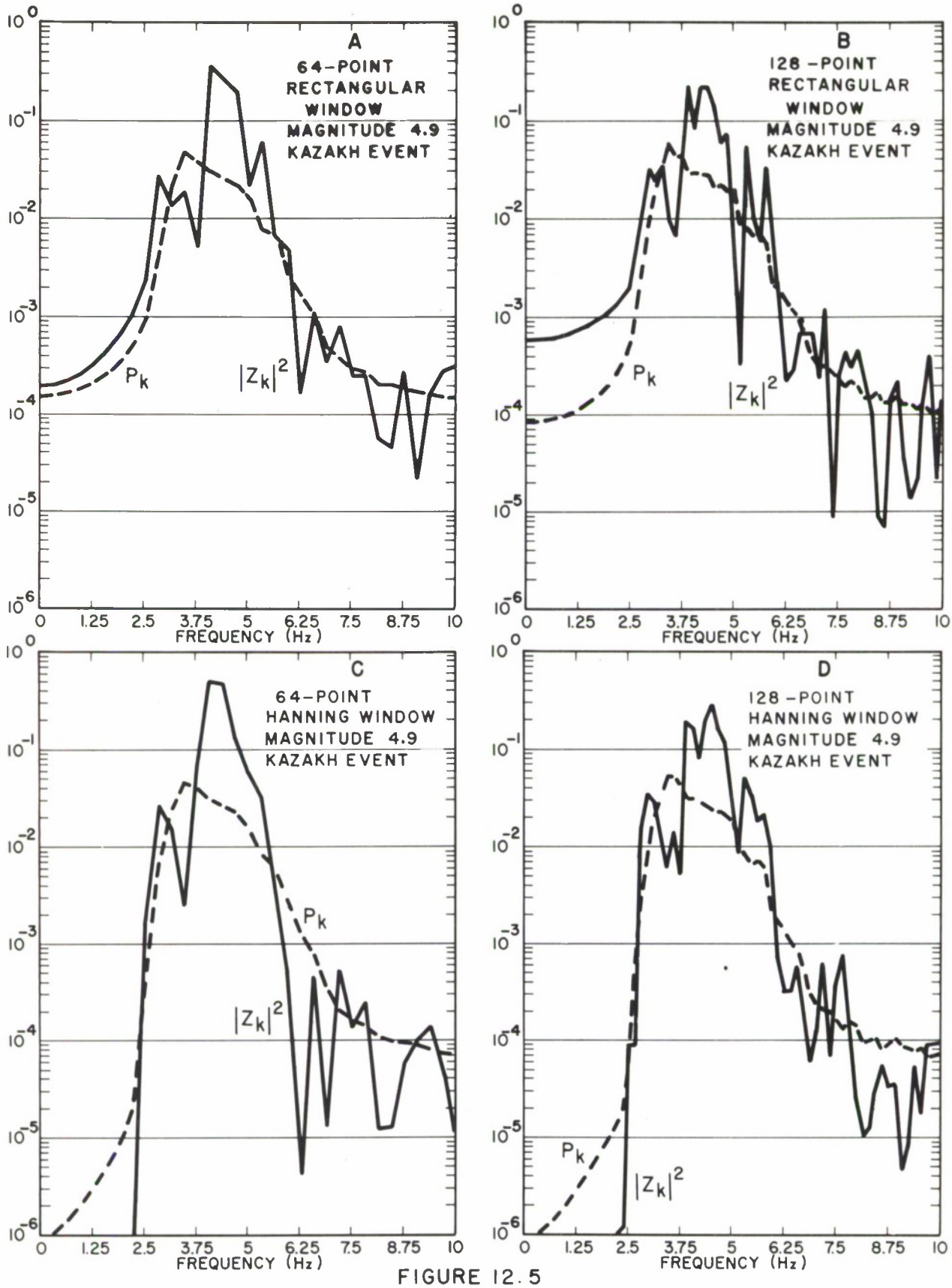


FIGURE 12.5
SAMPLE SPECTRAL CALCULATIONS - FILTERED

presented below. All of the spectral presentations are presented in semilogarithmic coordinates since such a large dynamic range is involved. However, the logarithmic vertical scale can be somewhat misleading when trying to read these figures. It has already been noted several times that in the case where there is no signal energy at a particular frequency the result of the spectral calculation should have an expected value equal to the corresponding value of the smoothed periodogram but a standard deviation that is also equal to that value. Fluctuations above or below the smoothed periodogram are therefore expected in the energy density spectrum at frequencies where there is little or no signal energy. The problem with the logarithmic vertical coordinates is that they accentuate the appearance of fluctuations below the smoothed periodogram. The effect is that in many cases it appears that the energy density spectrum goes further below than above the smoothed periodogram curve. It should be remembered that these two curves would appear quite different if plotted on linear paper and it would only be in the case of a linear vertical scale that the average of the fluctuations would be expected to be at least as large as the smoothed periodogram.

In the spectral curves of Figure 12.5, and also in those to be presented below, there seems to be a tendency for the smoothed periodogram to be consistently larger than the energy density spectrum, in the very low frequency region of the spectrum, that is, the region supposedly removed by the high-pass filtering. If this did not happen with such regularity it would probably be all right to dismiss it as a statistical fluctuation of the kind just discussed. However, it does happen so consistently that this does not seem an appropriate explanation. At the present time we do not have any good explanation for why this effect appears so often; however, it is easy to demonstrate that the total energy involved in this region of the spectrum is of a level that is sufficiently small that a quantization-noise effect is suggested. Why this effect should systematically favor the smoothed periodogram over the energy density spectrum is not clear, but given the very low-level energies involved, this problem does not seem to be a very important one; further attention to the quantization-noise effect is given below. In order to look at the signal energies involved, it is useful first to review some of the statistics of the calculations performed on this event.

As indicated in Table IX, the peak motion of the seismogram is only 344 counts. Since the output of the quantizer is a 14-bit number it is clear that only a small fraction of the available dynamic range in the output of the analog-to-digital converter is being employed. The rms value of the unfiltered noise is roughly 64 counts, or about 1/5

of the peak motion. On the same scale of quantizing levels, the rms value of the filtered noise is about 5 1/2 counts. The fact that this number is so small indicates that quantizing noise may be a problem in terms of the fidelity of the output of the high-pass filter. However, since this value is significantly above unity it appears that the output of the high-pass filter is not dominated by quantization noise.

Returning now to the problem of the 0-2.5 Hz region, the above numbers can be used to make a rough estimate of the signal energies involved in this portion of the spectrum. In the case of the noise waveform, the average power of the noise may be obtained from the smoothed periodogram. From Figure 12.5C it is clear that the smoothed periodogram is less than 10^{-4} for frequencies below 2.5 Hz. We can overbound the energy in this portion of the spectrum by assuming that it has a value of 10^{-4} in this region. Taking this value, it is easy to show that the average power in this portion of the spectrum would be simply $1/4 \cdot 10^{-4}$, which corresponds to an rms value of $1/2 \cdot 10^{-2}$. Recalling that all of these calculations follow the initial normalization of the noise waveform, which led to an rms value of unity, the value $1/2 \cdot 10^{-2}$ can be converted to the scale of the original quantization levels by multiplying by the rms value of the unfiltered noise, which was about 64 counts. The result of this multiplication indicates an rms value of approximately 1/3 of 1 quantization level. The rough calculations just described probably overbound considerably the true energy in the 0-2.5 Hz region. Even doing so, the resulting rms value is only 1/3 of a quantization level. This very clearly indicates that the energies in the 0-2.5 Hz region are of the same order as those that might be expected from quantization-noise effects. For this reason we are not troubled by the apparent trend for the smoothed periodogram to exceed the energy density spectrum in this portion of the spectrum. Incidentally, these comments apply to the spectra resulting from the Hanning window calculations. In the case of the rectangular windows, which have considerably larger sidelobes,the sidelobes contribute a good deal of energy to the 0-2.5 Hz region, as is clear from parts A and B of Figure 12.5.

There is one additional problem that has not yet been mentioned that may be important in interpreting these data and the data to be presented below. This problem relates to the dynamic range of the seismometer and recording system. There have been some suggestions recently that, with very large magnitude events, serious nonlinearities may occur in the seismometer-recording system. If such were the case, of course, spurious high frequencies could be introduced in the seismogram that were in fact not present in the original seismic signal. As yet there is no clear measure available of when these nonlinearities occur, so that it is impossible to say with con-

fidence which of the calculations to be presented below may and which may not suffer from non-linear distortions. It is our understanding from Lincoln Laboratory that when peak motions are less than 2000 counts, non-linearities are very unlikely in the recording system. If this criterion is valid, most of the data to be presented below may be considered as all right and, therefore, the conclusions to be presented will still stand. It is of course possible that non-linearities may occur with peak motions less than 2000 counts, and it seems even more likely that in some cases with peak motions greater than 2000 counts linearity is no problem. For lack of more precise information, we shall, for the present, assume that any seismogram with a peak motion less than 2000 counts is safely in the linear range. This arbitrary criterion is met by all of the data summarized in Table IX except the 13 February event and the LF4 record of the 21 November Kazakh event.

The data in this section were presented in order to show the effects of parameter choices and of high-pass filtering on the spectral calculations. In the next section, similar calculations will be presented for five seismic events as recorded at three different LASA seismometers. As we are principally interested in the high frequency region, only the high-pass filtered records will be used, and as it has the smallest sidelobes of any of the time windows, the 128-point Hanning window will be used for all the calculations presented in the next section. It is not clear at this time what the "best" time window to use would be. However, the calculations presented above suggest that it may not matter a great deal. Rounded windows such as the Hanning window certainly seem superior to the rectangular window in terms of sidelobe characteristics, but it may be that they should not be symmetric. The length of the window is also subject to some question. The longer windows give somewhat better resolution in frequency, but this presumably will be at the expense of signal-to-noise ratio, since the signal of interest probably decreases relative to the noise as the time since onset increases. For the present, the 128-point or 6.4-second time window seems satisfactory to indicate the presence and character of high frequencies in seismograms.

12.4 SUMMARY OF CALCULATIONS ON FIVE SEISMIC EVENTS

Spectral calculations are presented in this section on five seismic events. Table IX summarizes the events used and some statistics of the seismic records. Three Kazakh surface-focus events and two Kurile earthquakes were used. There are some difficulties in trying to compare the spectra of the surface-focus events with those of the earthquakes since they come from different locations. We have recently obtained information about earthquakes occurring in the Kazakh region and hope in the not too distant future to have spectral calculations that are more easily compared than those presented here.

The 13 February event, which was of magnitude 6.3, is presented separately (in Figure 12.6) from the others because it is thought that it may be sufficiently large that serious non-linearity problems are occurring in the amplifier. The other four events lead to more moderate peak motions at the seismometers and are thought, therefore, to be believable. Recordings at three different seismometers were used for each of these events. In addition, a fourth seismometer was used for the 7 May event and it is on the basis of that recording that the data of the previous section were calculated. The spectral data on these four events are grouped according to the seismometer used. Thus Figure 12.7 gives the A0 data for each of the four events; Figure 12.8 gives the B1 recording, and Figure 12.9, the F4 recording for each of the four events.

Several observations may be made from these figures. The most important observation is that, in the case of the surface-focus events, a significant amount of high frequency energy does appear to be present. In the case of the earthquakes the situation is less clear, with some seismometers indicating the presence of high frequency energy and others not. There are also some curious features to these figures for which we do not, at the moment, have a complete explanation. For example, in the case of the 21 November surface-focus event, signal-to-noise ratios on the order of 40 may be observed for the seismometers at A0 and B1 whereas for the seismometer of cluster F4 the signal-to-noise ratio is closer to 1000. Spectral calculations based on the data for the F4 cluster from the Kurile earthquake on 21 April also show a curious feature for which we, at the present time, have no explanation. Examination of the plots of the spectra of this event (Figure 12.9D) indicates that the spectra do not fall off appreciably at frequencies above 5 Hz. Since the aliasing filter should produce approximately 30 dB of attenuation between 5 and 10 Hz, it is rather surprising that the smoothed periodogram from this record does not show more of a decrease between 5 and 10 Hz. It is possible that this may be a result of the quantization noise problem referred to earlier, since the rms value of noise after high-pass filtering is something less than four quantization levels of the original record. However, it seems unlikely that this phenomenon would be sufficinet to account for the relatively large spectral energies observed at the higher frequencies. This high-frequency energy was also present in the calculations performed for all of the other time windows on this record.

TABLE IX SUMMARY TABLE FOR SPECTRAL ESTIMATES

SEISMOMETER	PEAK DEFLECTION IN COUNTS	CAL FACTOR IN COUNTS/mμ	PEAK DEFLECTION IN mμ	NOISE REDUCTION FACTOR	RMS NOISE IN COUNTS UNFILT.	RMS NOISE IN COUNTS FILT.	FIGURE NO.
EVENT: 13 February 1966 - MAGNITUDE: 6.3 - KAZAKH (NO. 45)							
LAO	7054	28.4	248	.056	78.78	4.41	12.6A
LB1	8193	28.9	284	.046	87.36	4.02	12.6B
LF4	8191	28.1	292	.049	87.54	4.29	12.6C
EVENT: 21 November 1965 - MAGNITUDE: 5.8 - KAZAKH (NO. 43)							
LAO	1941	34.2	57	.042	132.17	5.55	12.7A
LB1	2001	28.9	69	.046	111.20	5.12	12.8A
LF4	4859	26.7	182	.027	132.16	3.57	12.9A
EVENT: 7 May 1966 - MAGNITUDE: 4.9 - KAZAKH (NO. 47)							
LAO	238	27.8	9	.152	66.62	10.13	12.7B
LB1	322	27.3	12	.091	64.04	5.83	12.8B
LF4	614	28.5	22	.110	70.47	7.75	12.9B
LD4	344	27.9	12	.085	63.79	5.42	12.5
EVENT: 21 November 1965 - MAGNITUDE: 4.7 - KURILES (NO. 44)							
LAO	934	34.2	27	.040	161.03	6.44	12.7C
LB1	940	28.9	33	.051	120.69	6.16	12.8C
LF4	1356	26.7	51	.024	124.11	2.98	12.9C
EVENT: 21 April 1966 - MAGNITUDE: 4.5 - KURILES (NO. 46)							
LAO	268	28.1	10	.187	68.20	12.80	12.7D
LB1	234	26.7	9	.083	57.63	4.78	12.8D
LF4	353	28.1	13	.061	60.93	3.72	12.9D

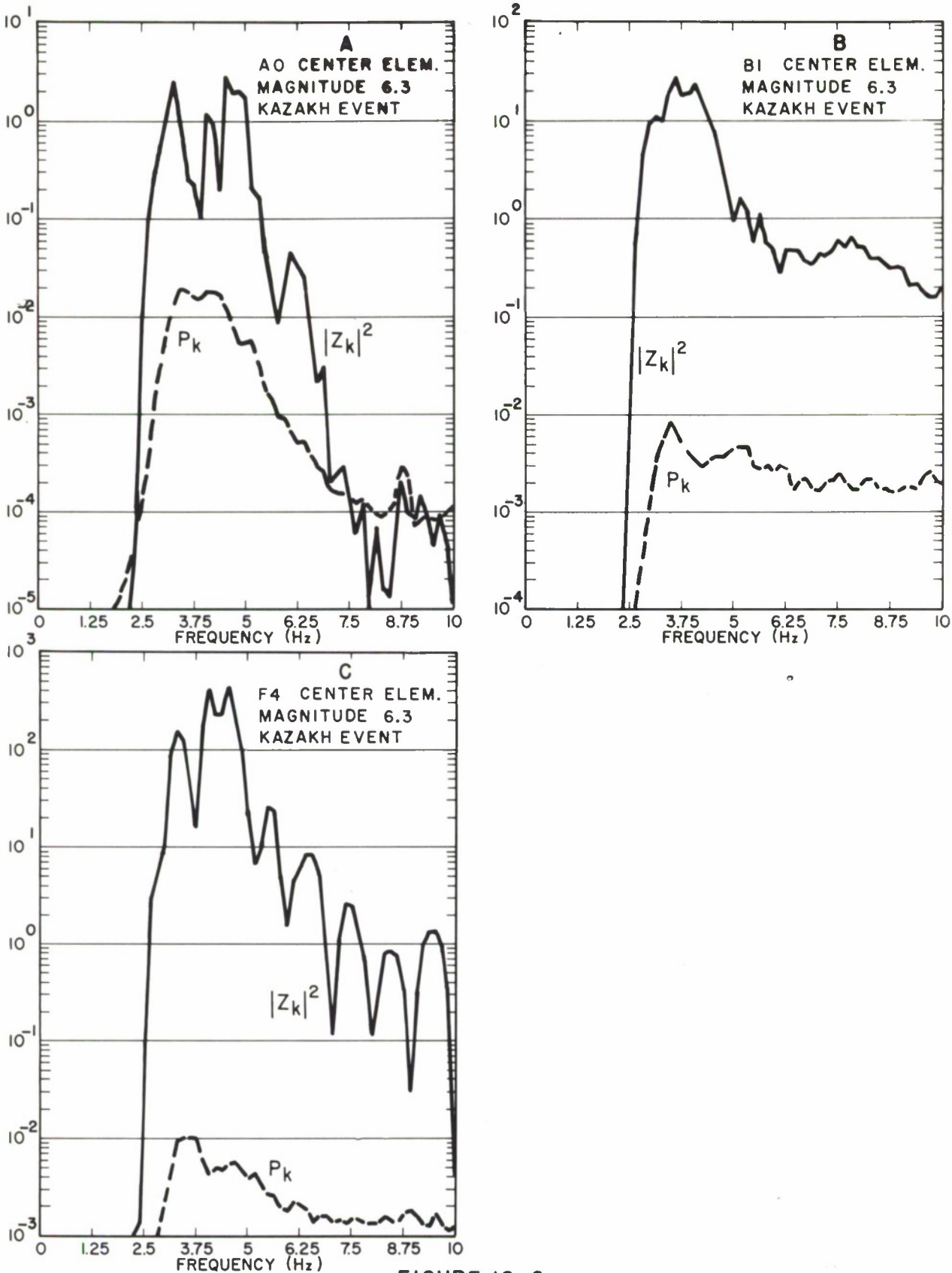


FIGURE 12.6
SPECTRAL CALCULATIONS MAGNITUDE 6.3 EVENT

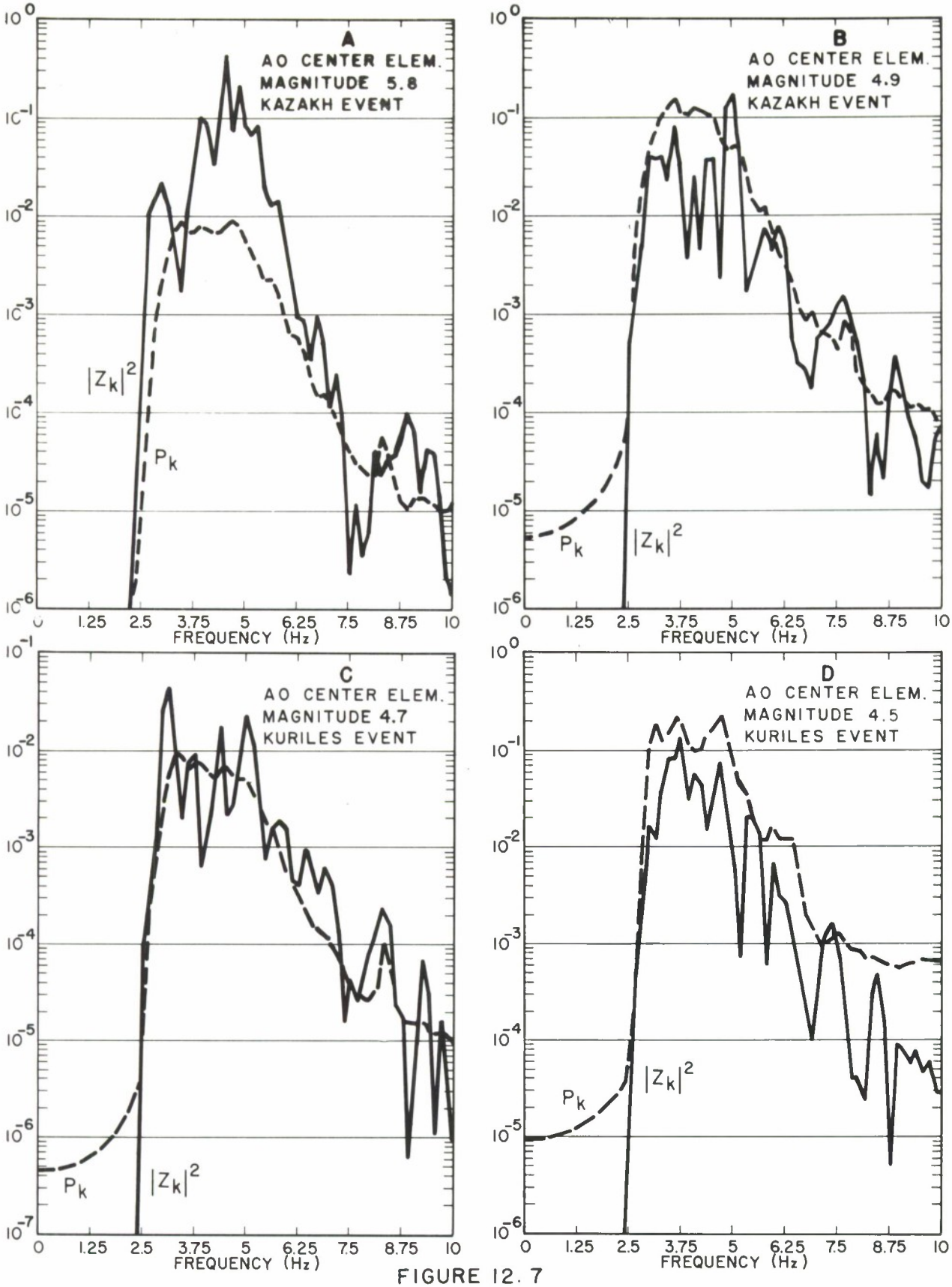


FIGURE 12.7
SPECTRAL CALCULATIONS AO CENTER ELEMENT – FOUR EVENTS

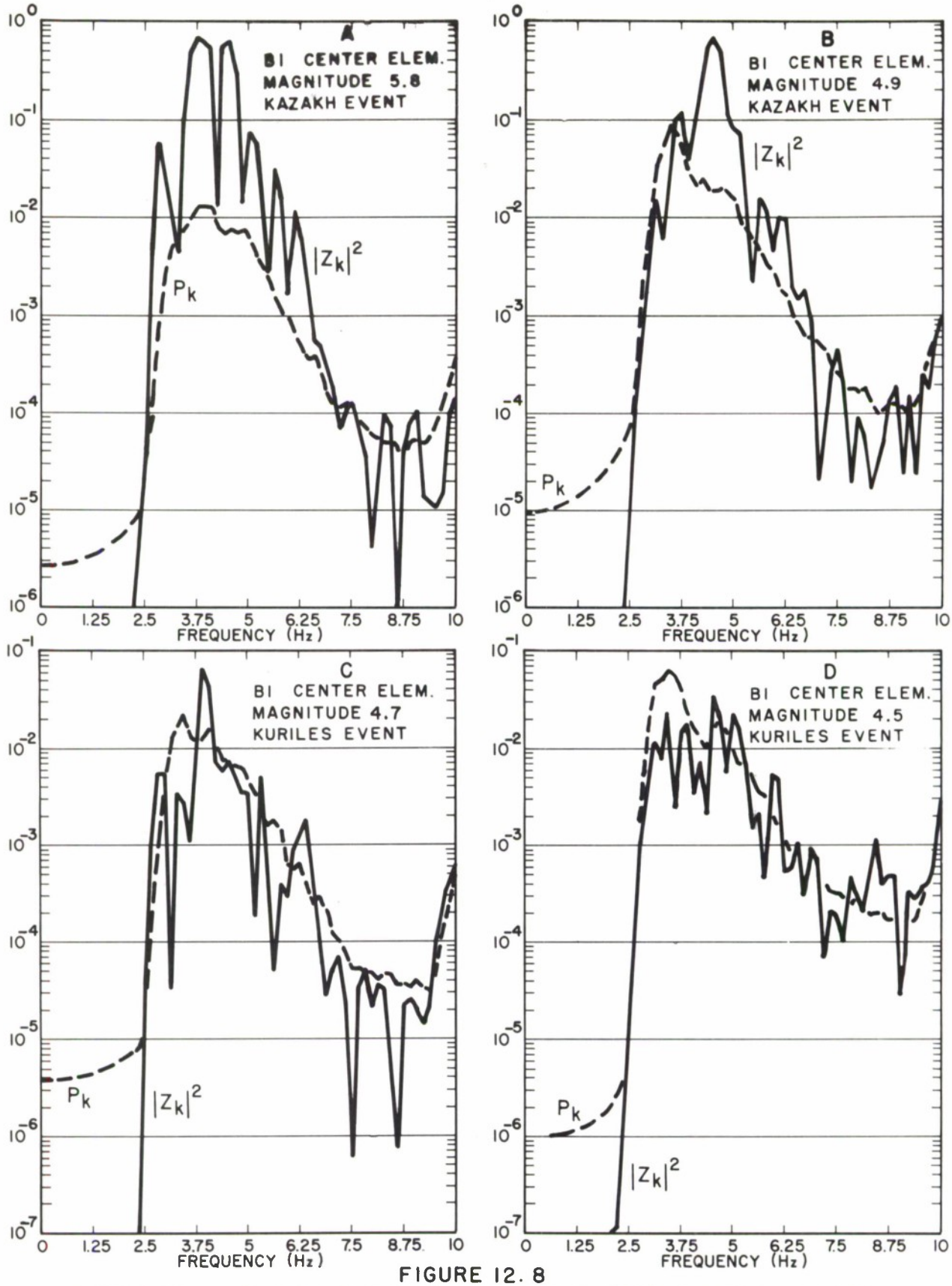


FIGURE 12.8
SPECTRAL CALCULATIONS BI CENTER ELEMENT - FOUR EVENTS

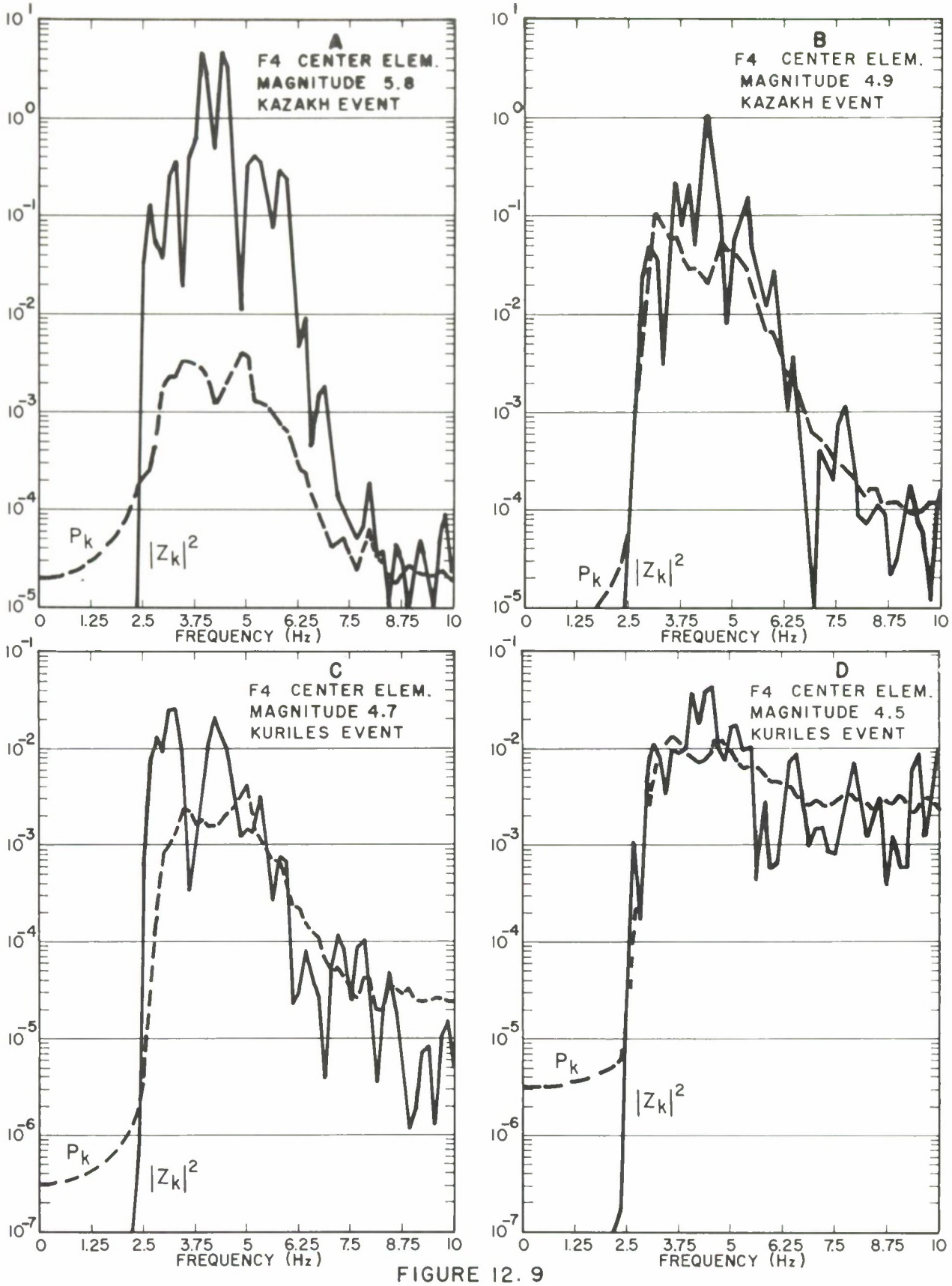


FIGURE 12.9
SPECTRAL CALCULATIONS F4 CENTER ELEMENT - FOUR EVENTS

12.5 SUMMARY OF ASSUMPTIONS AND POTENTIAL SOURCES OF ERROR

The theoretical analysis used in interpreting these calculations assumes that the seismic record consists of the desired transient plus stationary Gaussian noise. It is also assumed that a sufficient record of noise preceding the transient is available to make a good estimate of the power density spectrum of the noise. Interpreted in terms of this analysis, the data presented above indicate that there is a significant amount of high-frequency energy in most of the digital recordings from surface-focus events. The best method for determining exactly how much energy is present, especially in low signal-to-noise cases, remains to be determined. Very likely this best estimation procedure will involve some further smoothing over frequency in order to increase the signal-to-noise ratio where this is necessary.

The possibility that the apparent high frequency energy content of the seismograms might only be the low-frequency energy "smoothed" into the high frequency region by the sidelobes of the Fourier transform of the time window has been considered. To provide against this possibility, high-pass filtering of the records has been employed, and the resulting spectra still show significant high-frequency energy.

The computer implementation of these calculations is straightforward. Control calculations performed on intervals consisting of noise alone have indicated that no significant scale-factor errors exist either in the program or the analysis; i.e., performing the energy density spectrum calculation on an interval consisting only of noise should lead to a spectrum which is highly variable but has an expected value equal to the corresponding smoothed periodogram. Control calculations performed to date indicate that this is the case.

The question of possible nonlinearities in the seismometer and recording systems has not yet been thoroughly explored. It is quite possible that for the large Kazakh event of 13 February, the peak motion was sufficiently large that serious nonlinearities occurred, and that these may in fact have contributed a significant fraction of the observed high-frequency energy. For the other events, however, where the peak motion is only several times the size of the rms noise value, it appears likely that the amplifiers would be behaving properly and not be responsible for the apparent high-frequency energy. We understand from Lincoln Laboratory that linearity problems with peak motions smaller than 2000 counts are very unlikely; the majority of the calculations presented above are within this limit.

The question of quantization noise has been considered since after high-pass filtering, rms levels of the noise typically correspond to several quantization levels on the original output of the A/D converter. These numbers are too large to be attributed to quantization noise alone, but they are small enough that quantization noise may introduce some distortion in the observed spectra after high-pass filtering.

12.6 CONCLUSIONS

From the data and the analysis presented above, it appears that a significant amount of high-frequency energy is indeed present with surface-focus events of moderate size. A great deal of work remains to be done before it will be clear whether or not this high-frequency energy is of any potential value for purposes of discrimination. Indeed the principal point of this section is that the high-frequency energy does, in fact, exist, and so its possible use as a discriminant now appears worth pursuing. An obvious first step in pursuing this possibility is to perform spectral calculations on several events. In particular, it would be desriable to have spectral calculations on surface-focus events and earthquakes from approximately the same location. Furthermore, it would also be desirable to have these calculations performed on events of somewhat lower magnitude in order both to see if the characterisitcs of the spectra change with magnitude, and also to begin to consider the problem of estimating the spectrum when the signal-to-noise ratio is smaller than it has been in the examples considered in this report. Finally, it should be noted that all of the calculations presented in this section are based on the output of a single seismometer: no array processing has been performed. The output of the single seismometer has been sufficient to demonstrate the presence of high-frequency energy, but it is probably not the most useful way in which to take advantage of this energy. Array processing designed to utilize the high-frequency region of the spectrum raises many questions which to date have not been seriously considered. Most important among these may be the question of spatial coherence of the high-frequency portion of both signal and noise contributions to the seismic records.

SECTION XIII

ATTENUATION OF SEISMIC WAVES IN THE EARTH'S UPPER MANTLE

A suggestion by Dr. Eugene Herrin that the large discrepancies in the measured spectra from LONGSHOT as recorded at various stations might result from low Q regions in the earth's upper mantle prompted a brief study to discover whether it is possible to determine the existence of such layers by comparing the spectra of the P and pP phases of deep earthquakes. The motivation for this study lay in the hope of being able to choose sites of future seismic stations which maximize the high frequency capabilities of such stations. This section describes the results obtained.

The absorption characteristics of a linear propagation medium can be measured by the fractional energy absorbed per cycle, which is called Q. Experiments have suggested that the earth's Q is constant with frequency (28). A comparison of the frequency content of two phases of the same deep event, pP and P, makes it possible to find the average value of Q in the upper mantle at the epicenter region. Three events from the Fiji Islands region have been analyzed. These events all yield measurements of Q that are less than 500, indicating that the attenuation is one order of magnitude larger than expected from previous measurements. (29). The last topic in this section is a proposed method for extending the study to treat the upper mantle of aseismic regions.

13.1 DESCRIPTION OF THE EXPERIMENT

The attenuation suffered by a wave traveling through a medium is characterized by the dimensionless factor Q, which is defined in the following expression for the fractional energy absorbed per cycle.

$$\frac{2\pi}{Q} = \frac{\Delta E}{E} \qquad (13.1)$$

In general Q would be a function of frequency. As Howell points out (30), most observations indicate that the earth's Q does not vary with frequency, but no known linear relationship between stress and strain will produce the effect. In this section, we shall not be concerned with the details of the propagation mechanisms. Rather, we shall assume that the Q is constant with frequency and attempt to estimate this constant for the upper mantle at a particular location.

For a given range, a constant factor Q implies stronger attenuation for high frequencies than low frequencies. The (energy) attenuation function for a sinusoidal wave may be expressed in the following form

$$A(\Delta,\omega) = \exp[-2\alpha(\omega)\Delta] \tag{13.2}$$

Δ = length of the path

$\alpha(\omega)$ = absorption coefficient

To find the attenuation function that corresponds to a constant Q, let

$$\Delta = \lambda \text{ (wave length)} \tag{13.3}$$

$$\frac{\Delta E}{E} = \frac{2\pi}{Q} = 1 - e^{-2\alpha\lambda} = 1 - 1 + 2\alpha\lambda - 2\alpha^2\lambda^2 + \ldots$$

$$\alpha \simeq \frac{\pi}{\lambda Q} = \frac{\omega}{2cQ} \qquad \text{for } \alpha\lambda \ll 1$$

where c is the group velocity. Substituting the last approximation of Equation 13.3 into Equation 13.2 yields the following expression for the attenuation function

$$A(\Delta,\omega) = \exp(-\omega\Delta/cQ) \tag{13.4}$$

In studying attenuation in the upper mantle the pP and P phases of deep earthquakes are of particular importance. The path of pP is greater than the path of P. The additional path length consists of two crossings of the upper mantle and the crust in the region of the epicenter. This fact allows us to estimate the attenuation characteristics of the upper mantle, since the ratio of the energy spectra of P and pP is determined by the attenuation suffered during this extra path.

Figure 13.1 shows the model used for this study.

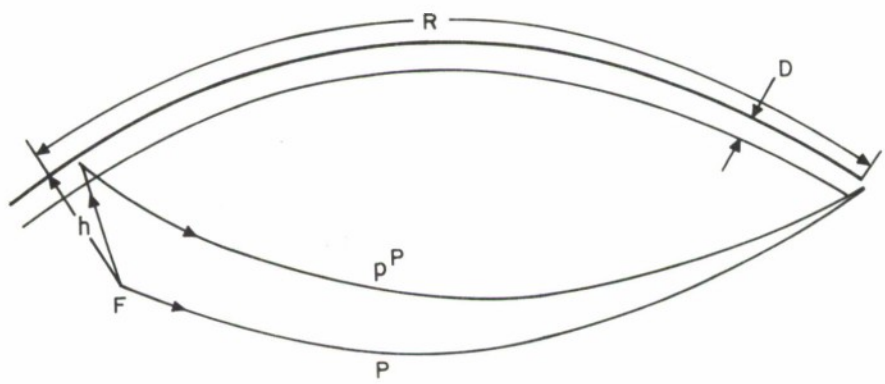


FIGURE 13.1
RAY PATHS FOR THE $_pP$ AND P WAVES

RAY PATHS FOR THE pP AND P WAVES

The attenuation function for pP is given by the following approximate expression

$$A_{pP}(R,\omega) = \exp\left(-\frac{\omega}{c}\sum\frac{\Delta_i}{Q_i}\right) \qquad (13.5)$$

where Δ_i = length of path in region i

Q_i = Q value in region i

It is useful to divide the exponent of the attenuation function into components.

$$\sum\frac{\Delta_i}{Q_i} = 2\left(\frac{h-D}{Q}\right) + \frac{2D}{Q_c} + T \qquad (13.6)$$

where h = depth of the event
D = thickness of the crust
Q = average Q value in the region between the hypocenter and the crust
Q_c = Q value in the crust
T = represents the terms corresponding to the attenuation in the lower mantle and the crossing of the upper mantle and crust at the receiver

Combining the last two equations yields:

$$A_{pP}(R,\omega) = \exp\left\{-\frac{\omega}{c}\left[2\left(\frac{h-D}{Q}\right) + \frac{2D}{Q_c} + T\right]\right\} \qquad (13.7)$$

The attenuation function for the P phase has only one of the three components in its exponent

$$A_P(R,\omega) = \exp\left(-\frac{\omega}{c}T\right) \qquad (13.8)$$

In the following we shall assume that the source spectra for P and pP are identical. This would be appropriate for either of the following two cases: an explosive type of source mechanism with a spherically symmetric radiation pattern, or a plane fault as the source mechanism with P and pP leaving the source in approximately opposite directions.

With this assumption, Equations 13.7 and 13.8 imply

$$\frac{E_P(R,\omega)}{E_{pP}(R,\omega)} = \frac{A_P(R,\omega)}{A_{pP}(R,\omega)} = \exp\left\{\frac{\omega}{c}\left[2\left(\frac{h-D}{Q}\right) + \frac{2D}{Q_c}\right]\right\} \qquad (13.9)$$

where E_P and E_{pP} are the energy spectra. This equation indicates that more attenuation will be experienced by pP because it crosses the crust and the upper mantle two additional times.

Since the thickness of the crust is small (25-60 km), the effect of the attenuation in the crust (assuming a Q of 200 for both crust and upper mantle) is very small compared with the effect of the upper mantle crossing. This is easily seen by comparing the two terms in the exponent of Equation 13.9.

$$\frac{2D}{Qc} = \frac{80}{200} = 0.4 \qquad \text{for } D = 40 \text{ km} \qquad (13.10)$$

$$2\left(\frac{h-D}{Q}\right) = 5.0 \qquad \text{for } h-D = 500 \text{ and } Q = 200 \qquad (13.11)$$

This example indicates, that if the average Q shows a low value, this phenomenon must be related to the upper mantle and not the crust.

For an earth without high attenuation in the upper mantle, the ratio of the energy spectra should have the following expression:

$$\frac{E_P(R,\omega)}{E_{pP}(R,\omega)} = \exp\left\{\frac{\omega}{c}\left[\frac{(2h-D)}{\bar{Q}} + \frac{2D}{Q_c}\right]\right\} \qquad (13.12)$$

where $\bar{Q}$ is the average Q over the ray path.

Assuming $h-D = 500$ km, $\bar{Q} = 2000$ (13.13)

yields $\frac{2(h-D)}{\bar{Q}} = .5$ $\qquad \frac{2D}{Q_c} = .4$ (13.14)

If these assumptions applied, the attenuation in the crust could not be neglected. In fact, interpretation of results would also be difficult should the upper mantle have an intermediate value of Q, such as 800. Since it was the purpose of this investigation to seek only the existence of very low Q's in some regions of the upper mantle, we have not had to consider this problem.

13.2 EXPERIMENTAL RESULTS

Three deep earthquakes in the Fiji Island region were chosen to test the hypothesis of a low Q layer for the upper mantle in this part of the earth. The epicenters of these events are indicated in the map presented in Figure 13.2. Depths,

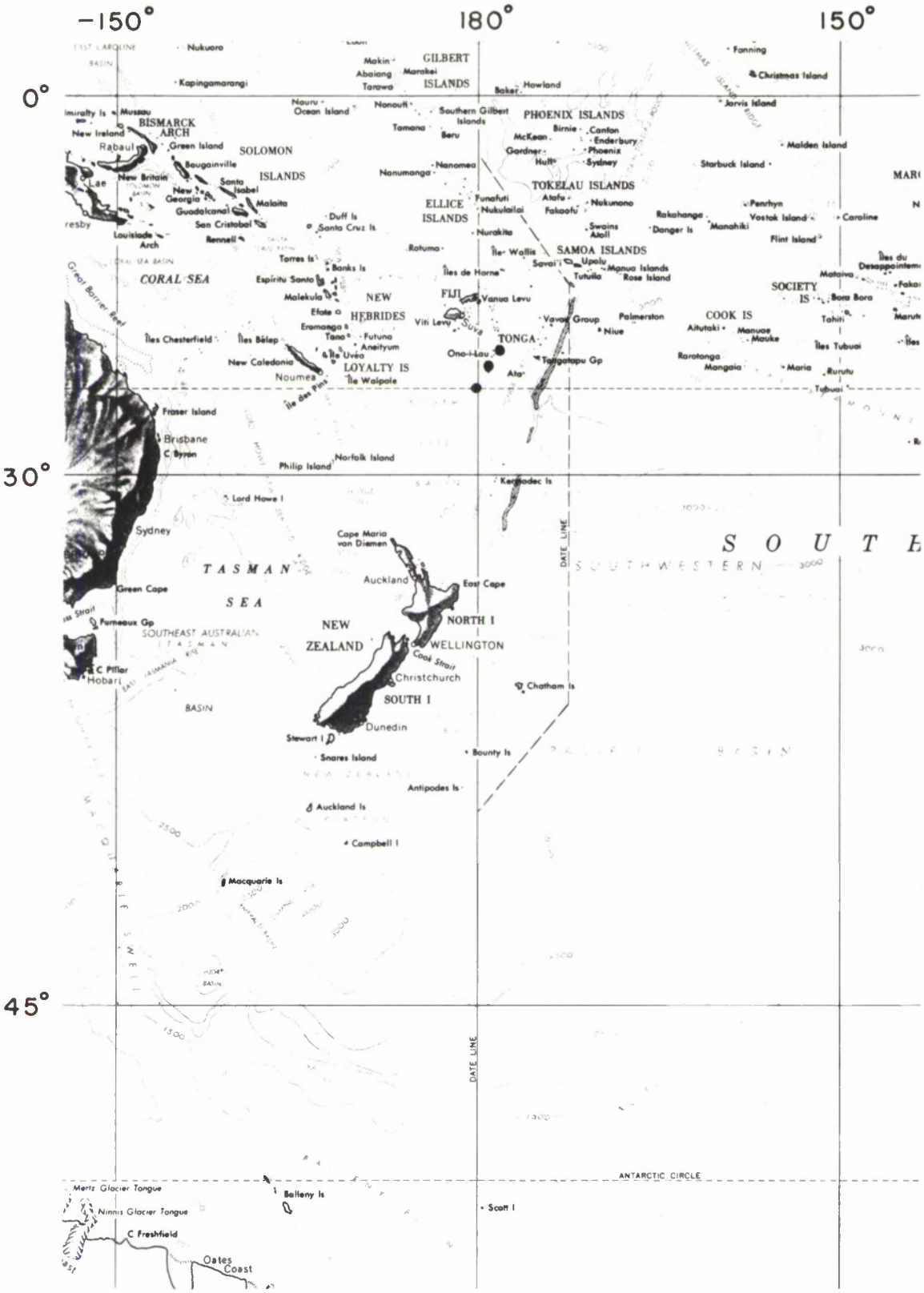


FIGURE 13.2
EPICENTER LOCATIONS

magnitudes and other information regarding these events may be found in Figures 13.3-13.5. The energy spectra for both the P and pP phases were computed for each of these events, and the ratio of the spectra of the two phases was then compared with the modeled functions for a layer with high Q and one with low Q.

The energy density spectra for both phases and the power density spectrum for the noise preceding the P phase were computed in the manner described in Section XII. The results of the calculations based on the 128-point Hanning window are summarized in Figure 13.6 - 13.8, where the smoothed periodogram appears as a "dashed line," and the energy density spectra for the P and pP phases appear as solid and "dot-dash" lines, respectively. One conspicuous difference between these spectral plots and those that appeared in Section XII is the large peak at 6 Hz that is apparent in Figures 13.6 - 13.8. This is presumed to be the result of 60 Hz interference in the A/D process, which is performed at ten times real time.

A plot of the logarithm of the ratio of the P and pP spectra as a function of frequency would be a straight line if Q were constant with frequency. This ratio was calculated for all frequencies between .313 and 1.88 Hz for the spectra obtained with a 64 point Hanning window and for all frequencies between .156 and 1.88 in the case of the 128 point Hanning window. The linear least squares fit was found for the log of the spectral ratios and the slopes obtained are presented in Figures 13.3 through 13.5. Also shown in those Figures are the theoretical slope for a Q value of 2000 in the upper mantle as well as the slope for h/Q = 1. The log of the experimental ratio was normalized to its value at .5 Hz and thus all curves cross the axis at that frequency. Different time windows were used and the results obtained are shown in the figures. The spread is too big to attach significance to anything other than the order of magnitude of the value of Q. Clearly the value of h/Q is bigger than 1.0 and this implies that the average Q value in the upper mantle should be less than 500.

If we arbitrarily take the average over the different windows used, the results for the different events are as follows:

$E.Q_o$ 7 Oct. 1963 : Q = 250

$E.Q_o$ 7 Dec. 1963 : Q = 170

$E.Q_o$ 26 Apr. 1964 : Q = 450

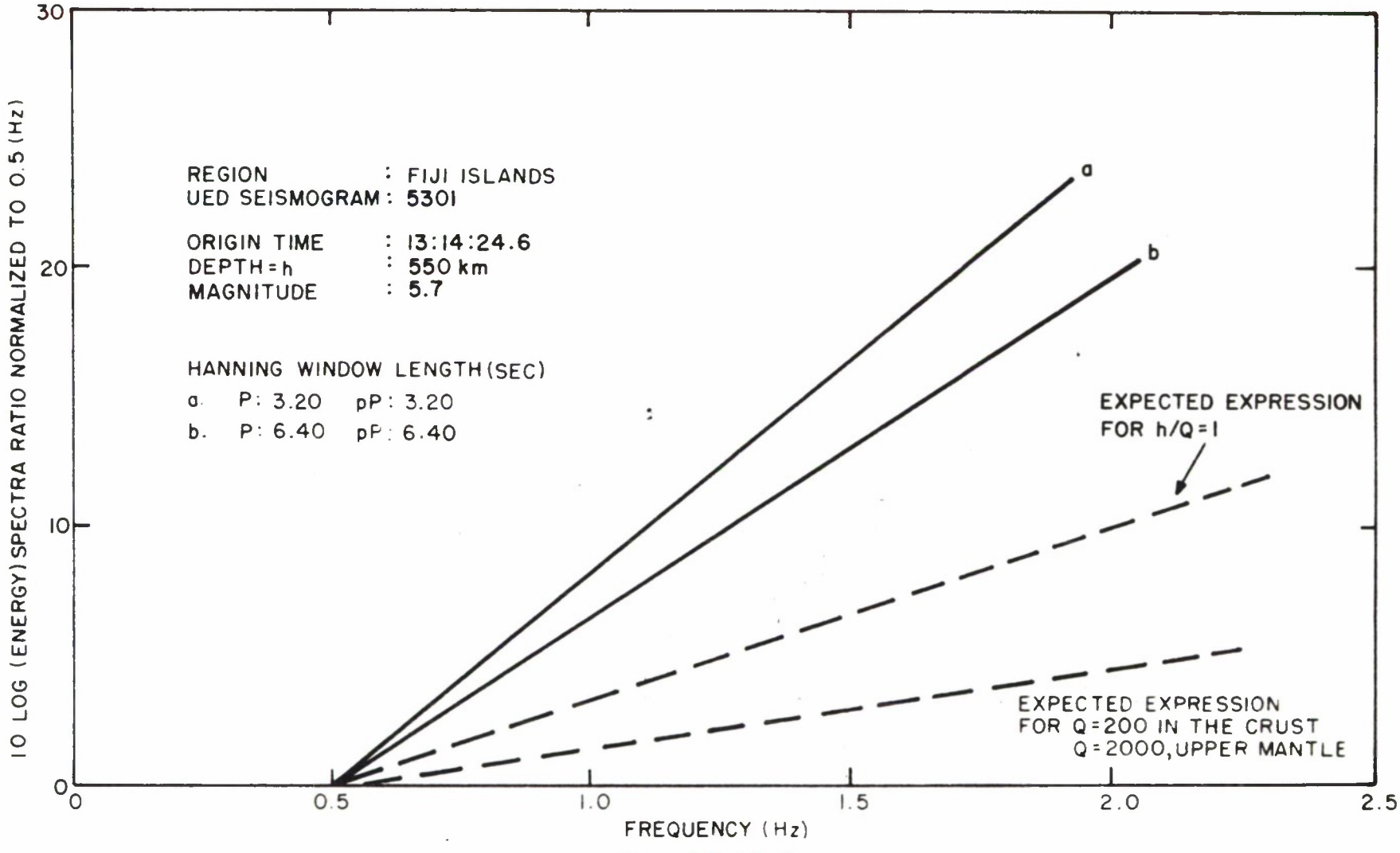


FIGURE 13.3

LEAST SQUARES FITS TO THE EXPERIMENTAL RATIOS OF ENERGY SPECTRA
7 OCTOBER 1963 EVENT

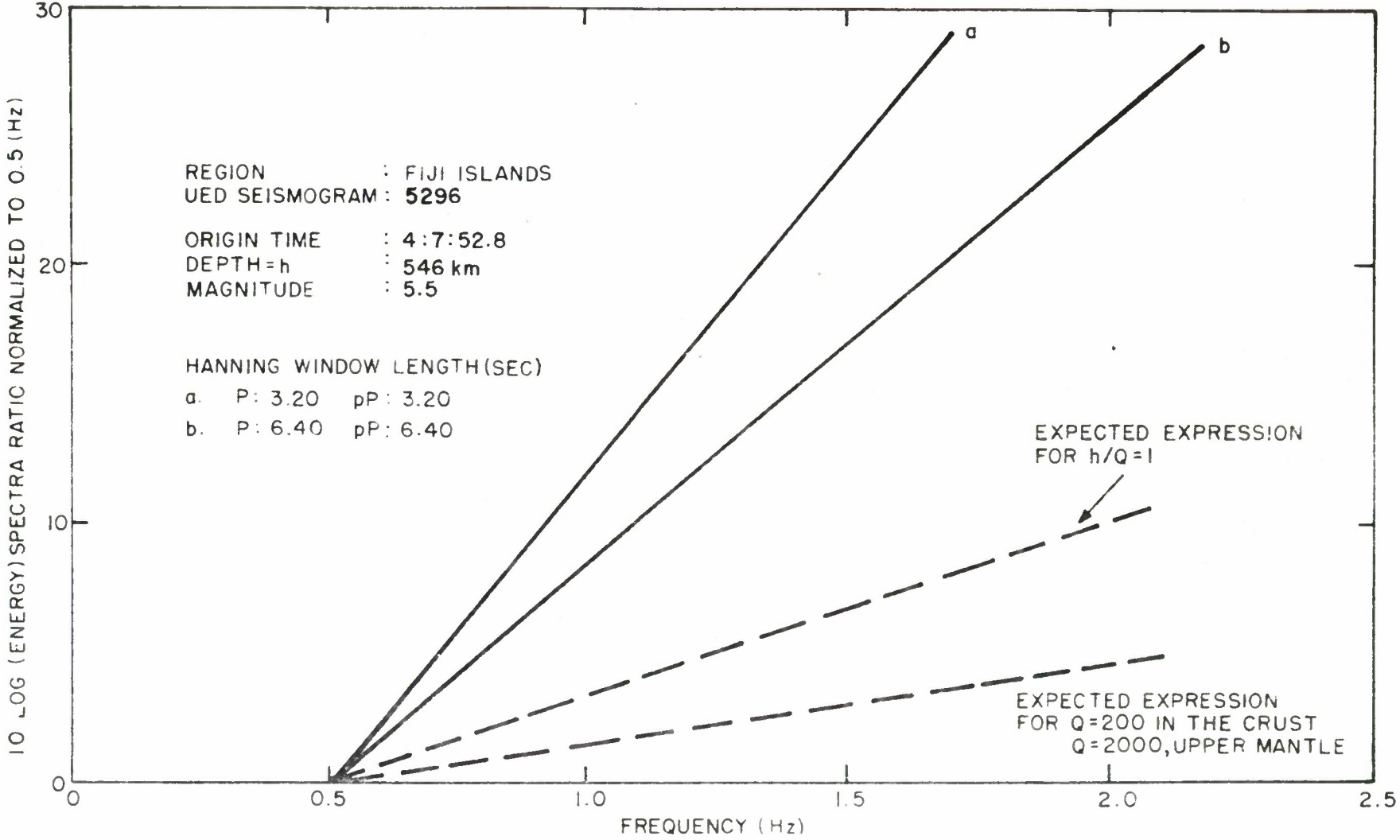


FIGURE 13.4

LEAST SQUARES FITS TO THE EXPERIMENTAL RATIOS OF ENERGY SPECTRA
26 DECEMBER 1963 EVENT

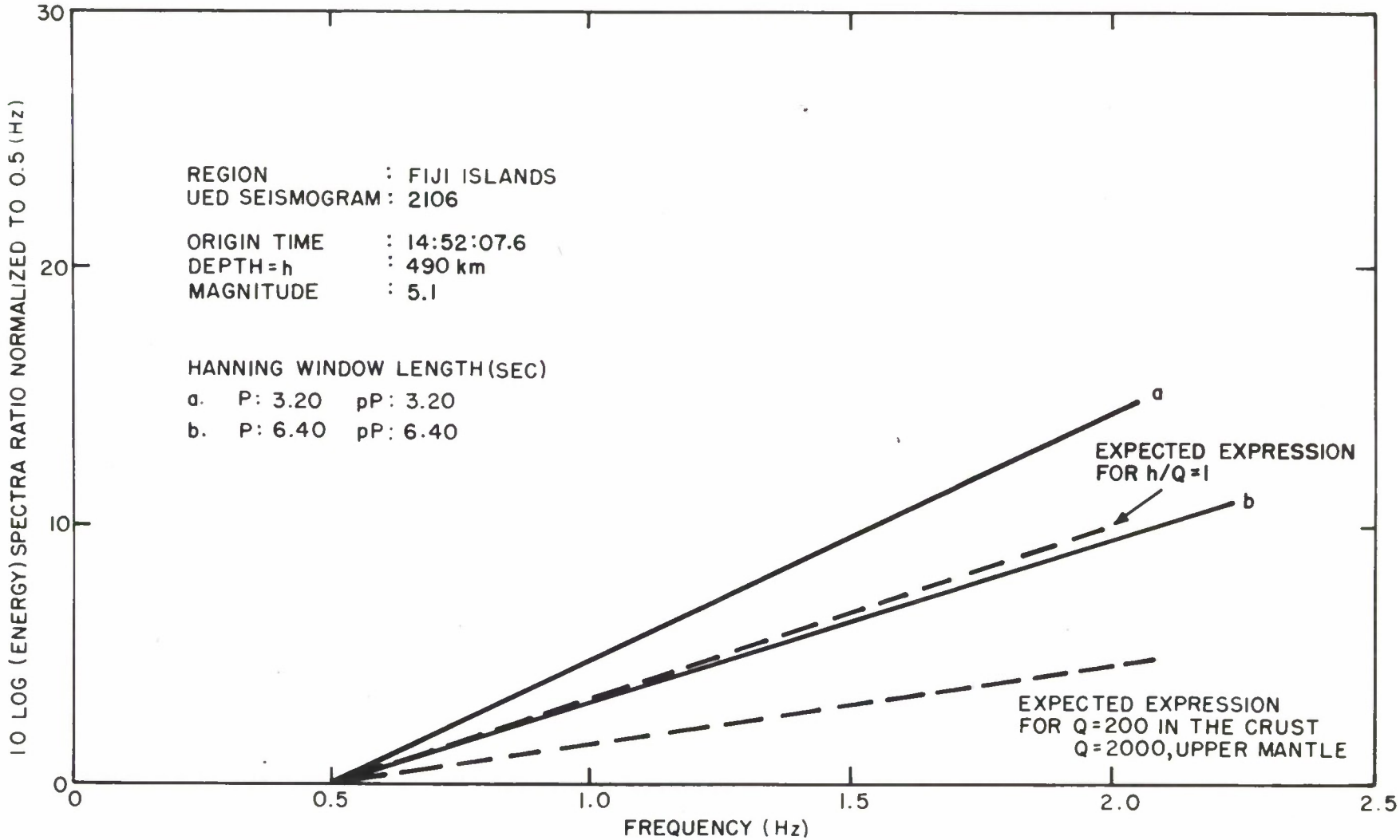


FIGURE 13.5

LEAST SQUARES FITS TO THE EXPERIMENTAL RATIOS OF ENERGY SPECTRA
26 APRIL 1964 EVENT

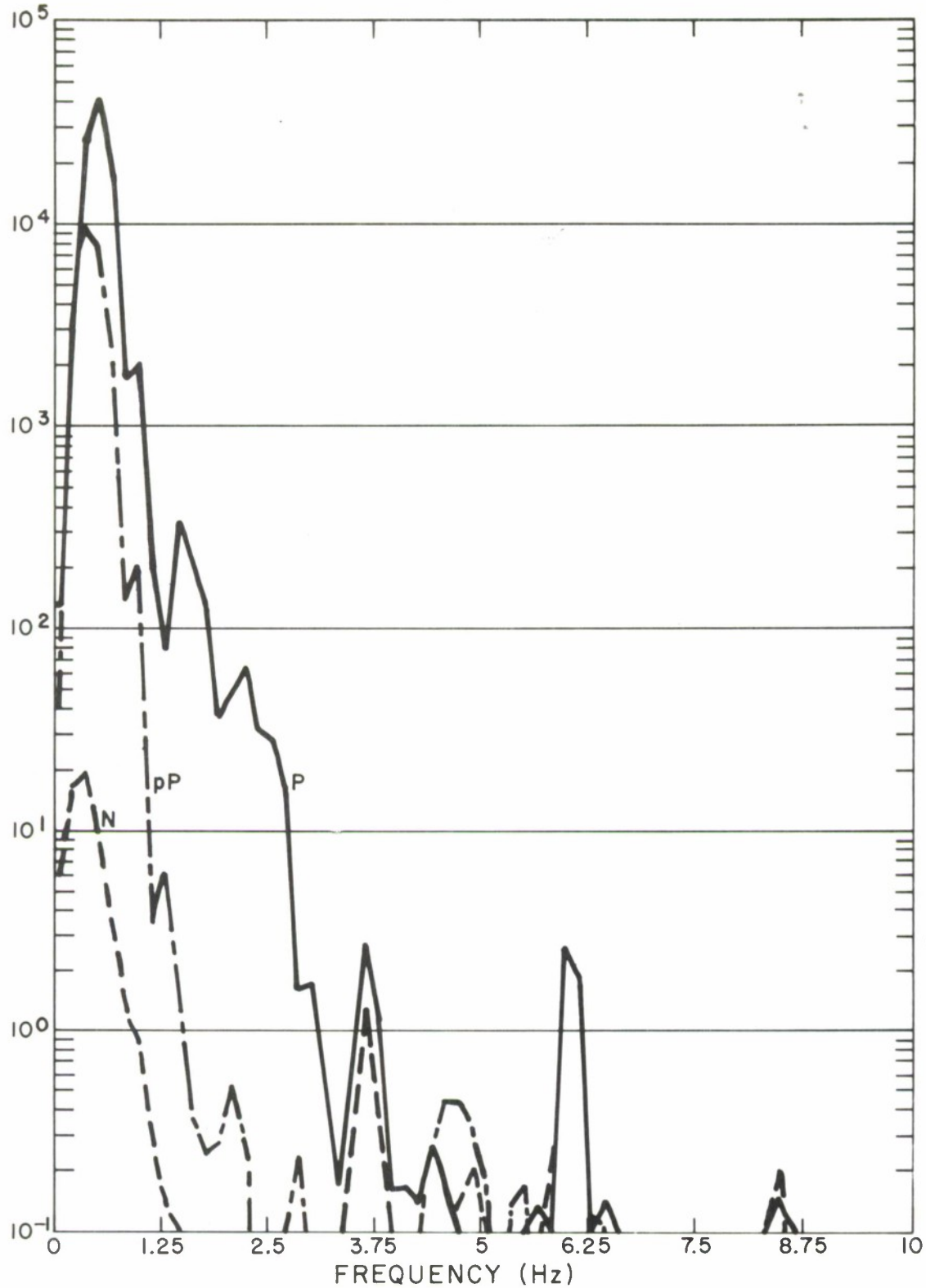


FIGURE 13.6

SPECTRA FOR 7 OCT 63 EVENT

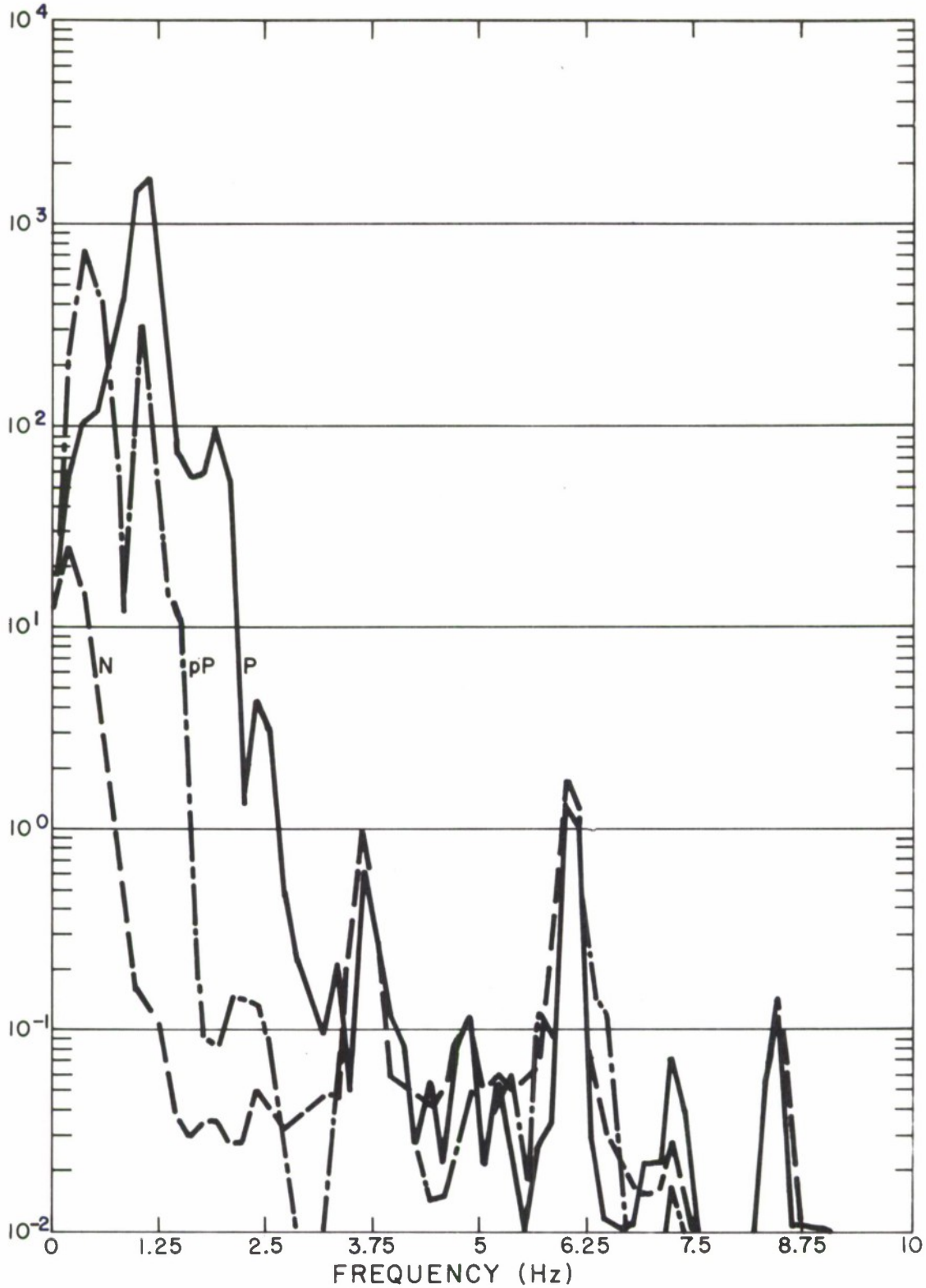


FIGURE 13.7
SPECTRA FOR 7 DEC 63 EVENT

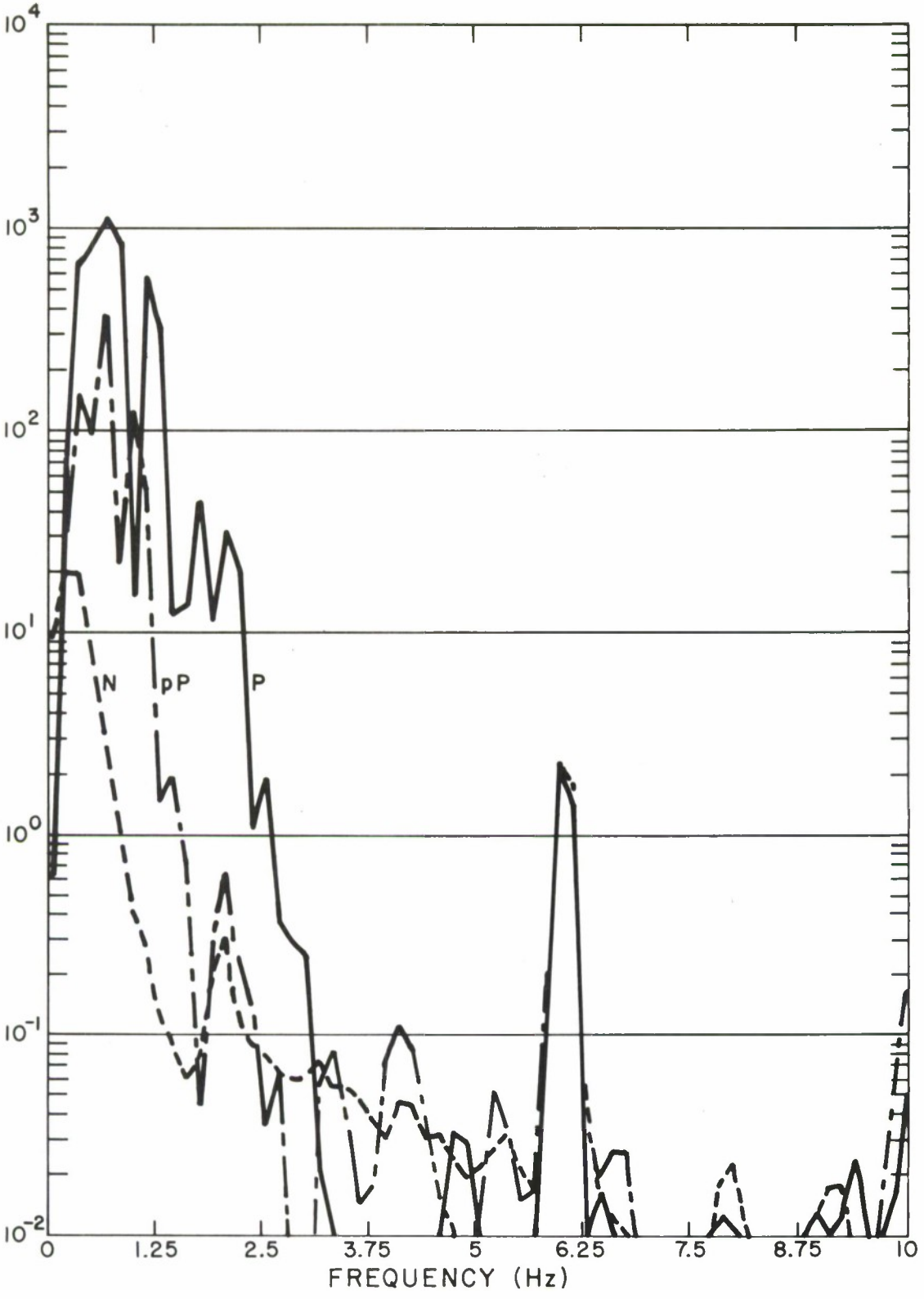


FIGURE 13.8
SPECTRA FOR 26 APR 64 EVENT

13.3 EXTENSION OF THE METHOD TO ANALYZE ASEISMIC REGIONS

Some seismic stations have shown a greater high frequency content in their records than others. This could mean that the attenuation characteristics of the upper mantle are regionally dependent. To analyze this hypothesis, the following method is suggested.

Let us assume that we are interested in studying the attenuation characteristics of the upper mantle of a certain region where there are no deep earthquakes. Let us call that area region S. We must first study some other region which possesses both deep earthquakes and a seismic station. Let us call this region A. Records obtained at A and a station in S may then be compared, taking the ratio of the energy spectra of the P arrivals. The ratio of the energy spectra of the P phase recorded at A and S enables us to compare the attenuation characteristics of the upper mantle in the region S with the value of Q determined for region A by the method suggested in Section 13.1. It is important to note that in following this procedure care must be taken to include any frequency dependent radiation pattern effects which will result from geometry of the measurement.

13.4 SUMMARY AND CONCLUSIONS

This section has presented calculations directed at estimating the Q for the upper mantle in the Fiji Island region. Data from three very deep earthquakes have been used. In each case the energy density spectrum for a 6.4 sec time window including the P phase and for another 6.4 sec time window including the pP phase has been calculated. On the assumption that the Q is independent of frequency, the constant value of Q was estimated in each case by fitting a straight line to a logarithmic plot of the ratio of these two energy density spectra vs frequency. For the purposes of this straight-line fit, frequencies in the range .156 to 1.88 Hz were used. Similar calculations were also performed using 3.2 sec time windows for both P and pP phases. Considerable variation occurs in the resulting estimates for the upper mantle Q; however, all values are below 500. It should be stressed that this estimate is intended to apply only to the Fiji Island region. In other regions of the earth the upper mantle Q might be quite different. The technique used in this chapter applied directly only to regions with very deep earthquakes; however, a method of extending this technique to aseismic regions was also discussed above.

APPENDIX A

TABLES

Tables that are referenced by more than one section, or are not essential to the understanding of a specific section, are presented in this appendix. A brief description of the contents of each table follows.

Table X is the event list that is referenced by several sections of this report. The event numbers have been assigned chronologically for convenience in this report. The information on these events was obtained from the Vela Seismological Center and the Seismic Data Laboratory, as indicated on the table.

Tables XI-XIII summarize calculations that are discussed in Sections VIII-X. These tables are organized according to the calculations presented in Section X (Automatic pP Test). The estimated depths are based on the Figures listed in the tables. The number of stations and the minimum and maximum range from the epicenter are also given in the tables. The actual stations used on each calculation are listed in Table XIV, in order of increasing range from the epicenter. The last three columns of Tables XI-XIII list calculated average paired correlation coefficients for noise, P-phase, and coda. The average value is followed by ± the standard deviation of the samples that determined the average. This calculation is defined in Section VII. The last column ($\overline{\rho}_c$) is discussed in Section IX. The preceding two columns ($\overline{\rho}_n$ and $\overline{\rho}_P$) are discussed in Section VIII.

Table XV and XVI are station lists corresponding to the calculated array patterns presented in Figures 5.8 and 5.9.

TABLE X LIST OF EVENTS

EVENT	DATE	REGION	LAT	LON	ORIGIN TIME	DEPTH	MAG
1	2 FEB. 62	KAZAKH	49.9N	78.2E	7/59/58.5	0	-
2	1 MAY 62	ALGERIA	23.8N	5.4E	9/59/57.1	0	-
3	10 JAN. 63	KAMCHATKA	52.6N	157.2E	17/14/07.3	160*	4.8*
4	12 MAY 63	KAMCHATKA	55.9N	163.1E	20/37/12.9	40*	5.0*
5	20 MAY 63	YAKUTSK,USSR	72.1N	126.3E	17/01/40.2	15*	4.9*
6	26 MAY 63	KAMCHATKA	55.2N	159.9E	23/06/55.0	15*	5.3*
7	27 MAY 63	KAMCHATKA	55.3N	160.1E	3/58/47.9	15*	5.7*
8	21 JUNE 63	MANCHURIA	47.9N	130.3E	13/44/24.6	15*	4.8*
9	2 JULY 63	KURILES	45.7N	149.1E	15/03/09.6	15*	4.6*
10	5 JULY 63	MONGOLIA	50.4N	90.6E	3/29/36.1	S*	4.4*
11	15 JULY 63	KAMCHATKA	55.6N	162.0E	8/41/07.5	60*	4.9*
12	16 JULY 63	GEORGIA,USSR	43.1N	41.5E	18/27/18.4	15*	6.0*
13	17 JULY 63	GEORGIA,USSR	43.1N	41.5E	11/57/06.7	S*	5.1*
14	30 JULY 63	KAMCHATKA	51.7N	158.1E	6/52/22.7	S*	5.4*
15	1 AUG. 63	KAMCHATKA	55.3N	161.8E	10/45/02.7	40*	5.1*
16	7 AUG. 63	SAKHALIN	54.0N	142.1E	4/33/42.7	20*	5.1*
17	25 AUG. 63	SEA OF OKHOTSK	48.7N	148.8E	2/20/12.7	134*	4.7*
18	9 SEPT. 63	KAMCHATKA	54.0N*	160.2E*	12/43/48.3*	S*	5.6*
19	20 OCT. 63	ALGERIA	24.1N	5.1E	12/59/58.6	QR**	5.6
20	2 JAN. 64	KAMCHATKA	53.0N	159.6E	5/01/53.5	40*	5.1*
21	2 JAN. 64	KAMCHATKA	54.6N	161.5E	5/21/00.5	40*	4.9*
22	6 JAN. 64	KAMCHATKA	50.9N	157.3E	23/45/23.4	60*	6.0*
23	14 JAN. 64	KAMCHATKA	52.9N	159.6E	1/11/12.6	40*	5.0*
24	15 MAR. 64	KAZAKH	49.7N	78.0E	7/59/58.0	0	5.6
25	22 MAR. 64	KAMCHATKA	54.0N	160.5E	0/52/38.8	S*	5.0*
26	16 MAY 64	KAZAKH	49.9N	78.3E	6/00/58.1	0	5.6
27	1 JULY 64	KURILES	46.3N	146.9E	2/47/33.9	35*	5.2*
28	21 JULY 64	LAPTEV SEA	72.1N	130.2E	9/56/16.6	S*	5.1*
29	24 JULY 64	SVALBARD	85.9N	20.6E	20/29/11.5	S*	4.6*
30	27 JULY 64	KAMCHATKA	61.5N	163.9E	0/15/44.7	10*	4.6*

TABLE X (Continued)

EVENT	DATE	REGION	LAT	LON	ORIGIN TIME	DEPTH	MAG
31	31 JULY 64	ARCTIC OCEAN	86.3N	40.5E	23/45/55.2	25*	4.9*
32	1 SEPT. 64	FOX ISLANDS	51.2N	170.6W	17/16/40.4	25	5.5
33	25 SEPT. 64	RAT ISLANDS	50.3N	176.6E	15/42/17.9	30	5.5
34	25 OCT. 64	NOVAYA ZEMLYA	73.5N	53.7E	7/59/58.8	0	4.9
35	16 NOV. 64	KAZAKH	49.7N	78.0E	5/59/57.4	0	6.0
36	27 FEB. 65	ALGERIA	24.2N	5.1E	11/29/59.0	0	5.8
37	3 MAR. 65	KAZAKH	49.8N	78.1E	6/14/57.0	0	5.6
38	3 MAR. 65	RAT ISLAND	53.1N	171.2E	16/47/25.7	23	5.6
39	5 MAR. 65	RAT ISLAND	51.2N	179.3E	6/15/01.1	25	5.6
40	17 MAR. 65	ALEUTIANS	52.8N	171.9E	14/27/12.4	23	6.0
41	8 OCT. 65	KAZAKH	49.9N	78.0E	5/59/58.6	0	5.7
42	29 OCT. 65	AMCHITKA	51.4N*	179.2E*	21/00/00.1*	0*	6.0*
43	21 NOV. 65	KAZAKH	49.8N	78.1E	4/57/57.9	0	5.8
44	21 NOV. 65	KURILE IS.	48.4N	154.7E	6/10/56.0	33	4.7
45	13 FEB. 66	KAZAKH	49.8N	78.1E	4/57/57.7	0	6.3
46	21 APR. 66	KURILE IS.	45.6N	150.1E	8/07/25.0	33	4.5
47	7 MAY 66	KAZAKH	49.7N	77.9E	3/57/58.0	0	4.9

*Information from Vela Seismological Center, 300 North Washington Street, Alexandria, Virginia. All other information from Seismic Data Laboratory, C&GS Epicenter List, 300 North Washington Street, Alexandria, Virginia.

**Restrained to 0 depth because of proximity to surface-focus event #36, C&GS depth = 33 km (implies no computer solution).

TABLE XI SUMMARY OF DEPTH ESTIMATES AND CORRELATIONS - 11 EARTHQUAKES

EVENT NO.	MAG	NO.OF STA.	STA. RANGE(km) MIN MAX	DEPTH (km)	DEPTH EST(km)	FIGURE NO.	$\bar{\rho}_n$	$\bar{\rho}_P$	$\bar{\rho}_c$
3	4.8	5	5985- 7128	160	not	10.2A	- .08±.19	.75±.18	-.01±.09
22	6.0	9	4430- 8652	60	10-40	10.2B	.00±.17	.92±.07	.11±.24
15	5.1	7	5573- 8095	40	40	10.2C	.05±.12	.91±.07	.18±.19
4	5.0	7	5471- 7372	40	40	10.2D	.03±.17	.92±.05	.35±.18
7	5.7	9	5684- 8190	15	13	10.2E	.01±.17	.94±.04	.41±.23
12	6.0	7	9792-11167	15	10	10.2F	- .01±.16	.91±.11	.37±.20
27	5.2	10	5194- 8621	35	32	10.2G	.02±.11	.95±.03	.58±.30
5	4.9	7	6134- 7815	15	14	10.2H	.04±.11	.58±.27	.42±.28
11	4.9	10	5823- 8211	60	19	10.2I	.00±.14	.89±.09	.28±.18
16	5.1	12	6740- 9090	20	24	10.2J	.00±.09	.95±.04	.35±.19
8	4.8	9	7803- 9651	15	16	10.2K	- .03±.11	.90±.07	.36±.31

TABLE XII SUMMARY OF ESTIMATES AND CORRELATIONS - 20 EARTHQUAKES

EVENT NO.	MAG	NO.OF STA.	STA. RANGE(km) MIN.	MAX.	DEPTH (km)	DEPTH EST(km)	FIGURE NO.	$\bar{\rho}_n$	$\bar{\rho}_P$	$\bar{\rho}_c$
21	4.9	5	5617-	8141	40	38	10.4A	- .05±.19	.95±.04	.23±.21
29	4.6	5	2930-	6570	S	14	10.4B	.01±.09	.96±.04	.24±.20
30	4.6	6	3178-	7067	10	14	10.4C	- .03±.16	.89±.10	.29±.26
18	5.6	5	4023-	8264	S	11	10.4D	- .02±.13	.95±.03	.16±.24
31	4.9	5	3010-	6482	25	13	10.4E	- .04±.14	.90±.08	.18±.17
28	5.1	5	6042-	7764	S	13	10.4F	- .02±.12	.96±.04	.24±.22
10	4.4	5	9120-	10546	S	10	10.4G	.12±.20	.94±.03	.23±.22
13	5.1	4	10039-	11004	S	17	1.04H	.02±.10	.89±.09	.29±.11
23	5.0	4	4144-	7009	40	>40	10.4I	.04±.03	.94±.04	- .02±.29
20	5.1	5	5820-	8372	40	>40	10.4J	- .01±.20	.93±.05	.06±.31
25	5.0	8	4031-	8267	S	not 10-40	10.4K	.00±.16	.87±.10	- .04±.21
14	5.4	4	5978-	8546	S	<10	10.4L	.12±.13	.93±.06	.03±.18
6	5.3	5	5689-	8197	15	14	10.4M	.03±.12	.98±.01	.68±.10
9	4.6	5	6871-	9459	15	11	10.4N	.01±.09	.87±.09	.26±.17
17	4.7	10	6300-	8628	134	13	10.4T	.01±.13	.95±.07	.37±.23
40	6.0	12	5455-	7703	23	22	10.4O 10.3C 10.3D	- .02±.19	.79±.22	.20±.24
33	5.5	11	5120-	7659	30	33	10.4P	.04±.16	.83±.11	.16±.27
39	5.6	9	4987-	6601	25	not 10-40	10.4Q	- .01±.19	.86±.12	.24±.29
38	5.6	7	5366-	7718	23		10.4R	.05±.10	.95±.05	.27±.20
32	5.5	15	4223-	6939	25	16	10.4S 10.6C	- .01±.13	.94±.05	.19±.21
32	5.5	7	4223-	6875	25	16	10.6A	- .03±.13	.94±.05	.15±.19
32	5.5	8	4284-	6939	25	17	10.6B	.00±.14	.94±.04	.22±.23

TABLE XIII SUMMARY OF DEPTH ESTIMATES AND CORRELATIONS-12 SURFACE-FOCUS EVENTS

EVENT NO.	MAG	NO.OF STA.	STA. RANGE(km) MIN.	MAX.	DEPTH (km)	DEPTH EST(km)	FIGURE NO.	$\bar{\rho}_n$	$\bar{\rho}_P$	$\bar{\rho}_c$
1	-	9	9597-10613		0	not 10-40 km	10.5A 10.3A 10.3B	.05±.19	.79±.20	.03±.15
34	4.9	6	3391- 7961		0		10.5B	- .04±.12	.79±.19	.20±.25
37	5.6	8	7970-10660		0		10.5C	.00±.17	.79±.19	.06±.13
43	5.8	9	5970-10117		0		10.5D	- .02±.16	.67±.25	- .01±.16
19	5.6	7	6834-10300		0 R*		10.5E	.12±.13	.87±.07	.02±.13
26	5.6	9	4235-10115		0		10.5F	- .01±.14	.82±.16	- .01±.16
42	6.0	20	3841- 8123		0		10.5G	.00±.10	.85±.13	.00±.20
24	5.6	5	9062-10421		0		10.5H	- .01±.11	.89±.10	.05±.10
41	5.7	6	8828-10648		0		10.5I	- .06±.31	.60±.24	.04±.19
35	6.0	12	4659-10653		0		10.5J 10.6F	- .05±.18	.82±.16	.04±.19
2	-	9	8898-10443		0		10.5K	- .01±.10	.83±.16	.05±.19
36	5.8	13	6694-10758		0		10.5L 10.6I	.01±.22	.82±.18	.03±.15
35	6.0	6	7973-10336		0		10.6D	.07±.19	.77±.20	.04±.12
35	6.0	6	4659-10653		0		10.6E	.13±.14	.85±.11	- .01±.18
36	5.8	6	6694-10699		0		10.6G	.02±.22	.76±.20	.02±.13
36	5.8	7	7834-10758		0		10.6H	.00±.18	.84±.14	.04±.12

*Restrained to 0 depth because of proximity to surface-focus event #36
C&GS depth = 33 km (implies no computer solution)

TABLE XIV STATION LIST FOR CALCULATIONS SUMMARIZED IN TABLES XI -XIII

EVENT	FIGURE	STATIONS
3	10.2A	BMO,HL-IDWI-NV,MN-NV,DR-CO
22	10.2B	NP-NT,FR-MA,GI-MA,KN-UT,TFO,WMO,HN-ME,GG-GR,CPO
15	10.2C	BMO,MN-NV,UBO,KN-UT,TFO,WMO,CPO
4	10.2D	BMO,MN-NV,UBO,KN-UT,TFO,LC-NM,WMO
7	10.2E	BMO,HL-ID,UBO,PM-WY,NG-WS,WMO,HN-ME,BR-PA,CPO
12	10.2F	FR-MA,CPO,BMO,UBO,WMO,MN-NV,TFO
27	10.2G	NP-NT,GI-MA,KN-UT,SG-AZ,NL-AZ,WO-AZ,TFO,SN-AZ, GE-AZ,LC-NM
5	10.2H	BMO,UBO,DR-CO,TFO WMO,LC-NM,CPO
11	10.2I	HL-ID,MN-NV,FR-MA,WW-UT,KN-UT,CP-CL,DR-CO,TFO, LC-NM,EU-AL
16	10.2J	BMO,HL-ID,WI-NV,FR-MA,GI-MA,MN-NV,RK-ON,EB-MT, KN-UT,TFO,LC-NM,CPO
8	10.2K	BMO,HL-ID,MN-NV,BF-CL,UBO,KN-UT,PM-WY,TFO,WMO
21	10.4A	BMO,UBO,TFO,WMO,CPO
29	10.4B	OO-NW,BMO,UBO,WMO,TFO
30	10.4C	NP-NT,BMO,UBO,OO-NW,TFO,WMO
18	10.4D	NP-NT,BMO,UBO,TFO,CPO
31	10.4E	OO-NW,GG-GR,BMO,UBO,WMO
28	10.4F	BMO,UBO,TFO,WMO,CPO
10	10.4G	BMO,UBO,TFO,CPO,WMO
13	10.4H	BMO,UBO,WMO,TFO
23	10.4I	NP-NT,BMO,UBO,TFO
20	10.4J	BMO,UBO,TFO,WMO,CPO
25	10.4K	NP-NT,BMO,UBO,TFO,OO-NW,WMO,GG-GR,CPO
14	10.4L	BMO,UBO,WMO,CPO
6	10.4M	BMO,UBO,TFO,WMO,CPO
9	10.4N	BMO,UBO,TFO,WMO,CPO
17	10.4T	TK-WA,BMO,WI-NV,MN-NV,UBO,KN-UT,BX-UT,TFO,RT-NM, WMO
40	10.40,10.3C 10.3D	MN-NV,RY-ND,KN-UT,RK-ON,JR-AZ,WO-AZ,SN-AZ,GE-AZ, RT-NM,VO-IO,DH-NY,BR-BA
33	10.4P	HL2ID,RY-ND,LG-AZ,SN-AZ,GP-MN,RT-NM,LC-NM,LS-NH, DH-NY,BL-WV,HN-ME

TABLE XIV (continued)

EVENT	FIGURE	STATIONS
39	10.4Q	MN-NV,KN-UT,SG-AZ,JR-AZ,LG-AZ,HR-AZ,RT-NM,LC-NM, FO-TX
38	10.4R	HL2ID,HR-AZ,SN-AZ,LC-NM,LS-NH,DH-NY,BR-PA
32	10.4S 10.6C	HL2ID,MN-NV,EK-NV,KN-UT,SG-AZ,RY-ND,NL-AZ,DR-CO, GE-AZ,RT-NM,BR-PA,BL-WV,DH-NY,LS-NH,HN-ME
32	10.6A	HL2ID,KN-UT,RY-ND,DR-CO,RT-NM,BL-WV,LS-NH
32	10.6B	MN-NV,EK-NV,SG-AZ,NL-AZ,GE-AZ,BR-PA,DH-NY,HN-ME
1	10.5A,10.3A 10.3B	VT-OR,WN-SD,WI-NV,PM-WY,MV-CL,MN-NV,DR-CO,WM-AZ, TN-CL
34	10.5B	NP-NT,VO-IO,EK-NV,WMO,HR-AZ
37	10.5C	SV2QB,RK-ON,BMO,HL2ID,UBO,RT-NM,WMO,TFO
43	10.5D	NP-NT,PG-BC,JP-AT,RK-ON,HV-MA,WN-SD,CR-NB,WMO, MN-NV
19	10.5E	HN-ME,BL-WV,RK-ON,EB-MT,GI-MA,FR-MA,HL-ID
26	10.5F	00-NW,GG-GR,EKA,NP-NT,RK-ON,TK-WA,GI-MA,HL2ID, MN-NV
42	10.5G	PG-BC,YR-CL,BMO,HL2ID,HV-MA,MN-NV,TE-GL,TF-CL, CH-MT,LAO,KN-UT,RG-SD,LC-NM,KC-MO,WMO,SV3QB, SJ-TX,CPO,HN-ME,BE-FL
24	10.5H	HH-ND,GI-MA,BR-PA,MN-NV,RT-NM
41	10.5I	RK-ON,BMO,HL2ID,MN-NV,WMO,TFO
35	10.5J 10.6F	GG-GR,NP-NT,SV2QB,RK-ON,BMO,HL2ID,VO-IO,BR-PA, UBO,MN-NV,DR-CO,WMO
2	10.5K	SE-MN,MP-AR,WMO,SJ-TX,VN-UT,HL-ID,EP-TX,LC-NM, LP-TX
36	10.5L 10.6I	SV2QN,HN-ME,BR-PA,RK-ON,VO-IO,RY-ND,WMO,RT-NM, UBO,WO-AZ,KN-UT,TF-EX,SN-AZ
35	10.6D	SV2QB,RK-ON,HL2ID,BR-PA,MN-NV,DR-CO
35	10.6E	GG-GR,NP-NT,BMO,VO-IO,UBO,WMO
36	10.6G	SV2QB,HN-ME,RK-ON,WMO,UBO,TF-EX
36	10.6H	BR-PA,VO-IO,RY-ND,RT-NM,WO-AZ,KN-UT,SN-AZ

TABLE XV STATION LIST FOR ARRAY PATTERN PRESENTED IN FIGURE 5.8

STATION	LATITUDE	LONGITUDE
MN-NV	38 26 10 N	118 08 53 W
HL2ID	42 33 40 N	114 25 08 W
FR-MA	46 06 00 N	106 26 25 W
GI-MA	47 11 34 N	104 13 10 W
RY-ND	48 05 50 N	101 29 40 W
HH-ND	48 56 53 N	98 41 33 W
KN-UT	37 01 22 N	112 49 39 W
RK-ON	50 50 20 N	93 40 20 W
SG-AZ	35 38 27 N	113 15 39 W
LG-AZ	34 24 28 N	111 32 45 W
DR-CO	37 27 53 N	107 47 00 W
SN-AZ	33 51 49 N	111 41 34 W
HR-AZ	34 40 11 N	110 45 59 W
RT-NM	36 43 46 N	104 21 37 W
HN-ME	46 09 43 N	67 59 09 W
LS-NH	44 14 18 N	71 55 21 W
DH-NY	42 14 39 N	74 53 18 W
BL-WV	37 47 56 N	81 18 36 W
WN-SD	43 15 08 N	100 11 46 W
GV-TX	32 53 09 N	96 59 54 W
NP-NT	76 15 08 N	119 22 18 W
LC-NM	32 24 08 N	106 35 58 W
BMO	44 50 56 N	117 18 20 W
UBO	40 19 18 N	109 34 07 W
CPO	35 35 41 N	85 34 13 W
WMO	34 43 05 N	98 35 21 W
TFO	34 17 12 N	111 16 03 W

TABLE XVI STATION LIST FOR ARRAY PATTERN PRESENTED IN FIGURE 5.9

STATION	LATITUDE	LONGITUDE
NP-NT	76 15 08 N	119 22 18 W
HL2ID	43 33 40 N	114 25 08 W
RT-NM	36 43 46 N	104 21 37 W
VO-IO	42 13 30 N	92 07 37 W
SV2QB	54 48 54 N	66 45 31 W
RY-ND	48 05 50 N	101 29 40 W
KN-UT	37 01 22 N	112 49 39 W
DH-NY	42 14 39 N	74 53 18 W
BR-PA	39 55 27 N	78 50 41 W
WO-AZ	34 52 53 N	110 37 15 W
SN-AZ	33 51 49 N	111 41 34 W
MN-NV	38 26 10 N	118 08 53 W
GE-AZ	35 38 27 N	113 15 39 W
JR-AZ	34 49 32 N	111 59 25 W
TFO	34 17 12 N	111 16 03 W
WMO	34 43 05 N	98 35 21 W
CPO	35 35 41 N	85 34 13 W

APPENDIX B

ANGULAR ACCURACY OF A PHASED SEISMIC ARRAY

A theory of angle measurements with phased arrays in radar has been presented by Brennan (31). In this appendix the errors due to additive noise in the measurement of angles of arrival with seismic arrays will be discussed. In particular we are interested in the effects of the signal-to-noise ratio of the event and the aperture of the array on the standard deviation of the error.

Brennan has obtained expressions for the standard deviation of the error in the measurement of angles with phased array radar. We will use his results, pointing out the assumptions used. Consider the linear array with equally spaced elements shown in Figure B.1. For such an array, there is a one-to-one correspondence between the angle of arrival of the signal at the array and the differential arrival times of the signal at two adjacent elements of the array. When the received signal is a continuous sine wave, it is possible to replace the differential time measurement with one of the phase difference of the signals at pairs of adjacent elements of the array.

Clearly, when the received signals are corrupted by noise, a coherent addition of the outputs of all of the elements of the array will give a better estimate of the arrival angle than would the measurement of the phase angle between any two elements. Once this addition has taken place, however, it is then possible to express the result in terms of the phase difference between pairs of adjacent elements. For the case where the noise is independent between elements and normally distributed, and both the signal and the noise occupy the same narrow band of frequencies, the mean value of the error in measurement is zero and the variance of the error in the measurement of the phase difference between each pair of adjacent elements is given by

$$\mathrm{var}(\hat{\delta}) = \frac{12\sigma^2}{N^3-N} \qquad \text{(B.1)}$$

where $\hat{\delta}$ = estimate of the phase difference between adjacent elements
σ^2 = noise power in one element
1/2 = signal power in one element
N = number of elements

It should be noted that this is a lower bound for the variance of the error. This bound is obtained using a theorem of statistics that applies to all regular unbiased estimates. How close we can approach this limit in accuracy depends on the actual method of estimation used. The phase difference δ is related to the angle θ between the direction of arrival of the wave and the axis of the array by the following expression.

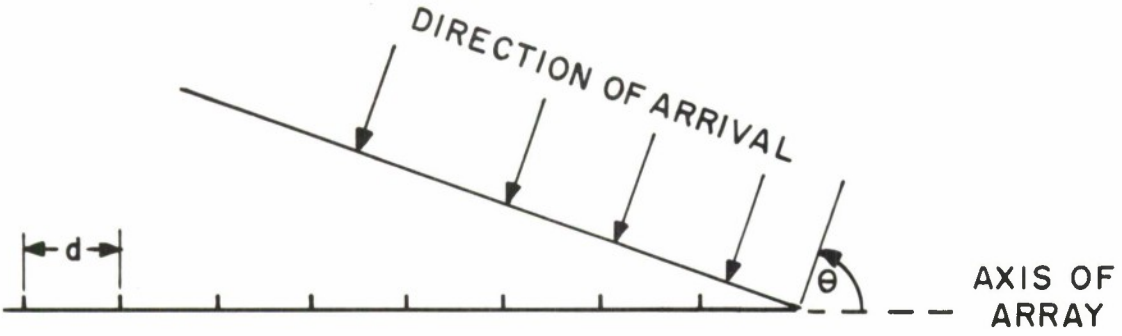


FIGURE B-1

LINEAR PHASED ARRAY GEOMETRY

$$\delta = \frac{2\pi d}{\lambda} \cos\theta \tag{B.2}$$

where d = distance between elements
λ = wavelength
For small errors,

$$\mathrm{Var}(\hat{\theta}) = \frac{1}{\sin^2\theta} \mathrm{Var}(\cos\hat{\theta}) \tag{B.3}$$

Now,

$$L \text{ (the length of the array)} = (N-1)d \simeq N \cdot d \tag{B.4}$$

$$\cos\theta = \frac{\delta\lambda N}{2\pi L} \tag{B.5}$$

$$\mathrm{Var}(\cos\hat{\theta}) = \frac{\lambda^2 N^2}{4\pi^2 L^2} \mathrm{Var}(\hat{\delta}) \tag{B.6}$$

$$\mathrm{Var}(\theta) = \frac{\lambda^2 N^2}{4\pi^2 L^2 \sin^2\theta} \cdot \frac{12\sigma^2}{N^3-N} \tag{B.7}$$

If the number of elements, N, is large, we can neglect N (compared to N^3), and letting the signal-to-noise power ratio at one element be given by

$$(S/N)_{P,1} = \frac{1}{2\sigma^2} , \tag{B.8}$$

$$\mathrm{Var}(\theta) = \frac{\lambda^2 6}{4\pi^2 L^2 N (S/N)_{P,1} \cdot \sin^2\theta} \tag{B.9}$$

The signal-to-noise ratio of the phased sum will be

$$N \cdot (S/N)_{P,1} = (S/N)_{P,T} = [(S/N)_{V,T}]^2 \tag{B.10}$$

since independent noise at the different sensors is assumed.

$$\text{St. dev. } (\hat{\theta}) = \frac{1.2\lambda}{\pi L (S/N)_{V,T} \sin\theta} \tag{B.11}$$

As an example, let us consider a linear seismic array and a seismic wave arriving from a direction broadside to the array ($\theta = \pi/2$).

$$\begin{aligned} &\text{Let } d = 10 \text{ km} \\ &\quad\; L = 200 \text{ km} \\ &\quad\; \lambda = 10 \text{ km} \end{aligned} \tag{B.12}$$

$$\text{St. dev. } (\hat{\theta}) = \frac{0.019}{(S/N)_{V,T}} \text{ radians}$$

(θ is the station to epicenter azimuth.) The range estimation has an additional problem since the effect of a change in range on the angle of incidence is small at teleseismic distances.

From Richter (32) we can see that for teleseismic distances

$$0.1 < \frac{di}{d\Delta} < 0.7 \qquad \text{(B.13)}$$

where i is the angle of incidence in degrees, and
Δ is the range in degrees
If we take, for instance, $\Delta = 60°$

$$\frac{di}{d\Delta} = 0.1 \qquad \text{(B.14)}$$

The standard deviation of the error in the range measurement will be one order of magnitude larger than was the case for the azimuth measurement.

REFERENCES

1. B.D. Steinberg, "Large Aperture Teleseismic Array Theory," in *First LASA Systems Evaluation Conference Proceedings*, Chapter 15, p. 140, 14-16 September 1965. [AD 648415]

2. General Atronics Corporation, "Final Study Report on Systems Aspects of Seismic Detection and Identification of Nuclear Explosions," Contract SD-283, January 1966.

3. H. Jeffreys and K.E. Bullen, *Seismological Tables*, Office of the British Association, 1958.

4. R.T. Lacoss, "Geometry and Patterns of Large Aperture Seismic Arrays," Lincoln Laboratory Technical Note 1965-64 31 December 1965.

5. H.W. Briscoe and R.M. Sheppard, "A Study of the Capability of a LASA to Aid the Identification of a Seismic Source," Lincoln Laboratory Technical Note 1966-38, pp.6-8, 11 July 1966.

6. D.E. Frankowski and F.A. Klappenberger, "Travel-Time Anomalies at LASA," Report No. LL-1, Earth Sciences Division of Teledyne Inc., 2 November 1966.

7. M. Simpson, *et al.*,"Applicability of Inertialess Scanning Techniques to the Design of Surveillance Radar Antennas," Sedco Systems Inc., p. 10, March 1966. [AD 481375]

8. J. Ruze, "Antenna Tolerance Theory - A Review," *Proceedings IEEE*, *54*, pp. 633-640, April, 1966.

9. J. Capon, R.J. Greenfield, R.T. Lacoss, "Off-Line Signal Processing Results for the Large Aperture Seismic Array," Lincoln Laboratory Technical Note 1966-37, 11 July 1966.

10. M. Schwartz, W.R. Bennett,S. Stein, *Communication Systems and Techniques*, Chapter 10, McGraw-Hill Book Co., 1966.

11. *Handbook of Tables for Probability and Statistics*, Chemical Rubber Company, 1966, p. 299.

12. H. Jeffreys and K.E. Bullen, *op.cit.*

13. C.F. Richter, *Elementary Seismology*, W.H. Freeman and Company, 1958.

14. *Ibid.*, p. 664.

REFERENCES (cont.)

15. V.C. Anderson, "Digital Array Phasing," *Jour. Acoust. Soc. Am., 32,* pp. 867-870, July, 1960.

16. W.B. Davenport, Jr., "Signal-to-Noise Ratios in Band-Pass Limiters," *Jour. Applied Physics, 24,* pp. 720-727, June, 1953.

17. V.C. Anderson, *op. cit.,* p. 870.

18. W.R. Remley, *Jour. Acoust. Soc. Am., 39,* pp. 702-707, April, 1966.

19. V.C. Anderson, *loc. cit.*

20. W.R. Remley, *loc. cit.*

21. R.B. Blackman and J.W. Tukey, *The Measurement of Power Spectra,* Dover Publications, Inc., 1959.

22. W.B. Davenport, Jr. and W.L. Root, *Random Signals and Noise,* McGraw Hill Book Co., Inc., pp. 107-108, 1958.

23. R.B. Blackman and J.W. Tukey, *op. cit.*

24. J.W. Cooley and J.W. Tukey, "An Algorithm for the Machine Calculation of Complex Fourier Series," *Mathematics of Computation,* vol. 19, no. 90, pp. 297-301, April 1965.

25. *Ibid.*

26. D.W. McCowan, "Finite Fourier Transform Theory and Its Application to the Computation of Convolutions, Correlations, and Spectra," Teledyne Industries, Inc., 11 Oct. 1966 [AD 800371].

27 T.G. Stockham, Jr., "High Speed Convolution and Correlation," presented at the Spring Joint Computer Conference of the ACM, Boston, April 1966.

28. B.F. Howell, Jr. "Absorption of Seismic Waves," Institute of Science and Technology, University of Michigan, May, 1963.

29. T. Asada and K. Takano, "The Attenuation of Short Period P Waves in the Mantle," in "Lakewood Conference Proceedings: High Frequency Seismic Energy," Institute of Science and Technology, The University of Michigan, April, 1964.

30. B.F. Howell, Jr., *loc. cit.*

REFERENCES (cont.)

31. L.E. Brennan, "Angular Accuracy of a Phased Array Radar," *IRE Transactions of Antennas and Propagation*, Vol. AP-9, p. 268, May, 1961.

32. C.F. Richter, *op. cit.*, p. 664.

Unclassified

Security Classification

DOCUMENT CONTROL DATA - R & D

(Security classification of title, body of abstract and indexing annotation must be entered when the overall report is classified)

1. ORIGINATING ACTIVITY *(Corporate author)*
General Atronics Corporation
1200 East Mermaid Lane
Philadelphia, Pennsylvania 19118

2a. REPORT SECURITY CLASSIFICATION
Unclassified

2b. GROUP
N/A

3. REPORT TITLE
LARGE APERTURE SEISMIC ARRAYS

4. DESCRIPTIVE NOTES *(Type of report and inclusive dates)*
Final Report

5. AUTHOR(S) *(First name, middle initial, last name)*
None

6. REPORT DATE
June 1967

7a. TOTAL NO. OF PAGES
210

7b. NO. OF REFS
32

8a. CONTRACT OR GRANT NO.
AF 19(628)-5981

b. PROJECT NO.

c.

d.

9a. ORIGINATOR'S REPORT NUMBER(S)
ESD-TR-67-453

9b. OTHER REPORT NO(S) *(Any other numbers that may be assigned this report)*

10. DISTRIBUTION STATEMENT
This document has been approved for public release and sale; its distribution is unlimited.

11. SUPPLEMENTARY NOTES

12. SPONSORING MILITARY ACTIVITY
Directorate of Planning and Technology,
Electronic Systems Division, AFSC, USAF,
L. G. Hanscom Field, Bedford, Mass. 01730

13. ABSTRACT

Theoretical derivations and calculated array patterns are presented for the following seismic arrays: the existing LASA-Montana, a random array with an aperture comparable to LASA-Montana (200 km), and continental-size array with an aperture of several thousand kilometers. The use of LASA-Montana for determining epicenters of seismic events is discussed and results are presented that indicate errors on the order of 60 kilometers. Data on the correlation across LASA of various portions of seismograms are presented, and the implications for array processing gains are briefly discussed. Two tests for identifying earthquakes with depths between 10 and 40 km are introduced, and experiments on approximately 40 seismic events, on which both tests performed quite well, are summarized. The possibility of using DIMUS processing on a seismic array is discussed. Calculations are presented based on the conventional DIMUS processing as well as on a modified DIMUS scheme that appears to be significantly better. Calculations based on several seismic events show a significant amount of "signal" energy in the spectral region of 4 Hz in most of the records resulting from surface-focus events. Calculations based on records from deep Fiji Island earthquakes suggest an upper mantle Q of less than 500 for that region.

DD FORM 1 NOV 65 1473

Unclassified

Security Classification

14. KEY WORDS	LINK A		LINK B		LINK C	
	ROLE	WT	ROLE	WT	ROLE	WT
Seismology						
Arrays						
Signal Processing						
Spectral Analysis						
Seismic Wave Propagation						
Seismic Discrimination						
Hypocenter Determination						